N° d'ordre: 42204

MINES DOUAI

UNIVERSITE LILLE 1

INDIANA UNIVERSITY

THESE

présentée en vue d'obtenir le grade de

DOCTEUR

en

Spécialité: Optique, Lasers, Physico-Chimie, Atmosphère

par

Sofia SKLAVENITI

DOCTORAT DE L'UNIVERSITE LILLE 1

Titre de la thèse:

Développement et déploiement sur le terrain d'un analyseur pour la mesure de la vitesse de formation d'ozone dans la troposphère

Soutenue le 21 Novembre 2016 devant le jury d'examen:

Président	Christa FITTSCHEN	Directeur de Recherche CNRS, Université Lille 1
Rapporteur	Jonathan WILLIAMS	Docteur, Max-Planck-Institut fur Chemie
Rapporteur	Yoshizumi KAJII	Professeur, Kyoto University
Examinateur	Geoff TYNDALL	Directeur de Recherche, University Corporation for Atmospheric Research
Directeur De These	Nadine LOCOGE	Professeur, Ecole des Mines de Douai
Codirecteur De These	Philip STEVENS	Professeur, Indiana University
Encadrant	Sebastien DUSANTER	Maitre Assistant, Ecole des Mines de Douai

Laboratoire(s) d'accueil:
Dépt. SAGE (Sciences de l'Atmosphère et Génie de l'Environnement), Mines Douai, France
School of Public and Environmental Affairs, Indiana University, Bloomington, IN, États-Unis

Université des Sciences & Technologies de Lille
Ecole Doctorale des Sciences de la Matière, du Rayonnement et de l'Environnement

THESIS

for the degree of

Doctor of Philosophy

in
Atmospheric Chemistry

by

Sofia SKLAVENITI

Title of thesis:

Development and field deployment of an instrument to measure ozone production rates in the troposphere

Defended on 21 November 2016

Hosting laboratories:
Department SAGE (Atmospheric Sciencies and Environmental Engineering), Mines Douai, France
School of Public and Environmental Affairs, Indiana University, Bloomington, IN, USA

University of Sciences and Technology of Lille
Doctoral School of Material Sciences, Radiation and Environment
Discipline: Optics and Lasers, Physical Chemistry, Atmosphere

Acknowledgments

First of all, I want like to thank École des Mines de Douai and Indiana University for my PhD fellowship, as well as the region Nord–Pas-de-Calais for funding this work though the project MESFOZAT.

I would also like to thank my committee members, Christa Fittschen, Jonathan Williams and Yoshizumi Kajii for accepting to review my work, Geoff Tyndal, for accepting to be part of my defence panel and my thesis director, Nadine Locoge for her suggestions and advice.

This work would have never been possible without my supervisor Sebastien Dusanter, whom I deeply want to thank for his limitless patience, his enthusiastic encouragement and for showing me how to think and grow as a scientist. I also want to thank my co-supervisor, Phil Stevens, for his guidance and support, but also for introducing me to the American culture (including beers and tailgating).

A big thank you to Bill Bloss and Leigh Crilley from Birmingham University for the collaboration on $P(O_3)$ measurements, their hospitality and the interesting conversations we shared.

I also wish to thank Jonathan Raff and his students, Nicole Scharko and Mulu Kabede for offering their time and help using the CIMS instrument.

Thank you to Vinayak Sinha and especially his student Vinod Kumar, for visiting the lab in Mines Douai and performing tests on the ozone analyser that were proven to be useful for this work.

I couldn't miss thanking Vincent Michoud, who offered me the essential help and guidance in the lab when I first arrived in Mines Douai. I also want to thank people from Mines Douai who indirectly contributed to this project: Nathalie Redon for her help with LabView and electronics, Thierry Leonardis for technical assistance and the VOC measurements, Alexandre Tomas for his help with UV lamps and Emmanuel Tison for his technical expertise. I also want to thank my lab mates, both in Mines Douai and Indiana University for the experiences and the time we shared in the same working environment.

My friends in France, for making my first 1.5 year away from home so easy and fun, you guys know who you are, thank you. My friends in US, for making my first 1.5 year in the other side of the Atlantic such an unforgettable experience, my roommate Marta and all the "Bloom peoples" gang, thank you. My friends in Greece or other places in the world, for always being there for me despite living so far away, thank you.

Of course, I truly want thank my family, especially my mom and dad, for their constant encouragement and for believing in me. Ένα μεγάλο ευχαριστώ για την απεριόριστη αγάπη, τη συνεχή ενθάρυνση και την υποστήριξή σας.

Finally, I want to thank Diogo, for supporting me and understanding so well the ups and downs of the past three years. You have been the ultimate personal motivation behind this work. Thank you.

Στους γονείς μου

Table of contents

List of Tables

List of Figures

Introduction

Tropospheric ozone is a key species regarding air quality and climate issues. In addition to being the third most important greenhouse gas (IPCC, 2013b) this compound controls the oxidizing capacity of the atmosphere (Prinn, 2003) and affects human health (WHO, 2013) and vegetation growth (Ashmore, 2005). The detrimental impact of ozone on human health has been the core of many studies, such as a modeling study by Silva et al. (2013) estimating that approximately 470 000 premature deaths occur each year globally due to increasing ozone levels associated to anthropogenic activities. Moreover, the damage to vegetation due to ozone has direct impacts on agricultural economy. For example, the global economic loss to the farming community due to staple crops losses has been estimated to be higher than $10 billion annually until 2030, even with the lower limit of O_3 concentrations scenario (Avnery et al., 2011). It is clear that in a context where socio-economic impacts are at stake, it is crucial to understand the long-term trends of ozone and its global budget to develop efficient strategies for ozone regulation.

The current understanding of ozone production chemistry indicates that ozone is formed through reactions of peroxy radicals (HO_2+RO_2) with nitrogen monoxide (NO), producing nitrogen dioxide (NO_2), whose photolysis leads to ozone (Seinfeld and Pandis, 2006) The production rate of ozone, $P(O_3)$, depends on concentrations of oxides of nitrogen (NO_x =NO+NO_2) and Volatile Organic Compounds (VOCs), but also on production rates of radicals. Since ozone is not emitted directly but is a secondary pollutant formed photochemically in the troposphere, the reduction of ozone levels are achieved by reducing the emissions of its precursors.

However, the formation of ozone follows a complex nonlinear chemistry that makes strategies for reducing ozone precursors difficult to implement (Xing et al., 2011). For NO_x mixing ratios lower than a few ppbv, ozone production usually follows a "NO_x-limited" regime, where it increases with an increase of NO_x and is not sensitive to the VOC loading. In such an environment, reducing NO_x emissions would lead to a decrease of ozone production. For higher NO_x mixing ratios, as in many polluted urban environments, ozone production can be driven by a "NOx-saturated" regime, where the ozone production rate decreases with an increase of NO_x and a decrease of VOCs. Therefore, a decrease in NO_x emissions in these environments could cause an increase in ozone production.

Atmospheric chemistry models are widely used to describe the photochemical processes in the atmosphere. These models can be used to investigate the ozone production regimes at various locations to develop emission regulations that should lead to lower rates of ozone formation. However, there are still uncertainties

in the chemical mechanisms implemented in atmospheric models. For instance, $P(O_3)$ values calculated from direct measurements of peroxy radical concentrations during field campaigns often disagree with modeled values for NO_x mixing ratios higher than a few ppbv (Griffith et al., 2016;Ren et al., 2013;Chen et al., 2010;Dusanter et al., 2009b), questioning our understanding of the ozone production chemistry. Therefore, testing the chemistry in atmospheric models is necessary to ensure the efficiency of air quality regulations.

Atmospheric models are usually tested by comparing measured ambient concentrations of ozone to model predictions. However, while differences between ambient observations and model outputs can be due to an incomplete chemical mechanism, it can also be due to incomplete or erroneous emission inventories and to uncertainties associated with air mass transport. As a consequence, this approach is not straightforward to investigate the chemistry implemented in models. An alternative approach would consist of comparing ambient measurements of $P(O_3)$ to values calculated by a constrained box model, that are independent of emissions and air mass transport.

A method for direct $P(O_3)$ measurements was first proposed forty five years ago (Jeffries, 1971) but was not published in the peer-reviewed literature. The first MOPS (Measurement of Ozone Production Sensor) instrument was developed by Cazorla and Brune (2010) at the Pennsylvania State University and was recently improved by Baier et al. (2015). These authors have shown that ozone production rate measurements are feasible, as the instrument responded well to the ambient conditions and yielded $P(O_3)$ values that are within a reasonable range. However, as every new technique, there are still experimental issues to be resolved.

In this study, a new instrument for ozone production rate measurements (OPR) was designed and developed, characterized through laboratory and modeling experiments, and finally deployed in the field. To our knowledge, this is the third instrument in the world for ozone production rate measurements, with the second one belonging to Birmingham University, UK (unpublished work). While the operating principle in these three instruments is the same, the Mines Douai OPR instrument differs significantly from the other two, as it includes a different sampling geometry and a different detection system.

The first chapter of this manuscript presents the context of this study, including overviews of the importance of ozone as a local but also global pollutant, the ozone chemistry in the trosposhere, $P(O_3)$ quantification methods, and observed values of ozone production rates in different environments. This chapter concludes on the objectives of this study. The second chapter describes the design and the development of the Mines Douai OPR instrument and reports the laboratory characterization experiments performed for each part of the instrument. The third chapter includes a modeling study that was performed to highlight potential sources of errors and assess their impact on the measurements of $P(O_3)$. This modeling study was performed to

quantify the accuracy of $P(O_3)$ measurements. Finally, the field deployment of the instrument is described in the fourth chapter, along with modeling results and a comparison of the measurements to model outputs. This field deployment allowed assessment of the limitations of the Mines-Douai OPR instrument and to propose future improvements.

This work was performed at the Atmospheric Sciences and Environmental Engineering department (SAGE) from Mines Douai, France, and at the School of Public and Environmental Affairs (SPEA) from Indiana University, US.

Chapter 1. Tropospheric ozone and ozone production chemistry

1.1 Introduction

This chapter discusses the importance of ground level ozone and its impacts on climate, human health and vegetation. Furthermore, the chemistry of ozone production in the troposphere is described in detail, as well as previous studies in various urban environments quantifying ozone production rates, $P(O_3)$, and investigating the sensitivity of ozone production to its precursors. Additionally, current chemical mechanisms used to model atmospheric chemistry are described, and discrepancies with measurements are highlighted.

Finally, the performances and limitations of the only instrument capable of measuring ozone production rates, the MOPS instrument (Cazorla and Brune, 2010), are reported in section 1.5.2. Building this type of instrument and using it to characterize the in-situ ozone formation chemistry was the motive for this work. The objective and originality of the present study are described in section 1.6.

1.2 Detrimental effects of ozone

Ozone (O_3) is a natural constituent of the atmosphere and is present in both the stratosphere and the troposphere. In the stratosphere, the ozone layer is located at 15 to 30 km above the earth surface, with a peak concentration of approximately $5 \cdot 10^9$ molecules/cm^3 at 25 km, and acts as a protective layer absorbing most of the biologically damaging ultraviolet sunlight (WMO, 1998). In the troposphere, ozone is a secondary pollutant generated when mixtures of NO_x and VOCs are irradiated by the sunlight. Concentrations of O_3 near the Earth's surface (ground-level O_3) currently range from a few parts per billion by volume (ppbv) up to a few hundreds of ppbv when high O_3 precursor emissions coincide with appropriate meteorological conditions, such as high irradiation and high temperatures (Jacob and Winner, 2009).

While the presence of ozone is crucial in the stratosphere for the development of life on earth, it can act as a greenhouse gas (IPCC, 2013b) and can lead to detrimental impacts on both human health and ecosystems (Ashmore, 2005;WHO, 2013) in the troposphere.

1.2.1 Impacts on climate

On a global average, the incoming solar radiation energy is balanced approximately by the outgoing terrestrial radiation. Any factor that alters the redistribution of energy within the atmosphere and between the atmosphere, land and ocean can affect the climate. The difference between the solar irradiance absorbed by the earth and the energy emitted back to space, called 'radiative forcing', is used by climate scientists to assess and compare anthropogenic and natural drivers of climate change. A positive radiative forcing tends to warm the Earth's surface and lower atmosphere, while a negative radiative forcing tends to cool them.

As shown in Fig. 1.1, ozone in the atmosphere can either have negative or positive radiative forcing. The negative radiative forcing is due to the stratospheric ozone. In the stratosphere, ozone absorbs UV radiation from the sun, leading to local warming, but also emits radiation back to space, leading to local cooling. On the other hand, tropospheric ozone, being closer to the earth's surface, absorbs a large amount of the terrestrial infrared radiation and has a positive radiative forcing.

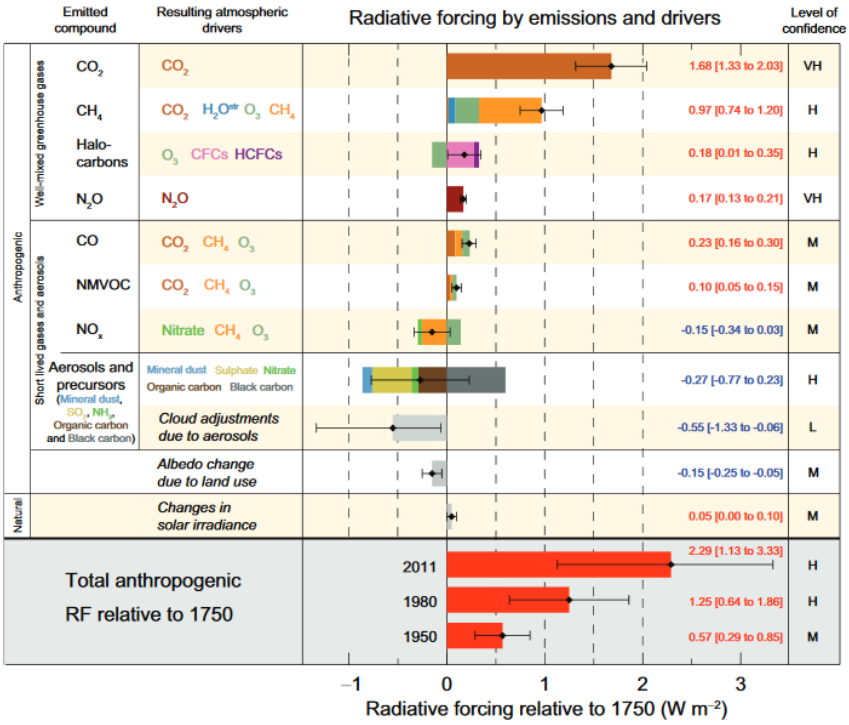

Figure 1.1: Radiative forcing estimates in 2011 relative to 1750 and aggregated uncertainties for the main different components affecting climate change (IPCC, 2013a).

The naturally occurring greenhouse gases that exhibit positive radiative forcing (water vapor, carbon dioxide, ozone, methane and nitrous oxide) absorb the infrared terrestrial radiation and, as a result, regulate the temperature and permit the development of life on earth. However, increases in the concentrations of these gases in the lower atmosphere will lead to increased temperature at the ground level.

he increase of tropospheric ozone since pre-industrial times (section 1.3), led to an increase of the global average radiative forcing due to tropospheric ozone by 0.35 ± 0.2 Wm^{-2} (IPCC, 2013b), making tropospheric ozone the third most important greenhouse gas after CO_2 and CH_4.

Additionally, except of being a greenhouse gas, ozone is an important precursor of the hydroxyl radical (OH) (see section 1.4.1), which is the main oxidant of the atmosphere. By altering the OH levels, ozone indirectly impacts the concentrations of other greenhouse gases that are oxidized by OH, making its impact on the climate more complicated.

1.2.2 Impacts on health

Ozone is an important pollutant at the urban and rural scales and a main constituent of photochemical smog. The impacts of ozone on human health are well established. It has been associated with a wide spectrum of human health effects, most of which are related to the respiratory system (WHO, 2008, 2013;EEA, 2013). Breathing ozone can trigger a variety of health problems including chest pain, coughing, throat irritation, and congestion and can worsen chronic bronchitis, emphysema, and asthma. Repeated exposure to ground level ozone can reduce lung function and inflame the linings of the lungs, but may also permanently damage the lung tissue.

It is accepted that detrimental effects occur above 50 ppbv (WHO, 2006), and although it is unclear whether there is a threshold for effects on humans, impacts are thought to occur at ambient concentrations even below 50 ppbv, especially for individuals that are more at risk than others (young and old people). People with lung diseases, children, older adults, and people who are active outdoors may be particularly sensitive to ozone. Children are at greatest risk from exposure to ozone because their lungs are still developing and they are more likely to be active outdoors when ozone levels are high, which increases their exposure. For this reason, children are more likely than adults to develop asthma (EPA, 2012).

Research studies indicate that ozone exposure may increase the risk of premature death from heart and lung diseases (Jerrett et al., 2009). In Europe, the average estimate for premature deaths due to increased ozone was 21,400 for the year 2000 (EEA, 2007). The European Union estimated the cost of health damage to € 11.9 billion for the year 2000, due to the premature deaths and an increased used of medicine for respiratory conditions. There is also evidence linking long-term exposure to ozone with deterioration in reproductive health and greater mortality effects than previously thought (WHO, 2013).

The health effects of O_3 increase with increasing concentrations and high ambient temperatures, although may vary for different areas. For example, the relative impact of O_3 and high temperatures on mortality during the European 2003 heat wave was investigated in nine French cities (Bordeaux, Le Havre, Lille, Lyon, Marseilles, Paris, Rouen, Strasbourg and Toulouse) (Filleul et al., 2006). The excess risk of mortality attributable to O_3 was very heterogeneous, ranging from 2.5% in Bordeaux to 85.3% in Toulouse. Various reasons were suggested for this heterogeneity, including the vulnerability of the population (poverty, age, social isolation, chronic disease burden) and differences in the urban temperature compared to the surrounding rural areas. These results show that the effect of O_3 during heat waves, while generally small in relation to the effects of temperature, is likely to constitute an additional health impact, but that the extent of this effect is likely to vary considerably from place to place.

1.2.3 Impacts on vegetation

Ozone has been shown to damage sensitive plant species and ecosystems, including forests, parks and wildlife refuges, and cause reductions in crop production and tree growth (Ashmore, 2005;EPA, 2006). In addition to reduced tree growth and visible injury to leaves, continued ozone exposure over time can lead to increased vulnerability of sensitive plant species to diseases, damage from insects, effects of other pollutants, and harm from severe weather. These effects can also have adverse impacts on ecosystems, including loss of species diversity and changes to habitat quality and water and nutrient cycles. Impacts on vegetation generally occur above 40 ppbv (WHO, 2006), although this is species dependent and varies according to environmental conditions.

Ozone not only affects the tree growth and the rates of photosynthesis, but also reduces the yield of staple crops. There is a substantial body of evidence from North America and Europe, supported by studies in Asia, Africa and Latin America, related to reductions in the yield of sensitive crop species because of elevated O_3 levels, along with estimates of the economic impacts of crop loss due to O_3 exposure.

For example, in a study from Mills and Harmens (2012) the economic impacts of ozone on wheat production in Europe were modeled for the year 2000, using a response function including ozone, wheat production and market prices. Approximately € 3.2 billion were estimated to be lost in 2000 due to ozone effects on wheat grain yield. Taking into account expected reductions in ozone concentrations in Europe due to emission controls, € 1.96 billion are expected to be lost in 2020, so ozone effects were found to be reduced only by one third in 20 years.

Another study (Sinha et al., 2015) estimated the ozone related crop yield losses for wheat, rice, cotton and maize for a region in northern India for 2011-2013, showing total economic cost losses in the range of $ 6.5 billion for 2012-2013 and $ 3.7 billion for 2013-2014 as a lower limit.

Finally, a study from Avnery et al. (2011) examined the costs associated with worldwide staple crops losses (soybean, maize and wheat) according to two different O_3 precursor emission scenarios until 2030: the IPCC A2 and B1 storylines, representing upper and lower limit projections of O_3 pollution. The first scenario showed yield loss of wheat due to O_3 exposure that ranged from 5.4% to 26%, 15% to 19% for soybean and 4.4% to 8,7% for maize. The total global agricultural losses were estimated at $17-35 billion annually. The second scenario showed less severe losses: 4-17% for wheat, 9.5-15% for soybean and 2.5-6% for maize, associated with total losses worth $12-21 billion annually.

All these results suggest that ozone pollution has clear implications on vegetation, not only regarding forest ecosystems but also future global food security, as future O_3 concentrations may place further pressure on agricultural systems.

1.3 Tropospheric ozone trends

In remote regions that are not impacted by anthropogenic emissions, ozone concentrations are often denoted as baseline or background ozone, consisting of two components: the local production from natural emissions of ozone precursors and (ii) the advection of ozone (or ozone precursors) produced further away by synoptic scale winds (Vingarzan, 2004).

The natural ozone component originates from its photochemical production involving naturally emitted NO_x and VOCs. Nitrogen oxides can naturally be emitted from soils, as a consequence of microbial processes (Fowler et al., 1998), or produced by lightning (Miyazaki et al., 2014) and forest fires (Mebust et al., 2011). The predominant source for naturally emitted VOCs is vegetation. Biogenic VOCs (BVOCs) are highly reactive with atmospheric oxidants and the magnitude of their emissions increases with increased sunlight and temperature. Other natural sources of VOCs are emissions from wetlands and geothermal leakage from underground deposits (Reid et al., 2008). Finally, an additional natural source of ozone in the troposphere is a transfer from the stratosphere during a phenomenon known as "tropopause folding", which occurs under specific dynamic conditions in the atmosphere (Beekmann et al., 1997).

In regions impacted by human activities, tropospheric ozone also depends on anthropogenic emissions of NO_x and VOCs. Anthropogenic VOCs are emitted due to either evaporation or incomplete combustion of fuels. Other anthropogenic sources of VOCs are biomass burning (Keywood et al., 2013) and emissions from chemical and petroleum industries (Wei et al., 2014). NO_x are formed from the combination of N_2 and O_2 under high combustion temperatures, while significant amounts of NO_x also originate from the combustion of fossil fuels in power plants, industrial processes, and home heaters (IPCC, 2013b).

Once formed (see section 1.4.1), the average lifetime of O_3 in the troposphere has been estimated to be 22±2 days, as calculated from 26 atmospheric chemistry models (Stevenson et al., 2006), which is long enough to transport it from polluted regions to remote areas and between continents. Figure 1.2 shows how model-calculated surface O_3 concentrations have increased from May through August between 1860 and 1993 (Akimoto, 2003). According to this analysis, the concentration of surface O_3 over the mid- and high-latitudes (Eurasian and North American continents) was 15-25 ppbv in 1860 but has increased to 40-50 ppbv, even in relatively remote areas. A similar picture is observed over the Pacific Ocean, where ozone increased from 10-15 ppbv to 20-30 ppbv. It is easily seen that the elevation of background levels of ozone along with long-range transport can add to ozone produced locally in amounts that would not otherwise have been substantial, leading to exceedances of critical levels. This contribution of transport from other continents makes ozone not only a regional problem, but an issue of global concern.

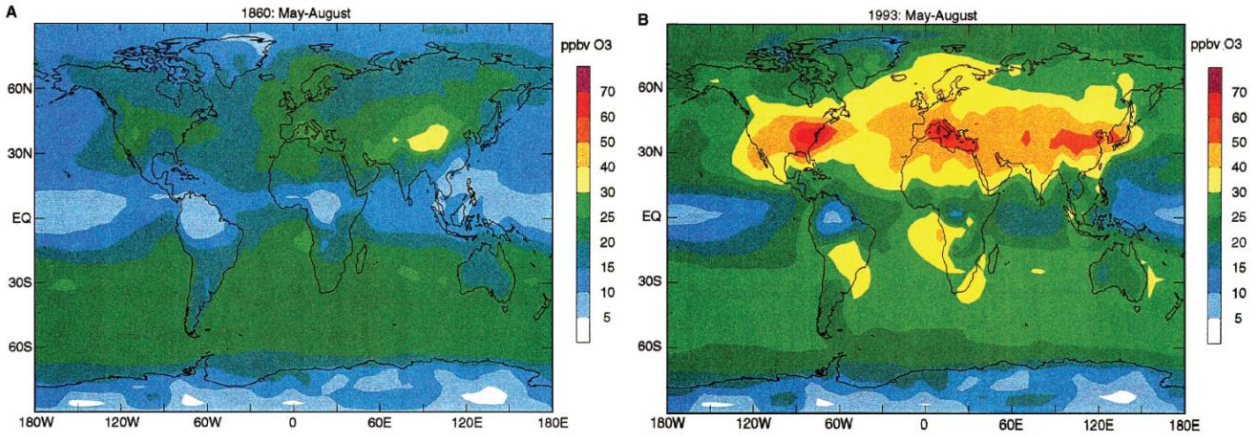

Figure 1.2: Model-calculated surface O_3 during the growing season in the Northern Hemisphere (May through August) in (A) 1860 and (B) 1993 (Akimoto, 2003)

Measurements at stations located in remote areas and/or at high elevations, are assumed to be less affected by anthropogenic influences and measurements performed at these locations can provide an indication of past changes of background ozone levels. The earliest ozone measurements began in the late 1800s, and even though these early observations are semi-quantitative, a range of 10-20 ppbv has been observed for stations in Europe and North America in the early 1900s (Bojkov, 1986;Varotsos and Cartalis, 1991). Although background ozone concentrations vary seasonally and with latitude, annual average ozone concentrations at background sites around the world ranged from 20-45 ppbv (Vingarzan, 2004) during the late 1900s to early 2000s, with hourly annual maximum ozone concentrations reaching levels of 50-100 ppbv. Comparisons of these measurements with values reported in the late 19th-early 20th centuries, indicate that ozone background levels have risen by approximately a factor two, with a rate of 0.5–2% per year.

Figure 1.3 shows measurements of O_3 mixing ratios in various rural stations around the world. The left panel shows measurements mainly performed at mountaintops of western Europe, representative of the free troposphere, indicating an increase in background ozone of approximately 0.5 ppbv/year for the period 1950 – 2000. After 2000, with the implementation of air quality regulations (section 1.4.5), background ozone concentrations in Europe either decreased or leveled off. The middle panel of Fig. 1.3 indicates that ozone levels measured in stations of East Asia or western N. America kept increasing at a rate of approximately 0.3 ppbv/year for the period 1990 – 2010. The rest of the world includes less contaminated sites, and therefore lower ozone trends have been observed.

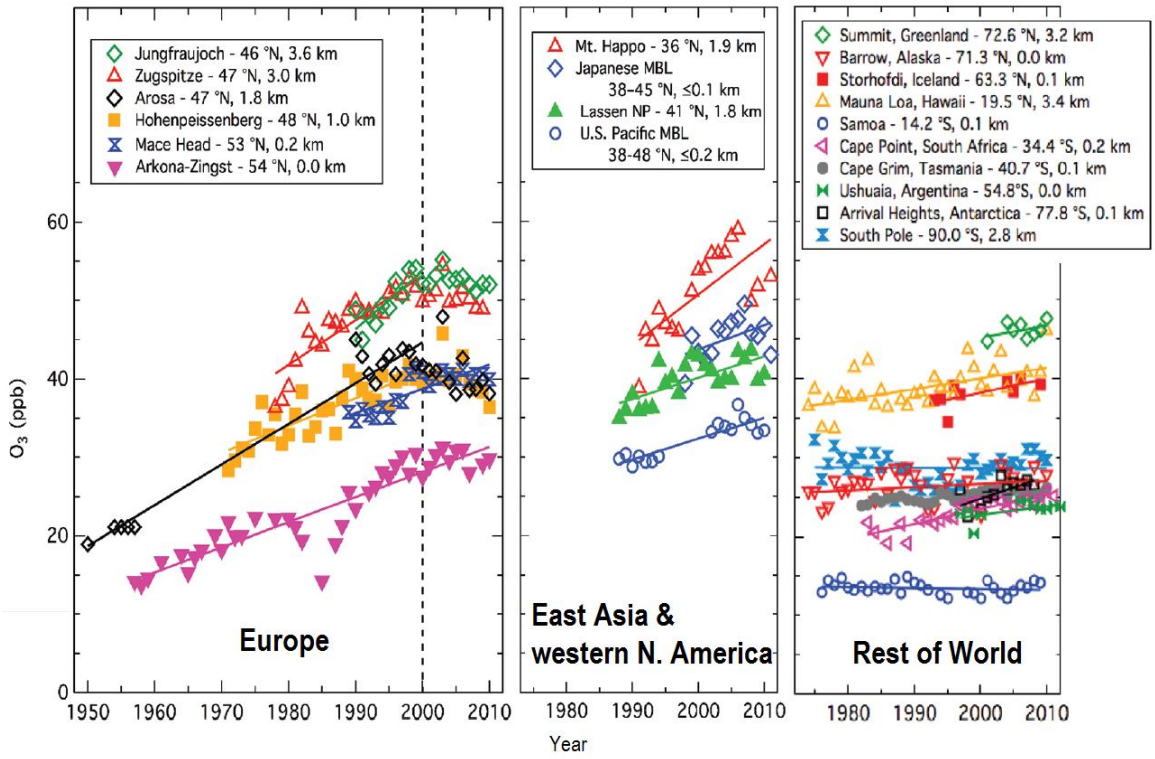

Figure 1.3: Surface ozone mixing ratios at various rural sites in Europe (left), East Asia and western N. America (middle) and rest of the world (right) (modified from the original of IPCC (2013b)).

1.4 Chemistry of ozone production and emission controls

Following the increase of ozone concentrations over the past century, it is essential to efficiently reduce ozone levels in the troposphere. As mentioned above, ozone is not emitted directly in the atmosphere, but is produced photochemically as a secondary pollutant. The local ozone production is driven by levels of ozone precursors: nitrogen oxides (NO_X), carbon monoxide (CO) and volatile organic compounds (VOCs).Therefore, for efficient ozone controls, a complete understanding of the ozone formation chemistry is essential. However, ozone concentrations observed at a specific location not only depend on the availability of chemical precursors, but also on deposition rates of ozone and meteorological processes, such as irradiation, advection, cloud cover formation, and precipitation. This dependence is expressed by Eq. 1.1 (Cazorla and Brune, 2010):

$$\frac{\partial[O_3]}{\partial t} = P(O_3) - \frac{\upsilon}{H}[O_3] + u_i \frac{\partial[O_3]}{\partial x_i} \qquad \text{(Eq. 1.1)}$$

where the first term $P(O_3)$ is the net chemical ozone production rate (described in section 1.4.2), the second term the surface deposition, υ being the deposition velocity, H the mixed layer height and $[O_3]$ the ozone concentration, and the last term the local advection, consisting of the velocity u_i in three spatial directions and the ozone gradient in those three directions.

1.4.1 Radical and ozone formation chemistry

The formation chemistry of ozone has been summarized in a very comprehensible way by many authors (Seinfeld and Pandis, 2006;Finlayson-Pitts and Pitts, 1999) According to our current understanding of tropospheric chemistry, the main source of ozone during daylight hours is the photolysis of NO_2 (R1.1-1.2), whose rate peaks at 398 nm. The production of ozone from cross-reactions of peroxy radicals is negligible and is not discussed below.

In the troposphere, NO, NO_2 and O_3 reach a photostationary state (PSS), represented by reactions R1.1-1.3:

$NO_2 + h\nu \rightarrow NO + O(^3P)$ (R 1.1)

$O(^3P) + O_2 + M \rightarrow O_3 + M$ (R 1.2)

$NO + O_3 \rightarrow NO_2 + O_2$ (R 1.3)

$O(^3P)$ is an atom of oxygen whose energy is at the ground-state. Atomic oxygen is very reactive and, under tropospheric conditions of pressure (200–1000 mbar) and temperature (220–300 K), most $O(^3P)$ atoms react with molecular oxygen to produce ozone. Assuming that $O(^3P)$ is in steady state in R 1.1-1.2, the steady state ozone concentration can be expressed as:

$$[O_3] = \frac{j_{NO_2}[NO_2]}{k_{NO+O_3}[NO]} \quad \text{(Eq. 1.2)}$$

where the brackets represent concentrations, j_{NO_2} the photolysis rate of NO_2, and k_{NO+O_3} the bimolecular rate constant for the reaction between NO and O_3. If each side of Eq. 1.2 is divided by $[O_3]$, the result is termed the Leighton ratio, Φ (Leighton, 1961), which should equal unity if O_3+NO is the only process to convert NO into NO_2 :

$$\Phi = \frac{j_{NO_2}[NO_2]}{k_{NO+O_3}[NO][O_3]} \quad \text{(Eq. 1.3)}$$

However, the sunlight also photolyzes ozone, producing excited oxygen atoms, $O(^1D)$, as expressed by R1.4. Collisions of $O(^1D)$ with molecular oxygen or nitrogen (M in R 1.5) quench it back to its ground atomic state, $O(^3P)$. The large abundance of water vapor in the troposphere opens a path for collisions of $O(^1D)$ with H_2O, as shown by R1.6, towards the formation of the hydroxyl radical (OH).

$O_3 + h\nu \rightarrow O_2 + O(^1D)$ (R 1.4)

$O(^1D) + M \rightarrow O(^3P) + M$ (R 1.5)

$O(^1D) + H_2O \rightarrow 2OH$ (R 1.6)

The hydroxyl radical along with ozone, and to a smaller extend the nitrate radical (NO_3), make up the oxidative nature of the atmosphere. Reactions R 1.4 and R 1.6 are thought to be the main contributors to the formation of OH in the global troposphere (Monks, 2005). Other sources of OH include the photolysis of nitrous acid (HONO, R 1.7) and hydrogen peroxide (H_2O_2, R 1.8) as well as the reaction of ozone with alkenes (R 1.9):

$$HONO + h\nu \rightarrow OH + NO \quad \text{(R 1.7)}$$

$$H_2O_2 + h\nu \rightarrow 2OH \quad \text{(R 1.8)}$$

$$O_3 + \text{alkenes} \rightarrow \alpha OH + \text{other species} \quad \text{(R 1.9)}$$

The reaction of OH with CO, CH_4 or VOCs generates the hydroperoxyl (HO_2) and organic peroxy (RO_2) radicals (R 1.10-1.11). These radicals (RO_2 and HO_2) subsequently react with NO (R 1.12, R 1.14), converting NO into NO_2 without consumption of O_3, thus leading to higher concentrations of ozone, different from that calculated from the photostationary state (Eq. 1.2). Meanwhile, the peroxy radicals are converted back into OH, which can then oxidize other VOCs and form additional peroxy radicals.

$$CO + OH \xrightarrow{O_2} HO_2 + CO_2 \quad \text{(R 1.10)}$$

$$RH + OH \xrightarrow{O_2} RO_2 + H_2O \quad \text{(R 1.11)}$$

$$RO_2 + NO \rightarrow RO + NO_2 \quad \text{(R 1.12)}$$

$$RO + O_2 \rightarrow R'CHO + HO_2 \quad \text{(R 1.13)}$$

$$HO_2 + NO \rightarrow OH + NO_2 \quad \text{(R 1.14)}$$

As a consequence, the value of Φ can deviate positively from unity since chemical processes other than the reaction between NO and O_3 convert NO into NO_2. This deviation can be expressed by Eq. 1.4, where $[O_3]$ is the measured ozone concentration:

$$\Phi = 1 + \frac{k_{HO_2+NO}[HO_2] + \sum k_{RO_2+NO}[RO_2]}{k_{NO+O_3}[O_3]} \quad \text{(Eq. 1.4)}$$

Assuming a similar rate constant for R 1.12 and R 1.14 ($k_{NO+\text{peroxy}}$), the total concentration of peroxy radicals can be derived from Eq. 1.5:

$$[HO_2] + \sum[RO_2] = ([O_3]_{SS} - [O_3]) \frac{k_{NO+O_3}}{k_{NO+peroxy}} \quad \text{(Eq. 1.5)}$$

Here, $[O_3]_{SS}$ is calculated from Eq. 1.2 and $[O_3]$ is the measured ambient ozone concentration. Other pathways can also lead to the conversion of NO into NO_2 without O_3 consumption, e.g. the reactions of NO

with the nitrate radical (NO_3) and halogen monoxide compounds (XO, with X=Cl, Br, I). Therefore, the Leighton ratio is usually regarded as an indicator for photochemical ozone production.

Additional processes that take place involve O_3 consumption through its reaction with OH and HO_2 as shown in reactions R 1.15-1.16:

$$O_3 + OH \rightarrow HO_2 + O_2 \quad \text{(R 1.15)}$$

$$O_3 + HO_2 \rightarrow OH + 2O_2 \quad \text{(R 1.16)}$$

Ozone is produced continuously through the catalytic cycling of HO_x and NO_x, until a termination reaction stops the cycle. There are two types of termination reactions; if the reactivity of OH with NO_x species is large compared to the reactivity of OH with VOCs, the OH radicals react with NO_2 to form nitric acid (R 1.17) instead of continuing to oxidize VOCs, and a fraction of RO_2 radicals react with NO to produce organic nitrates (R 1.18).

$$OH + NO_2 + M \rightarrow HNO_3 + M \quad \text{(R 1.17)}$$

$$RO_2 + NO + M \rightarrow RONO_2 + M \quad \text{(R 1.18)}$$

In contrast, when the reactivity of OH with VOCs is much larger than for NO_x, radical terminations are due to self- and cross-reactions of radicals. These termination reactions are shown in R 1.19-1.21.

$$RO_2 + HO_2 \rightarrow ROOH \quad \text{(R 1.19)}$$

$$HO_2 + HO_2 \rightarrow H_2O_2 + O_2 \quad \text{(R 1.20)}$$

$$OH + HO_2 \rightarrow H_2O + O_2 \quad \text{(R 1.21)}$$

These two types of radical terminations are very important in atmospheric chemistry and lead to different regimes of ozone formation as discussed in section 1.4.3.

The chemical reactions discussed above form a complex system of chain reactions that are the basis of ozone production. These reactions are of three types: *initiation*, where closed shell molecules lead to radical production, *propagation*, where a radical species is converted into another radical, and *termination*, where a radical species is transformed into a closed shell molecule. A schematic of the radical chain reactions (initiation, propagation and termination) is given in Fig. 1.4. Initiations are in orange, propagations in red and terminations in purple color.

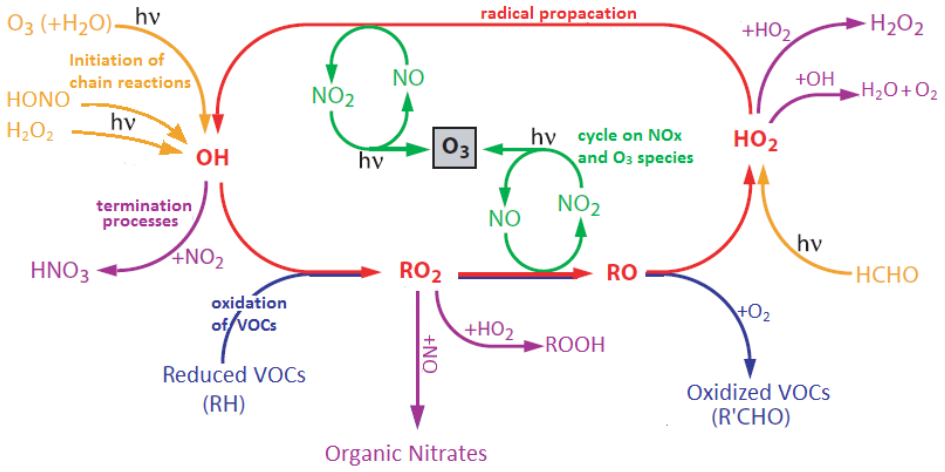

Figure 1.4: Radical chain cycling (Aumont, 2005)

A simple example to illustrate the radical chain cycling displayed in Fig. 1.4 is the oxidation of methane. The product of reaction R 1.22 is the methyl radical, CH_3, which is rapidly oxidized to form the methyl peroxy radical, CH_3O_2, as shown in R 1.23. Depending on the concentration of NO, methyl peroxy radicals lead to the formation of methoxy radicals, CH_3O, and NO_2 (R 1.24), and therefore ozone production, or react with another peroxy radical (R 1.27) to terminate the radical propagation chain by the formation of methyl peroxide, CH_3OOH. It is interesting to note that CH_3OOH is a radical reservoir species since a fraction of it can photolyze, releasing a new methoxy radical (R 1.28), which resumes the conversion of NO into NO_2, and hence the production of ozone. Another pathway of the reaction of CH_3O_2 with NO can terminate the radical propagation chain through the production of methyl nitrate (R 1.25), CH_3ONO_2 with a yield of approximately 3%.

If the oxidation of methane follows the path of ozone production, formaldehyde (HCHO) is also formed as shown in R 1.26. The photolysis of formaldehyde has two paths. One produces the neutral species H_2 and CO, as indicated by R 1.30. The second paths produces H atoms and HCO radicals that quickly combine with O_2 to produce HO_2 as shown in R 1.31 (R 1.32 and R 1.33). HO_2 radicals then react with NO producing more NO_2 and reproducing OH (R 1.14).

$CH_4 + OH \rightarrow CH_3 + H_2O$ (R 1.22)

$CH_3 + O_2 + M \rightarrow CH_3O_2 + M$ (R 1.23)

$CH_3O_2 + NO \rightarrow CH_3O + NO_2$ (R 1.24)

$CH_3O_2 + NO + M \rightarrow CH_3ONO_2 + M$ (R 1.25)

$CH_3O + O_2 \rightarrow HCHO + HO_2$ (R 1.26)

$CH_3O_2 + HO_2 \rightarrow CH_3OOH + O_2$ (R 1.27)

$CH_3OOH + h\nu \rightarrow CH_3O + OH$ (R 1.28)

$CH_3OOH + OH \rightarrow CH_3O_2 + H_2O$ (R 1.29)

$HCHO + h\nu \rightarrow H_2 + CO$ (R 1.30)

$HCHO + h\nu \rightarrow H + HCO$ (R 1.31)

$H + O_2 \rightarrow HO_2$ (R 1.32)

$HCO + O_2 \rightarrow HO_2 + CO$ (R 1.33)

$HO_2 + NO \rightarrow OH + NO_2$ (R 1.14)

For the path that yields the maximum production of ozone, if we neglect the small yield for the formation of methyl nitrate, the full oxidation of a molecule of methane would lead to the conversion of 4 molecules of NO into NO_2, and as a consequence the production of 4 ozone molecules (Seinfeld and Pandis, 2006). If CO produced in R 1.33 would be further oxidized, it would lead to an additional ozone molecule, resulting in 5 O_3 molecules for one CH_4 molecule.

1.4.2 Ozone production rates

As described above, ozone production is the production rate of NO_2 molecules from HO_2+NO (R14) and RO_2+NO (R11) reactions, assuming that NO_2 is then photolyzed during daytime. The gross instantaneous ozone production rate can thus be written as follows:

$$p(O_3) = k_{HO_2+NO}[HO_2][NO] + \sum_i(\Phi_i k_{RO_{2,i}+NO}[RO_{2,i}][NO]) \quad \text{(Eq. 1.6)}$$

where k_{HO_2+NO} is the rate constant of the reaction between HO_2 and NO, $k_{RO_{2,i}+NO}$ the rate constant of the reaction between $RO_{2,i}$ and NO, and Φ_i the branching ratio of the reaction between RO_2 and NO that leads to the production of RO and NO_2 (the other pathway could be the production of $RONO_2$).

For $p(O_3)$ calculations, Φ_i is usually considered equal to unity. However, studies have shown that this branching ratio decreases with increasing carbon number, increasing pressure and decreasing temperature, reaching about 0.7 for carbon atoms >10 and atmospheric conditions (Orlando and Tyndall, 2012). Therefore, calculations assuming a branching ratio of unity for all RO_2+NO reactions would significantly overestimate $p(O_3)$.

In order to quantify the net ozone production rate, the chemical ozone loss rate also needs to be determined. The ozone loss is mainly due to five different reaction pathways:

(i) ozone photolysis leads to the formation of an excited oxygen atom, $O(^1D)$, which reacts with H_2O towards the formation of hydroxyl radicals (R 1.4 - 1.6).

(ii) ozone reacts with OH to form hydroperoxyl radicals (R 1.15).

(iii) ozone reacts with HO_2 leading to OH as shown in reaction R 1.16.

(iv) ozone is lost through reactions with alkenes.

(v) ozone can be lost indirectly, through the loss of NO_2 to reservoir species such as HNO_3 (Monks, 2005), so the reaction between OH and NO_2 is also accounted as an O_3 loss. The ozone loss rate from each pathway can be described by Eqs. 1.7 – 1.11 respectively:

$$l_1(O_3) = k_{O(^1D)+H_2O}[O(^1D)][H_2O] \quad \text{(Eq. 1.7)}$$

$$l_2(O_3) = k_{OH+O_3}[OH][O_3] \quad \text{(Eq. 1.8)}$$

$$l_3(O_3) = k_{HO_2+O_3}[HO_2][O_3] \quad \text{(Eq. 1.9)}$$

$$l_4(O_3) = \sum_i (k_{O_3+Alkene_i}[O_3][Alkene_i]) \quad \text{(Eq. 1.10)}$$

$$l_5(O_3) = k_{OH+NO_2}[OH][NO_2] \quad \text{(Eq. 1.11)}$$

The excited oxygen atom, besides reacting with H_2O (R 1.6), can be quenched back (R 1.5) to its ground atomic state, $O(^3P)$, by collisions of $O(^1D)$ with oxygen or nitrogen (M). Thus, in a steady state, the formation of $O(^1D)$ is equal to its consumption:

$$J(O_3) * [O_3] = k_{O(^1D)+H_2O}[H_2O][O(^1D)] + k_{O(^1D)+M}[M][O(^1D)] \quad \text{(Eq. 1.12)}$$

where $J(O_3)$ is the photolysis frequency (J-value) for ozone photolysis and $[M]$ the concentration of N_2+O_2. $[O(^1D)]$ can be calculated as follows:

$$[O(^1D)] = \frac{J(O_3) * [O_3]}{k_{O(^1D)+H_2O}[H_2O] + k_{O(^1D)+M}[M]} \quad \text{(Eq. 1.13)}$$

The quantity $f = \frac{k_{O(^1D)+H_2O} * [H_2O]}{k_{O(^1D)+H_2O} * [H_2O] + k_{O(^1D)+M} * [M]}$ expresses the fraction of $O(^1D)$ atoms reacting with H_2O. Replacing *f* into Eq. 1.7 and adding all the loss terms (Eq. 1.7 – 1.11) the ozone loss rate is given by:

$$l(O_3) = f \times J(O_3) \times [O_3] + k_{OH+O_3}[OH][O_3] + k_{HO_2+O_3}[HO_2][O_3] + \sum_i \left(k_{O_3+Alkene_i}[O_3][Alkene_i]\right) + k_{OH+NO_2}[OH][NO_2] \quad \text{(Eq. 1.14)}$$

Finally, the net production of ozone results from the imbalance between chemical production (Eq. 1.6) and chemical loss (Eq. 1.14), as shown by Eq. 1.15:

$$P(O_3) = p(O_3) - l(O_3) \quad \text{(Eq. 1.15)}$$

It is important to note that $p(O_3)$ and $P(O_3)$ are the gross and net ozone production rates, respectively. Generally, these values are close because the loss term is small. While $p(O_3)$ can reach values of 80 ppbv/h or more in a polluted urban environment, $l(O_3)$ exhibits values of a few ppbv/h (Sommariva et al., 2011). From an environmental viewpoint, the important term to be known is the net rate of ozone production, $P(O_3)$, rather than the individual components that contribute to that rate.

1.4.3 Ozone production regimes

Figure 1.5 shows the results of model calculations where O_3 concentration isopleths, simulated over the eastern United States, are plotted as a function of NO_x and hydrocarbon emissions (Sillman et al., 1990). The thick line on the figure separates the two different regimes of O_3 production: the NO_x-limited and NO_x-saturated regimes. To the left of the line is the NO_x-limited regime: O_3 concentrations increase with increasing NO_x and are insensitive to hydrocarbons. To the right of the line is the NO_x-saturated regime (also called VOC-limited): O_3 concentrations increase with increasing VOCs and decrease with increasing NO_x.

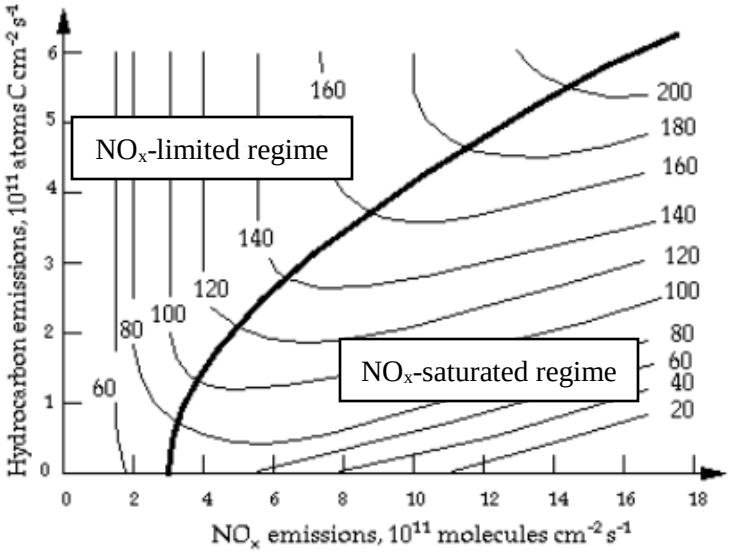

Figure 1.5: Ozone concentration isopleths simulated by a regional photochemical model as a function of NO_x and hydrocarbon emissions. The thick line separates the NO_x-limited (top left) and NO_x-saturated (bottom right) regimes (Sillman et al., 1990)

The non-linear dependence of O_3 on precursor emissions is readily apparent in Fig. 1.5. In the NO_x-limited regime, hydrocarbon emission controls are of no benefit for decreasing O_3. In the NO_x-saturated regime, reduction of NO_x emissions causes an increase in O_3.

The two different regimes can also be identified in Fig. 1.6, where the net ozone production rate, $P(O_3)$, and the OH concentration are presented as a function of NO_x concentrations. The calculations for $P(O_3)$ have

been done from measurements of HO_x and NO_x species in a clean rural site of eastern Germany, during summertime (Ehhalt, 1998). At the left side of the figure is the NO_x-limited regime, while in the right side the NO_x-saturated regime. The position of the maximum in OH and $P(O_3)$ indicates the turnover point between the two regimes. The exact position of this turnover point characterizes the sensitivity of $P(O_3)$ to ozone precursors and depends on the NO_x mixing ratio, the VOC reactivity (Σk_{VOC+OH} [VOC]) and the radical initiation rates (Kleinman, 2005).

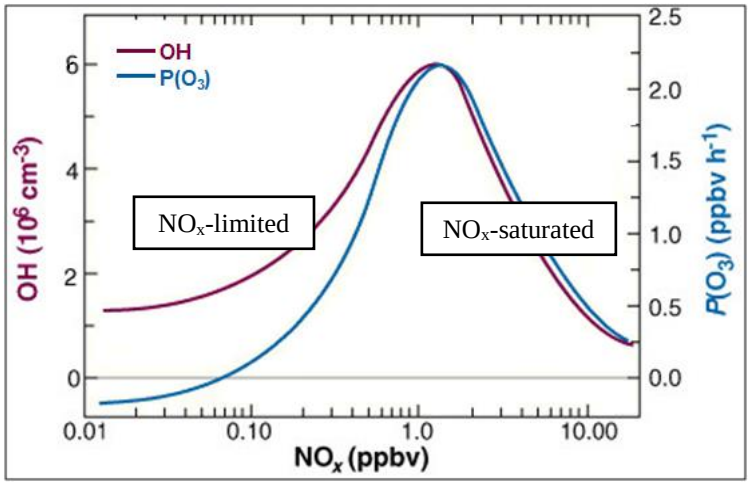

Figure 1.6: OH concentration and net $P(O_3)$ as a function of NO_x concentration, calculated for a clean rural site in eastern Germany (Ehhalt, 1998)

The determination of the ozone production regime is the result of a "competition" between the radical propagation and termination processes discussed in section 1.4.1. In a NO_x poor environment (NO_x-limited regime), the termination reactions are based on radical-radical reactions (R 1.19 – R 1.21), so an increase of NO_x would favor propagation processes (R 1.12, R 1.14) more than termination processes (R 1.17-R 1.21), and finally would increase the conversion rate of NO into NO_2, and as a consequence ozone production. On the other hand, in a NO_x rich environment (NO_x-saturated regime), the termination processes are driven by radical-NO_x reactions (R 1.17-1.18), and an increase in NO_x would enhance the termination rates more than the propagation rates, leading to a decrease in ozone production.

Assessing the ozone production regime and the $P(O_3)$ sensitivity to ozone precursors has been the subject of various studies (Kleinman, 1994, 2005;Sillman et al., 1990;Sillman, 1995;Jaeglé et al., 2001;Tonnesen and Dennis, 2000). Sillman (1995) and Sillman et al. (1998) identified several secondary reaction products that show different correlation patterns for NO_x-limited and NO_x-saturated regimes. The idea behind this work was to identify indicator species or species ratios in order to examine the O_3-NO_x-VOC sensitivity directly from ambient measurements rather than from models. These authors built metrics based on compound ratios to identify ozone production regimes from ambient measurements of these compounds. The most important

metrics are ratios such as O_3/NO_y, O_3/NO_z, O_3/HNO_3 and H_2O_2/NO_z (NO_y includes all the oxidized forms of nitrogen in the atmosphere such as nitric oxide (NO), nitrogen dioxide (NO_2), nitric acid (HNO_3), and organic nitrates, while $NO_z = NO_y – NO_x$). For example, the transition between VOC-sensitive and NO_x-sensitive chemistry happens at a value of the O_3/NO_y indicator of 6-8, O_3/NO_z of 8-10, O_3/HNO_3 of 12-15 and H_2O_2/NO_z of 0.2-0.25. Lower values of the indicators correspond to VOC-sensitive chemistry, while higher values correspond to NO_x sensitive chemistry. The correlations between O_3 and NO_y, and O_3 and NO_z are especially important because measurements of NO_y and NO_x are usually available during intensive field campaigns.

Kleinman (2005) derived a general relationship between $P(O_3)$ and ozone precursors, resulting in a formula which gives the power law dependence of $P(O_3)$ on NO_x concentration, VOC reactivity, and radical initiation rate. The VOC reactivity, VOC_R, is defined as the fraction of the OH reactivity that is due to the reaction of OH with VOCs, as shown in Eq. 1.16:

$$VOC_R = \sum_i k_{VOC_i+OH}[VOC_i] \quad \text{(Eq. 1.16)}$$

where k_{VOC_i+OH} is the rate constant for reaction between each VOC and OH, and $[VOC_i]$ is the concentration of each VOC.

The derivation of the $P(O_3)$ relationship started from the usual photochemical equations of initiation, propagation and termination reactions, calculating ozone production with several assumptions. For a NO_x-limited regime, it was assumed that radical loss by peroxide formation is equal to radical production, while for a NO_x-saturated regime it was assumed that the reactions of OH with VOCs are rate limiting, that radical + radical reactions (R 1.19–R 1.21) can be ignored and that the reaction of OH with NO_2 (R 1.17) is the predominant radical sink. The formula derived by Kleinman (2005) to describe the dependence of ozone production on its precursors depends on a single quantity, L_N/Q, where L_N is the rate of radical removal by reactions with NO_x and Q is the rate of radical initiation (including OH, HO_2 and RO_2). This analytical formula is shown in Eq. 1.17:

$$P(O_3) = KQ^{C1}[NO_x]^{C2}(VOC_R)^{C3} \quad \text{(Eq. 1.17)}$$

where Q is the total rate of radical initiation, $[NO_x]$ the NO_x concentration and VOC_R the VOC reactivity. C1, C2, and C3 are constant values depending only on L_N/Q, as shown in Table 1.1. The dependence of K on L_N/Q, however, has not been evaluated.

Table 1.1: Dependence of $P(O_3)$ on Q, NO_x and VOC_R (Kleinman, 2005)

$P(O_3)$ regime	L_N/Q	Exponents for $P(O_3) = KQ^{C1}[NO_x]^{C2}(VOC_R)^{C3}$		
		C1	C2	C3
NO_x limited	0.0	0.5	1.0	0.0
	0.5	0.67	0.33	0.3
	0.67	0.75	0.0	0.5
NO_x saturated	1.0	1.0	–1.0	1.0

If L_N/Q is zero, no radicals are removed by reactions with NO_x. The regime is NO_x-limited and $P(O_3)$ is linearly proportional to NO_x and to the square root of Q, but doesn't depend on VOC_R. If L_N/Q is unity, all radicals are terminated by reactions with NO_x. The regime is NO_x-saturated and $P(O_3)$ is inversely proportional to NO_x and proportional to both VOC_R and Q. It is interesting to note that in both cases, $P(O_3)$ increases with Q and is always dependent on radical initiation rates. From this metric, L_N/Q values lower than 0.5 and higher than 0.7 will indicate a NO_x-limited and a NO_x-saturated regime, respectively. L_N/Q is thus an indicator of the ozone production regime.

The transition point from NO_x-limited to NO_x-saturated conditions is highly spatially and temporally dependent. The three factors presented in Eq. 1.17 (NO_x concentration, VOC reactivity and radical initiation rate) determine both the level of NO_x for the turnover point between the two ozone production regimes, but also the amplitude of ozone production. Therefore, the $P(O_3)$ sensitivity to ozone precursors has to be well understood to develop efficient strategies of O_3 reduction.

1.4.4 Investigation of ozone formation regimes in urban environments

In most urban and suburban environments, where concentrations of NO_x are significant (10-80 ppbv), ozone production rates are on the order of a few tens of ppbv/h (Mao et al., 2010). In highly polluted environments, such as Mexico City or Houston, TX, $P(O_3)$ can even exceed 100 ppbv/h (Shirley et al., 2006;Chen et al., 2010). Ozone production is generally low in more remote areas or forested environments that are not impacted by anthropogenic activities (less than 2-3 ppbv/h), due to the lack of NO_x (Geng et al., 2011). However, if NO_x emission sources are located downwind of a forested area, highly reactive biogenic VOCs (e.g. isoprene) can lead to an enhancement of ozone production (6-8 ppbv/h) (Geng et al., 2011;Thornton et al., 2002).

Most studies defining the $P(O_3)$ sensitivity to ozone precursors have taken place in urban environments. Table 1.2 provides a non-exhaustive list of these studies for a few urban centers around the world, indicating the peak ozone concentrations that were observed in each study, the peak value for $P(O_3)$ and the NO_x-VOC sensitivity. Some of these campaigns are briefly discussed below.

Kleinman et al. (2002) compared ozone production rates in Houston to 4 other cities in the USA: Nashville, TN (Daum et al., 2000), New York City, NY (Kleinman et al., 2000), Phoenix, AZ (Kleinman et al., 2001) and Philadelphia, PA (Fast et al., 2002). Inorganic and organic species were measured from an aircraft in the urban plume of these cities and $P(O_3)$ was calculated using peroxy radical concentrations (see Eq. 1.6) simulated by a zero dimensional box model.

In New York, model calculations showed that $P(O_3)$ chemistry is VOC-sensitive in the urban plume, with higher NO_x, O_3 and $P(O_3)$ values and $L_N/Q>0.5$, while the chemistry is NO_x sensitive downwind the city. Interestigly, L_N/Q could approach unity in the center of the urban plumes, indicating a strong NO_x-saturated (VOC-limited) regime (Kleinman et al., 2000).

In Nashville during 1995, ozone production was found to be VOC-sensitive at the center of the urban plume during some early mornings. However, later in the day, $P(O_3)$ was NO_x-limited in the aged urban plumes exhibiting low NO_x concentrations (<2 ppbv). However, NO_x were low during most of the day and $P(O_3)$ was mostly NO_x-limited. Measurements were also taken in Nashville during 1999 (Martinez et al., 2003) showing similar $P(O_3)$ values as the previous study, although the authors didn't examine the sensitivity on ozone precursors.

In Phoenix, ozone production is VOC-sensitive downtown, close to emission sources. L_N/Q strongly depends on NO_x and VOC-limited conditions ($L_N/Q >0.9$) are usually observed when NO_x is higher than 3 ppbv. On the other hand, NO_x-limited conditions ($L_N/Q<0.1$) are observed when NO_x is lower than 0.3 ppbv. The NO_x threshold depends on the chemical composition of the air mass, especially the concentration of VOCs and the rate of radical production (see Eq. 1.17). Ozone production rates were often lower than 10 ppbv/h though, most probably due to dry atmospheres leading to low initiation rates of OH from ozone photolysis.

Ozone production rates were 2 to 5 times higher in Houston than in the other cities, with ozone concentrations exceeding 250 ppbv sometimes. This is due to high concentrations of reactive VOCs in the area, while NO_x concentrations were similar than in the other cities. Indeed, Houston does not only have the usual urban mix of anthropogenic and biogenic VOCs, but there are also some of the world's largest petrochemical complexes in the area, leading to emissions of highly reactive VOCs such as alkenes. As can be seen from the table, median $P(O_3)$ values in Houston were in the same range as in Philadelphia, while the 90^{th} percentile is about 40 ppbv/h. However, individual values in the top 10^{th} percentile could exceed 150 ppbv/h of ozone production. The authors showed that, overall, ozone production is usually NO_x limited in Nashville, Phoenix and Philadelphia, while it is closer to VOC-limited in Houston and New York City.

Table 1.2: Summary of studies in various urban environments, investigating the NOx-VOC sensitivity of ozone production.

Location	Campaign & Date	Type of environment	Max O_3 (ppbv) [a]	Peak median $P(O_3)$ (ppbv/h)	Ozone production NO_x-VOC sensitivity	References
Nashville	SOS Jun-Jul 1995		146	15.2 [b]	mostly NO_x sensitive mornings: VOC sensitive	Daum et al. (2000) (Kleinman et al., 2002)
	SOS Jun-Jul 1999	Urban	110	15 [c]	-	(Martinez et al., 2003)
NYC	NARSTO-NE July 1996	Urban	119	14.7 [b]	VOC sensitive	(Kleinman et al., 2000) (Kleinman et al., 2002)
	PMTACS-NY July 2001	Urban	50 [d]	20	VOC sensitive	(Ren et al., 2003) (Mao et al., 2010)
Phoenix	May-Jun 1998	Urban	101	7.6 [b]	mostly NO_x sensitive downtown: VOC sensitive	(Kleinman et al., 2001) (Kleinman et al., 2002)
Philadelphia	NE-OPS Jul-Aug 1999	Urban	147	22.3 [b]	NOx sensitive	(Fast et al., 2002) (Kleinman et al., 2002)
Houston	TexAQS Aug-Sep 2000	Urban	211	39.1 [b]	mostly VOC sensitive afternoons: transition	(Kleinman et al., 2002) (Mao et al., 2010)
	TRAMP Sep-Oct 2006	Urban	70 [d]	45	mornings: VOC sensitive afternoons: NO_x sensitive	(Chen et al., 2010) (Mao et al., 2010)
	SHARP Apr-May 2009	Urban	110	18	mornings: VOC sensitive afternoons: NO_x sensitive	(Ren et al., 2013)
	DISCOVER-AQ Sept. 2013	Urban	125	20	mornings: VOC sensitive afternoons: NO_x sensitive	(Mazzuca et al., 2016)
Atlanta	Aug 9-11 1992	Urban	145	-	NO_x sensitive	(Sillman et al., 1997)
Los Angeles	Aug 26-28 1987	Urban	150	-	VOC sensitive	(Sillman et al., 1997)
	CalNex May-Jul 2010	Urban	110	55 [c]	Weekdays & weekend mornings: VOC sensitive Weekend afternoon: NO_x sens.	(Griffith et al., 2016)
Mexico City	MCMA Apr-May 2003	Urban	115 [d]	48 [c]	mornings: VOC sensitive afternoons: NO_x sensitive	(Shirley et al., 2006) (Mao et al., 2010)
	MCMA March-Apr 2006	Urban	95 [d]	85 [c]	-	(Dusanter et al., 2009a)
Beijing	Jun-Jul 2005	Rural	286 [e]	15 [e]	-	(Xue et al., 2014)
Shanghai	May-Jun 2005	Suburban	127 [e]	50 [e]	VOC sensitive	(Xue et al., 2014)
Guangzhou	Apr-May 2004	Suburban	178 [e]	100 [e]	VOC sensitive	(Xue et al., 2014)
Lanzhou	Jun-Jul 2006	Suburban	143 [e]	45 [e]	NO_x sensitive	(Xue et al., 2014)

[a] Unless otherwise noted, this column reports individual days maximum mixing ratio of the whole campaign.
[b] 90th percentile of $P(O_3)$ values
[c] Calculated from measurements of HO_2*
[d] Peak of the diurnal average
[e] Peak during individual ozone episodes

Several other studies have taken place in Houston, as it is an interesting urban site combining anthropogenic and biogenic VOC emissions, including emissions from large petroleum refineries. For example, Chen et al. (2010) compared several different chemical mechanisms to model ozone production chemistry during TRAMP-2006. Individual ozone production values could be as high as 180 ppbv/h, with a median $P(O_3)$ that

did not exceed 45 ppbv/h for any of the tested chemical mechanisms. The diurnal profile of $P(O_3)$ was similar for all models, exhibiting a peak in the morning around 9:30, with an intense production of ozone for 3 hours, before decreasing in the afternoon. Mao et al. (2010) performed a sensitivity analysis for this campaign calculating the L_N/Q ratio and showed that ozone production is VOC sensitive during morning hours but NO_x-sensitive in the afternoon. Ren et al. (2013) and Mazzuca et al. (2016) reported similar results for SHARP 2009 and DISCOVER-AQ 2013, respectively, with individual $P(O_3)$ values as high as 100-140 ppbv/h and a $P(O_3)$ regime that is VOC-sensitive in the early morning and NO_x-sensitive during the afternoon. Mazzuca et al. (2016) also showed that high $P(O_3)$ values were linked to the VOC-sensitive regime.

In a recent study from Griffith et al. (2016), ozone production rates in the Los Angeles area were calculated for the CalNex-2010 campaign using measured and modeled radical concentrations, while the NO_x-VOC sensitivity was determined from calculations of the L_N/Q ratio. The authors showed a clear difference in the radical chemistry between weekdays and weekends. During weekdays, with higher NO_x emissions, the diurnal average $P(O_3)$ calculated by radical measurements would reach 55 ppbv/h, while in during weekends $P(O_3)$ hardly exceeds 25 ppbv/h. On individual days, $P(O_3)$ values were sometime as high as 120 ppbv/h for weekdays and 60 ppbv/h for weekends. The authors also showed that $P(O_3)$ from modeled radicals consistently underestimates $P(O_3)$ from measured radicals during the weekdays, while the agreement is better during the weekends. The sensitivity analysis showed that ozone production was VOC limited during weekdays and weekend mornings, but closer to a transition regime or NO_x limited during weekend afternoons.

While the studies discussed above used the L_N/Q ratio to examine the sensitivity of ozone production to its precursors, a different method has been used by Sillman et al. (1997). The authors focused their study on a NO_x-VOC sensitivity analysis and did not report $P(O_3)$ values. They used model simulations to predict how O_3 would change under different emission scenarios, in order to identify the VOC-NO_x regime in Atlanta, GA and Los Angeles, CA. Using the photochemical indicators discussed in section 1.4.3, i.e. O_3/NO_y, O_3/NO_z, O_3/HNO_3, H_2O_2/HNO_3 and H_2O_2/NO_x, as well as ambient measurements, the authors examined the $P(O_3)$ regime and evaluated the model performances. They showed that O_3 production chemistry in Atlanta is mainly NO_x-sensitive (high indicators values) while in Los Angeles it is mainly VOC-sensitive (low indicators values).

A similar study has been conducted for Paris in Europe (Sillman et al., 2003). Airborne measurements performed during three days in July 1999 were used as constraints for a 3-dimensional model, in order to simulate different emission scenarios. Indicator ratios similar to the ones mentioned above were also used in the analysis. The behavior of O_3 with increased or decreased emissions of anthropogenic VOCs, NO_x or

isoprene and the comparison of the measurements with the model calculations showed that ozone production regime in the Paris area is close to a transition from NO_x-sensitive to VOC-sensitive regime, and the NO_x-VOC sensitivity may vary from day to day.

Xue et al. (2014) analyzed measurements of ozone, NO_x and hydrocarbons made in rural or suburban sites downwind four large cities in China: Beijing, Shanghai, Guangzhou and Lanzhou. Ozone production rates were calculated from modeled (0-D) concentrations of peroxy radicals. The authors showed that the suburban sites of Shanghai, Guangzhou and Lanzhou were characterized by high ozone production rates, with $P(O_3)$ values on the order of 50 ppbv/h in Shanghai and Lanzhou and up to 100 ppbv/h in Guangzhou. On the other hand, at the rural site near Beijing, $P(O_3)$ hardly exceeded 20 ppbv/h. However, O_3 levels could exceed 200 ppbv in the afternoon at this site. The authors compared the calculated $P(O_3)$ values to the rate of change of ozone mixing ratios to assess the impact of transport, and attributed the increase of O_3 to the transport of urban plumes from Beijing, that had undergone extensive photochemical processing. For the other suburban sites, transport was not found to be significant, as the local ozone production could explain the changes in ambient ozone. Furthermore, the authors did a sensitivity analysis for the three sites exhibiting the largest ozone production rates, modeling the response of O_3 to a decrease in precursor concentrations. Ozone production chemistry in the eastern sites of Shanghai and Guangzhou was found to be VOC-sensitive, while it was found to be NO_x-sensitive in the western site of Lanzhou.

From the studies presented above, it is interesting to note that the ozone production regime in urban locations can change from day to day, or even during the same day, usually being VOC-sensitive in the morning and NO_x-sensitive in the afternoon. Depending on the sensitivity of ozone production to its precursors, different air quality strategies have to be implemented, either reducing NO_x, VOCs or both. However, as ozone pollution is not only a regional problem but can affect neighboring countries or a whole continent, it is essential to take into account the ozone production sensitivity on a larger scale before proceeding into air quality regulations.

1.4.5 Emission regulations and ozone standards

The increase of ozone levels over the past century (see section 1.3) made the implementation of air quality regulations essential. Since the dependence of O_3 on precursor emissions is not linear, different control strategies need to be implemented depending on the ozone production regime in a particular region. Many generations of atmospheric chemistry models have been developed to address this issue, such as the Comprehensive Air quality Model with Extensions (CAMx) (ENVIRON, 2002), the Community Multiscale

Air Quality (CMAQ) model used by the U.S. Environmental Protection Agency (EPA) (Byun and Schere, 2006), or joint meteorological and chemistry transport models (Zaripov et al., 2011).

After the 1970 Clean Air Act federal law in the US, most models had shown that ozone formation was VOC-sensitive and control strategies had focused on reducing hydrocarbon emissions, which were indeed decreased by 10% between 1977 and 1989 (Sillman, 1993). However, following the reduction in VOC emissions, a significant decrease in ozone concentrations was not observed. During the 1990's, measurements and model calculations showed that O_3 formation over most of the United States was mainly NO_x-limited and not hydrocarbon-limited as previously though. The reason for the error in identifying the right O_3 production regime came from the models that were used at the time (Sillman, 1993), in part because they underestimated emissions of hydrocarbons from vehicles, and in part because they did not account for natural emissions of biogenic VOCs, such as isoprene. Therefore, the 1990 Clean Air Act introduced NO_x emission standards for the automobile industry and since then, the focus in the US is mainly on reducing NO_x emissions.

In Europe, ozone regulation strategies are focused on both NO_x and VOC reductions, depending on the region (EEA, 2015). For example, Aksoyoglu et al. (2012) modeled air quality in Europe during June and January 2006 using the MM5/CAMx model to investigate the sensitivity of ozone formation to precursor emissions such as isoprene, NO_x and other VOCs. Model results suggested that increased isoprene emissions by a factor of 4 in June 2006 would lead to an increase in ozone by up to 10%, mainly in southern Europe. They also investigated the sensitivity of ozone formation in Europe to 30% reductions in anthropogenic NO_x and VOC emissions for June 2006. Figure 1.7 shows the difference in ozone concentrations derived from two simulations including a 30% emission reduction of NO_x on one side and VOCs on the other side (O_3 from reduced NO_x minus O_3 from reduced VOCs). The results suggested that NO_x reductions were effective to reduce ozone in the rural part of Europe while causing an increase in ozone by a few ppbv in urban areas. On the other hand, reducing VOC emissions led to a decrease in ozone mainly around large cities. In Fig. 1.7, blue areas indicate a NO_x-sensitive regime, while red areas a VOC-sensitive regime. Therefore, while NO_x regulations would be successful for ozone reduction in the biggest part of Europe, VOC regulations are needed in the biggest cities and industrial areas.

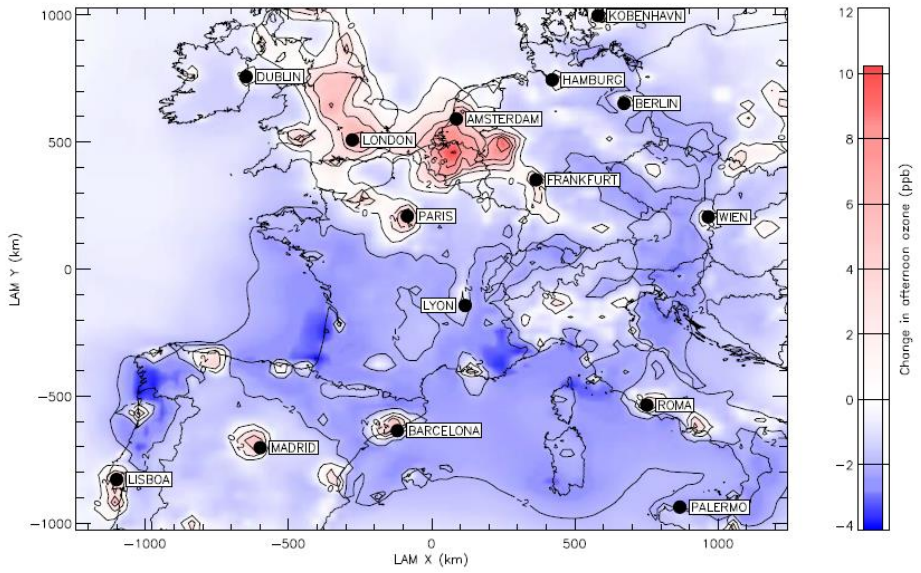

Figure 1.7: Difference in ozone concentrations between two simulations with a 30% emission reduction of either NO_x or VOC in June 2006. Blue areas indicate NO_x-sensitive regime and red areas VOC-sensitive regime (Aksoyoglu et al., 2012).

Many jurisdictions worldwide have established standards or guidelines for tropospheric ozone. These standards represent upper limits of ambient concentrations, which are intended to protect sensitive individuals. Most standards are set to protect human health, but some have also been established to be protective of crops. The science of determining a "safe" level for a pollutant such as ozone is very complex, as it is unclear if there is a threshold below which there is no impact on human health (Fowler et al., 2008). As a result, other considerations also enter into the setting of standards, including the feasibility of achieving the desired level, the costs of the measures required to achieve the concentration limit, and the costs of the damages which will result if this level is exceeded. For these reasons, there tends to be some divergence between the standard limit values set in different jurisdictions as summarized in Table 1.3.

These thresholds are periodically revised by the local authorities. For example, the US standard was set at 120 ppbv in 1979. Then was reduced to 80 ppbv in 1997 and was revised in 2008 at the level of 75 ppbv. In November 2014, the EPA proposed lowering the ozone standard of 75 ppbv to a range between 65 and 70 ppbv. Finally, the US ozone standard was finalized in October 1st, 2015 at 70 ppbv (EPA, 2015a). In addition to setting a numerical value as a standard, a specification is normally also attached, defining how the measurements are to be compared with the standard. For example, in Canada and the US, the standard for ozone is specified as an 8-hour running average, while an 1-hour average is used in Australia and China.

However, ozone concentrations often fail to meet the standards. Based on 2012-2014 data, 241 counties in the U.S. had concentrations that exceeded the new 70 ppbv standard (EPA, 2015b), while during 2013, 18 out of 28 EU countries exceeded the EU thresholds (EEA, 2015). Since the formation of O_3 requires sunlight,

exceedances of O_3 standards increase as one moves from the northern parts to the southern parts of the continent, with the highest O_3 concentrations in some Mediterranean countries (EEA, 2013, 2015).

Table 1.3: Ozone guidelines for selected jurisdictions

Jurisdiction	Value	Running average	Last Revised	Reference
Canada	63 ppbv	8-hour	2010	*(CCME, 2013)*
United States	0.070 ppm [75 ppbv]	8-hour	2015	*(EPA, 2015a)*
Mexico	0.08 ppm [80 ppbv]	8-hour	2002	*(INECC, 2002)*
European Union	120 μg/m^3 [60 ppbv]	8-hour	2008	*(EU, 2008)*
China I *	160 μg/m^3 [80 ppbv]	1-hour	2010	*(CAI-Asia, 2010)*
China II, III *	200 μg/m^3 [100 ppbv]	1-hour	2010	*(CAI-Asia, 2010)*
Australia	0.10 ppm [100 ppbv]	1-hour	2005	*(Australian Gov., 2005)*
India	100 μg/m^3 [50 ppbv]	8-hour	2010	*(CAI-Asia, 2010)*
WHO Guideline (recommendation)	100 μg/m^3 [50 ppbv]	8-hour	2005	*(WHO, 2006)*

***** **China I:** specially protected areas, such as natural conservation areas, scenic spots, and historical sites;
China II: residential areas, mixed commercial/residential areas, cultural, industrial, and rural areas;
China III: special industrial areas**;**

With the implementation of air quality regulation strategies, emissions of ozone precursors have decreased considerably during the last years. Between 2002 and 2011, NO_x emissions in the European Union decreased by 27%, and NMVOC and CO emissions decreased by 28% and 32%, respectively (Guerreiro et al., 2014). Despite these significant decreases of precursor emissions, 80% of the monitoring stations in Europe did not exhibit a clear trend of O_3 concentrations between 2002 and 2011. 18% of the stations registered a statistically significant decreasing trend (usually by 0.5-1 ppbv per year), while 2% registered a significant increasing trend (less than 0.2 ppbv per year), most of them in the Iberian Peninsula (EEA, 2013).

These results indicate that reductions in anthropogenic precursor emissions do not necessarily lead to significant reductions in O_3 concentrations, as the relationship between O_3 concentration and its precursors is not linear. For this reason, a better understanding of the ozone formation chemistry and the improvement of chemical mechanisms used in models are essential to develop efficient strategies for ozone control.

1.5 Quantification of $P(O_3)$ from field measurements

1.5.1 Calculations of $P(O_3)$ using measured and modeled radical species

As described previously, the quantification of ozone production rates, $P(O_3)$, is done traditionally through Eqs. 1.6, 1.14 and 1.15. Concentrations of NO_x and O_3 are usually measured during intensive field campaigns or air quality networks, while concentrations of radicals can be obtained either from the output of box models or by direct measurements.

1.5.1.1 Techniques deployed in the field for radical measurements

Instruments developed for RO_x (OH, HO_2, RO_2) measurements are based on four different techniques (Heard, 2006): Differential Optical Absorption Spectroscopy (DOAS) for OH (Mount and Harder, 1995;Dorn et al., 1995;Hausmann et al., 1997), Chemical Ionization Mass Spectrometry (CIMS) for OH, HO_2, and HO_2+RO_2, (Eisele and Tanner, 1991;Edwards et al., 2003;Kukui et al., 2009), Laser-Induced Fluorescence (LIF) for OH, HO_2 and HO_2+RO_2, known as FAGE – Fluorescence Assay by Gas Expansion (Hard et al., 1995;Brune et al., 1995;Kanaya et al., 2001;Dusanter et al., 2009a), and PEroxy Radical Chemical Amplification (PERCA) for HO_2+RO_2.

The DOAS technique is based on monitoring OH by UV absorption on a long open path of several hundreds of meters to several kilometers. This technique has mainly been used as a reference method since no calibration is needed. However, having a relatively high detection limit of approximately 1×10^6 molecules cm^{-3} for time resolution of about 100 s, it has seen limited use in the field (Ren et al., 2012). Currently, only the Julich DOAS instrument remains in service inside the SAPHIR (Simulation of Atmospheric PHotochemistry In a large Reaction) chamber. This instrument is mainly used for kinetic experiments but has also been used during intercomparison studies with the CIMS or FAGE instruments (Fuchs et al., 2012;Schlosser et al., 2009) at the SAPHIR chamber.

OH is measured directly by LIF-FAGE by exciting OH at 308 nm in a low pressure sampling cell. The OH fluorescence is collected at the same wavelength using a time-gated detection system and the fluorescence signal is converted into an absolute concentrations. HO_2 is measured indirectly as OH through the addition of NO to the ambient sampling inlet, HO_2 being converted into OH (R 1.14). The addition of NO was initially though to only convert HO_2 into OH (R 1.14), with no conversion of RO_2, due to the reduced oxygen concentration in the low pressure cell. However, recent studies showed that there are interferences from RO_2 compounds, as some β-hydroxyperoxy radicals are also quickly converted to HO_2 at low pressure and care must be taken to reduce this artifact using optimized operating conditions (Fuchs et al., 2011;Griffith et al., 2013;Whalley et al., 2013;Lew et al., 2013). As a result, the LIF-FAGE instrument measures HO_2 plus a fraction of RO_2 radicals, usually referred to as HO_2* (= $HO_2 + \alpha RO_2$, $\alpha \leq 1$).

For CIMS instruments, OH is first converted to H_2SO_4 by addition of SO_2 in the sampling inlet, which is then detected by mass spectrometry. The sum HO_2+RO_2 is usually measured by adding NO in the inlet since it has been difficult to prevent the simultaneous conversion of RO_2 when HO_2 is converted to OH. More recently, CIMS instruments were adapted to speciate between HO_2 and the sum of RO_2 by using controlled ratios of NO/O_2 inside the sampling inlet, e.g. the RO_x Chemical Conversion/CIMS (ROXMAS) (Hanke et al., 2002) and the Peroxy Radical Chemical ionization Mass Spectrometer (PeRCIMS) (Hornbrook et al., 2011;Edwards et al., 2003).

The PERCA technique is also used to measure the sum of peroxy radicals (HO_2+RO_2). In PERCA, HO_2 and RO_2 are converted into NO_2 (R 1.12, R 1.14) by adding NO in the sampling cell. The OH and RO coproducts are propagated back to HO_2 in subsequent reactions of OH with CO and RO with O_2. These radical chain reactions are repeated and lead to an amplification of the NO_2 level. NO_2 is then measured by a sensitive NO_2 monitor, such as LIF (Fuchs et al., 2008;Sadanaga et al., 2004a), Cavity Ring Down Spectroscopy (Liu et al., 2009), or Cavity Attenuated Phase Shift spectroscopy (Wood and Charest, 2014)

1.5.1.2 Chemical mechanisms used in atmospheric models

If all the parameters that affect the production and loss of RO_x radicals are successfully measured (O_3, NO_x, volatile organic compounds, water vapor, J-values, etc.) then RO_x concentrations can be estimated with a box model that is constrained with these measurements. The mechanism used in the model can be tested by comparing the observed and calculated RO_x concentrations, since their chemical lifetimes are too short to be influenced by transportation or deposition processes (Kanaya and Akimoto, 2002).

Chemical mechanisms that are often used in box models are the Regional Atmospheric Chemistry Mechanism – version 1 and 2 (RACM and RACM2), the Carbon Bond Mechanism Version 2005 and version 6 (CB05 and CB6), the Statewide Air Pollution Research Center mechanism Version 2007 (SAPRC-07), the NASA Langley Research Center mechanism (LaRC) and the Master Chemical Mechanism version 3.2 (MCMv3.2). This list is not exhaustive and other mechanisms have been used in the literature.

The MCM is a near-explicit chemical mechanism which describes the detailed gas-phase chemical processes involved in the atmospheric degradation of a series of primary emitted VOCs. These include a large number of major emitted anthropogenic species (hydrocarbons and oxygenated VOCs). The resultant mechanism contains about 17000 elementary reactions of 6700 species. The chemistry was developed using protocols described by Jenkin et al. (1997), Jenkin et al. (2003) and Saunders et al. (2003). The latest version, MCMv3.2, is available at the MCM–University of Leeds website (http://mcm.leeds.ac.ukh).

RACM (Stockwell et al., 1997) is a condensed gas-phase chemical mechanism developed for the modeling of regional atmospheric chemistry and includes 17 stable inorganic species, 4 inorganic intermediates, 32

stable organic species and 24 organic intermediates for a total of 237 chemical reactions. Organic compounds are grouped together to form a manageable set of compounds. Only 8 organic species are treated explicitly (methane, ethane, ethene, isoprene, formaldehyde, glyoxal, methyl hydrogen peroxide and formic acid) and 24 are surrogates that are grouped based on emission rates, chemical structure and reactivity with the OH radical. More details are given in chapter 3 (section 3.3). The Regional Atmospheric Chemistry Mechanism v2 (RACM2) (Goliff et al., 2013) is the updated version of RACM and is designed to simulate remote to polluted conditions from the Earth's surface to the upper troposphere. The RACM2 mechanism includes a total of 363 reactions and 119 species, 17 stable inorganic species, 4 inorganic intermediates, 55 stable organic species (3 of these are primarily of biogenic origin) and 43 organic intermediates. Additional details about RACM2 are given in chapter 4 (section 4.4.1).

SAPRC-07 (Carter, 2007) is the updated version of SAPRC from the previous SAPRC-99 (Carter, 1999). It includes updated rate constants and reactions, revised aromatic chemistry, a representation of chlorine chemistry and a better representation of peroxy radical reactions for secondary organic aerosol formation. Another important revision was that mechanisms for many types of VOCs were added or improved, resulting in an increase of VOC types by over 20%. The mechanism includes 26 inorganic species, 84 organic species and 291 reactions, from which 34 are photolytic reactions.

The NASA Langley Research Center mechanism (LaRC) (Crawford et al., 1999) has been updated from Davis et al. (1993) and includes basic HO_x-NO_x-CH_4 gas phase chemistry, NMHC chemistry, photolysis reactions and heterogeneous losses for soluble species. Modifications included updated rate coefficients, additional reactions for remote low NO_x environments (e.g. formation of organic peroxides) and explicit chemistry for acetone, propane and benzene. The last version, updated in 2005, contains 109 chemical species and 279 reactions, 35 of which are photolytic reactions.

The Carbon Bond Mechanism (CB05) (Yarwood et al., 2005) is updated from the 4th version, CB4, and contains 51 species, 23 photolysis reactions and 156 gas-phase reactions. In this version, methane, ethane, methylperoxy radical, methyl hydroperoxide and formic acid are treated explicitly while other organic species are lumped according to the carbon bond type. Additionally, there is an optional mechanism extension for reactive chlorine chemistry or explicit reactions for air-toxics. Reactions are aggregated based on the similarity of carbon bond structure so that fewer surrogate species are needed in the model. The Carbon Bond mechanism was lastly updated in 2010 to the 6th version (CB6) (Yarwood et al., 2010), containing 77 species, 28 photolytic reactions and 218 gas-phase reactions. The main updates were the addition of propane, acetone, benzene, acetylene to be treated explicitly, updating reactions for isoprene and aromatics and adding alpha-dicarobnyl coumpounds (glyoxal and analogues) to improve secondary aerosol modeling.

Explicit mechanisms such as MCM usually offer a better representation of the chemistry, but are more complex and demand more resources, such as computer memory, disk storage and computational time. On the other hand, when species are grouped together according to their structure and reactivity, the condensed mechanisms reduce the computational cost of the model. In this work, the chemical mechanisms that were used are RACM in chapter 3 and RACM2 in chapter 4. Condensed mechanisms have been widely used in the literature and have been shown to provide similar results than the explicit MCM mechanism for radical predictions (Chen et al., 2010). RACM and RACM2 have been employed in this study for the ease of use and convenience they provide in constraining the model and in investigating the radical budget.

1.5.1.3 Comparisons of radical measurements to model outputs

Studies performed in urban and suburban environments, whose objectives were to test our understanding of the RO_x chemistry by comparing measured to modeled RO_x concentrations, showed that models tend to underestimate HO_2 under high NO_x conditions, i.e. for NO mixing ratios higher than a few ppbv (Ren et al., 2013;Chen et al., 2010;Dusanter et al., 2009b;Kanaya et al., 2007;Ren et al., 2003;Griffith et al., 2016). For example, Griffith et al. (2016) showed that HO_2* measurements performed in Pasadena during the CalNex 2010 field campaign were severely underpredicted by the model (RACM2) during weekdays for NO_x mixing ratios higher than 20 ppbv. The observed concentrations of HO_2* were underpredicted by a factor of approximately 3 at midday. Interestingly, this underprediction was lower during weekends (less than 20%) when NO_x mixing ratios were lower (5-20 ppbv).

In contrast, models tend to overestimate HO_2 in forested areas and regions characterized by large concentrations of biogenic VOCs and low concentrations of NO_x, i.e for NO mixing ratios lower than a few hundreds of pptv (Pugh et al., 2010;Mao et al., 2012;Griffith et al., 2013). Indeed, during the PROPHET 2008 and CABINEX 2009 field campaigns, performed in a forest in northern Michigan (Griffith et al., 2013), the modeled sum of HO_2 and isoprene-based peroxy radicals, which are the dominant RO_2 species contributing to the HO_2* interference, tends to overestimate the measured HO_2* concentrations by approximately 25% and 35% respectively, for the two campaigns. Large disagreements are also present in the modeling of OH, with the models underestimating the measurements at forested environments (Pugh et al., 2010;Lu et al., 2013;Whalley et al., 2011;Lelieveld et al., 2008), while the agreement may be better when colder temperatures lead to lower concentrations of isoprene and other biogenic VOCs (Griffith et al., 2013).

These results directly lead to discrepancies between $P(O_3)$ values calculated from measured radicals and from box model outputs, where values calculated from measured radicals usually exceed modeled values under high NO_x conditions. It is interesting to note that similar results were also reported by Spencer et al.

(2009) for Mexico City in 2006, using peroxynitric acid (HO_2NO_2) measurements to infer $P(O_3)$ values. These authors showed that for NO_x levels higher than 15 ppbv, the model underpredicted the HO_2NO_2 measurements, with an observed-to-calculated ratio of approximately 1.6. As a result, ozone production rates calculated using measured HO_2NO_2 concentrations were larger by up to a factor 5 than modeled values.

The HO_2-to-OH ratio is often used as an indicator of the propagation chemistry between OH and HO_2 radicals since it does not depend on initiation or termination processes. A good description of this ratio in atmospheric models is therefore crucial to correctly model $P(O_3)$. Chen et al. (2010) compared OH and HO_2 radical concentrations calculated by several chemical mechanisms, implemented in the same box model, constrained by measurements from the TRAMP-2006 field campaign performed in Texas. As shown in Fig. 1.8, the modeled and measured HO_2-to-OH ratios agree when NO is close to 1 ppbv, but the modeled ratio is higher than the measurements when NO is lower than 1 ppbv (up to a factor 4-5). In contrast, the modeled ratio is lower than the measurements when NO is higher than 1 ppbv (up to a factor 10). It can also be seen that the different mechanisms are consistent with each other and the disagreement is not due to the methodology used to treat the chemistry in each mechanism.

A similar behavior has been observed by many authors such as Griffith et al. (2016) in Pasadena, Dusanter et al. (2009b) in Mexico City, Kanaya et al. (2007) in Tokyo, Shirley et al. (2006) in Mexico City, Ren et al. (2003) in New York City and others.

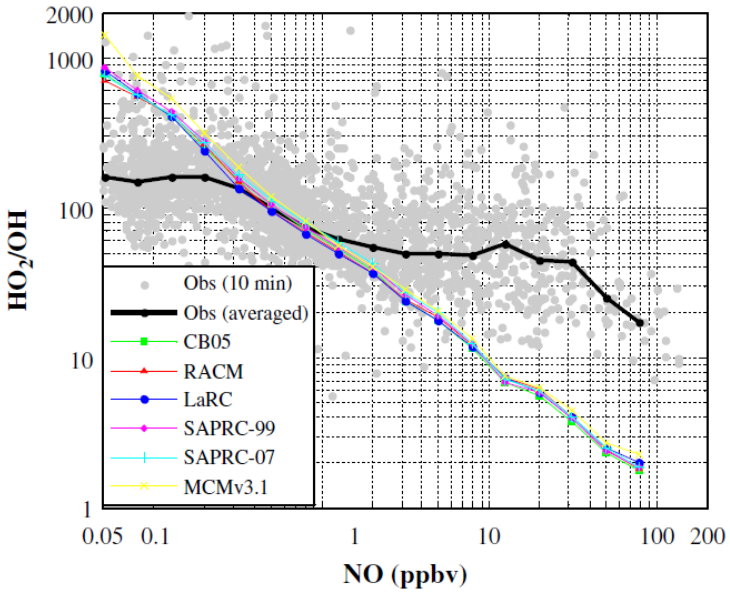

Figure 1.8: Measured and modeled HO_2-to-OH ratio as a function of NO mixing ratio. Grey dots are measured HO_2-to-OH ratios based on 10-min average data, the solid black line the averaged measurements and the colored lines the different chemical mechanisms described in section 1.5.1.2 (Chen et al., 2010)

While recent studies have shown that there were several artifacts in the measurement of radical species with the LIF-FAGE technique (Dusanter and Stevens, 2016) for HO_2 (Fuchs et al., 2011) and OH (Mao et al., 2012), recent studies (Griffith et al., 2013;Griffith et al., 2016) were performed using a LIF-FAGE instrument equipped with a new scrubber technique capable of quantifying OH interferences. In addition, HO_2 interferences were well characterized and taken into account during these studies. The results from Griffith et al. (2013) for a forested area and from Griffith et al. (2016) for an urban environment show a better measurement/model agreement for OH but still indicate that the concentration of peroxy radicals is significantly overpredicted when NO is lower than 1 ppbv and underpredicted when NO is higher. These results strongly suggest that $P(O_3)$ may be miscalculated by atmospheric models when NO is significantly different from 1 ppbv.

As mentioned in section 1.4.3, an important parameter for the quantification of ozone production is the VOC reactivity (VOC_R). This quantity can be inferred from the total OH reactivity, which is defined as the first order loss rate of OH calculated as the sum of all the sink terms due to OH reactive species, including VOCs, NO_x and other inorganic species. Eq. 1.16 reports the VOC contribution to the total OH reactivity and adding inorganic species in this equation would lead to the total OH reactivity. Direct measurements of total OH reactivity have recently been made available using different methods (Dusanter and Stevens, 2016): the Total OH Loss Rate Method (TOHLM) (Kovacs and Brune, 2001;Ingham et al., 2009), the Pump-probe (LP-LIF) (Sadanaga et al., 2004b;Lou et al., 2010;Stone et al., 2016;Parker et al., 2011), and the Comparative Reactivity Method (CRM) coupled to a Proton-Transfer-Reaction Mass Spectrometer (PTR-MS) (Sinha et al., 2008;Kim et al., 2011;Dolgorouky et al., 2012;Kumar and Sinha, 2014;Hansen et al., 2015) or a Gas Chromatographic Photoionization Detector (GC-PID) (Nölscher et al., 2012a).

During recent studies performed in different environments (Dusanter and Stevens, 2016), comparison between the measured total OH reactivity and that calculated from trace gas measurements highlighted the so-called “missing OH reactivity”, as measured values were higher than values calculated from trace gas measurements. The missing reactivity is defined as the calculated-to-measured total OH reactivity ratio. These studies showed that the missing OH reactivity, which is very likely due to unmeasured VOCs, can be up to 40% in megacities and other urban environments (Dusanter and Stevens, 2016), and up to a factor 4-10 in some forested areas, especially under prolonged heat stress (Dusanter and Stevens, 2016;Nölscher et al., 2012b).

The discrepancies observed between model calculations and field measurements of free radicals and total OH reactivity question our ability to successfully model ozone production rates and indicate that there are still unknowns in our understanding of the radical and ozone production chemistry, including unknown or unmeasured species that influence RO_x concentrations and missing chemical processes. For example, Brune

et al. (2016) recently proposed the reaction of $OH+NO+O_2 \rightarrow HO_2+NO_2$ to tentatively explain the HO_2 discrepancy observed during the CalNex-SJV study (2010). However, laboratory and modeling kinetic studies are needed to test the suggested reaction.

1.5.2 Direct measurements of $P(O_3)$

In order to address the model-measurement discrepancies discussed above, but also to improve our current understanding of ozone production chemistry in the troposphere, an instrument for direct ozone production measurements (MOPS) was developed by Cazorla and Brune (2010). The principle of the MOPS is based on differential ozone measurements between two sampling chambers made of Teflon. One chamber is exposed to the sunlight to get an ozone production rate inside the chamber that mimics atmospheric $P(O_3)$ (sample chamber). The other chamber is covered with a UV filter that blocks wavelengths below 400 nm to shut down the radical chemistry and, as a consequence, ozone production (reference chamber). A schematic of the first version of the MOPS instrument (MOPSv1) is show in Fig. 1.9.

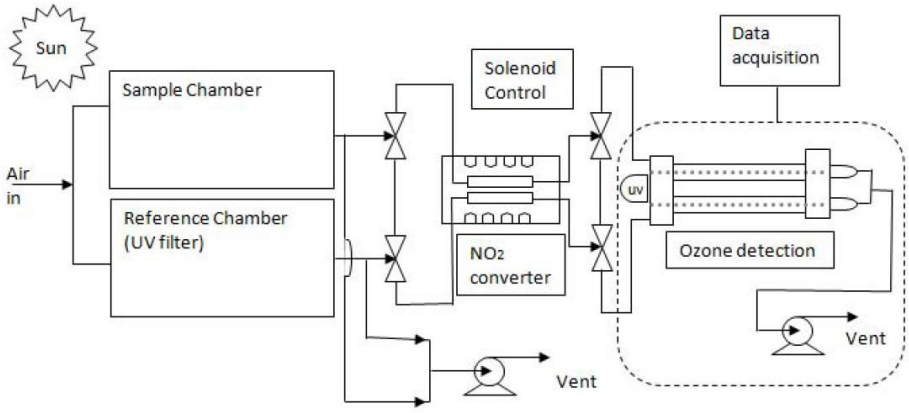

Figure 1.9: Schematic of the MOPSv1 instrument (Cazorla and Brune, 2010)

The difference in ozone between the two chambers divided by the exposure time yields the ozone production rate. However, NO_2 can act as a reservoir molecule for O_3 due to a rapid interconversion between these two species under ambient conditions. Therefore, NO_2 has to be converted into O_3 before measuring ozone. The differential O_x ($O_x=O_3+NO_2$) measurement, referred to as ΔO_x in the following, divided by the residence time in the flow tubes, τ, yields $P(O_x)$ values as shown in Eq. 1.16, which represents $P(O_3)$ when NO_2 is efficiently photolyzed during daytime.

$$P(O_x) = \frac{\Delta O_x}{\tau} = \frac{O_{x_{amb}} - O_{x_{ref}}}{\tau} \quad \text{(Eq. 1.16)}$$

The first version of the MOPS instrument was tested on the campus of Pennsylvania State University in the late summer of 2008. These tests demonstrated the feasibility of this new technique, as the instrument responded to the presence of solar radiation and ozone precursors and yielded rates of ozone production that were within a range of reasonable values (up to 8 ppb/h) for a polluted rural environment. A correlation of $P(O_3)$ with NO at these low $P(O_3)$ values was also observed, as shown in Fig. 1.10. In addition, this preliminary study showed that the MOPS could be used to further investigate the sensitivity of $P(O_3)$ to its precursors by adding them into the sampled air masses.

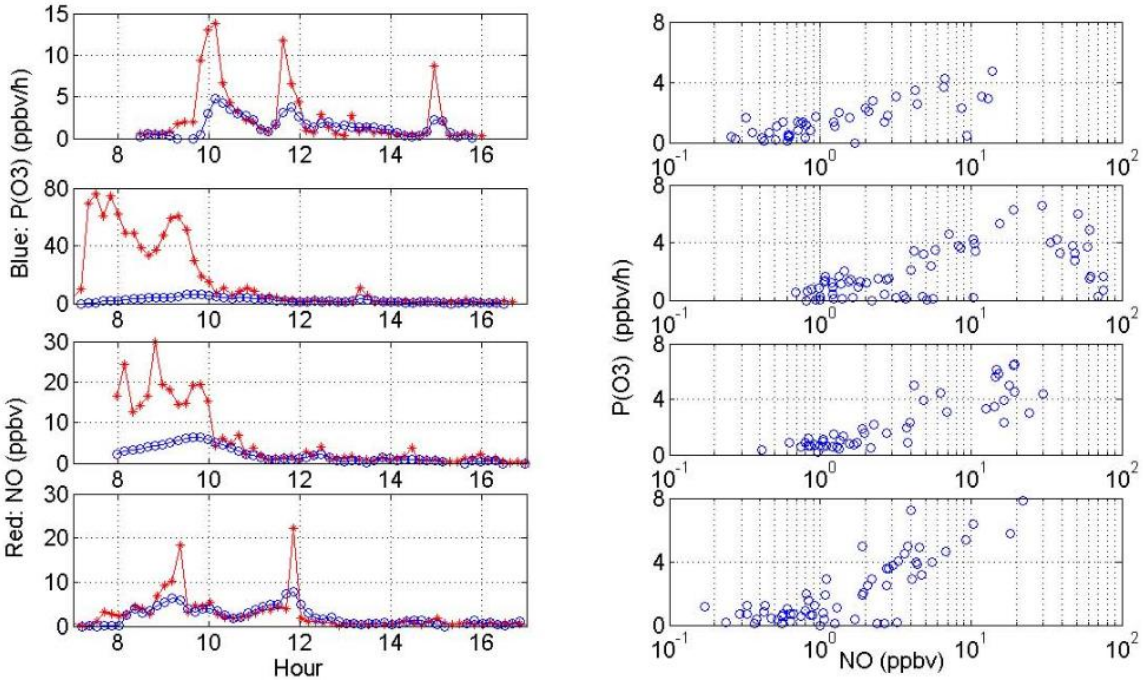

Figure 1.10: Rates of ozone production measured on the campus of the Pennsylvania State University from 1 to 4 September 2008. The blue circles indicate $P(O_3)$ values and the red stars NO mixing ratios (Cazorla and Brune, 2010)

The MOPSv1 instrument was then deployed during the Study of Houston Atmospheric Radical Precursors (SHARP, 2009) (Cazorla et al., 2012). Time series of $P(O_3)$ values measured by MOPS, as well as calculated by measured and modeled radical concentrations are shown in Fig. 1.11.

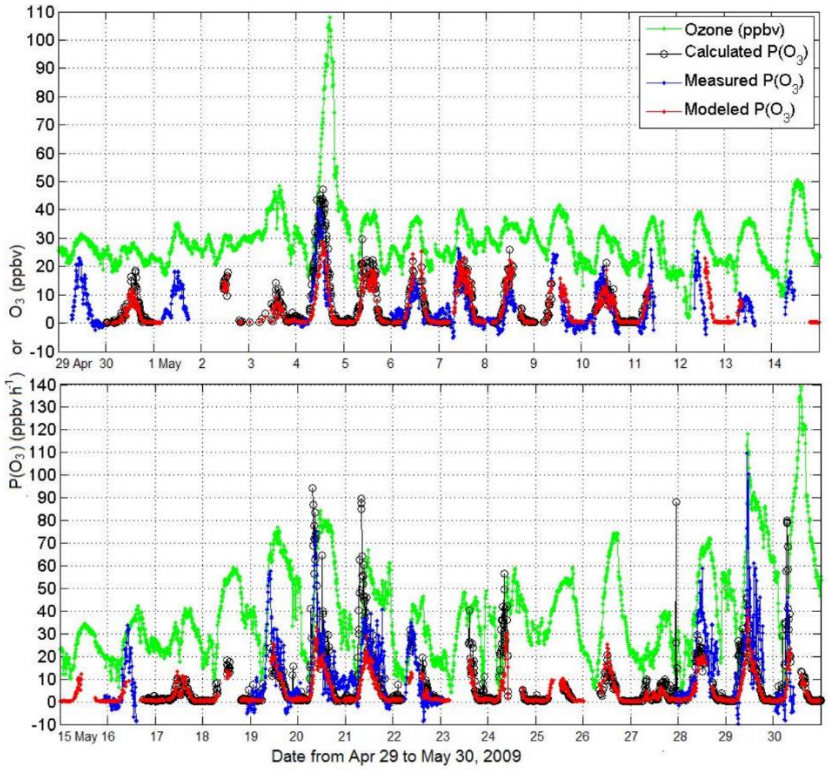

Figure 1.11: Time series of ambient ozone (green dots), calculated $P(O_3)$ values from measured radicals (black circles), MOPS measurements (blue dots), and $P(O_3)$ values modeled with the RACM2 mechanism (red dots) for the SHARP 2009 field campaign (Cazorla et al., 2012)

Measured $P(O_3)$ values peaked in the late morning, with values ranging from 15-100 ppbv/h, although values of 40–80 ppbv/h were typical for high ozone days. The measurements were compared to ozone production rates calculated from measurements of HO_2 and NO (referred to as calculated $P(O_3)$) as well as modeled radical concentrations from a box model using the RACM2 mechanism (referred to as modeled $P(O_3)$). Measured and calculated $P(O_3)$ exhibit similar peak values but the calculated $P(O_3)$ tended to peak slightly earlier in the morning, with a shift of 1-2 hours, when NO values were higher. Measured and modeled $P(O_3)$ had a similar diurnal profile, but the modeled $P(O_3)$ was only half of the measured $P(O_3)$ during morning hours, due to modeled HO_2 concentrations that were lower than the measurements. The deployment of the MOPS instrument during this campaign showed the potential of this instrument for contributing to the understanding of the ozone-producing chemistry, but was limited by high measurement uncertainties due to potential wall effects. The heterogeneous loss of NO_2 on the sampling chambers under humid conditions (RH> 50%) was reported as a main issue.

Recently, a second generation of the MOPS instrument (MOPSv2) was deployed during the NASA's DISCOVER-AQ field campaign in 2013, in Houston, Texas (Baier et al., 2015). The instrument had an

improved design of the sampling chambers (shape and size) compared to MOPSv1. Airflow characteristics were also optimized to reduce wall effects and the measurements made over one month were consistent with ambient ozone observations and model-derived $P(O_3)$ values from previous field campaigns in Houston. The authors, however, highlighted a possible bias due to the heterogeneous formation of HONO in the sampling chamber, which then could photolyze and lead to an increase of radical concentrations, as well as unresolved ozone analyzer issues related to temperature and humidity changes. The chamber HONO concentrations were reported as two to five times higher than ambient values, which could cause a bias up to 5-10 ppbv/h of measure in the $P(O_3)$ measurements.

These studies have shown that the MOPS is a promising instrument. Although the technique is relatively new, the first results have shown that ozone production rate measurements are feasible, since the instrument responded well to the ambient conditions and yielded measurements that are within a reasonable range. These results showed that the MOPS instrument could potentially clarify the discrepancies in the calculated ozone production rates from measured and modeled peroxy radicals.

However, as for every new technique, more research is needed to investigate the reliability of the measurements. The comparison between measured, calculated and modeled $P(O_3)$ values didn't provide enough evidence to draw general conclusions, as some aspects of the comparisons showed that the measured $P(O_3)$ values were in better agreement with values calculated from measured radicals and others with values calculated from modeled radicals. As a primary conclusion, the authors indicated that the model underestimated $P(O_3)$. Furthermore, there are still experimental issues to be resolved. The issues of the first version of the MOPS included O_3, NO_2 and radical losses is the chambers, as well as NO_x and VOC degassing from the chamber walls. The second version, MOPSv2, was improved, but the authors still reported a bias from HONO in the two chambers, biases due to temperature and relative humidity differences between the chambers and unresolved ozone analyzer issues.

As more experience will be acquired with this technique, the precision and the accuracy of $P(O_3)$ measurements will be improved. Therefore, the MOPS technique can be a useful tool for evaluating model-derived ozone production rates and ozone transport over a region. Including this type of measurements in more studies and field campaigns could help improving our understanding of ozone production chemistry.

1.6 Objectives

Given the photochemical nature of tropospheric ozone, strategies implemented to reduce the concentration of this pollutant are based on the use of atmospheric chemistry models. However, as shown in the previous sections, recent scientific studies question the reliability of these models. It is therefore essential to test and validate the chemical mechanisms used in the models.

One way towards this direction is to perform direct measurements of ozone production rates in the troposphere. This new type of measurements, combined with existing methods of quantifying $P(O_3)$, could help resolve the discrepancies between measured and modeled radical concentrations discussed in section 1.5.1.3, contribute to the understanding of ozone formation regimes and provide useful real-time data regarding the management of anthropogenic emissions (timing and magnitude of $P(O_3)$). Finally, if the MOPS technique is thoroughly tested and the $P(O_3)$ measurements are shown to be reliable, this type of instruments could be of interest for existing air quality networks to help improving air quality regulations.

The main objectives of this work were therefore to (i) advance the technological understanding of $P(O_3)$ measurements and (ii) improve our knowledge on the ozone formation chemistry. These objectives were achieved through the construction of a new $P(O_3)$ instrument, its characterization in the laboratory, and its deployment in the field.

These different steps are summarized below:

- Construction of an OPR (Ozone Production Rates) instrument (Chapter 2)

Previous studies using the MOPS instrument have highlighted uncertainties associated to interactions between ambient trace gases and the sampling chambers (see section 1.5.2). Therefore, while the principle of the OPR instrument is similar to the MOPS instrument, the instrument constructed in this work was designed to minimize these interactions. The design of the Mines Douai OPR is described in section 2.2. Compared to the MOPS, this instrument employs quartz flow tubes instead of Teflon chambers, an O_3-to-NO_2 conversion unit instead of a NO_2-to-O_3 unit, and a sensitive NO_2 monitor for O_x detection instead of an O_3 monitor.

It is worth noting that it is the third instrument for $P(O_3)$ measurements in the world, the other two being the MOPS from Pennsylvania State University, USA (Baier et al., 2015;Cazorla and Brune, 2010) and the OPR from Birmingham University, UK (William Bloss' group, unpublished work).

- Full characterization of the instrument (Chapters 2 & 3)

The characterization of the instrument included laboratory testing and an extensive modelling exercise to evaluate measurement errors. The different parts of the instrument (sampling flow tubes, conversion unit, detection system) have been characterized and the operating conditions have been investigated to determine

the instrument's detection limit and to pinpoint possible sources of errors. The laboratory characterization is described in section 2.3.

The modelling study aimed at investigating the impact of potential sources of errors on the $P(O_3)$ measurements. The accuracy of the OPR instrument was evaluated by combining the modelling and laboratory results. The modelling is described in Chapter 3.

- Field deployment of the OPR instrument (Chapter 4)

An important part in developing a new instrument is to investigate its behaviour in the field. The most important field testing of the OPR instrument took place in July 2015 during the IRRONIC (Indiana Radical, Reactivity and Ozone Production Intercomparison) field campaign, in Bloomington, IN, USA. This field campaign is described in Chapter 4, with a focus on investigating the sensitivity of ozone production to NO. This campaign allowed evaluation of the limitations of this version of the OPR instrument.

The OPR instrument has also been tested in the parking lot of Mines Douai, France, as well as on the campus of Birmingham University, UK, with the collaboration of William Bloss' group (not shown in this manuscript). Finally, the instrument was recently deployed in PROPHET-AMOS (Program for Research on Oxidants: PHotochemistry, Emissions, and Transport – Atmospheric Measurements of Oxidants in Summer) field campaign in a forested area of northern Michigan during July 2016. Data from this field campaign are not included in this manuscript, but relevant information is given in the perspectives section.

- Measurement and model comparison of $P(O_3)$ values (Chapter 4)

Organic and inorganic compounds, as well as meteorological parameters, were also measured during the IRONNIC field campaign and were used as constraints for a box model, using RACM2. As thoroughly explained in Chapters 2 and 4, significant limitations of the OPR instrument made the use of a model essential to extract $P(O_3)$ values from the raw measurements. This method is described in details in Chapter 4.

The results from this study are expected to expand our knowledge on direct measurements of ozone production rates and to help to investigate the $P(O_3)$ sensitivity in specific environments. Furthermore, as a new instrument, the OPR will offer great intercomparison opportunities with the few existing similar instruments: the MOPSv2 of Pennsylvania State University and the OPR of Birmingham University. A new scientific community will likely start being formed, specifically focused on ozone production rates measurements, where sharing experiences, recommendations, methods and results will further improve this technique.

Chapter 2. Development and characterization of the OPR instrument

2.1 Introduction

This chapter describes the construction and the characterization of the OPR (Ozone Production Rates) instrument developed at Mines Douai in collaboration with Indiana University. As mentioned in Chapter 1, main uncertainties reported for the MOPS instrument (Cazorla and Brune, 2010) were due to wall effects in the sampling chambers, mainly NO_2 losses under high relative humidity conditions, and to differences in relative humidity between the two chambers. Another source of errors was the possible release of HONO from heterogeneous chemistry at the chamber surface ((Baier et al., 2015)), which can be photolyzed to form additional OH, altering the chemistry in the chambers. The NO_2-to-O_3 conversion efficiency reported for the MOPS instrument was 88% at 17 ppbv of NO_2 (Cazorla and Brune, 2010) but was increased to 88-97% at NO_2 mixing ratios lower than 35 ppbv for the MOPSv2 (Baier et al., 2015). However, the NO_2-to-O_3 conversion efficiency decreases for higher NO_2 mixing ratios and may be different for the two chambers, since different O_3-NO_2 partitioning will take place in each chamber. Finally, another issue that was reported by Baier et al. (2015) was the baseline drift of the ozone monitor and its dependence on temperature and relative humidity.

In light of these findings, it was decided to use sampling chambers whose design would be optimized to reduce the wall effects mentioned above. We chose to use quartz flow tubes instead of Teflon chambers as described in section 2.1.1. In addition, we tested the detection approach proposed by Cazorla and Brune (2010), i.e. converting NO_2 into O_3 and measuring O_x ($=O_3+NO_2$) using an ozone monitor. However, it was also decided to test a new approach based on the conversion of O_3 into NO_2 and the subsequent measurement of NO_2 with a sensitive NO_2 monitor. The different parts of the instrument are described in the following section.

2.2 Description of the OPR instrument

2.2.1 Sampling flow tubes

Based on promising experiments performed by William Bloss' group from Birmingham University (unpublished results), it was decided to use cylindrical flow tubes for the sampling part of the OPR instrument. The flow tubes would allow a laminar flow regime to develop, minimizing turbulent mixing and air recirculation, which would in turn reduce the mixing of molecules close to the walls into the core of the flow tube. Quartz was selected because it is a hard material, suitable for the construction of flow tubes, and also transparent to UV radiation, which is needed for the radical chemistry to take place in the ambient chamber.

The flow tube geometry was designed through fluid dynamics simulations, using the STAR CCM+ V.8 software (CD-adapco). The objective was to find the optimum geometry that would lead to a laminar flow, taking into account the physical limitations for the construction of the instrument. These limitations are mainly related to the size of the flow tube, since a portable instrument is needed, and the total sampling flow rate. The latter should be at least equal to the sampling flow rate of the monitor used to quantify O_x but also low enough to get a residence time that enables the photochemistry of ozone production to take place in the flow tubes, which in turn would lead to a measurable difference between the 'ambient' and 'reference' flow tubes.

In computational fluid dynamics, usually referred to as CFD, numerical methods and algorithms are used to solve and analyze problems of fluid flows. The basis of almost all CFD problems is the Navier-Stokes equations, which define any single-phase flow. The Navier-Stokes equations can be solved for a physical problem in a CFD software dividing the physical space into cells and using calculations of finite differences.

In all CFD softwares, the same basic procedure is followed. Initially, the geometry of the problem is defined, which contains all the physical boundaries. For example, Fig. 2.1 shows one of the tested geometries, which consists of a cylindrical tube with a diameter of 20 cm, with two small inlet and outlet of 2.5 cm diameter. The volume occupied by the fluid is divided into discrete cells - the mesh. There are different kinds of mesh – e.g. cubic or polyhedral cells. The mesh may also be uniform (same size of cells everywhere) or non-uniform as in Fig. 2.1 (different sizes of cells, usually smaller cells near the boundaries to better describe the flow pattern in this region). The next step is to define the physical constraints such as the phase of the fluid (gas/liquid), its density, the equations of motion, the compressibility of the fluid, etc. Then, the boundary and initial conditions are applied, e.g. mass flow rate on a boundary surface or pressure at an inlet/outlet. In Fig. 2.1, the boundary conditions are a flow rate of 2.25 L/min in the outlet, atmospheric pressure at the inlet, and zero velocity at the walls of the flow tube. The simulation then starts running and the equations are solved iteratively, until the root mean square (RMS) error of velocity residuals (or another quantity) reach a small value, which is an indicator that the solution has converged. Usually an accepted threshold of the residuals for a converged solution is below 1×10^{-6}. In the end, a postprocessor is used for the analysis and visualization of the resulting solution.

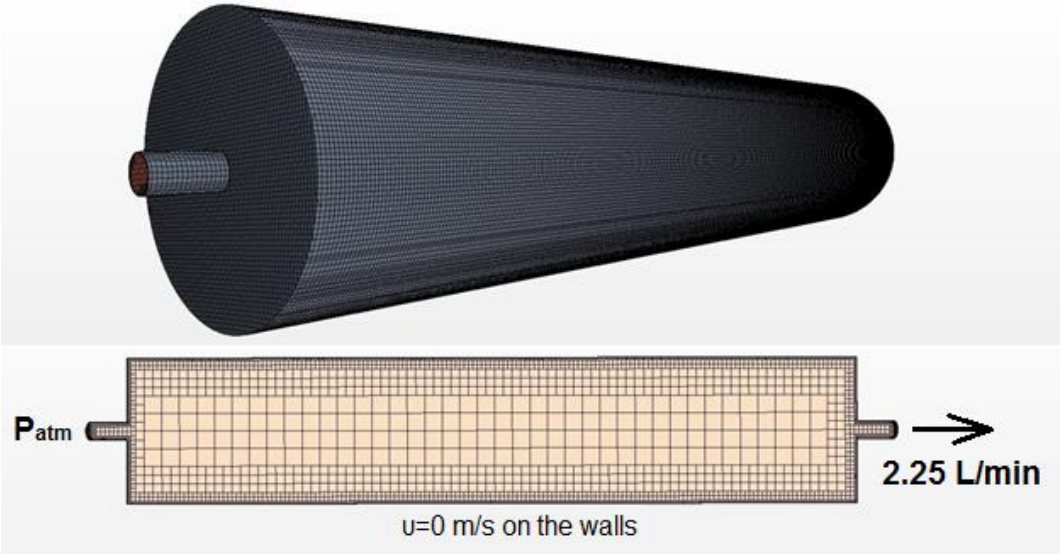

Figure 2.1: Example of a flow tube geometry, mesh and boundary conditions for a CFD simulation

The simulations performed using STAR CCM + started from the simple geometry of a cylindrical flow tube (Fig. 2.1) and evolved to more complex geometries, with the objective to achieve a flow pattern that minimizes recirculation eddies, and therefore wall effects. The physical constraints for the design are the length of approximately 1 m, and a flow rate of at least 0.75 L/min which is close to the flow rate of conventional O_3 or NO_2 monitors.

A total flow rate of 2.25 L/min was used, leading to a theoretical residence time of 4.8 min assuming laminar plug flow in a volume of 10.8 L. This residence time is shorter than the one used in Cazorla and Brune (2010) (7.5 min for a laminar plug flow) and was chosen because a short residence time would allow the OPR instrument to respond faster to a change in the sampled air mass composition, and could possibly reduce wall losses, since the sampled air stays in touch with the walls for a shorter time. However, the low residence time is associated to a higher flow rate which leads to larger recirculation eddies near the inlet of the flow tubes and more turbulences. As a result, the optimum flow rate depends on a tradeoff between the turbulence generated by higher flow rates and the slow instrumental response due to lower flow rates.

In total, approximately 25 simulations were performed to find a good design, and three different geometries were selected below to illustrate the evolution of the geometry until the final design, as shown in Fig. 2.2. The dimensions and total flow rate are equal among these simulations to allow a direct comparison, altering only the geometries of the inlet and outlet. The length of the flow tube is 70 cm, the diameter 14 cm and the total flow rate 2.25 L/min. On the left side of Fig. 2.2, the geometry is shown in opaque and transparent forms, while on the right side the streamlines of the flow are color coded with the flow velocity. The

streamlines describe lines that are tangential to the instantaneous velocity direction and show the direction in which a massless fluid particle will travel at any point in time. In all cases, the flow is entering the tube from the left side, and exiting from the right.

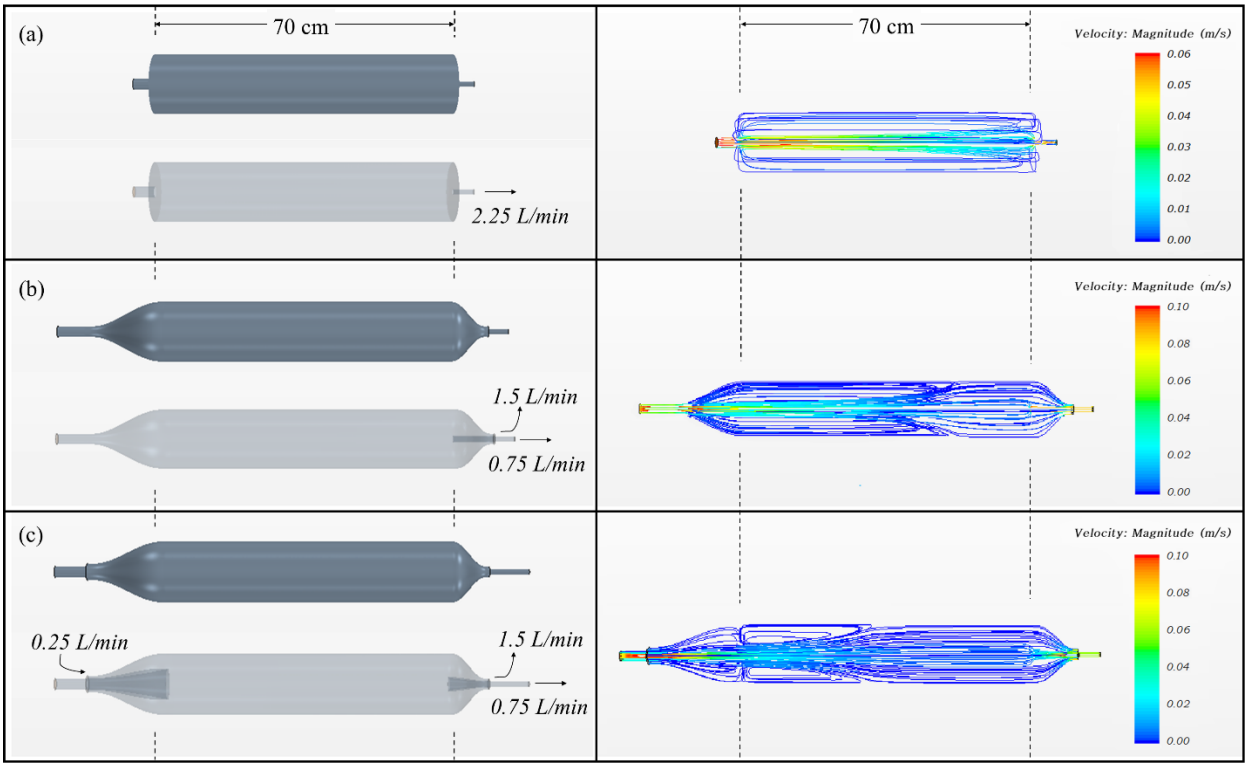

Figure 2.2: Evolution of the simulations to optimize the geometry of the sampling flow tubes – on the left, the geometry in opaque and transparent form with the flow rate boundary conditions, and on the right the streamlines.

The first geometry (a) consists of a simple cylindrical tube, with inlet and outlet outer diameters of 2.54 cm (1") and 1.27 cm (½"), respectively. As shown on the right side of the figure, the streamlines form recirculation eddies all along the length of the flow tube. For this geometry, a large fraction of the air entering the tube stays in contact with the walls and is sampled by the monitor. This will likely alter the composition of the air mass, including possible loss of O_x on the walls, or release of other species, e.g. HONO. In this case, recirculation effects are undesirable, since wall contacts are amplified.

The eddies appearing here result from the sudden increase of the cross section of the tube near the inlet, often referred to as backward facing step. The size of these eddies depend on the geometry and the flow velocity, generally with larger and more intense eddies for higher flow rates and higher Reynolds numbers (Biswas et al., 2004).

The second geometry (b) includes a curved conical inlet that smoothens the backward facing step. The length of this inlet is 20 cm, and the cross section increases from 2.54 cm (1") to 14 cm. The flow in a pipe of increasing or decreasing diameter is known as Venturi flow. It has been shown (Tutty, 1996;Singhal and

Parveen, 2013) that the best flow pattern is achieved when a small diverging angle is implemented (5 to 12°, depending on the Reynolds number). In our case, in order to keep a reasonable length for the flow tube, it is not possible to use an angle smaller than 35°. This inlet geometry is expected to reduce the recirculation issues but the flow separation is unavoidable. On the outlet side, the air is sampled at 0.75 L/min through an internal outlet (Ø=1.27 cm, ½") that is located at the center (radial position) of the flow tube. The purpose is to sample air coming along the central axis of the flow tube that has interacted less with the walls, while the air in contact with the walls is extracted using an external pump at 1.5 L/min on the outer periphery of the outlet.

A close inspection of the streamlines of this geometry shows that eddies are reduced to the first 45 cm of the tube. Geometry (b) is improved compared to geometry (a), regarding the extent of the recirculation eddies and the sampling taking place only at the central axis of the tube.

The third geometry (c), which is the final geometry that was used in the OPR instrument, has a similar sampling collector (inner outlet), but using a conical shape to reduce the perturbation of the flow near the area of the outlet. The internal outlet starts from an outer diameter of 3 cm at the point where the flow is sampled, decreasing to a diameter of 1.27 (½") cm after 10 cm. The flow rates at the outlet are the same as in geometry (b). At the inlet side, ambient air is sampled by a curved conical internal inlet at the center of the flow tube, while zero air is injected at 0.25 L/min at the periphery of the inlet inside the flow tube. The injection flow rate was limited to approximately 10% of the total flow rate, to minimize the impact of a dilution on $P(O_3)$ measurements. This additional air is expected to help keeping the flow forward, minimizing recirculation eddies, and therefore reducing the impact of the walls on the chemical composition of the sample. The internal inlet has an initial inner diameter of 2.2 cm that increases to 7 cm over a length of 20 cm, until the point where the flow enters the cylindrical flow tube, leading to an entrance angle of 11.4°.

As can be seen from the streamlines of geometry (c), the recirculation eddies are minimized to the first 30 cm of the flow tube, resulting to a clear improvement compared to geometries (a) and (b). It is important to note here, that by lowering the extraction flow rate, a lower total flow rate would decrease the extent of these eddies. For example, a total flow rate of 1.5 L/min would lead to eddies on the first 18 cm of the flow tubes. However, as mentioned previously, the 2.25 L/min flow rate was chosen to reduce the overall response time of the OPR instrument, which is particularly important during field measurements, as the chemical composition of ambient air can quickly change.

For the construction of the flow tubes, several details were added to the final design. Issues to be addressed were the feasibility of constructing two flanges for each flow tube (inlet and outlet) providing a curved internal shape, the material to be used, the connections between the flanges and the flow tubes, the connections of the inlet and outlet flanges to Teflon tubes, and finally, the injection and extraction of air at

the periphery of the internal inlet and outlet. Taking into account these constraints, the design of the flow tubes was finalized as shown in Fig. 2.3 with additional details explained with arrows. Detailed schematics of the flanges, including dimensions and technical characteristics are presented in Annex I.

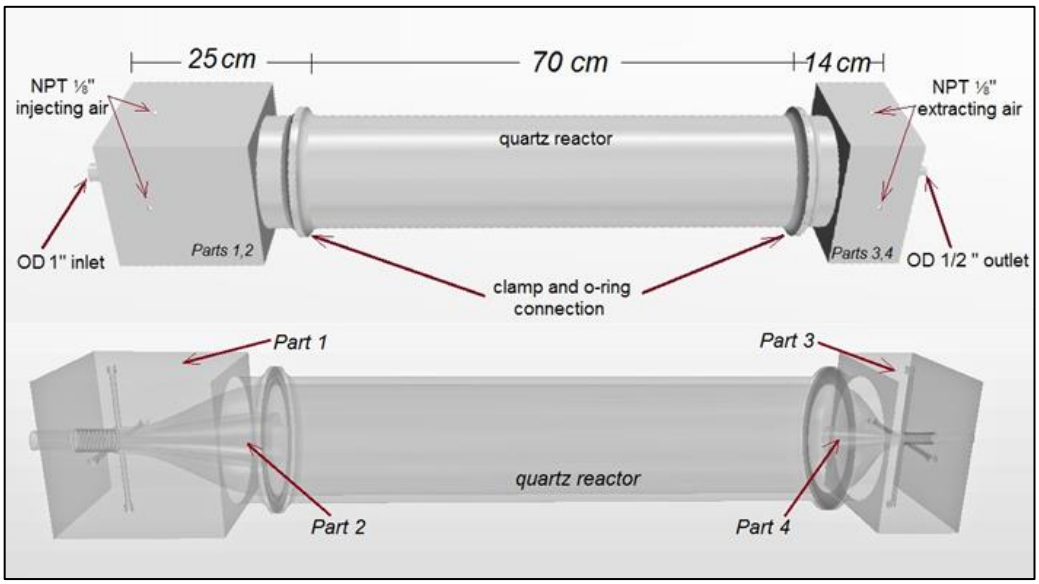

Figure 2.3. Final design of the flow tubes in opaque and transparent form.

To simplify the construction of the flanges, each one consists of two parts. For the inlet, Part 2 (internal inlet) is screwed inside Part 1 (external flange), while for the outlet, Part 4 (internal outlet) is screwed inside Part 3 (external flange). Since Parts 1 and 3 wouldn't be in contact with ambient air, it was decided to be built using aluminum, while Teflon was preferred for the inner surfaces in contact with ambient air, i.e. Parts 2 and 4. The connection of the flanges with the cylindrical flow tube is achieved using a round clamp. A groove was added on the flanges to insert an o-ring providing a good sealing at the interface.

The left side of Part 2 has a diameter of 2.54 cm (1"), so a reduction connector of 1-to-½" was used along with ½" Teflon tubing to build a sampling line. Similarly, Part 3, with a diameter of 1.27 cm (½"), is connected to a reduction connector of ½-to-¼" with ¼" Teflon tubing to provide the sample to the conversion unit. The injection/extraction of air is realized through four holes placed symmetrically around the flanges, using NPT ⅛" connections. The two flow tubes are placed on an aluminum board, while the four flanges and the board are anodized with a grey color.

The reference flow tube is covered by a filter that blocks UV radiation. The UV filter used is an Ultem® film (polyetherimide, 0.25 mm thick, CS Hyde Co, USA) that blocks radiations with wavelengths below 400 nm. However, a direct contact of the filter with the quartz tube could lead to a temperature increase in this flow tube and, as a consequence, possible differences in the flow pattern and the reaction rates. For this reason,

the UV filter was placed on a rectangular aluminum frame outside of the reference flow tube, which was designed to flow ambient air between the filter and the tube using fans. This setup allows removal of the excess of heat released by the filter when the solar actinic flux is filtered and helps keeping the two flow tubes at the same temperature. For similar reasons, a frame covered by a Teflon film (.002" thick, DuPont Teflon® FEP) that is transparent to the solar radiation is used for the ambient flow tube, to reduce heat dissipation by the wind. Figure 2.4 shows the two flow tubes being tested outside, with and without the Teflon film frame.

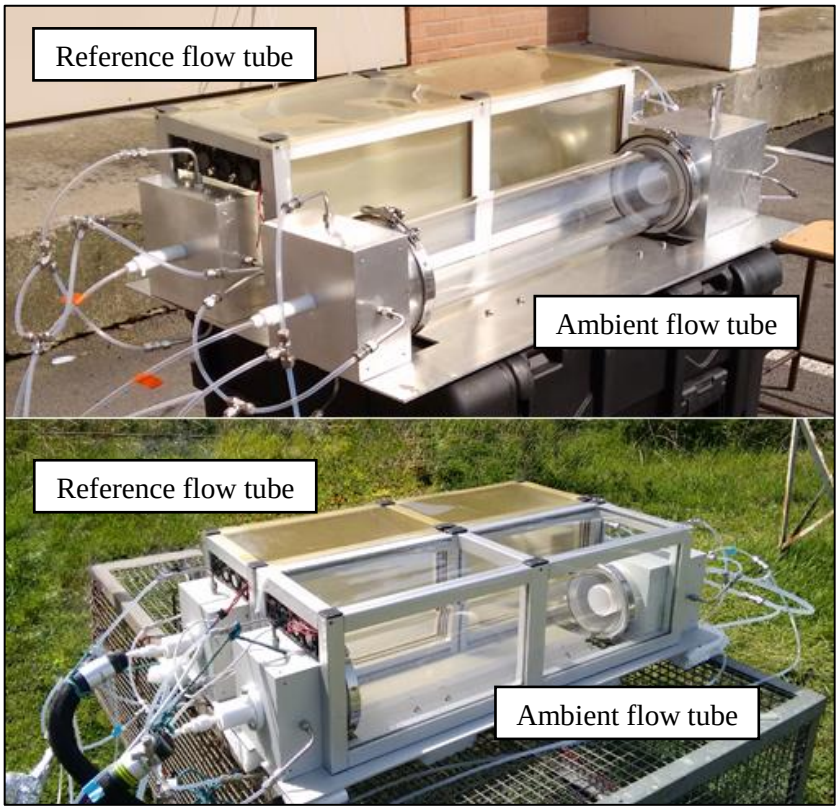

Figure 2.4: The flow tubes being tested outside – on top only with the UV filter frame, on the bottom with the UV filter and the Teflon frames.

2.2.2 Conversion unit and O_x detection

The UV filter is used to stop the radical chemistry and ozone production in the reference flow tube by lowering the photolysis frequencies of radical precursors. By blocking wavelengths below 400 nm, the filter also leads to a lower photolysis frequency for NO_2, resulting in a shift of the NO_x-O_3 photostationary state (PSS) towards NO_2. In addition, the radical chemistry occurring in the ambient reactor also disturbs the NO_x-O_3 PSS. As a consequence, the partitioning between O_3 and NO_2 will be different between the two reactors,

and a differential measurement of only O_3 wouldn't provide an accurate value of the amount of ozone produced in the ambient flow tube. To overcome this issue, it is necessary to measure the sum of O_3 and NO_2 (known as O_x), to accurately quantify the production of new ozone molecules in the ambient flow tube from the difference in O_x between the two flow tubes.

In order to measure O_x in the OPR instrument, two methods can be applied:

- Convert NO_2 to O_3 through NO_2 photolysis as in Cazorla and Brune (2010) and quantify ozone with an O_3 monitor,
- Convert O_3 to NO_2 using a NO titration scheme and quantify NO_2 with an NO_2 monitor.

Both methods were tested during the development of the OPR instrument. Initially, a converter using the first method was constructed and tested in the laboratory, quantifying the conversion efficiency at different NO_2 and relative humidity levels. A second conversion unit based on the other method was also constructed and compared to the first method. Both converters will be described here, as well as in the characterization section 2.3.2.

2.2.2.1 Photolytic NO_2-to-O_3 converter coupled to an O_3 monitor

The conversion of NO_2 into O_3 is based on the photolysis of NO_2 in $O(^3P)$ atoms, which quickly react with molecular oxygen in ambient air to produce ozone. This is the same mechanism that leads to atmospheric ozone formation as discussed in section 1.4.1. The UV radiation for NO_2 photolysis is generated by a 40-Watt Phoseon FireFly UV lamp that emits wavelengths peaking at 395 nm. As shown in Fig. 2.5, this wavelength is where the maximum quantum yield for NO_2 photodissociation meets the maximum absorption cross section and, as a result, there is the highest NO_2 photolysis efficiency.

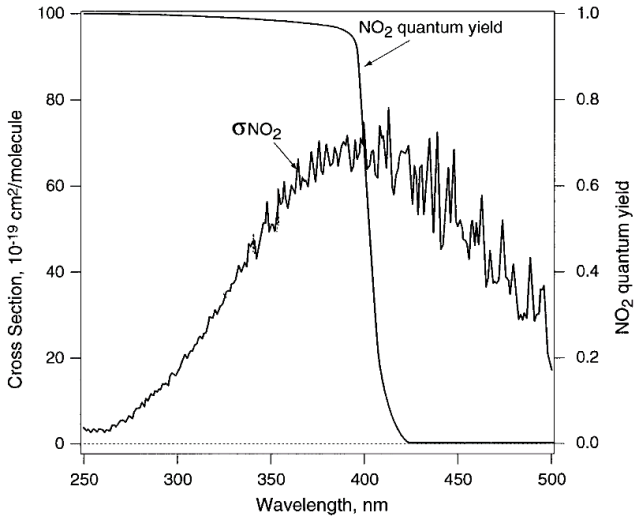

Figure 2.5: Absorption cross section of NO_2 and quantum yield for photodissociation into $O(^3P)$ (adjusted from Buhr (2007))

Fig. 2.6 shows a schematic of the NO_2-to-O_3 converter (a), a first version of the converter using two quartz cells (b), and a second version using four cells (c). The first version of the converter consisted of two 1"-OD / 20 cm length quartz cells – one for each flow tube (1-cell converter). The cells are placed in a rectangular box (10 × 25 × 25 cm), while their position was decided to be as far as possible from the lamp to get a similar homogeneous irradiation in the two cells (beam expansion from the source). The walls of the box were covered with a reflective tape to achieve a homogeneous photon flux everywhere inside the box. As a result, even if one cell is closer to the lamp than the other one, the conversion efficiency is expected to be similar in the two cells. A rectangular hole was also opened on one side of the box to attach the lamp using two "L" brackets. Finally, the converter was completed with a screwed cover on top of the box (not shown in the pictures).

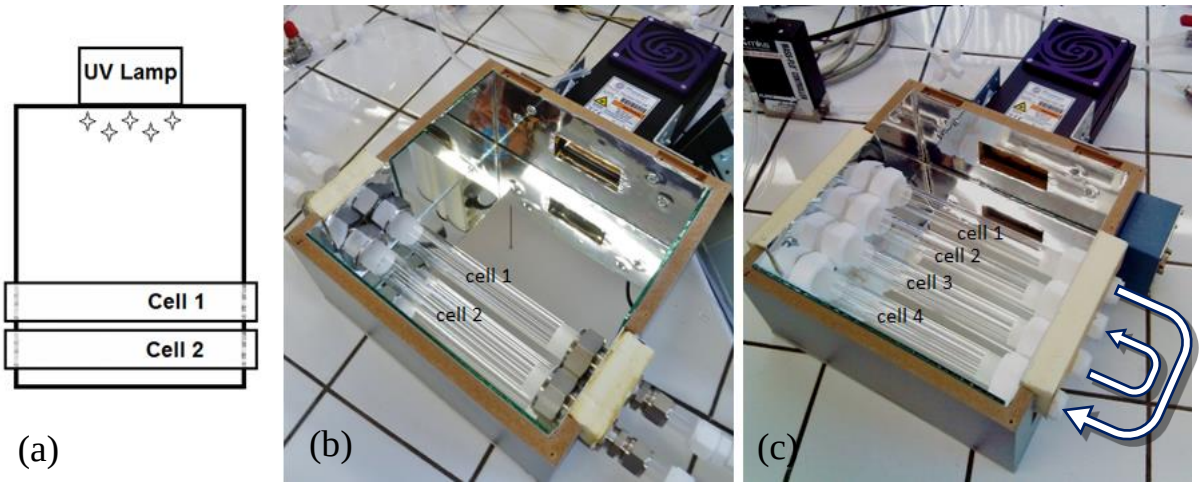

Figure 2.6: Initial schematic of the NO_2-to-O_3 converter (a), two-cells version (b), and four-cells version (c). The arrows on (c) show the connection setup between the different cells.

Tests performed with the first version of the converter, described in section 2.3.2.1, showed a conversion efficiency of less than 55%, more than 37.5% lower than the highest conversion efficiency observed by Cazorla and Brune (2010) for their homemade conversion unit. This was mainly caused by the short residence time in the quartz cells (approximately 5.5 sec, calculated assuming a plug flow of 1 L/min in the cells), that did not allow enough NO_2 to be photolyzed. An additional reason was the reflective tape inside the converter, exhibiting a reflectivity far from 100%. To increase the reflectivity, real mirrors were placed on inner walls of the converter. To increase the residence time, the two cells were connected in series with a short piece of ¼" Teflon tubing, leading to a longer conversion cell, doubling the residence time to 11 sec. For this setup, four cells were used in the converter, two for each flow tube (2-cells converter), connecting the first cell with the last one and the second with the third one, as shown in Fig. 2.6(c).

The NO_2-to-O_3 converter was coupled to an O342M ozone monitor (Environnement SA) for the quantification of O_x in each flow tube. The sampling flow rate of this ozone monitor is 1 L/min and its limit of detection is 0.4 ppbv for a response time of 20 s.

Cazorla and Brune (2010) used an ozone monitor with two optical cells (Thermo Scientific, Model 49i). This monitor was modified to perform differential O_x measurements by connecting each chamber to one optical cell. Our ozone monitor had only one UV absorption cell and the measurements from the reference and ambient flow tubes were taken sequentially, using a set of solenoid valves at the entrance of the monitor. The difference between the ambient and reference measurements is calculated in near real-time during the data post processing using a homemade acquisition software.

2.2.2.2 Chemical O_3-to-NO_2 converter coupled to a CAPS NO_2 monitor

The conversion of O_3 into NO_2 is based on the following reaction (R 1.3), where O_3 and NO react to produce NO_2.

$$O_3 + NO \rightarrow NO_2 + O_2 \qquad \text{(R 1.3)}$$

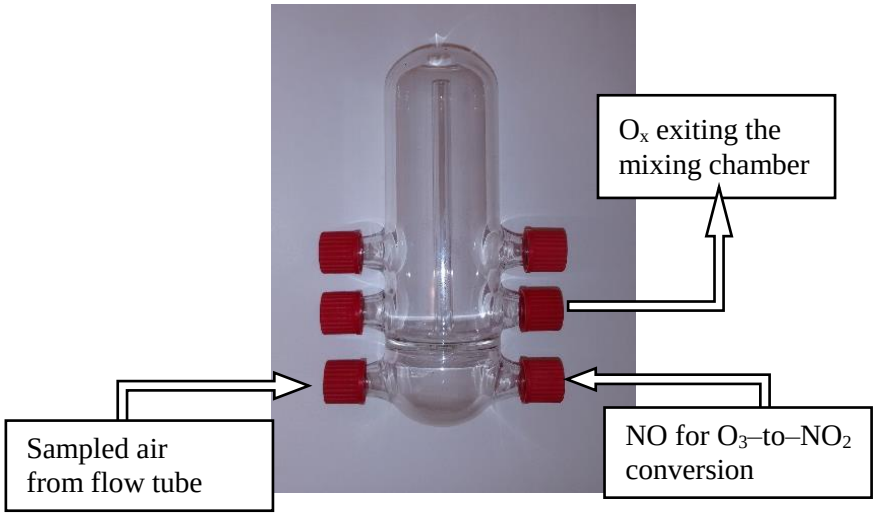

Figure 2.7: Mixing chambers used for the O_3-to-NO_2 converter

The O_3-to-NO_2 converter consists of two identical pyrex mixing chambers shown in Fig. 2.7, one for each flow tube, with a volume of 290 cm^3, leading to a residence time of 23 seconds at a flow rate of 750 SCCM (Standard Cubic Centimeter per Minute). This flow rate corresponds to the sampling flow rate of the NO_2 monitor. Based on kinetic considerations for the titration reaction of O_3 by NO, which exhibits a rate constant of 1.80×10^{-14} cm^3 $molecule^{-1}$ s^{-1} at a temperature of 298 K (Atkinson et al., 2004), calculations showed that 500 ppbv of NO would lead to a conversion of approximately 99.5% of O_3 for a reaction time of 23 seconds.

The addition of NO is performed using two mass flow controllers (MKS, 50 mL/min range) set at flow rates of 10 SCCM, one for each mixing chamber, using a NO cylinder (Praxair or Indiana Oxygen) at 50 ppmv.

This setup leads to a NO mixing ratio of 667 ppbv in the mixing chambers, corresponding to a conversion efficiency of approximately 99.9%.

The O_3-to-NO_2 converter was used along with an Aerodyne Cavity Attenuated Phase Shift Spectroscopy (CAPS) NO_2 monitor (Kebabian et al., 2005;Kebabian et al., 2008) that samples air at 750 SCCM. Unlike chemiluminescence-based monitors, the CAPS monitor doesn't require conversion of NO_2 to NO and is not sensitive to other species containing nitrogen. Its principle is based on producing a long optical path (up to 2 km) using very high reflectivity mirrors in a sampling cell that is less than 30 cm in length. A light emitting diode (LED) is used as an optical source and the presence of NO_2 in the cell causes a phase shift in the signal received by a photodetector that is proportional to the NO_2 concentration. The time resolution of the CAPS monitor can be as low as 1 second, while the limit of detection (3σ) for a 10-sec integration time is less than 100 pptv.

2.2.3 OPR schematic and measurement sequence

A detailed schematic of the OPR instrument is shown in Fig. 2.8 for the setup based on the O_3-to-NO_2 conversion method. Both flow tubes sample ambient air from a common external ½"-OD Teflon inlet. The injection of zero air at the periphery of each internal inlet is performed using two mass flow controllers (MFCs) (MKS, 2 L/min range), set at 250 SCCM. A flow rate of 750 SCCM of air is sampled from each flow tube through the internal outlet and is sent to the conversion unit. Additional air is extracted at the periphery of the internal outlet at a flow rate of 1500 SCCM using two MFCs (MKS, 2L/min range) connected to a pump (KNF, N86KN). Relative humidity and temperature are monitored both at the exit of the flow tubes and at the conversion unit with RH sensors (Measurement Specialties, HTM2500LF).

The flow tubes are connected to the conversion unit using two 4 m long heated Teflon lines. The temperature of the heated lines is set at a higher value than the ambient temperature, i.e. 40 ºC, to minimize potential losses of NO_2 in the lines. After the converter, the sampled mixture is sent to the CAPS monitor.

Since the CAPS is a single-cell monitor, the measurements from the ambient and reference flow tubes are taken sequentially, using two 3-way solenoid valves at the entrance of the CAPS monitor (SV1 and SV2 in Fig.2.8). When the flow from the ambient (or reference) flow tube is sampled by the CAPS monitor, the flow from the reference (or ambient) flow tube is extracted by a pump and a MFC (MKS, 2 L/min range) set at the sampling flow rate of the CAPS monitor. The valves switch every 1 min, alternating the flows that are sampled by the CAPS monitor and the pump. The difference in O_x between the two flow tubes, ΔO_x, is calculated as the difference between an ambient flow tube measurement and the average of the 2 surrounding reference flow tube measurements. The first 15 seconds of each 1-min measurement are removed since they

describe a transient regime between ambient and reference flow tube measurements, therefore each O_x measurement is averaged over 45 s. As mentioned in section 1.5.2, ozone production values are calculated dividing ΔO_x by the residence time in the flow tubes, so each $P(O_3)$ measurement refers to the middle time of each ambient flow tube measurement, leading to 2-min $P(O_3)$ values.

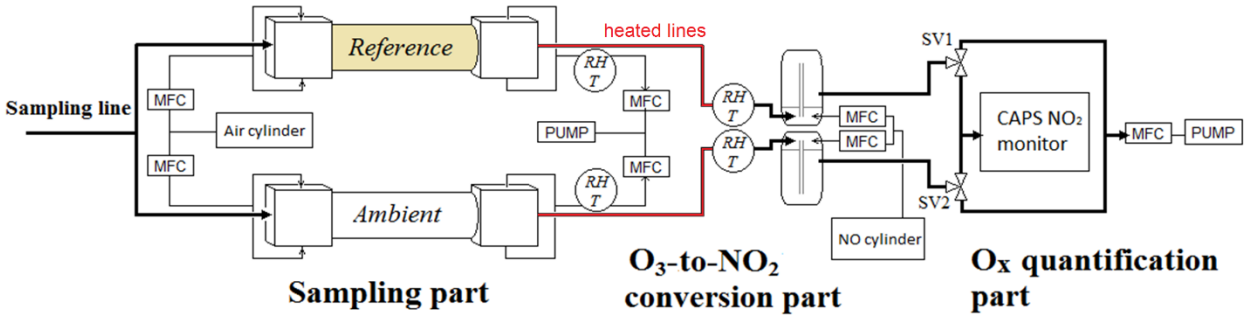

Figure 2.8: Schematic of the OPR instrument. O_3 is converted into NO_2 by reaction with NO. The O_x difference between the two flow tubes is quantified by a CAPS NO_2 monitor. Two solenoid valves (SV1-2) switch every one minute to allow subsequent measurements from the two flow tubes.

The measurement sequence is automated and controlled through a National Instruments LabView 2013 interface. Three USB data acquisition (DAQ) boards are used (NI-9264, NI-6008, NI-6009) to control the solenoid valves and the mass flow controllers and to record data from the CAPS monitor and the humidity and temperature sensors. The LabView software records the raw O_x measurements, as well as the $\Delta(O_x)$ difference in real time. In total, 21 parameters are stored in a data file every second (timestamp, 4 CAPS parameters, 7 flow rates from the MFCs, 4 values of relative humidity and temperature, and solenoid valve states). The mixing chambers, the mass flow controllers, the data acquisition boards, the solenoid valves, as well as electronic circuits are placed on a plexiglass board (61 cm × 41 cm), as shown in Fig. 2.9.

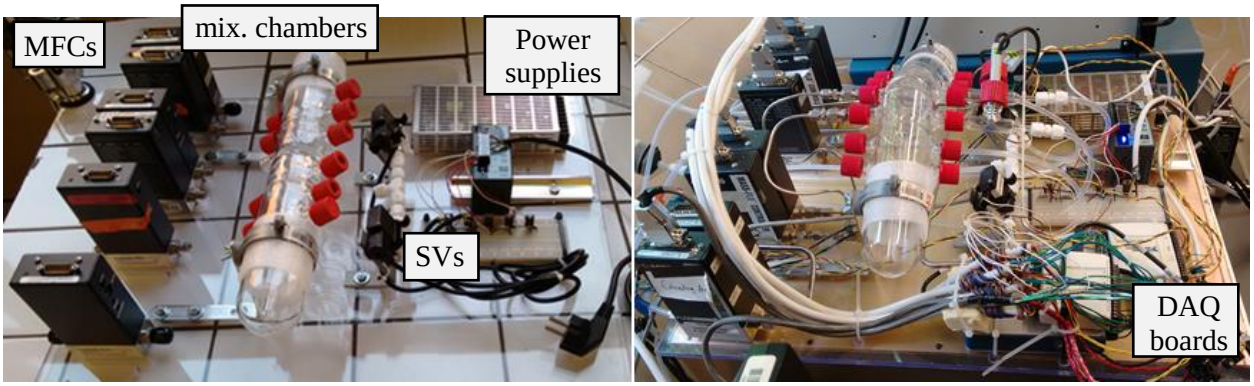

Figure 2.9: The board with the conversion unit, mass flow controllers, solenoid valves, power supplies and electronic circuits, used for the OPR instrument.

2.2.4 Synthetic irradiation cover

Experiments performed under fully controlled conditions of illumination would allow a better understanding and characterization of the OPR instrument. For this purpose, an enclosure equipped with fluorescent lamps was constructed to cover the flow tubes, with the goal to perform experiments under constant J-values conditions.

The artificial light used for $P(O_3)$ experiments should be in the UV range, with wavelength near 310 nm to initiate the radical production (e.g. O_3 photolysis leading to OH production) and 390 nm to efficiently photolyse NO_2 (O_3 formation). For this purpose, two types of lamps were used: the first ones with a peak of emission at 312 nm (Vilber, T-15.M) and the second ones with a peak of emission at 365 nm (Philips, Sylvania).

The lamps are connected on a wooden board (60 × 100 cm) with switches to be turned on and off. There are 4 lamps of 365 nm with independent switches and 4 lamps of 312 nm with switches paired by two. The lamps are placed diagonally on the board, with the 312 nm lamps in the middle. The board is placed on the top of an enclosure that covers both flow tubes (56W × 90L × 75H cm). The frame is made using aluminum struts (Norcan), while the walls are made of plexiglass and are covered by a reflective film to get an homogeneous photon flux everywhere inside the enclosure. Four fans are used to ventilate the interior and prevent the temperature from increasing. The lamp cover is shown in Fig. 2.10.

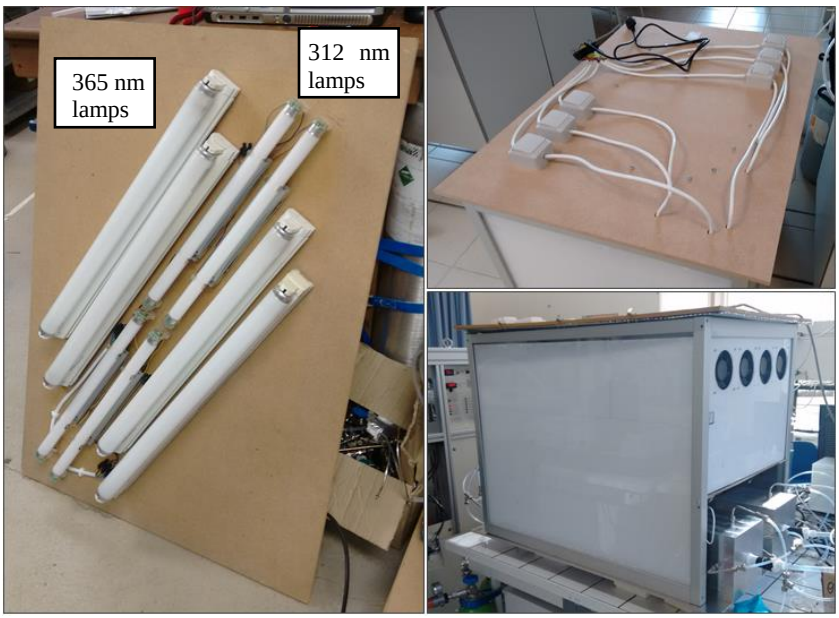

Figure 2.10: Lamp cover of the OPR instrument.

Photolysis frequencies were measured below the enclosure using a UV-Visible spectroradiometer (METCON, CCD-detector-spectrometer) at different locations to verify the homogeneity of the photon flux. J-values were measured for NO_2, O_3 ($O(^1D)$ pathway), HONO, H_2O_2, NO_3 (two pathways) and HCHO (two pathways). The spectroradiometer was placed at the center of the enclosure, at the four corners, and at the middle of the two longer sides, at a height of 20 cm.

Fig 2.11 presents the measured J-values in s^{-1} when all the lamps are turned on, at each of the above mentioned spots, while the position of the lamps is shown at the top left. The letters R and M for $J(NO_3)$ and J(HCHO) indicate the different pathways of the photolysis of NO_3 or HCHO towards a radical (R) or a closed shell molecule (M). Compared to J-values observed at the ground level in the ambient atmosphere, the J-values from these lamps are approximately four times lower at the center of the enclosure. However, the synthetic irradiation cover was proven to be a very useful tool for the characterization of the OPR instrument and the modeling of laboratory experiments.

Regarding the homogeneity of the photon flux, J-values at the corners are lower than at the center by 28% on average. When the spectroradiometer is placed at the positions of the two flow tubes, the J-values are lower by only 8% on average compared to the center of the enclosure. These measurements show that the photon flux inside the enclosure can be considered homogeneous for the OPR experiments.

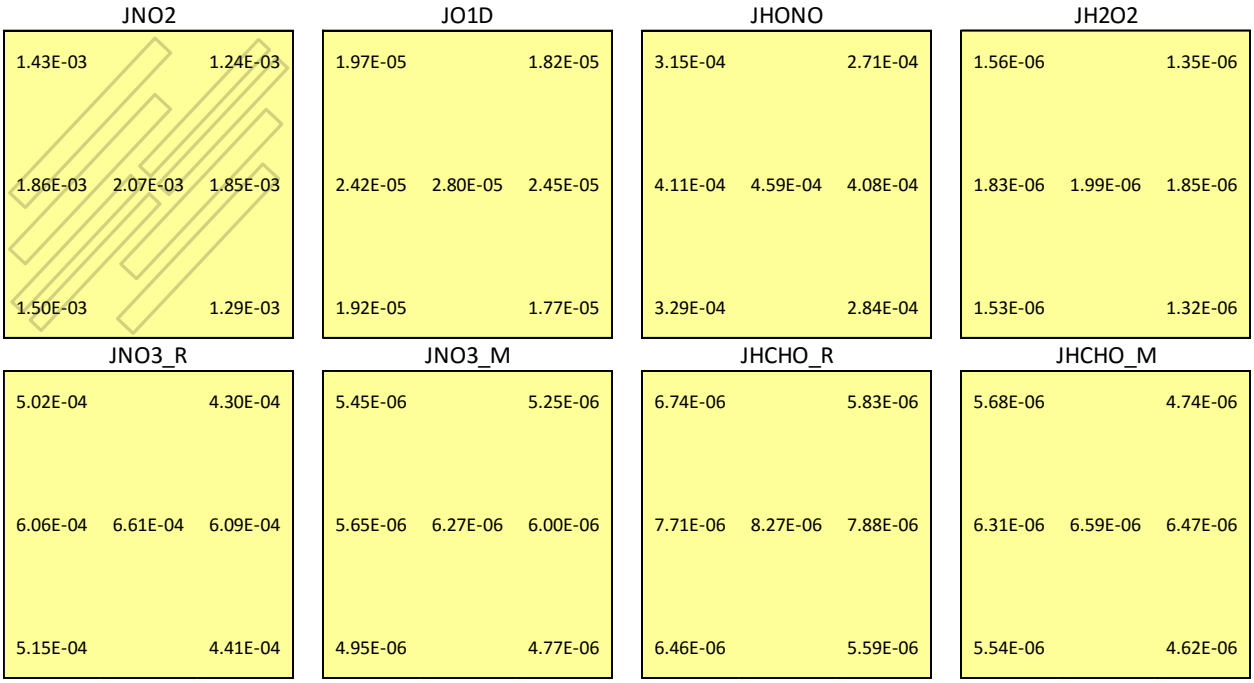

Figure 2.11: J-values measured inside the enclosure. The orientation of the eight lamps is shown on the top left for $J(NO_2)$. Each number represents the J-value measured at 7 different locations inside the enclosure: center, four corners and middle of the longer sides. Units are s^{-1}.

Additional measurements were performed by placing the aluminum frame with the UV filter inside the lamp enclosure, and the spectroradiometer at the position of the ambient flow tube. This was done in order to investigate whether the UV filter frame shades the ambient flow tube, which could lead to a decrease of the J-values. A 15% decrease on average was observed in this configuration. Table 2.1 reports the J-values that were measured under different irradiation conditions and that can be used for modeling purposes, since they better describe the operating conditions of the OPR instrument under the lamp cover.

Table 2.1: J-values measured at the position of the ambient flow tube, with the UV filter frame inside the enclosure. Units are s^{-1}.

Lamp status	JNO_2	$JO(^1D)$	JHONO	JH_2O_2	JNO_3_R	JNO_3_M	JHCHO_R	JHCHO_M
all lamps ON	1.4×10^{-3}	2.2×10^{-5}	3.1×10^{-4}	1.5×10^{-6}	6.0×10^{-4}	5.7×10^{-5}	6.4×10^{-6}	4.9×10^{-6}
1/2 lamps ON (above amb. flow tube)	7.1×10^{-4}	1.1×10^{-5}	1.6×10^{-4}	8.0×10^{-7}	3.4×10^{-4}	2.9×10^{-5}	3.4×10^{-6}	2.8×10^{-6}
1/2 lamps ON (above ref. flow tube)	6.0×10^{-4}	1.1×10^{-5}	1.3×10^{-4}	6.9×10^{-7}	3.1×10^{-4}	2.2×10^{-5}	2.9×10^{-6}	2.1×10^{-6}
4 x 365 nm ON	1.4×10^{-3}	2.7×10^{-7}	3.1×10^{-4}	4.2×10^{-7}	5.5×10^{-4}	5.7×10^{-5}	5.5×10^{-7}	1.6×10^{-6}
4 x 312 nm ON	1.0×10^{-4}	2.2×10^{-5}	1.6×10^{-5}	1.1×10^{-6}	7.1×10^{-5}	0	5.8×10^{-6}	3.5×10^{-6}

2.3 Characterization of the OPR

2.3.1 Sampling flow tubes

2.3.1.1 Quantification of the residence time

The mean residence time in the flow tubes was quantified from pulse experiments, sending pulses of toluene at the inlet of the flow tubes and quantifying the time it takes for the pulse to exit the flow tube. A PTR-ToFMS (Proton Transfer Reactor – Time of Flight Mass Spectrometer) from KORE Technology (second generation model) was connected to the outlet to detect toluene. The setup is shown in Fig. 2.12. The time resolution of the PTR-ToFMS was set at 3 seconds. A canister of 3 ppmv of toluene was used, along with a micro-orifice and a solenoid valve at the inlet, to inject 300 SCCM of gas for a duration of 11 seconds.

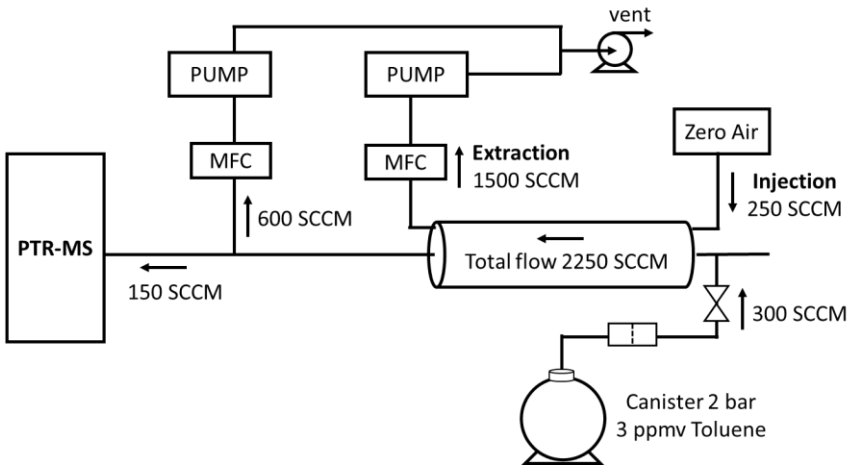

Figure 2.12: Schematic of the experimental setup to measure the residence time in the flow tubes, with the operating conditions (flow rates) of the OPR instrument.

Since the sampling flow rate of the PTR-ToFMS is 150 SCCM, a pump and a mass flow controller set at 600 SCCM were used to reproduce the flow rate of the CAPS monitor (750 SCCM). Four different flow rate setups were tested, with a total flow rate ranging from 950 to 3450 SCCM, in order to examine how the residence time and the shape of the pulse change with the flow rate. The flow rate was modified by altering the zero-air injection and air extraction flow rates, keeping the dilution close to 10%.

When a pulse of toluene was sent at the entrance of the flow tube (time t=0 sec), the PTR-ToFMS acquisition was trigged to measure toluene over 1500 s, creating a probability distribution of the time variable t. The probability mass function, P(t), which expresses the probability that the time variable is equal to a certain value, is calculated by the counts measured by the PTR-ToFMS as shown in Eq. 2.1. The average residence time in the flow tube is the mean of the probability distribution and is calculated by Eq. 2.2 as a weighted average of the possible values that the time variable can take.

$$P(t) = \frac{counts\ (t)}{\sum counts} \qquad \text{(Eq. 2.1)}$$

$$\bar{t} = \sum t\, P(t) \qquad \text{(Eq. 2.2)}$$

Additionally, given the volume of the flow tubes (10.8 ± 0.3 L), a theoretical residence time can be calculated for each experiment, assuming plug flow conditions, and compared to the experimental observations.

Four pulses are presented in Fig. 2.13 for different total flow rates. The red dashed line shows the theoretical residence time for each flow rate setting, while the black dashed line the experimental average residence time. This figure shows that the shape of the time distribution, as well as the relative difference between the experimentally and theoretically quantified residence times, vary among the four settings.

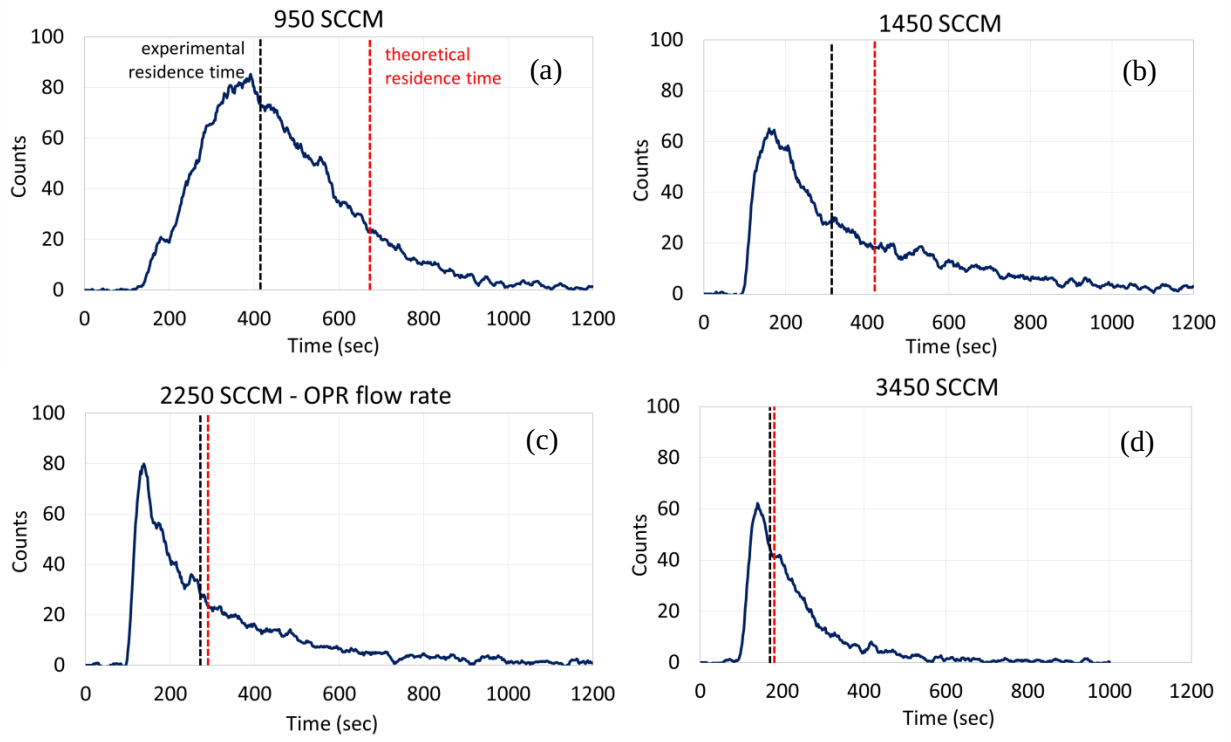

Figure 2.13. Example of four pulse experiments characteristic of different flow rate settings. The red dashed line shows the theoretical residence time and the black dashed line the average residence time determined experimentally.

It is interesting to note that, in all cases, the experimental residence time is shorter than the theoretical value. The theoretical residence time corresponds to a laminar plug flow where all the molecules have the same velocity. In reality, the flow rate at the central axis of the flow tube, where air is sampled, is faster than the flow rate near the walls. During these experiments, the sampling flow rate at the outlet is kept constant at 750 SCCM, while the extraction flow rate is modified. For this reason, at a low total flow rate, the gradient of the flow velocity, as one moves from the central axis towards the edge of the flow tube, is larger compared to a higher flow rate. A larger gradient of the velocity leads to a larger disagreement between the theoretical and experimental residence times.

Table 2.2 summarizes the different flow conditions that were tested, as well as the measured residence times, the standard errors of the means and the theoretical residence times. The setting (c) corresponds to the operating conditions of the OPR instrument in the field, as also described by the fluid dynamic simulations (section 2.2.1). The values reported here are the average of 4 pulse experiments for settings (a), (b) and (d) and 5 pulse experiments for setting (c).

Table 2.2: Experimental and theoretical quantifications of residence times in the flow tubes under different flow rate conditions.

Setting	Injection	Extraction	Pump + PTRMS	Total flow rate	Dilution	Experimental res. time		SEM	Theoretical res. time
	(SCCM)	(SCCM)	(SCCM)	(SCCM)		(min)	(s)	(s)	(s)
(a)	106	200	750	**950**	11.2%	**6.8**	407.4	7.8	680.2
(b)	161	700	750	**1450**	11.1%	**5.4**	321.5	7.4	445.7
OPR - (c)	250	1500	750	**2250**	11.1%	**4.5**	271.2	13.0	287.2
(d)	383	2700	750	**3450**	11.1%	**3.0**	178.9	11.7	187.3

Figure 2.14 shows how the residence time changes with the total flow rate. The residence time decreases almost linearly with the flow rate within this range of flow conditions. For the flow rate settings of the OPR instrument (c), the average residence time was quantified at 4.52 ± 0.22 min. The uncertainty on the residence time can therefore contribute to a 4.9% error (1σ) on the $P(O_3)$ measurements.

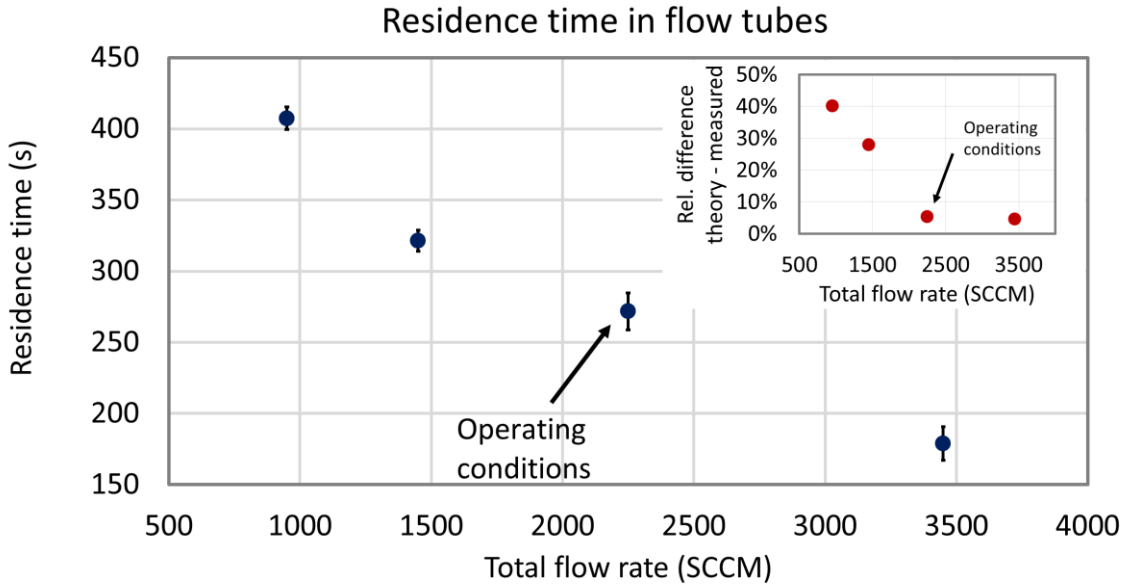

Figure 2.14: Average residence time in the flow tubes as a function of the total flow rate. Error bars are the standard error of the means (1σ) of the 4 pulse experiments for settings (a), (b) and (d) and 5 pulse experiments for the OPR settings (c).

Another point that should be addressed is that, as can be seen from Fig. 2.13, the detected pulses are asymmetric and exhibit a long tail, indicating that a large range of residence times is observed in the flow tubes. As shown by fluid dynamics simulations (section 2.2.1), recirculation eddies near the internal inlet keep the gas in the flow tube for a longer time than the calculated average residence time. For this reason, a

"air-exchange time" of the flow tubes needs to be determined, which corresponds to the time it takes to reach 95% of a stable signal when a change in the air composition occurs at the inlet.

In order to quantify this air-exchange time, tests were performed by introducing a constant concentration of O_x species inside the flow tubes until a stable signal was observed on the OPR. The O_x level was then quickly changed to quantify how long it takes for the signal to stabilize to a new value. Fig. 2.15 shows one of these experiments, where an O_3 mixture of approximately 40 ppbv is introduced into the flow tubes. The O_3 addition is turned off at t=400 s, while zero air continues flowing inside the flow tubes. This test was done for the flow rate corresponding to the operating conditions of the OPR instrument (i.e. total flow rate of 2250 SCCM). Figure 2.15 shows that the signal stabilizes at zero at approximately t=1600 s, leading to an air-exchange time of 20 minutes. An air-echange time of 20 min corresponds to a maximum residence time of 1200 s, as observed in Fig. 2.13(c). Experiments performed using lower total flow rates have led to longer air-exchange times, e.g. 1450 SCCM corresponds to a 30 min air-exchange time (max residence time 1800 sec). Additionally, for comparison purposes, an exponential fit performed on the decay shown in Fig. 2.15 indicates a decay rate λ of 0.00374 s^{-1}, or a mean life time $\tau = 1/\lambda = 267.4$ s, which is within 2% of the residence time quantified from the pulse experiments.

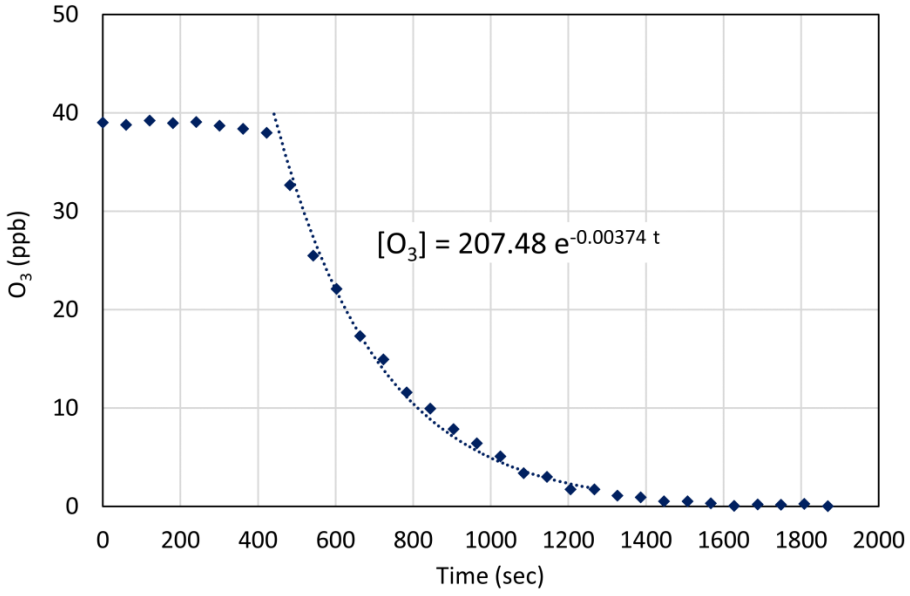

Figure 2.15: Experiment showing the air-exchange time in the flow tubes under field operating conditions. Air-exchange time estimated at 1200 sec.

Minimizing the air-exchange time allows the instrument to respond faster to changes in atmospheric composition. This time could be further reduced by increasing the extraction flow rate, and as a consequence, the total flow rate in the tubes. However, as discussed in section 2.2.1, if the total flow rate is increased,

larger recirculation eddies could increase wall effects in the reactors. For the reasons discussed above, a total flow rate of 2250 SCCM was found to be suitable for the OPR instrument.

As mentioned in section 2.2.3, a $P(O_3)$ value is recorded every 2 minutes. Since the air-exchange time is approximately 20 minutes, the 2-minute $P(O_3)$ values are not independent from each other and therefore the OPR instrument cannot detect sudden $P(O_3)$ changes. This means that in order to observe trends in ozone production during the day, we need to look at a longer timescales than a few minutes, and the OPR measurements should be averaged every 20 minutes in order to get independent measurements.

2.3.1.2 Quantification of O_x losses

This section describes tests performed for the quantification of O_3 and NO_2 losses on the walls of the flow tubes. These tests were performed both in the laboratory and during the field deployment of the instrument. Additionally, this section describes the investigation of the O_3 loss dependence on absolute humidity and J-values, through tests performed in the field.

Quantification of O_3 and NO_2 losses – The principle of the OPR instrument requires that the difference in O_x between the two flow tubes is only due to ozone production in the ambient flow tube. All other characteristics, including residence time, flow pattern and potential wall reactions should be the same in the two flow tubes so that their effect on Ox levels would cancel out in the differential O_x measurement.

However, if surface-O_x losses were different between the two flow tubes, it would have a strong impact on the $P(O_3)$ measurements. For example, for an ambient O_x level of 50 ppbv and a residence time of 4.5 min in the flow tubes, a 1.5 % difference in O_x losses between the two tubes would lead to a bias of 10 ppbv/h on the $P(O_3)$ measurements. This source of errors has also been observed by Cazorla and Brune (2010) for the MOPS instrument, where the wall loss of NO_2 in the chambers was found to be significant under high relative humidity conditions.

O_x losses inside both flow tubes were tested in the laboratory and during the field deployment of the OPR instrument by injecting known mixing ratios of O_3 or NO_2 inside the flow tubes at different relative humidity values and measuring O_x at the exit of the tubes. O_x mixing ratios were always measured with the CAPS monitor, either directly during the NO_2 loss tests, or through the O_3-to-NO_2 converter during the O_3 loss tests. The relative O_x loss was calculated as described by Eq. 2.3, using measured mixing ratios of O_x.

$$O_x\ loss = \frac{O_{x\ before\ flow\ tubes} - O_{x\ after\ flow\ tubes}}{O_{x\ before\ flow\ tubes}} \qquad \text{(Eq. 2.3)}$$

Figure 2.16 shows results of NO_2 (top) and O_3 (bottom) loss tests performed in the laboratory by introducing O_x mixing ratios from approximately 15 to 95 ppbv in the ambient (left) and the reference (right) flow tubes.

The results presented here were obtained after two days of flowing 200 ppbv of O_3 in the flow tubes at a relative humidity of 60% (cleaning process). These tests were performed at relative humidity values of 40% and 65% for NO_2 and 45% and 70% for O_3. The measured O_x mixing ratios are compared to the 1:1 line, as well as with the 0.95:1 and 1.05:1 lines.

For NO_2, these laboratory tests showed a relative loss lower than 2% for individual measurements, without any water dependence. On average, the NO_2 loss was quantified at approximately 0.4% and 0.7% for the ambient and the reference flow tubes, respectively.

For O_3, the tests presented here indicate an average ozone loss of 2.9% and 1.8% for the ambient and reference flow tube, respectively, including both relative humidity values that were examined. The difference observed between the two flow tubes, if significant, is on the same order of magnitude as the example given above and could impact ambient measurements of $P(O_3)$. In addition, first laboratory tests performed before flowing concentrated mixtures of O_3 at high relative humidity inside the flow tubes for a few days (cleaning process) had showed elevated losses of O_3 on the walls, on the order of 20%. These results strongly suggest that losses of O_3 in the flow tubes should be tracked during field measurements to evaluate the error introduced on the $P(O_3)$ measurements.

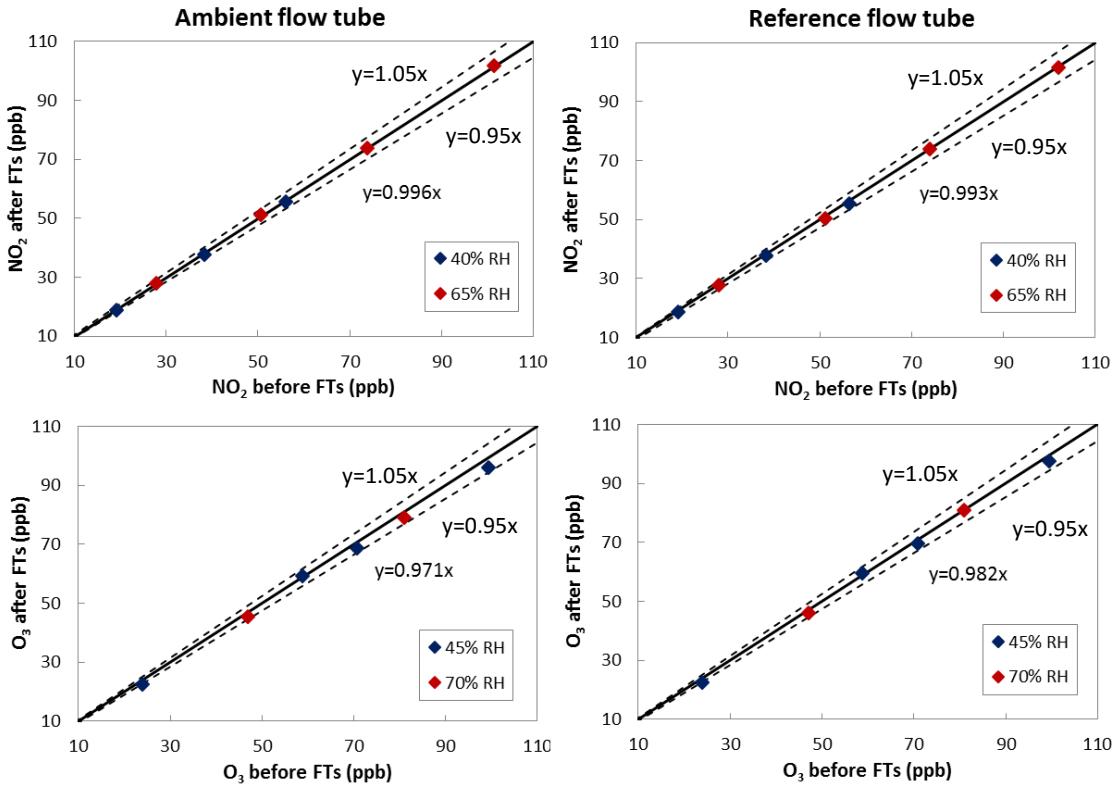

Figure 2.16: NO_2 (top) and O_3 (bottom) loss tests performed in the laboratory for the ambient (left) and the reference (right) flow tubes. The abbreviation "FTs" indicates "flow tubes".

O_x losses were also tested during field deployments of the instrument. Figure 2.17 presents the results of NO_2 (left) and O_3 (right) loss tests in the ambient (top) and reference (middle) flow tubes, as well as the comparison of the relative NO_2 and O_3 losses between the two flow tubes (bottom). These tests were performed at different relative humidities and dates during the IRRONIC field campaign (see chapter 4), using the same methodology as in the laboratory.

During the IRRONIC field campaign, the NO_2 loss tests were performed under dark conditions, with the flow tubes covered by a plastic tarp, so no NO_2 photolysis is expected. The NO_2 loss was found to be lower than 5%, as shown in Fig. 2.17(a, b). Indeed, the NO_2 loss was 2.7% and 3.2% on average for the ambient and reference flow tubes, respectively. In addition, as shown in Fig. 2.17(e), a decrease in relative humidity from 65% to 0% on the 6th of August led to a slight decrease of the NO_2 loss by 1.5 % in both flow tubes. When the two flow tubes were operated under the same conditions, the losses in the reference tube were higher than in the ambient tube by 0.5% on average. For ambient NO_2 levels of 30 ppbv, such a small difference in NO_2 losses could lead to a positive $P(O_3)$ bias of 2 ppbv/h.

Moreover, questions also arise when the relative humidity is different in the two flow tubes. As explained above, a difference of 65% in relative humidity may cause a 1.5 % difference in NO_2 loss between the two flow tubes, which in turn would lead to a bias of approximately 6 ppbv/h in the $P(O_3)$ measurements for an ambient NO_2 mixing ratio of 30 ppbv. However, the fans used on the OPR instrument to flow ambient air between the UV filter or the Teflon film and the flow tubes minimize temperature differences between the two tubes, leading to relative humidity differences lower than 4%, as observed during the field testing and differences in NO_2 losses due to differences in relative humidity should be greatly reduced.

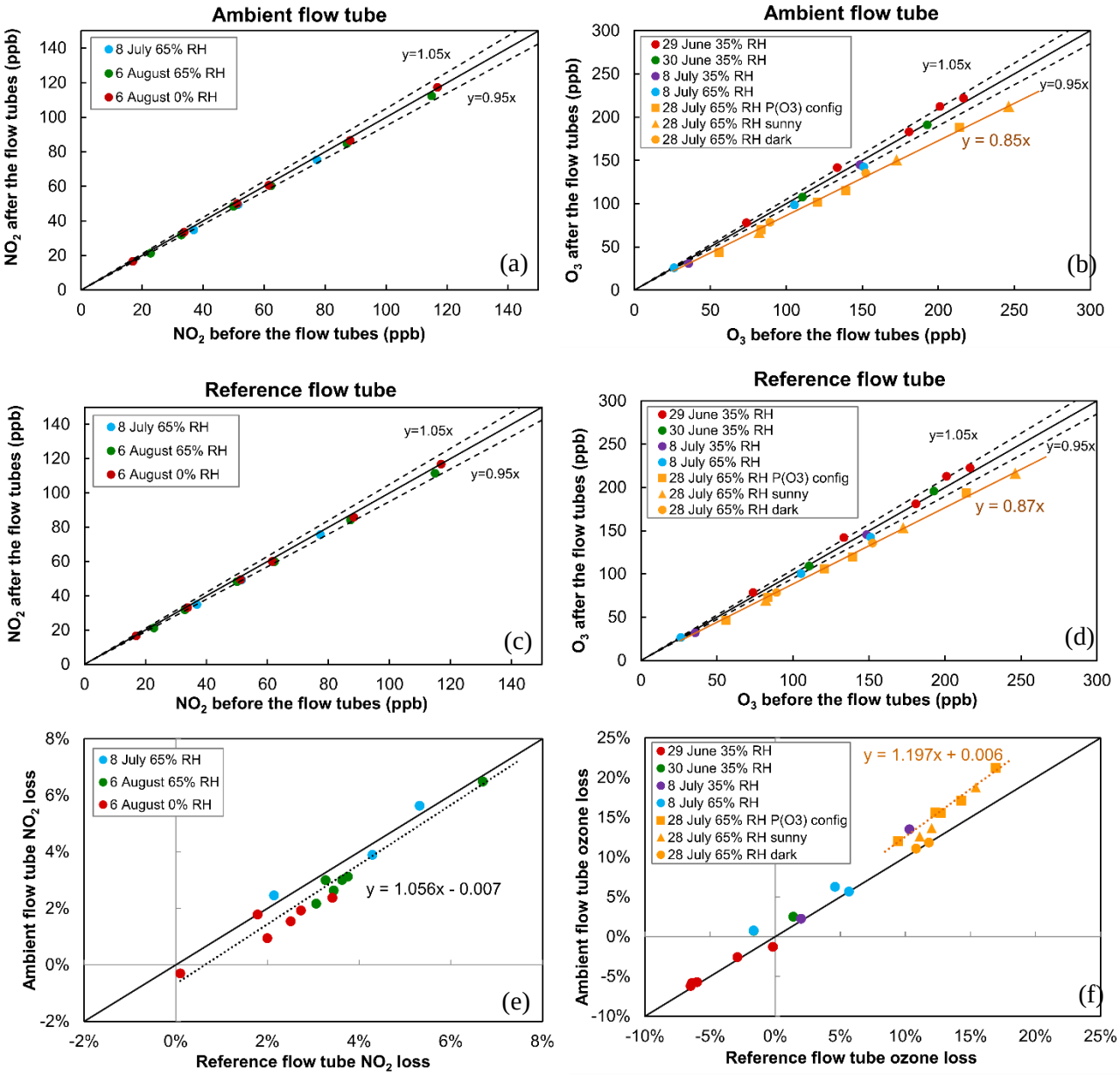

Figure 2.17 NO_2 and O_3 loss tests performed on different dates during the IRRONIC field campaign at different relative humidity values. The bottom panel indicates the difference in relative losses between the 2 flow tubes. On 28 July O_3 losses were measured under sunny conditions with the configuration of $P(O_3)$ measurements (orange squares), under sunny conditions with both flow tubes irradiated (orange triangles) and both tubes covered by an opaque cover (orange circles).

The importance of NO_2 losses also depends on the environment in which the OPR instrument is deployed. For this study, the instrument was deployed in forested environments, where ambient NO_x levels were lower than a few ppbv. For the reasons discussed above, the NO_2 losses are not thought to be critical for the field measurements presented in this study. Further analysis over the impact of the NO_2 losses on the $P(O_3)$ measurements is discussed in the modeling section 3.5.2 for NO_x-rich environments.

Regarding the O_3 loss shown in Fig. 2.17 (b, d, f), tests were performed mainly during cloudy or rainy days, when ambient J-values were low ($J(NO_2) < 0.006\ s^{-1}$), with the flow tubes covered by a plastic tarp. On 28th of July, however, O_3 losses were measured (i) under sunny conditions with the configuration of the $P(O_3)$ measurements: ambient flow tube exposed to the light and reference tube covered by the UV filter (orange squares), (ii) under sunny conditions with both flow tubes exposed to the sunlight (orange triangles), and (iii) dark conditions with both tubes covered by an opaque tarp (orange circles).

During the first days of the campaign (29 June-8 July) a close inspection of the measurement scatter shown in Fig. 2.17(b, d) indicates that the relative loss of O_3 is lower or close to 5%, similar to that observed in the laboratory for clean flow tubes. However, ozone loss tests performed on 28th of July, after one month of operation in the field, reveal an increase up to about 13% and 15% for the reference and ambient flow tubes, respectively. In this case, the absolute loss of ozone is linearly dependent on the ozone mixing ratio. The increase of ozone loss after a long exposure in the field indicates that unsaturated organic species may adsorb on the quartz surface and may react with O_3.

Particular attention should be paid on the three different tests performed on July 28 regarding the irradiation conditions. When the losses are quantified under dark conditions (orange circles in Fig. 2.17(f)), the losses are equal between the two flow tubes and close to 13%. However, when the ambient flow tube is irradiated and the reference is covered by the UV filter (orange squares – $P(O_3)$ configuration), one can see that the O_3 loss in the ambient tube is higher than in the reference by approximately 3%. In other words, there seems to be a photoenhanced ozone loss, linearly dependent on O_3 mixing ratios, that mainly takes place in the ambient flow tube when it's irradiated. For ambient O_3 levels of 50 ppbv, this difference in O_3 losses would lead to a negative $P(O_3)$ bias of approximately 20 ppbv/h.

Box modeling has shown that the gas-phase photolysis of O_3 in the ambient flow tube could account for 0.05% of the observed ozone loss at most. Moreover, when both flow tubes are irradiated (orange triangles – sunny), the losses in the ambient flow tube are still higher than for the reference. This result suggests that differences in the surface composition of each tube or their irradiation history may play a significant role in the surface chemistry, and the two flow tubes don't necessarily behave the same way when they are operated under the same conditions.

Investigation of the O_3 loss dependence on absolute humidity and J-values **–** Additional tests were performed to further investigate a potential photolytic O_3 loss, specifically regarding its dependence on absolute humidity and J-values. These tests were realized using the lamp cover and the artificial UV light described in section 2.2.4, introducing known amounts of ozone in the flow tubes and varying the humidity or light conditions. These O_3 loss experiments were performed during the deployment of the instrument on

the campus of Birmingham University (May 2016) and during the PROPHET – AMOS field campaign (July 2016).

Initially, the ozone loss was quantified from Eq. 2.3, under dark conditions and at a specific absolute humidity. Then the lamps were turned ON using different settings: (i) all lamps ON (4 × 312 nm & 4 × 365 nm), (ii) side A ON (2 × 312 nm & 2 × 365 nm, above ambient flow tube), (iii) side B ON (2 × 312 nm & 2 × 365 nm, above reference flow tube), (iv) 4 × 365 nm lamps ON, (v) 4 × 312 nm lamps ON. These steps were repeated for two or three different humidity values for each experiment. The objective was to investigate the humidity dependence of the dark and photolytic ozone losses, as well as the wavelengths that mostly contribute to the photolytic loss of O_3 in the ambient flow tube.

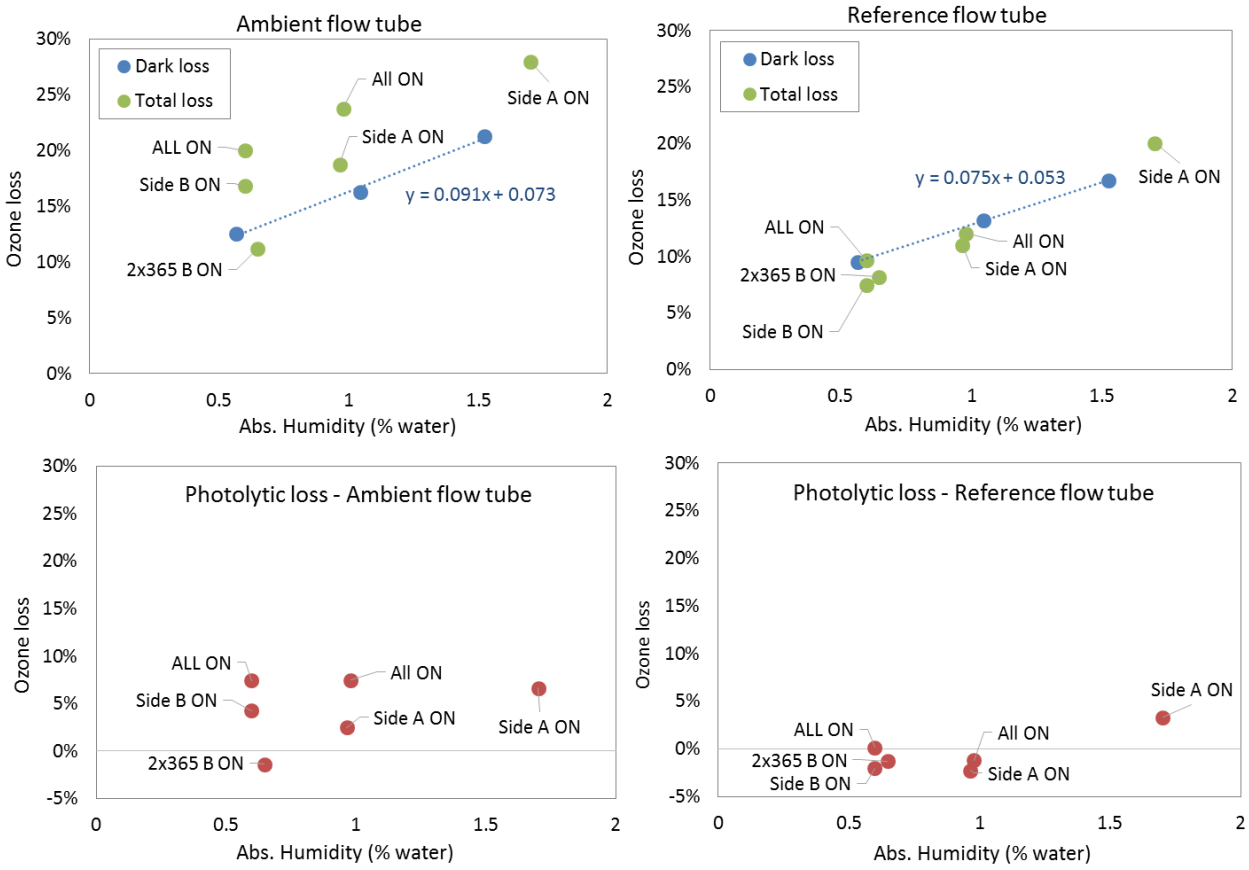

Figure 2.18: Relative ozone loss in each flow tube as a function of absolute humidity during field testing performed in Birmingham. The blue circles indicate losses under dark conditions and the green circles total losses under irradiated conditions. The difference between them is shown using the red circles.

Figure 2.18 shows the relative ozone loss in each flow tube as a function of absolute humidity during field testing performed in Birmingham, after four days of outdoor testing with ambient air. It is interesting to note that a large dark loss was observed in the flow tubes (≈10-20%), indicating contamination of the flow tubes.

The O_3 mixing ratio used in these tests was 55 ppbv. The blue markers represent the dark loss of O_3 when the lamps are OFF and the green markers the total loss (dark + photolytic) observed when the lamps were turned ON. Labels on the green markers describe the different irradiation conditions. Assuming that the dark loss does not change when the lamps are turned ON, the difference between the total loss and the dark loss yields the photolytic component of the loss, which is shown using red markers in the bottom panels.

These tests indicate a linear humidity dependence of the dark ozone loss in both flow tubes, with a slightly stronger dependence for the ambient flow tube. Additionally, in this experiment, the dark loss seems to be higher in the ambient flow tube by 3.6% on average.

For the ambient flow tube, when all lamps are turned ON (for the two lower humidity conditions), the photolytic ozone loss is approximately 7.5%. Turning OFF half the lamps also leads to a decrease of the photolytic loss by half. This result seems to indicate that the photolytic loss depends linearly on J-values. In addition, there is not a clear humidity dependence of the photolytic loss in this test. For absolute humidity values between 0.5% and 1%, the photolytic loss does not change when all the lamps are on. However, there may be a humidity dependence for higher absolute humidities (AH> 1.5%), since the photolytic loss measured with half lamps ON for an AH of 1.75% is close to the photolytic loss measured when all lamps are ON for the lower humidity values. Finally, it is clear that the wavelengths causing the photolytic ozone loss are close to 312 nm, since the photolytic loss is approximately zero when the 365 nm lamps are used alone.

Similar tests shown in Fig. 2.19 were performed during the PROPHET field campaign to further investigate the contribution of each wavelength (312 nm and 365 nm) to the photolytic ozone loss. The ozone mixing ratio used was 80 ppbv. The methodology described above for the irradiation was also used during these tests. It is interesting to note that the dark ozone loss (≈5%) was lower than during the other tests discussed above, indicating a lower level of contamination of the flow tubes. However, the flow tubes had not been used for about a month before these tests and a loss of 5% still indicates a significant level of contamination.

As seen in Fig. 2.19, absolute humidity values of 0.54% and 1.5% were tested on 9 July 2016, with the experiment performed at 1.5% humidity being chronologically the first one. The following day (10 July), a higher humidity level of 2% was tested, and in the end of the day the 1.5% humidity condition was repeated again for comparison with the previous day. The tests of the second day are shown in Fig. 2.20.

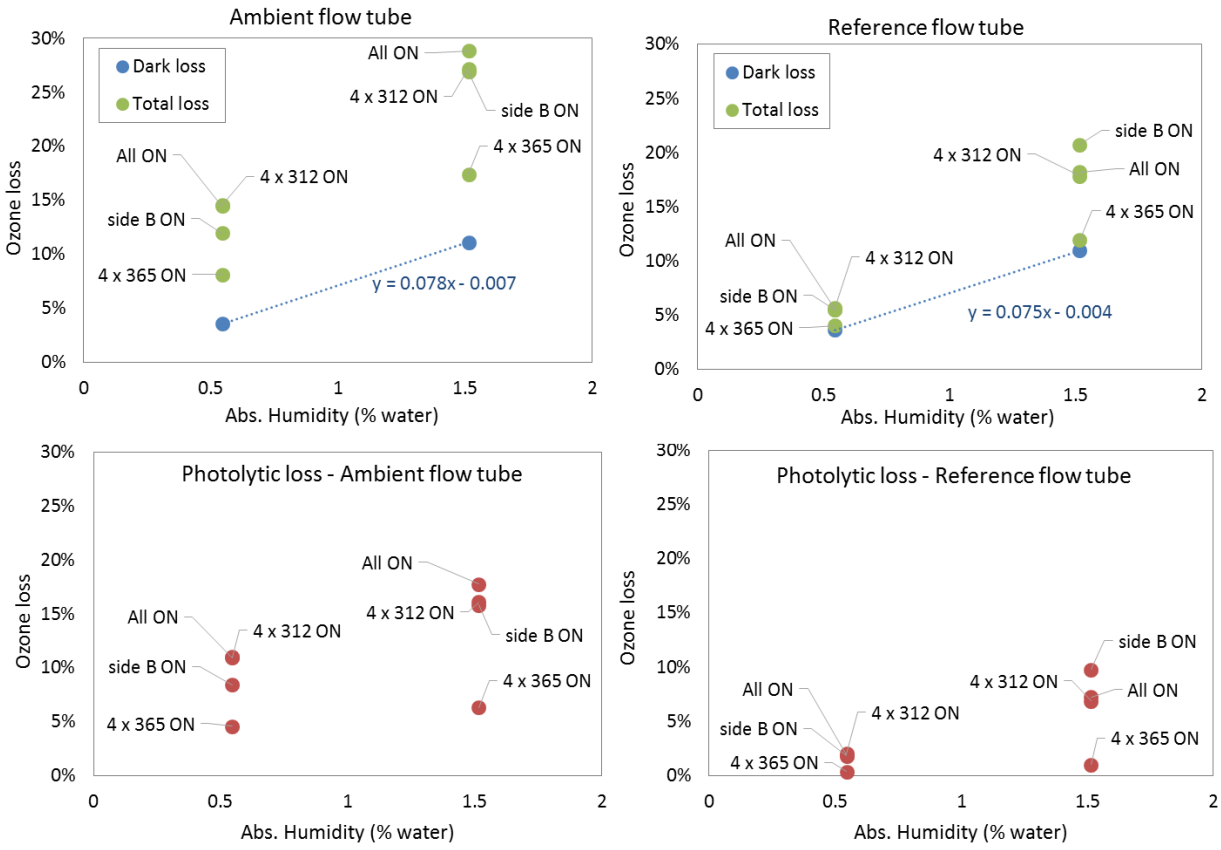

Figure 2.19: Relative ozone loss in each flow tube as a function of absolute humidity during PROPHET-AMOS 2016. Tests performed on 9 July 2016. The blue points indicate loss under dark conditions, the green points the total loss under irradiated conditions and the red points the difference between them.

During 9 July 2016, the results from the PROPHET-AMOS campaign generally support the findings from the tests performed in Birmingham, with the 312 nm lamps clearly contributing the most to the observed ozone loss. A positive water dependence of the dark loss is also observed, with a similar slope as in Birmingham. However, this linear water dependence of the dark loss is not observed the next day (Fig. 2.20), with the dark loss being much lower for the highest humidity value (less than 5% compared to 10% on the previous day). Therefore, we can conclude that the dark loss changes from day to day, decreasing over time when zero humid air was used, consistent with contamination of the flow tubes.

Looking more carefully at the tests made in the ambient flow tube for both days (Fig. 2.19 and Fig 2.20), there seems to be a linear water dependence of the photolytic loss (red points), when all lamps are turned on, as the photolytic loss increases with increasing humidity on both days. Regarding the reference flow tube and the test made on 9 July 2016 (Fig.2.19), one could say that there are photoenhanced processes that lead to ozone losses in this tube as well. However, since the test at 1.5% humidity was the first one performed

after a long time of not using the flow tubes, contamination issues on the walls may question the reliability of these results.

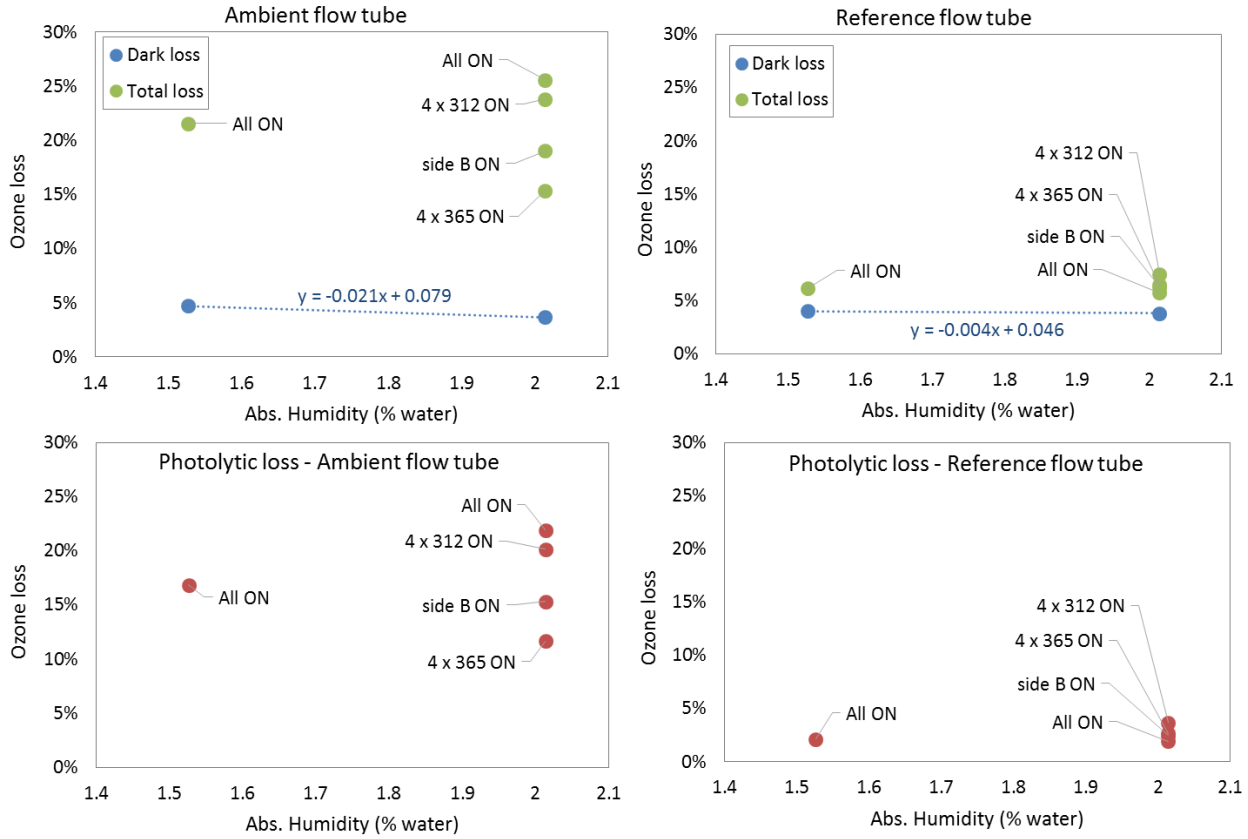

Figure 2.20: Relative ozone loss in each flow tube as a function of absolute humidity during PROPHET-AMOS 2016. Tests performed on 10 July 2016. The blue points indicate loss under dark conditions, the green points the total loss under irradiated conditions and the red points the difference between them.

On the next day, after flowing humid air with ozone, these photoenhanced processes in the reference flow tube decrease, as seen from Fig. 2.20, where the same humidity conditions were used. For 1.5% absolute humidity, the photoenhanced loss in the reference tube (red points) decreases from 10% to 2%. Therefore, while there is not strong indication of the photoenhanced processes in the reference flow tube, there are experiments suggesting that photoenhanced surface chemistry may take place in this flow tube as well, and this possibility cannot be ruled out. In any case, these processes are reduced after cleaning the flow tubes with humid air and ozone.

To sum up, the dark loss of ozone in the flow tubes varies from a few % to 15-20% after a long exposure in the field. This loss is linearly dependent on O_3 mixing ratios. It is usually different between the two flow tubes and seems to be water dependent. Frequent flushing periods with humid air and ozone during nighttime are suggested to decrease this dark loss. Additionally, there is a photo-encanced ozone loss in the ambient

flow tube, and may be present to a smaller extend in the reference flow tube.Short UV wavelengths are mainly responsible for this loss, which seems to be linearly dependent on O_3 mixing ratios, J-values and absolute humidity.

Suggested surface chemistry mechanisms - Since O_3 losses are thought to be critical for the OPR instrument, it is important to understand the mechanisms that drive these processes, in order to be able to improve the instrument in the future. The uptake of ozone on surfaces including Saharan dust, alumina films and mineral oxides under dark conditions has been studied by many authors (Michel et al., 2002;Sullivan et al., 2004;Chang et al., 2005;Hanisch and Crowley, 2003). For the dark loss, most authors suggest that the uptake of O_3 takes place on strong Lewis acid sites, where adsorbed O_3 molecules dissociate into O_2 and O. The O atom can then further react with O_3 to form two oxygen molecules for each O_3 molecule adsorbed.

Another possible mechanism could involve the reaction of O_3 with unsaturated organic compounds that have been adsorbed on the walls of the quartz tubes. For example, studies have been performed on the reaction of ozone with polycyclic aromatic hydrocarbons (PAHs) adsorbed on solid surfaces, like a glass microscope slide (Kahan et al., 2006) or a pyrex flow tube (Kwamena et al., 2006). These two studies suggested a Langmuir–Hinshelwood mechanism for the ozone uptake, where O_3 and PAHs adsorb on neighboring sites on the surface and undergo a bimolecular reaction.

Regarding the photoenhanced loss, Nicolas et al. (2009) studied the decomposition of ozone on illuminated TiO_2-SiO_2 solid mixtures, in a coated-wall flow-tube system. Additionally, Chen et al. (2011) also studied ozone decomposition on illuminated oxide surfaces, including TiO_2. Both studies showed a large photoenhanced ozone uptake using UV light. In these studies, the suggested mechanism for the photoenhanced ozone uptake by TiO_2 is described by the reactions R 2.1-R 2.7:

$$TiO_2 + hv \rightarrow TiO_2\ (e^- + h^+) \quad \text{(R 2.1)}$$

$$O_3 + e^- \rightarrow O_3^- \quad \text{(R 2.2)}$$

$$O_3^- + H^+ \rightarrow HO_3 \quad \text{(R 2.3)}$$

$$HO_3 \rightarrow O_2 + OH \quad \text{(R 2.4)}$$

$$OH + O_3 \rightarrow O_2 + HO_2 \quad \text{(R 2.5)}$$

$$O_2 + e^- \rightarrow O_2^- \quad \text{(R 2.6)}$$

$$O_2^- + O_3 \rightarrow O_3^- + O_2 \quad \text{(R 2.7)}$$

Ozone can be reduced either directly by a photo-generated electron (R 2.2) or indirectly by reactions (R 2.5-R 2.7). In the presence of water, the ozonide anion radical (O_3^-) can react with hydrogen cations, producing hydroxyl radicals (R2-3, R2-4), which reacts with ozone to produce HO_2 (R 2.5). It is interesting to note that

HO_2 can also react with O_3 to reproduce OH. While quartz is mainly composed of SiO_2, traces of other elements such as TiO_2 may contribute to the photoenhanced loss observed in the flow tubes.

It is also possible to speculate that another loss mechanism may involve the adsorption of O_3 on the quartz surface and its direct photolysis into excited atoms of oxygen, $O(^1D)$. If water molecules are available in the proximity of $O(^1D)$, this reactive species may quickly react with water to produce the OH radical. Additional adsorbed O_3 molecules will then be consumed through reaction R 2.5. It is very likely that such a mechanism would be enhanced by increasing ambient water concentrations since the production rate of OH will depend on the surface concentration of water.

These findings strongly indicate that both the dark and photolytic ozone losses are critical for the OPR instrument. Firstly, as discussed above, a difference in ozone loss between the two flow tubes can trigger false ozone production signals. Secondly, the ozone loss rate can change over time in each flow tube since during a field deployment of one month the dark loss increased from less than 5% to approximately 15%. Even higher losses (up to 25%) have been measured in the laboratory when the flow tubes were "dirty". Thirdly, a photolytic ozone loss in the ambient flow tube can lead to a negative bias on the ΔO_x signal since more O_3 will be lost in the ambient flow tube, giving the false impression of "negative ozone production" if the gas-phase ozone production rate is lower than the ozone surface loss rate in the ambient flow tube.

For these reasons, monitoring the ozone loss is essential when the OPR instrument is used in the field. The dark component of the total loss can be kept low (<5%) by frequent flushing of the flow tubes with zero humid air and O_3 during the night. On the other hand, it's not straightforward to track the photolytic loss during the day, since it depends on J-values and humidity, which vary during the day and from day to day depending mainly on the weather conditions. A way to deal with this issue would be to parameterize the photolytic component of the ozone loss as a function of J-values, O_3 mixing ratio and absolute humidity. This parameterization is further discussed in chapter 4 (section 4.4).

2.3.1.3 Quantification of HONO production

Nitrous acid (HONO) is a major source of the OH radical in the troposphere and therefore affects ozone production. Many authors have shown that HONO can be produced on surfaces of laboratory systems under dark conditions, from the heterogeneous hydrolysis of NO_2 (Wainman et al., 2001;Finlayson-Pitts et al., 2003;Ramazan et al., 2004) as shown in (R 2.8)

$$2\ NO_2 + H_2O \rightarrow HONO + HNO_3 \qquad \text{(R 2.8)}$$

Many authors have also highlighted photoenhanced HONO sources, including the reduction of NO_2 in the presence of organic photosensitizers such as humic acids (Stemmler et al., 2006;Stemmler et al., 2007), as

well as the photolysis of adsorbed nitrate (NO_3^-) or nitric acid (HNO_3) in low NO_x environments (Zhou et al., 2003;Zhou et al., 2011;Scharko et al., 2014;Laufs and Kleffmann, 2016). Laufs and Kleffmann (2016) have studied the photolysis of adsorbed HNO_3 on pure clean quartz glass surfaces previously treated with HF (5%), but did not observe a direct photochemical formation of HONO. On the other hand, in a study realized by Ndour et al. (2008), mixed TiO_2-SiO_2 solid samples were exposed to NO_2 in a coated wall flow tube reactor and a photoenhanced uptake of NO_2 leading to HONO production was observed. Rohrer et al. (2005) have also showed a photolytic formation of HONO on Teflon surfaces with a strong dependence on temperature, relative humidity and $J(NO_2)$ for the SAPHIR atmospheric chamber. If HONO was produced on surfaces inside the OPR instrument, it would impact the $P(O_3)$ measurements by enhancing the oxidation rate of VOCs in the ambient flow tube.

Tests on HONO formation in the quartz flow tubes of the OPR instrument were performed in the laboratory using a CIMS (Chemical Ionization Mass Spectrometer) instrument (Dr. G. Huey, Georgia Tech) with the kind help of Dr. Jonathan Raff's group in Indiana University. The calibration of the CIMS was performed at 5 different relative humidities (0%, 20%, 40%, 60% and 80% at 18ºC). For the calibration of the CIMS, HONO was generated by passing gaseous hydrochloric acid (HCl) from a permeation device through a glass frit reservoir filled with sodium nitrite ($NaNO_2$). The amount of HONO generated from this source was quantified by FTIR (Fourier Transform Infrared Spectroscopy) using a spectrometer (Vertex 70, Bruker Optics). Mixing ratios of 0.5-10 ppbv of HONO were generated during the calibration and the response was linear with the HONO concentration.

The flow tubes were tested after the IRRONIC field campaign (see chapter 4), during which organic compounds had adsorbed on the walls of the flow tubes, contaminating the quartz surface. Later during these tests, the flow tubes were cleaned with acetone and distilled water and the HONO tests were repeated using the clean flow tubes.

Fig. 2.21 shows the experimental setup used to infer HONO production rates in the flow tubes. Mixtures of NO_2 and zero humid air were generated at 5000 SCCM and provided to the flow tubes with the excess of air sent to a vent open to the atmosphere. NO_2 was provided from a canister of 50 ppmv (60 psi, ≈4 bars), which was filled using a cylinder of 1% NO_2 in helium (Matheson Tri-Gas, Inc.) and zero air (Indiana Oxygen). The flow rates during the experiments were adjusted using mass flow controllers. The injection and extraction flow rates were set at the field operating conditions of the OPR instrument, i.e. 250 SCCM and 1500 SCCM, respectively. Since the CIMS instrument requires a sampling flow rate of 1000 SCCM, 250 SCCM of zero dry air were injected near the inlet of the CIMS, to achieve a sampling flow rate of 750 SCCM at the outlet of the flow tubes, similar to the sampling flow rate of the CAPS monitor. The irradiation was provided by the lamp cover described in section 2.1.4.

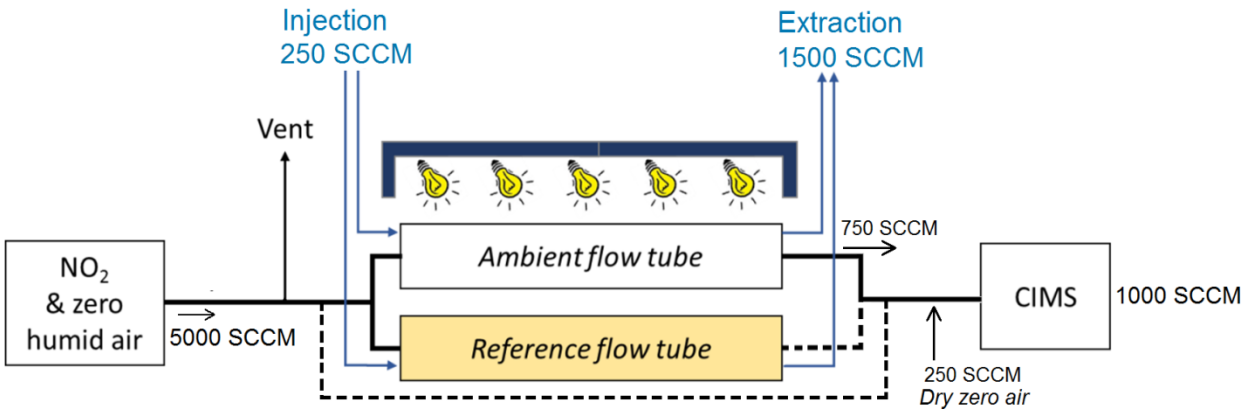

Figure 2.21: Experimental setup for the measurement of HONO production rates in the flow tubes, under dark or irradiated conditions. The CIMS can sample from the ambient or reference flow tubes, or before the flow tubes as shown by the dashed lines.

The measurement procedure was as follows:

a. zero air was sampled by the CIMS right before the inlet of the flow tubes, to test the zero of the CIMS instrument.
b. the humid NO_2 mixture was sampled right before the flow tubes. This measurement allowed to determine how much HONO was produced in the NO_2 dilution system;
c. the mixture was introduced inside the flow tubes and the HONO production rate was quantified in each flow tube under dark conditions;
d. the UV lamps were then turned ON, tracking the change in HONO in each flow tube. This measurement allowed assessment of the photolytic production rate of HONO;
e. the lamps were turned OFF, and the system was left to stabilize for a second measurement of "dark" HONO production. The final "dark" HONO value was calculated as an average of the two "dark" measurements.
f. in the end, a measurement was taken again at the inlet of the flow tubes. An average value of the two measurements before the flow tubes (steps b. and f.) was subtracted to all other measurements performed during the experiment to calculate HONO mixing ratios resulting from the formation of HONO in the flow tubes.

Several experiments were performed at different NO_2 mixing ratios (0, 40 and 100 ppbv) and relative humidities (25%, 50% and 80%). One of these experiments is presented in Fig. 2.22. The different light settings are indicated by different color shadings, where "1/2 lamps" corresponds to 2×312 nm & 2×365 nm lamps and "all lamps" to 4×312 nm & 4×365 nm lamps. The flow tube from which HONO is sampled is indicated at the top using a brown color for the reference and a yellow color for the ambient flow tube.

For the experiment presented in Fig 2.22, an average of 740 pptv of HONO was measured before the flow tubes (non-shaded areas). Subtracting this value from the measurements performed at the exit of the flow tubes, the mixing ratio of HONO under dark conditions is 721 pptv and 571 pptv in the ambient and reference flow tubes, respectively. Dividing these values by the residence time in the flow tubes (i.e. 271 s), one can calculate an average production rate of HONO under dark conditions. These concentrations correspond to production rates of 9.6 ppbv/h and 7.6 ppbv/h for the ambient and reference flow tubes, respectively.

When the lights are turned ON, there is a fast increase of HONO in the ambient flow tube, while no change is observed in the reference. It is important to note, however, that HONO is also photolyzed at the wavelengths emitted by the lamps (312 nm and 365 nm) and production rates calculated from the measured HONO concentrations as above represents lower bounds. It is estimated that for a J(HONO) value of 3.1×10^{-4} s^{-1} (Table 2.1, all lamps ON) and a negligible loss from OH+HONO, the production rate will be underestimated by less than 8%. When all the lamps are ON, the HONO production rate (dark + photoenhanced) increases from 9.6 to 59 ppbv/h in the ambient flow tube.

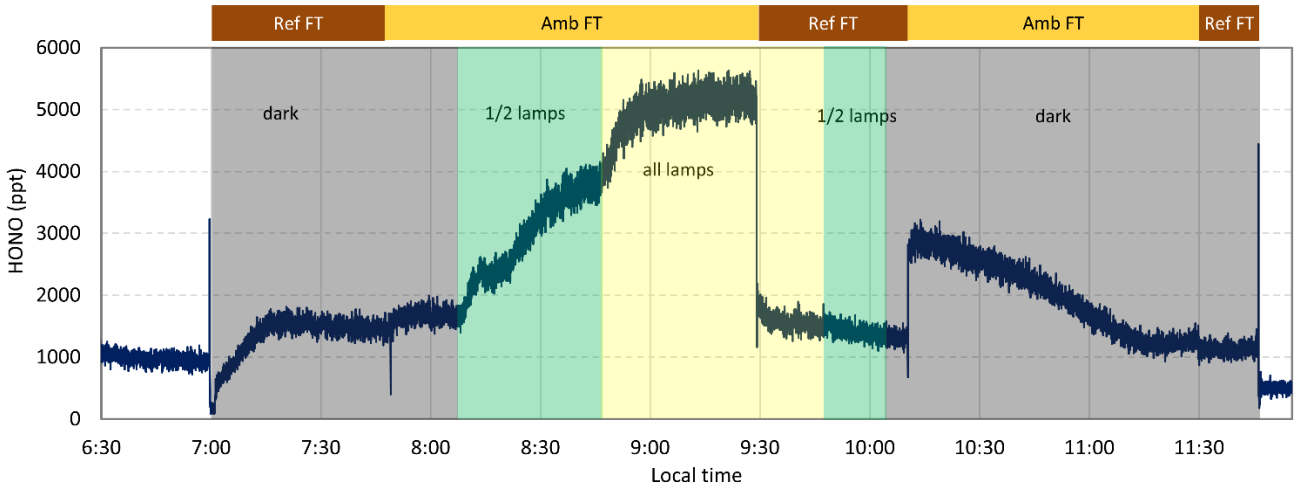

Figure 2.22: HONO concentrations measured in the two flow tubes under different irradiation conditions (19 November 2015).

A summary of the HONO experiments for the ambient flow tube is presented in Fig. 2.23. Each bar corresponds to a separate experiment that took place on the date indicated on the x axis. The dark blue bars indicate HONO mixing ratios measured under dark conditions. The yellow bars indicate the total HONO mixing ratio (from dark + photoenhanced production) measured in the ambient flow tube when all the lamps were turned ON. The mixing ratio of NO_2 introduced into the flow tubes and the relative humidity are indicated above each bar. The flow tubes were cleaned on the 6th of December, as shown with the arrow. In the reference flow tube, HONO is produced at levels of ±25% of that observed in the ambient flow tube

under dark conditions. When the flow tubes were irradiated, no change in HONO was observed in the reference flow tube.

Comparing experiments performed on 19 November and 4 December, which are characterized by similar operating conditions, indicates that both the dark and photoenhanced production of HONO strongly decreased over time. In addition, the experiment performed on 21 November clearly show that HONO is released both under dark and irradiated conditions without NO_2 in the flowing mixture. These results strongly suggest that nitro-containing compounds and organic photosensitizers were adsorbed on the walls since the field deployment of the instrument. One may argue that the experiment performed on 19 November, where 100 ppbv of NO_2 were injected in the flow tubes, could have led to the adsorption of NO_2 on the quartz and its conversion into HONO during the following day experiments. However, experiments performed on 8-9 December rule out this possibility.

A clear decreasing trend of both the dark and photoenhanced HONO production is observed from 19 November to 4 December, whatever the experimental conditions are. Regarding the experiments performed after cleaning the flow tubes with acetone and distilled water, even though HONO observed on 8 December is slightly higher than what was observed on 30 November under the same NO_2 and RH conditions, almost no HONO is measured for the last two experiments on 9 December. Flowing humid air inside the flow tubes for hours seems to decrease both the dark and the photoenhanced HONO formation. From these results, no clear dependence of HONO formation on NO_2 levels or relative humidity is observed. As mentioned above, the contamination inside the flow tubes seems to be the most important cause of HONO production during the first experiments.

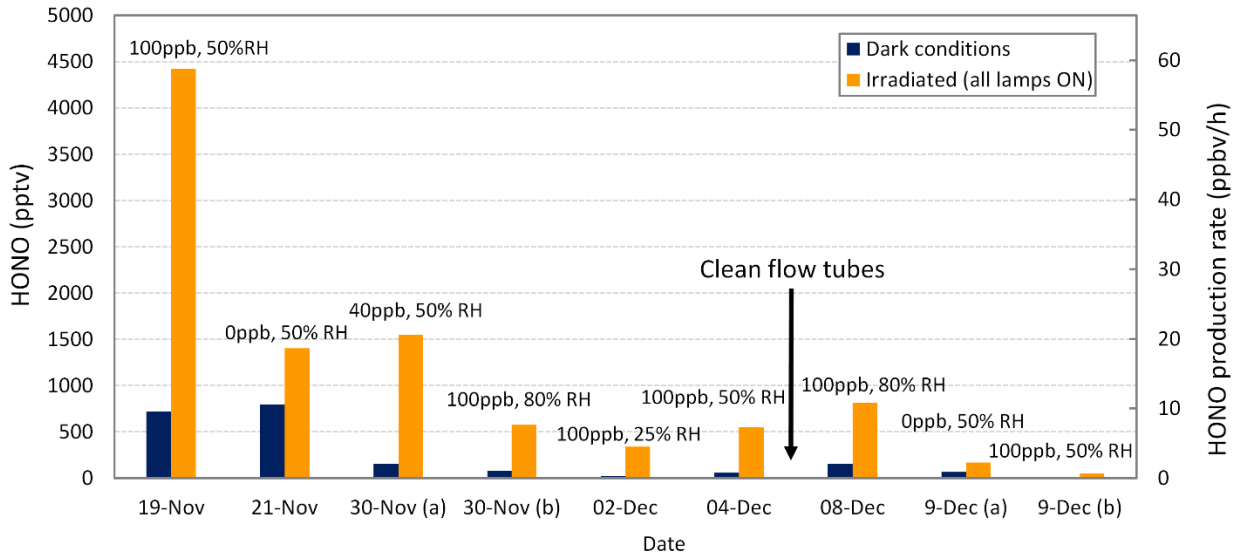

Figure 2.23: HONO mixing ratios measured at the exit of the ambient flow tube and calculated HONO production rates (see text) under dark (blue) or irradiated (yellow) conditions, with all lamps ON.

To conclude, it is clear that HONO can be produced at the surface of the quartz flow tubes and can be released in the gas phase. In the tests discussed above, HONO production rates in the ambient flow tube reached up to 10 ppbv/h under dark conditions and up to 60 ppbv/h under irradiated conditions, when the flow tubes were contaminated, and were lower than 3 ppbv/h and 10 ppbv/h, respectively, for clean flow tubes. The HONO production rate depends on contamination levels and it is not straightforward to determine what the production rate will be during ambient measurements. However, these numbers provide constraints that can be used to estimate the impact of a spurious HONO production in the flow tubes. The impact of HONO production in the flow tubes on the $P(O_3)$ measurements is further discussed in section 3.5.2 using box modeling.

2.3.2 Conversion units

As previously described, two different types of conversion units were developed and tested in this work:

- An NO_2-to-O_3 converter through NO_2 photolysis, to be used with an O_3 monitor
- an O_3-to-NO_2 converter through O_3 titration by NO, to be used with a CAPS NO_2 monitor

Characterization experiments for both converters are described in the following sections. We then conclude on the advantages and drawbacks of the two different units.

2.3.2.1 NO_2-to-O_3 converter

In MOPSv1 (Cazorla and Brune, 2010) the NO_2-to-O_3 conversion was performed by photolyzing NO_2 using a UV lamp made of light-emitting diodes (395 nm wavelength, 5.4 watts of power), achieving a maximum conversion efficiency of 88% at 17 ppbv of NO_2 for a residence time of 103±14 s in the conversion cells. In MOPSv2 (Baier et al., 2015), while the residence time was decreased to 34 s, the conversion efficiency was increased to 88 – 97% for NO_2 mixing ratios lower than 35 ppbv using a highly-efficient UV lamp that provided ten times more photons than the MOPSv1 diodes.

As described in section 2.2.2.1, there are two versions of the OPR NO_2-to-O_3 converter: 1-cell and 2-cells converters. The second version was built to increase the residence time of air in the conversion unit and, as a result, the photolysis efficiency of NO_2. In this section, conversion efficiency tests are first described under dry conditions for the two versions of the converter and under humid conditions for the 2-cells converter. Results from O_3 and NO_2 loss tests under humid conditions are also presented for the 2-cells converter. In the end, a few experimental issues are discussed.

Quantification of the conversion efficiency – Conversion efficiency tests were performed under dry conditions using the setup shown in Figure 2.24 for both the 1-cell (a) and 2-cells (b) conversion units. For the 1-cell unit, the conversion efficiency was quantified separately in each cell to determine whether the NO_2-to-O_3 conversion was similar for each of them.

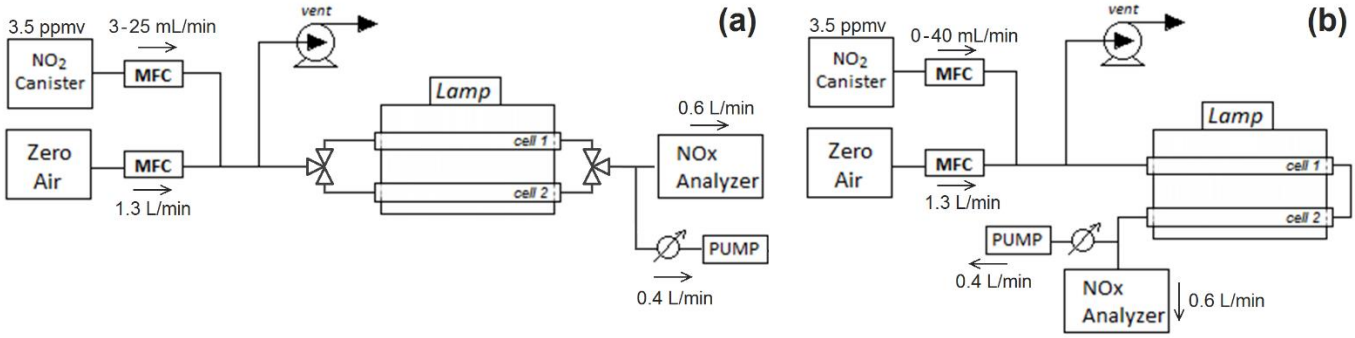

Figure 2.24: Experimental setup used to measure the conversion efficiency of NO_2 for the 1-cell (a) and 2-cells (b) conversion units.

An NO_2 mixture from a canister was diluted using zero air and mass flow controllers to generate a large range of NO_2 mixing ratios (10-100 ppbv), characteristic of ambient conditions. The canister was filled with approximately 1.8 L of NO_2 (35 ppmv, Praxair) and 16.2 L of zero dry air, to get a mixture of 3.5 ppmv of NO_2. The flow rate of dry zero air was set at 1.3 L/min. The flow rate of NO_2 was less than 40 mL/min, leading to NO_2 mixing ratios of up to 100 ppbv. The flow from the canister was kept small compared to the zero air flow, so that the change of the NO_2 flow rate had a negligible impact on the dilution factor. The NO_2 mixture was then passed inside the converter and NO_2 was measured using a NO_x analyzer (Thermo 42C) at the exit of the converter. Since the sampling flow rate of this analyzer was 600 mL/min, a pump set at 400 mL/min was used in parallel of the analyzer to achieve a total flow rate of 1 L/min in the cells, similar to the sampling flow rate of the O_3 monitor. This total flow rate leads to residence times of 5.5 and 11.0 s for the 1-cell and 2-cells converters, respectively.

For each NO_2 flow rate, i.e. each NO_2 mixing ratio, NO_2 was measured with the UV lamp OFF (${NO_2}^{OFF}$), then with the lamp turned ON (${NO_2}^{ON}$), and switched OFF again (${NO_2}^{OFF\,(2)}$). The conversion efficiency was calculated from Eq. 2.4:

$$Conv.Eff. = \frac{Average\left({NO_2}^{OFF}, {NO_2}^{OFF\,(2)}\right) - {NO_2}^{ON}}{Average\left({NO_2}^{OFF}, {NO_2}^{OFF\,(2)}\right)} \qquad \text{(Eq. 2.4)}$$

For the 1-cell converter, two 3-way valves allowed switching between the two cells when operated simultaneously, and NO_2 was measured with a measurement precision (1σ) of 0.3 ppbv. For the 2-cell

converter, in order to investigate the dependence of the conversion efficiency on the residence time in the cells, three different setups were used to vary the flow rate inside the converter. The schematic shown in Fig. 2.24(b) corresponds to a residence time of 11.0 s in the photolytic cells as mentioned above. Removing the pump, a total flow rate of 0.6 L/min was achieved inside the cells, leading to a residence time of 15.8 s. Similarly, removing the pump but placing the vent after the cells, led to a flow rate of 1.3 L/min and a residence time of 8.2 s. Additionally, a DAQ board from National Instruments (USB-6009) was used together with a control software written using LabView to aquire the signals from the NO_x monitor. The measurements were averaged over two minutes when the NO and NO_2 mixing ratios were stable.

Results for the 1-cell and 2-cells converters, compared with values from the literature (Cazorla and Brune, 2010), are reported in Table 2.3 and Fig. 2.25, where "cell 1" is the cell closer to the lamp as indicated in Fig. 2.24. For the 2-cells converter, results presented here are the mean values of 3 replicates for each setup.

Figure 2.25 shows that the conversion efficiency for the 1-cell unit increases with the residence time, with lower values for the low NO_2 mixing ratios. For a residence time of 5.5 s, a conversion efficiency in the order of 45-55% was observed. Additionally, a close look at Fig. 2.25 suggests that the conversion efficiency in cell 1 is higher than in cell 2 by 3.9% on average, indicating that the photon flux is higher in cell 1. For the 2-cells unit and residence times of 15.8 and 11 s, the conversion efficiency meets the values published by Cazorla and Brune (2010) when NO_2 mixing ratios are higher than 30 ppbv. This conversion efficiency is expected to be high enough for the OPR instrument. For NO_2 mixing ratios below 30 ppbv, a drop is observed in the conversion efficiency, leading to values significantly lower than what was observed in the literature. Chemical simulations performed using the known NOx-O_3 (+hν) chemistry (Annex II) were not able to reproduce this drop and no robust explanation was found. However, conversion efficiencies measured at NO_2 mixing ratios lower than 30 ppbv are still comparable to the values measured at mixing ratios ranging from 30-100 ppbv. Overall, the conversion efficiency of NO_2 at a flow rate of 1 L/min is 70±5 % on average on a large range of NO_2 mixing ratios (10-100 ppbv).

Table 2.3: NO_2–to-O_3 conversion efficiency as a function of the residence time in the conversion cells.

Total flow rate in the converter	Residence time in the converter	NO_2 (ppbv)	Conversion efficiency	
			cell 1	**cell 2**
1.0 L/min	**5.5 s**	8.6	54.7%	48.8%
		23.4	53.0%	51.3%
		33.2	52.4%	45.5%
		66.7	45.3%	44.1%
1.3 L/min	**8.2 s**	11.0	67.2%	
		19.6	69.4%	
		32.3	68.3%	
		57.6	66.8%	
		99.6	61.5%	
1.0 L/min	**11.0 s**	12.0	63.7%	
		19.8	71.0%	
		31.1	73.9%	
		60.2	71.3%	
		75.0	68.3%	
		100.3	64.8%	
0.6 L/min	**15.8 s**	11.1	65.8%	
		20.2	75.8%	
		33.3	77.5%	
		60.0	71.7%	
		97.5	67.7%	

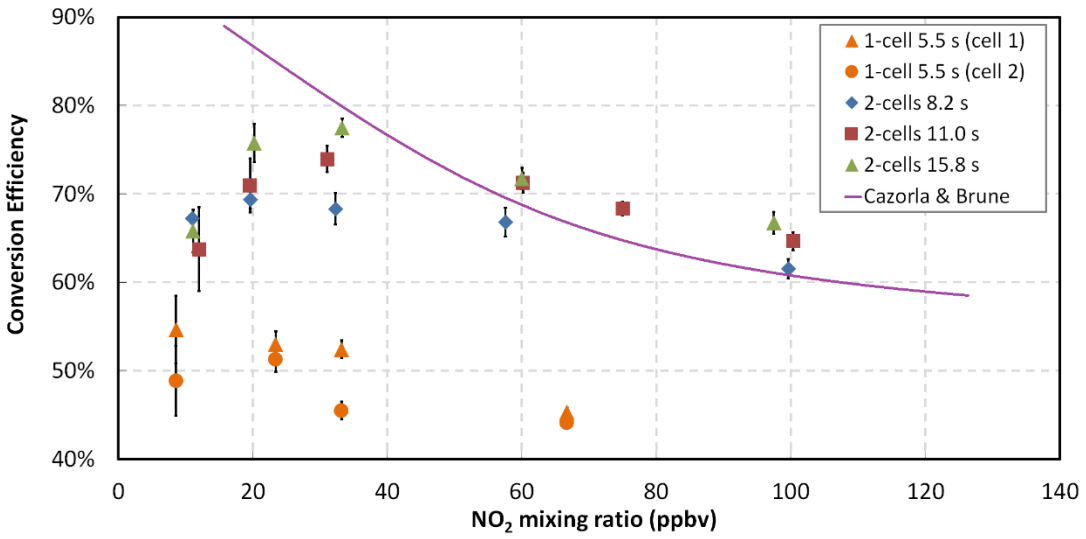

Figure 2.25: Experimental and literature values of conversion efficiency for the NO_2-to-O_3 converter. Error bars indicate the standard error of the mean among three replicates (1σ) for the 2-cells unit and the propagation of a 0.3 ppbv measurement error for the 1-cell unit.

Figure 2.25 also shows that the conversion efficiency decreases significantly when the NO_2 mixing ratio increases, for NO_2 > 30 ppbv. This behavior has already been reported by Cazorla and Brune (2010) and is due to a competition between NO_2 photolysis, that leads to the formation of O_3 and NO, and the back reaction between O_3 and NO, which reproduces NO_2. When one molecule of NO_2 is photolyzed, a molecule of O_3 and a molecule of NO are produced. Therefore, doubling the NO_2 mixing ratio, which will double the NO_2 photolysis rate, will lead to a 4-fold increase of the reaction rate for $NO+O_3 \rightarrow NO_2+O_2$, thus shifting the NO_x photostationary state away from O_3 and towards NO_2.

The conversion efficiency was also quantified at different relative humidity values for the 2-cells unit over the same range of NO_2 mixing ratios, adding an additional mass flow controller and a water bubbler to generate humid zero air (≈100% RH) on the schematic of Fig. 2.24(b). The sum of the flow rates of dry zero air and humid zero air was kept constant at 1.3 L/min. Relative humidity values ranging from 35-90% were achieved by varying the ratio between these two zero air flow rates. NO_2 mixing ratios ranging from 7-80 ppbv were used for these experiments. The flow rate in the converter was kept at 1 L/min, leading to a residence time in the cells of 11 seconds.

The results of these experiments are presented in Fig. 2.26. Error bars indicate the standard error of the mean for 3 repeated experimets (1σ). Results presented above for dry conditions at a flow rate of 1 L/min are also displayed in Fig. 2.26 for comparison.

The conversion efficiency quantified at different relative humidity values seems to be independent of humidity, except for the set of measurements performed at 90% RH (ambient temperature of approximately 21°C). For the latter, conversion efficiencies measured at NO_2 mixing ratios lower than 30 ppbv are lower by 10-15%. Generally, for relative humidity values up to 75%, there is no significant change in the conversion efficiency with the increase in humidity and only a small decrease (≈7% on average) is observed for relative humidity values higher than 75%.

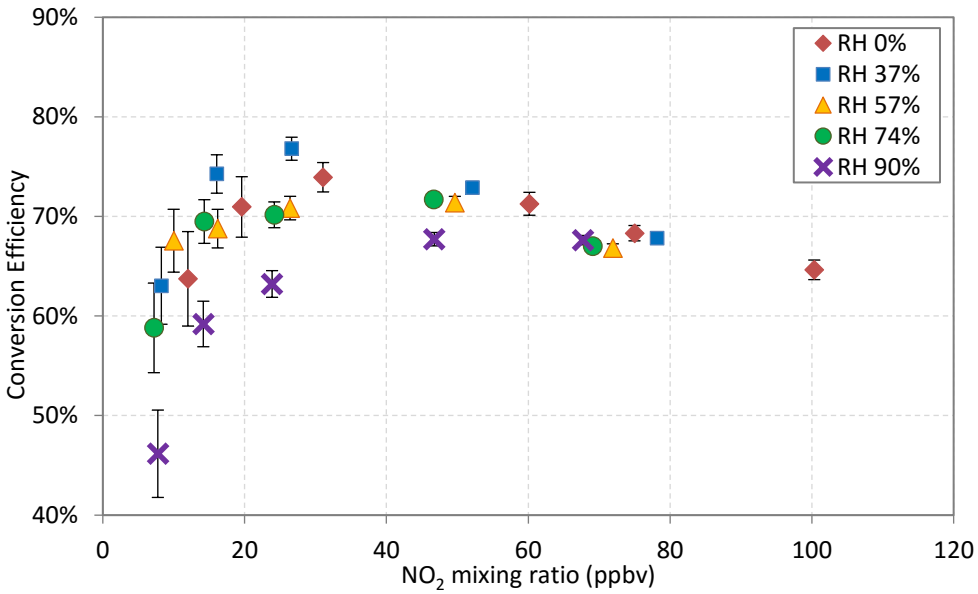

Figure 2.26: Conversion efficiency as a function of NO_2 mixing ratios for different relative humidity values (at T ≈ 21°C). Error bars indicate the standard error of the mean for 3 replicates (1σ).

As a conclusion, the 2-cells conversion unit with a residence time of 11 s seems to be suitable for the OPR measurements. This residence time corresponds to the operating conditions of the instrument and the conversion efficiency is in the order of 70% for a large range of NO_2 mixing ratios. Therefore, this setup was used to quantify possible O_3 or NO_2 losses in the converter.

Quantification of O_x losses in the conversion cells **–** Tests regarding heterogeneous O_x losses in the quartz cells for the NO_2-to-O_3 converter were performed using the setup shown in Fig. 2.27, either with a diluted NO_2 canister or with an O_3 generator (Ansyco SYCOS KT-O3M) for NO_2 or O_3 loss tests, respectively. These tests were performed under dark conditions with the lamp off.

The NO_2 canister was filled with 3 ppmv of NO_2 NO_2 flow rates of 5–35 mL/min were used together with a total flow rates of dry and humid zero air kept constant at 1.3 L/min to generate 7-80 ppbv of NO_2 at 0 – 95% RH (≈ 21°C). The ozone generator was used to produce 20 to 300 ppbv of O_3 at a flow rate of 1 L/min. The sum of the flow rates of dry and humid zero air was kept constant at 1 L/min and O_3 mixing ratios were generated in the range 10-150 ppbv at 0 – 90% RH (≈ 21°C). The flow rate in the cells was set at 1 L/min using either a pump and the NO_x monitor or the O_3 monitor to sample air at the exit of the converter. Two 2-way valves were placed before the converter, so that NO_2 and O_3 were measured upstream and downstream of the converter at different relative humidity values. Signals from the NO_x analyzer and from the humidity

and temperature sensors were recorded through LabView using a National Instrument DAQ board (USB6009).

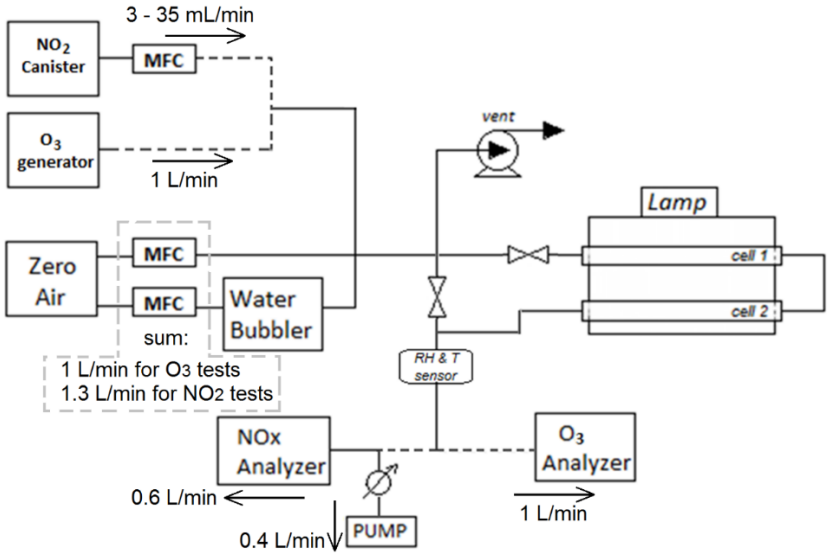

Figure 2.27: Experimental setup for measuring heterogeneous NO_2 or O_3 losses in the quartz cells of the NO_2-to-O_3 converter.

The relative O_3 or NO_2 loss was calculated using Eq. 2.5, for each relative humidity value:

$$Rel.\,Loss = \frac{O_{x(before\ cells)} - O_{x(after\ cells)}}{O_{x(before\ cells)}} \qquad \text{(Eq. 2.5)}$$

The results are shown in Fig. 2.28 for both NO_2 and O_3. The error on the relative loss was calculated by a quadratic propagation of errors of the NO_2 or O_3 measurements (1σ).

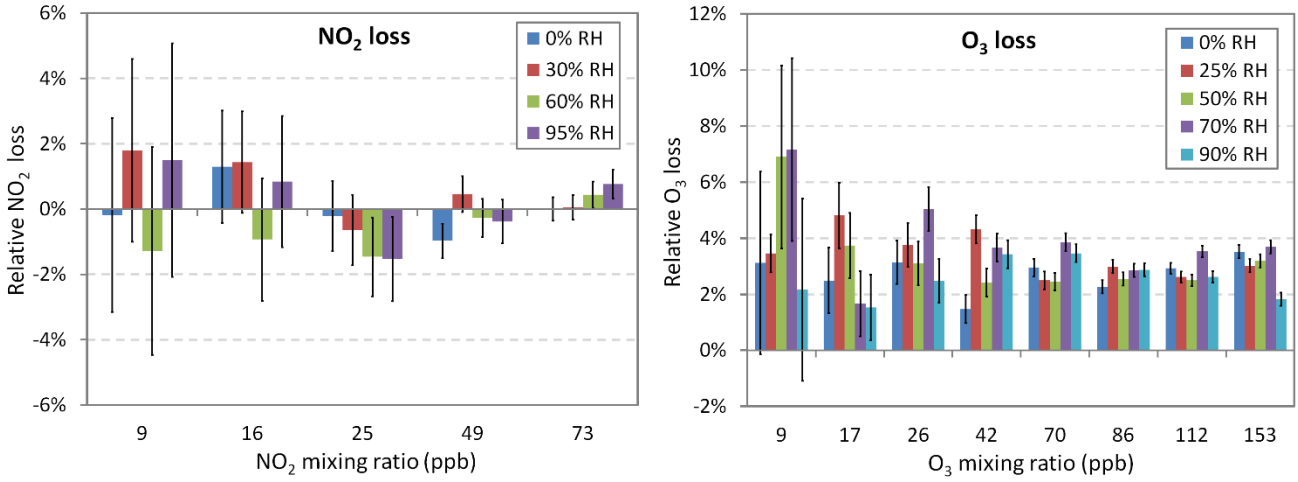

Figure 2.28: Relative NO_2 and O_3 losses in the 2-cells converter as a function of NO_2 and O_3 mixing ratios respectively, under different humidity conditions. Errors (1σ) are from a quadratic propagation of errors from the NO_2 or O_3 measurements.

For NO_2, the measurements of the relative loss are scattered around zero, exhibiting both positive and negative values associated with absolute errors (1σ) of 0.5-4% (error bars). These values are not statistically significant and one can safely assume that the loss of NO_2 is lower than 2% in the quartz cells. For O_3, the relative loss values are always positive, indicating that there is some ozone loss in the cells or/and the connections between the two points of measurement. The average relative loss of O_3 is 3.2%. For both NO_2 and O_3, the relative loss does not significantly depend on the absolute mixing ratio and relative humidity.

Experimental issues – For this converter, three methods can be used to calculate the NO_2-to-O_3 conversion efficiency:

a) The first method was presented above and is based on quantifying the loss of NO_2 observed when the lamp is turned ON (Eq. 2.4). This formula was used to estimate the conversion efficiency giving values up to 75% at 30 ppbv of NO_2.

b) When one molecule of NO_2 is photolyzed, one molecule of NO is formed. Therefore, as the NO_x monitor also measures NO, the second method to calculate the conversion efficiency is to quantify the increase in NO when the lamp is turned ON, as shown by Eq. 2.6:

$$Conv.Eff. = \frac{NO^{ON} - NO^{OFF}}{NO_2^{OFF}} \quad \text{(Eq. 2.6)}$$

where NO^{ON} is the NO mixing ratio with the lamp ON, NO^{OFF} the NO mixing ratio with the lamp OFF, and NO_2^{OFF} the NO_2 mixing ratio with the lamp OFF. For the experiments shown above, this method led to similar results as the previous one, with conversion efficiency values lower by only 2.5% on average.

c) The third method of calculating the conversion efficiency relies on measuring O_3 at the exit of the converter with the ozone analyzer. Since one molecule of NO_2 is converted into one molecule of ozone, the conversion efficiency is calculated as:

$$Conv.Eff. = \frac{O_3^{ON}}{NO_2^{OFF}} \quad \text{(Eq. 2.7)}$$

where O_3^{ON} is the O_3 mixing ratio with the lamp ON and NO_2^{OFF} the NO_2 mixing ratio with the lamp OFF. Since in the MOPS instrument O_x is measured as O_3 by an ozone analyzer, this method should be the one to follow. However, experiments using this method showed significantly lower values for the conversion efficiency. Measured ozone mixing ratios were lower by approximately 20% than what was expected at any NO_2 mixing ratio. A possible reason for this is ozone losses in the converter cells, not only in dark conditions (3.2% loss on average) but also photoenhanced losses on the quartz surface. As shown by the characterization of the flow tubes (section 2.3.1.2), photoenhanced ozone losses on the quartz surface caused by UV radiation could be as high as 15-20%, especially in the photolytic conversion

cells with the low surface/volume ratio. In this case, the NO_2-to-O_3 conversion system could cause additional artifacts on the $P(O_3)$ measurements, underestimating the amount of O_x exiting the flow tubes.

2.3.2.2 O_3-to-NO_2 converter

The conversion of O_3 to NO_2 is based on the titration of O_3 with an excess of NO, and the converter unit was described in section 2.2.2.2. The O_3-to-NO_2 conversion efficiency was quantified by injecting zero air and O_3 at known mixing ratios (3.5–170 ppbv) inside the mixing chambers of the conversion unit (Figures 2.7 and 2.9), changing the flow of NO and measuring NO_2 with the CAPS monitor. These tests were performed at 25% and 60 % relative humidity.

A schematic of the experimental setup is shown in Fig. 2.29. Ozone is provided by an O_3 generator (Ansyco SYCOS KT-O3M or Enaly 1000BT-12) at 1000 SCCM, leading to mixing ratios in the range 10 – 500 ppbv. A dilution system with one or two water bubblers and zero air was used to modify the relative humidity, with a total flow of zero air adjusted at 2000 SCCM. After mixing zero humid air with O_3, an ozone analyzer (O342M, Environnement S.A. or 400E, Teledyne) was used for a rough quantification of ozone before the mixing chambers. NO was provided by a NO cylinder of 50 ppmv in nitrogen (Indiana Oxygen). The addition of NO was performed through two mass flow controllers, set at flow rates of 1–12 SCCM, corresponding to NO mixing ratios in the range of 60–800 ppbv. Each flow tube (ambient or reference) is equipped with a mixing chamber. A system made of two 3-way solenoid valves, a pump and a mass flow controller set at the sampling flow rate of the CAPS monitor (750 SCCM) were used to achieve a continuous flow in both mixing chambers simultaneously. The valves were used to switch the sampling from the CAPS between each mixing chamber every 1 min.

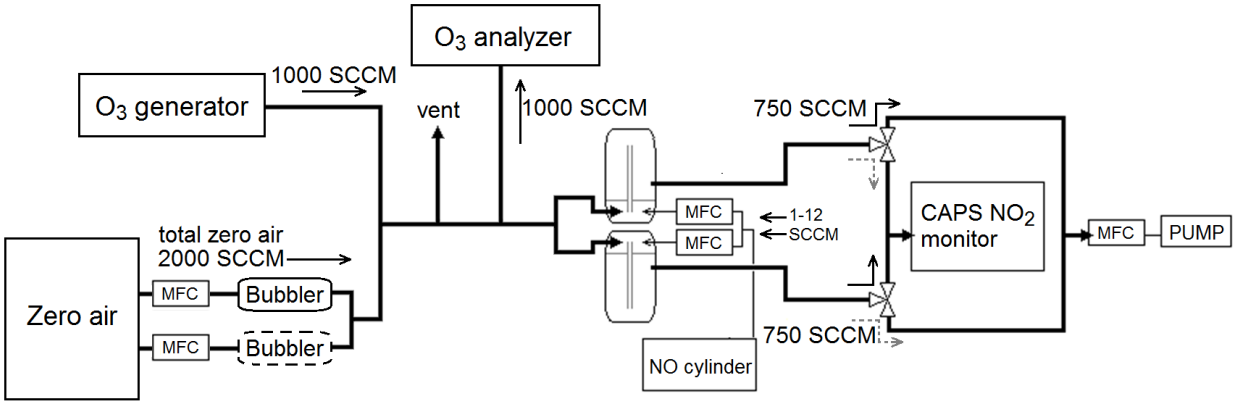

Figure 2.29: Experimental setup for the quantification of the O_3-to-NO_2 conversion efficiency

An important issue observed during these tests, is that NO_2 impurities were observed during the NO addition, which can either come from the NO cylinder or from NO oxidation in the lines. Using stainless steel lines instead of Teflon and purging the air from the lines with a pump before adding NO allowed reducing these

impurities to less than 2% of the amount of NO. The amount of NO_2 that comes as impurity from the NO line can by quantified by injecting zero air into the mixing chambers and measuring NO_2 with the CAPS monitor. This NO_2 impurity was usually on the order of a few ppbv after a few hours of operation.

Considering that there is 100% conversion efficiency at NO mixing ratios > 700 ppbv (section 2.2.2.2), the conversion efficiency was quantified for both the ambient and the reference mixing chambers from Eq. 2.8.

$$Conv.Efficiency = \frac{NO_2\ after\ mix.\ chamber - NO_2\ impurity}{NO_2\ after\ mix.chamber, at\ highest\ NO - NO_2\ impurity} \quad \text{(Eq. 2.8)}$$

Figure 2.30 presents results of four tests, for different O_3 mixing ratios (3.5, 85 and 170 ppbv) and different relative humidities (25% and 60%). Additionally, based on kinetic considerations for the titration reaction of O_3 by NO, which exhibits a rate constant of 1.8×10^{-14} cm^3 $molecule^{-1}$ s^{-1} (Atkinson et al., 2004), the conversion efficiency was theoretically calculated for a reaction time of 23 seconds (section 2.1.2.2). For example, 500 ppbv of NO would lead to a conversion of 99.5% of O_3 into NO_2. These calculations are shown in Fig. 2.30 (black solid line) for different mixing ratios of NO (50-800 ppbv) together with the laboratory and field tests (symbols) mentioned above.

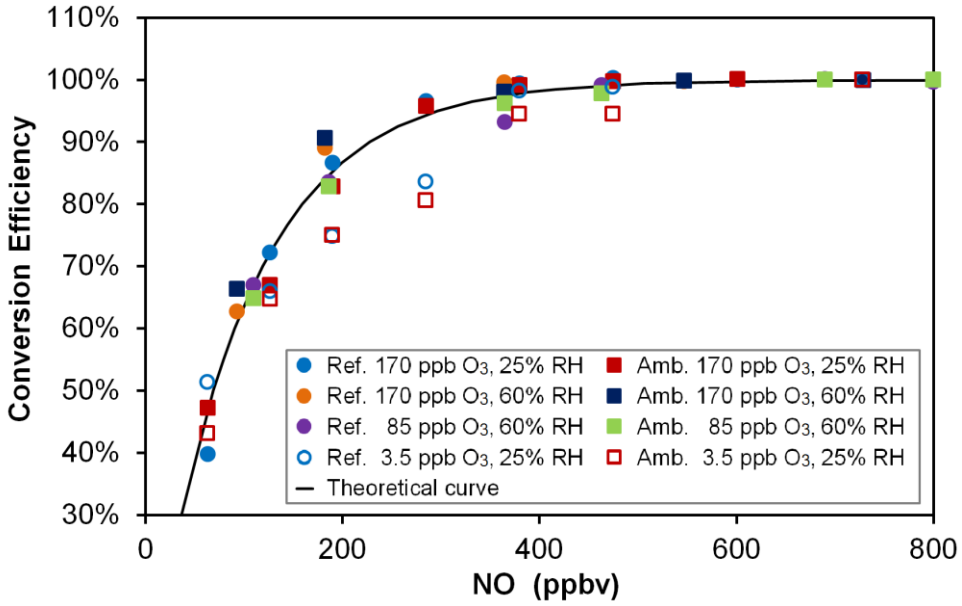

Figure 2.30: Conversion efficiency for the O_3-to-NO_2 converter for two O_3 levels: 170 ppbv and 3.5 ppbv. The theoretical curve (black line) was calculated for a reaction time of 23 s (see text). Open symbols are hidden behind the plain symbols for NO>500 ppbv.

Figure 2.30 shows that, indeed, a plateau of almost 100% of conversion is observed at NO mixing ratios higher than 500 ppbv. Moreover, there does not seem to be an impact of the relative humidity on the conversion efficiency. The theoretical curve is well reproduced by the experimental results, although the low

O_3 level of 3.5 ppbv is slightly below the curve when NO is lower than 500 ppbv. However, the experimental results successfully represent the plateau of the conversion efficiency at 500 ppbv of NO for all O_3 levels and both flow tubes.

For the OPR instrument, two mass flow controllers are used, one for each mixing chamber, set at a flow rate of 10 SCCM, leading to 667 ppbv of NO in the mixing chambers when a total flow rate of 750 SCCM is sampled by the CAPS monitor. This mixing ratio corresponds to 99.9% conversion efficiency and does not depend on O_3 levels, neither does it depend on humidity.

2.3.3 O_x quantification

As indicated in section 2.2.2, each conversion unit presented above requires a specific monitor to quantify either O_3 or NO_2.

The techniques that have been developed for in situ O_3 measurements include UV absorption (Proffitt and McLaughlin, 1983;Gao et al., 2012), chemiluminescence (Ridley et al., 1992;Zahn et al., 2012), electrochemical sensors (Ebeling et al., 2009), and semiconductor-based sensors (Kim et al., 2000). For the OPR instrument, UV-absorption was chosen over other techniques as it is the conventional technique used to quantify ozone in the troposphere and commercial instruments are easily available.

For NO_2 measurements, many different techniques have been developed, with some of them including a conversion of NO_2 to NO and NO detection. The most widely used technique with many commercial instruments is chemiluminescence, which includes a molybdenum or photolytic NO_2-to-NO converter (Kley and McFarland, 1980;Ryerson et al., 2000). Other techniques for NO_2 detection are optical differential absorption spectroscopy (DOAS) (Platt et al., 1979;Thornton et al., 2003), tunable diode laser based absorption spectroscopy (TDLAS) (Gregory et al., 1990;Li et al., 2004), resonance enhanced multiphoton ionization (REMPI) (Garnica et al., 2000;McKeachie et al., 2001) and laser induced fluorescence (LIF) (Thornton et al., 2000;Fuchs et al., 2010). During the last decade, cavity attenuated phase shift spectroscopy (CAPS) (Kebabian et al., 2005;Kebabian et al., 2008) has been proven to be a powerful technique for selective NO_2 measurements. For the OPR instrument, CAPS was chosen over other techniques, especially chemiluminescence, because it is very selective to NO_2, with a low detection. Note that using a chemiluminescence instrument is prevented in this instrument since it would require measuring small NO_2 variations over a large background of NO (added in the converter).

Both the O_3 monitor (O342M, Environnement SA) and the CAPS NO_2 monitor (Aerodyne) were tested in the laboratory for their suitability on $P(O_3)$ measurements. Tests performed on the ozone monitor were mostly focused on its sensitivity to relative humidity. Tests on the CAPS monitor were focused on its limit

of detection, the drift of the zero, and its sensitivity to NO and relative humidity. These tests are described in this section.

2.3.3.1 Ozone analyzer

The O_3 analyzer used in this study (O342M, Environnement S.A.) is a UV absorption monitor equiped with one absorption cell and an ozone scrubber. The ozone analyzer draws air continuously through the cell, a beam of UV radiation (254 nm) produced by a mercury lamp is used to probe the absorption of ozone. The intensity of the UV radiation that passes through the absorption cell is measured by a photodetector and converted into an electrical signal that correlates with the ozone concentration. The measurement sequence requires two cycles automated by the use of solenoid valves; during one cycle, the air passes through the O_3 scrubber, removing ozone, and therefore this signal corresponds to the reference "zero" signal. During the next cycle, the air bypasses the scrubber and this signal corresponds to the "ozone measurement" signal. Using the Beer-Lambert law, the ozone concentration is calculated from the two measured signals. The sampling flow rate of this ozone monitor is 1 L/min and its limit of detection is 0.4 ppbv for a response time of 20 s.

Measurements performed with this analyzer to quantify O_3 losses in the NO_2-to-O_3 converter (section 2.3.2.1) showed a strange response of the analyzer when relative humidity was varied. During these experiments, the flow rate of the O_3 mixture was kept constant, as well as the sum of the flow rates of dry and humid zero air. Modifying the ratio between dry and humid zero air flow rates, only leads to a change in relative humidity and the ozone reading on the monitor shoud not change. However, increasing relative humidity from zero to approximately 90%, the ozone reading decreased by at least 50%.

Various tests were therefore performed on the ozone analyzer, to test its response to humidity and its suitability for the OPR instrument. During these tests, ozone was generated from an ozone generator (Ansyco SYCOS KT-O3M) and was mixed with humid zero air. The humidity was modified either gradually from dry to high (75%) values, either from dry to a certain RH level multiple times, monitoring the response of the ozone analyzer.

One of these experiments is shown in Fig. 2.31. The flow of zero air (dry + humid) was kept constant at 1 SLPM. The flow rate of the O_3 mixture (200 ppbv) from the generator was set at 340 SCCM, leading to 51 ppbv of ozone after dilution with zero air. The ozone analyzer sampled 1 SLPM of this mixture at atmospheric pressure and the rest was sent to a vent. The relative humidity was varied between 0 – 75% by adjusting the flow rates of humid and dry air. The transition periods after a change in humidity (approximately 30 min) have been removed from the plot for clarity. As shown in Fig. 2.31, the reading from the ozone analyzer decreases as relative humidity increases. While the decrease is on the order of 15% for

RH < 60%, it increases to 34% at a RH value of 75%. This experiment was repeated three times, showing a decrease of the ozone reading with humidity, but leading to unreproducible results. The test presented in Fig. 2.31 is the first one performed, which exhibits the highest O_3 change.

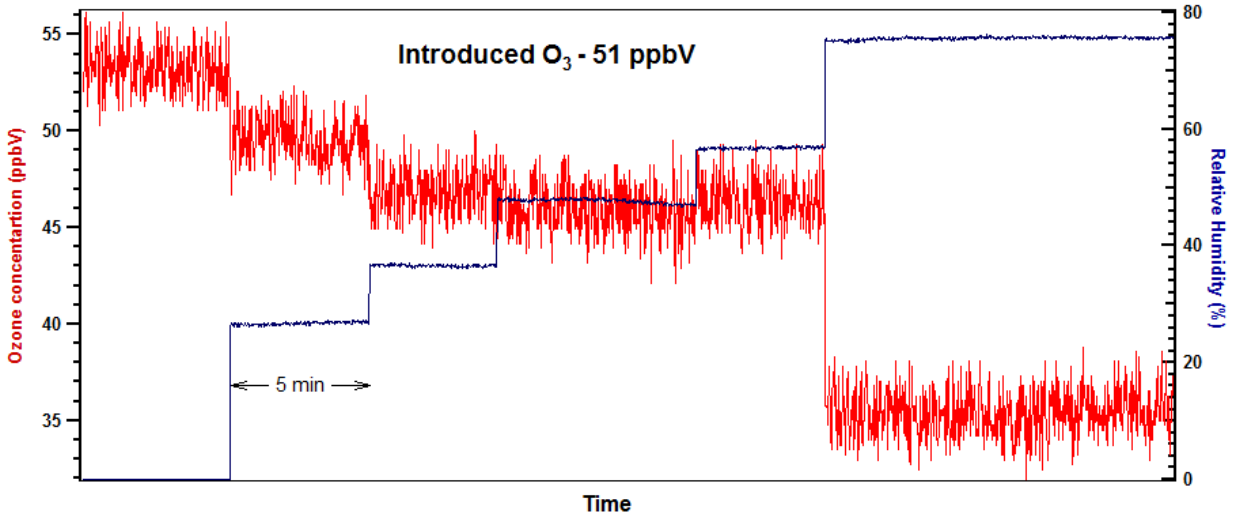

Figure 2.31: Change in the reading of the O_3 analyzer when relative humidity increases. The transition steps between each change have been removed from the plot.

Another experiment is presented in Fig. 2.32. During this test, 73 ppbv of O_3 were supplied to the ozone monitor, while the relative humidity was modified multiple times from zero to 40%. The transition periods after each change in humidity have also been removed from the plot. According to this test, the impact of humidity on the ozone measurement decreases over time during the same day, even if the introduced humidity does not change.

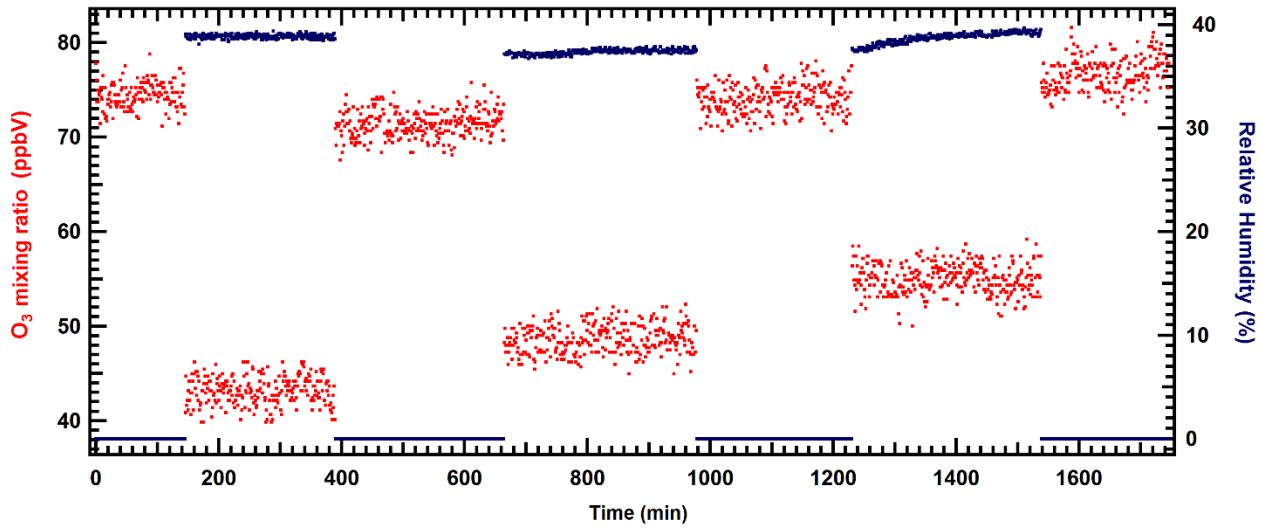

Figure 2.32: Change in the reading of the O_3 analyzer when relative humidity is successively changed from 0 to 40%. The transition steps between each change have been removed from the plot.

The tests described above clearly indicate that the ozone monitor is sensitive to relative humidity. A way to deal with this issue would be to calibrate the monitor for different relative humidity values. However, as shown from Fig. 2.32 these tests were not reproducible, and the sensitivity of the monitor to relative humidity can change over time. After approximately one month of tests with zero humid air and ozone, the response of the monitor was improved, with the largest humidity-related errors close to 15% (from 0 to 75% RH). A second monitor of the same brand (same model) was also tested to examine if this behavior was due to a malfunctioning analyzer, but the new analyzer behaved the same way.

These results suggest that a continuous flow of zero humid air with ozone over a few weeks reduces the dependence of the O_3 monitor on relative humidity. The most likely reason for this behavior is thought to be a passivation of the O_3 scrubber, whose role is to remove ozone during the "zero" signal measurement. It is possible that the ozone scrubber released compounds that absorb UV light under high humidity conditions. If these compounds absorb at 254 nm, the wavelength used to monitor O_3, a positive bias on the reference "zero" signal would lead to an overall underestimation of the O_3 measurements. Similarly, operating the O_3 monitor under zero humid air conditions for one month, the scrubber got cleaner, improving the overall performance of the monitor This water interference has been observed in several studies in the literature (Spicer et al., 2010;Wilson and Birks, 2006;Leston et al., 2005) and new ozone analyzers, scrubbing O_3 by titration with NO, have been developed to address this issue (Ollison et al., 2013).

The long passivation time observed in these experiments and the residual remaining impact of humidity on the ozone measurement are limiting factors for the use of this type of ozone monitor on the OPR instrument. Moreover, a detection limit of 0.4 ppbv for ozone and a residence time of 271 s in the flow tubes should translate into a detection limit of approximately 7.5 ppbv/h for $P(O_3)$. Based on the tests made on the ozone monitor, we estimate that a 5% difference in RH between the two flow tubes, which could occur if the temperature of the two flow tubes is different, could impact the O_3 measurement by at least 0.5 ppbv for an ambient ozone concentration of 50 ppbv. This would translate to a bias of approximately 7 ppbv/h in $P(O_3)$ measurements.

2.3.3.2 CAPS NO_2 monitor

The CAPS monitor was described in section 2.2.2.2. The time resolution can be as low as 1 second, while the instrument's specifications indicate a detection limit (DL, 3σ) of 100 pptv for a 10-s integration time. Tests were performed on the CAPS monitor to verify this limit of detection and to check how fast the zero can drift. The monitor sensitivity to other species such as NO and water was also tested.

To quantify the detection limit, zero dry air was provided to the CAPS monitor for an hour, after several days of conditioning on ambient air. The time step of data recording was 1 second. The zero values were then averaged over 45-s segments, corresponding to the averaging time of the O_x measurements (section 2.2.3). The error bars were calculated as 3σ for a 45 sec integration time and the detection limit (3σ) of the O_x measurements of the CAPS monitor was quantified at 34 pptv. Our findings lead to a DL of 72 pptv for an integration time 10 s, confirming the specifications of the CAPS monitor (DL ≤100 pptv, 3σ, 10 s). With this detection limit for the O_x measurements and a residence time of 271 s in the flow tubes, the detection limit of the OPR instrument is estimated at 0.64 ppbv/h.

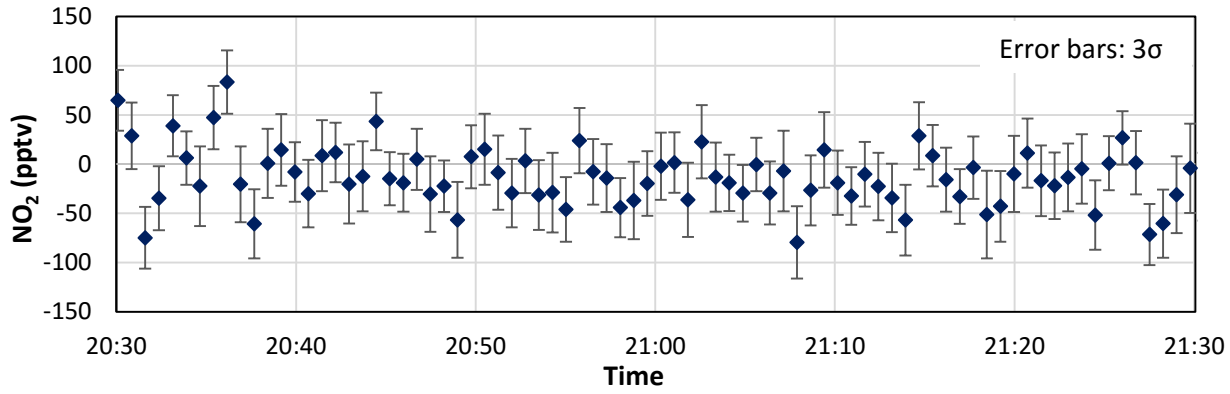

Figure 2.33: Zero of the CAPS monitor to quantify the limit of detection. Each point was averaged over 45 s and the error bars are 3σ for this integration time.

Figure 2.33 also shows that the zero of the instrument can vary from -75 to 80 pptv over the course of this experiment. The drift of the zero was also tested by flowing zero dry air into the CAPS monitor over 12 hours. The drift of the zero was less than 0.3 ppbv in 12 hours, consistent with the CAPS specifications indicating a drift of less than 1 ppbv in 24 hours. However, it has been observed that when the CAPS monitor is turned on for the first time after a long period of inactivity, the drift can exceed 5 ppbv in 24 hours. This has implications for field deployments, showing that the monitor needs to be operated on ambient air for a few days before it is used for $P(O_3)$ measurements.

The impact of water on the monitor's response was tested by generating mixtures of constant NO_2 mixing ratios, varying relative humidity from 0 to 90%. The deviation from the generated NO_2 mixing ratio was calculated from Eq. 2.9.

$$Relative\ NO_2\ deviation = \frac{NO_{2_{RH=0\%}} - NO_2}{NO_{2_{RH=0\%}}} \qquad \text{(Eq. 2.9)}$$

The CAPS measurements showed a deviation from the generated NO_2 mixing ratio increasing exponentially with humidity above 40% RH. This deviation could reach up to 12% at a RH of 90%. A positive sign of the deviation in Fig. 2.34 indicates a decrease of the measured mixing ratio. However, additional measurements

were performed for comparison with two other NO_x analysers, Thermo 42C and Thermo 42i-TL, with the latter having already been demonstrated free of a water dependence in our laboratory. The comparison tests are shown in Fig. 2.34, where the error bars are 1σ, calculated by propagation of errors on the NO_2 measurements. These experiments revealed a similar behavior for all the analyzers, including the Thermo 42i-TL. As a conclusion, the deviation seen in Fig. 2.34 is not thought to be due to the CAPS monitor but is very likely due to NO_2 losses in the Teflon lines and stainless steel connections of the gas generation system.

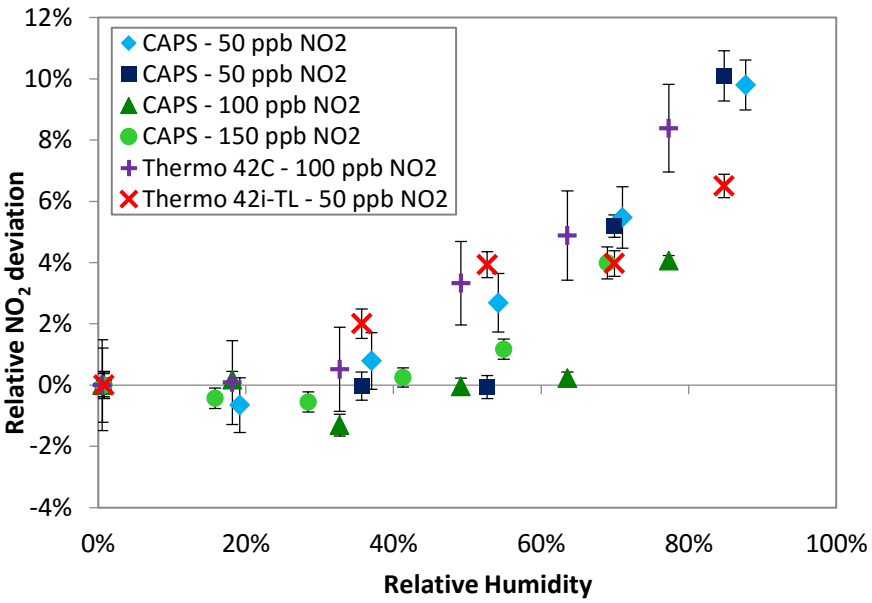

Figure 2.34: Relative deviation of NO_2 as a function of relative humidity for the CAPS, a Thermo 42C, and a Thermo 42i-TL analyzers at various levels on NO_2. Error bars are 1σ values calculated from a quadratic propagation of errors on the NO_2 measurements.

Additional tests were performed to investigate whether the CAPS monitor could be sensitive to NO, especially at the high mixing ratio used in the mixing chambers of the O_3-to-NO_2 converter. For the NO sensitivity, known mixtures of dry NO were provided to the CAPS monitor. An increase of 0.02% in the NO_2 signal was observed for 500 ppbv of NO, showing that the CAPS monitor is no significantly sensitive to NO.

To conclude, the CAPS NO_2 monitor is a fast responding analyzer that is not sensitive to relative humidity and NO, which exhibits a low limit of detection and, therefore, is suitable for the OPR instrument.

2.4 Conclusions

This chapter provides a detailed description of the OPR instrument constructed in this study. The methodology consisted in optimizing the geometry of the sampling flow tubes, as well as the inlet and outlet, using CFD calculations. The goal was to find an optimum geometry that would minimize interactions between ambient trace gases and the surface of the tubes. In addition, two different conversion/detection schemes were tested to perform the differential Ox (O_3+NO_2) measurements between the two flow tubes, the idea being to select the most reliable one for the OPR instrument.

The flow tubes were tested to quantify (i) the mean residence time, (ii) heterogeneous NO_2 and O_3 losses and (iii) heterogeneous HONO production on the quartz surface. The mean residence time was quantified at 4.52 ± 0.22 min for a total flow rate of 2250 SCCM, which was chosen to operate the OPR instrument in the field. The uncertainty on the residence time was found to lead to 4.9% error (1σ) on the $P(O_3)$ measurements. These experiments also showed an air-exchange time of approximately 20 min in the flow tubes, which indicates that $P(O_3)$ measurements have to be averaged every 20 minutes in order to be considered independent.

Experiments performed to quantify dark heterogeneous NO_2 losses in the flow tubes showed a relative loss lower than 5% when the flow tubes were used in the field, and lower than 1% when the flow tubes were clean. Dark O_3 losses were found to be significant after a long exposure in the field, with a relative loss on the order of 10-15% after 1 month of operation, while a relative loss lower than 5% was observed for clean flow tubes. These losses could, therefore, be kept at low values by frequent flushing of the flow tubes with zero humid air and O_3 during nighttime, i.e. when $P(O_3)$ measurements are not necessary.

A photoenhanced heterogeneous ozone loss was also found in the ambient flow tube, mainly driven by short wavelengths close to 312 nm. This loss is expected to be critical for the OPR instrument, since it can trigger false negative $P(O_3)$ signals. Additionally, while there is no strong indication, experiments suggest that there may be a smaller photoenhanced loss in the reference flow tube. The laboratory and field testing showed that this loss depends on O_3 levels, J-values and on humidity levels, suggesting that the loss rate could be parameterized with these variables.

Experiments aimed at quantifying the potential production of HONO in the flow tubes showed that HONO production rates depend on wall contamination levels. These experiments clearly showed a photoenhanced HONO production in the ambient flow tube, which could also be drastically reduced by flowing humid zero air in the flow tubes during nighttime.

Regarding the two different O_x conversion/detection schemes, it was found that the NO_2-to-O_3 conversion efficiency depends on NO_2 levels, being always lower than 80% for the converter built in this study, and

close to 70% on average over a wide range of NO_2 mixing ratios (10–100 ppbv). The conversion efficiency also depends on the intensity of the lamp that can possibly drift during a long period of use in the field. In addition, the response of the ozone monitor was found to depend on relative humidity. During the experiments described above, an ozone bias as high as 50% was observed at high relative humidity.

For the O_3-to-NO_2 converter, it was found that the conversion efficiency was close to 100%, and was independent of O_3 mixing ratios and humidity. The only drawback of this method is the addition of NO_2 impurities together with the large amount of NO required to convert ozone. However, the impurity level was found to be low for the NO cylinder used in this study. Additionally, the CAPS monitor was found to be insensitive to NO and water and to exhibit a much lower detection limit at a time resolution of 1 s than the O_3 monitor at a time resolution of 20 s. For these reasons, the O_3-to-NO_2 converter, along with the CAPS monitor, were chosen for the OPR instrument.

This work allowed to pinpoint potential sources of errors for the OPR built in this study. The impacts of heterogeneous processes occurring on the quartz surface, such as O_3 and NO_2 losses, as well as HONO production, and a lower-than-100% conversion efficiency of the converter were studied through zero-dimensional box modeling and are also presented in chapter 3.

Chapter 3. Investigation of the accuracy of OPR measurements

3.1 Introduction

As discussed in chapter 2, the measurement principle of the OPR is based on the assumption that (i) $P(O_3)$ in the ambient flow tube is similar to $P(O_3)$ in the atmosphere and (ii) no significant production of ozone occurs in the reference flow tube. Numerical simulations of the chemistry occurring in the flow tubes were performed using 0-D modeling to check whether these assumptions are valid. The selected approach relies on modeling ozone production using real field measurements from two campaigns performed in urban environments by our groups. The air composition in urban environments (high levels of NO_x and anthropogenic VOCs) is expected to lead to high ozone production rates and, therefore, this type of environment was considered the most suitable to perform this modeling study.

In addition, simulations were also conducted to investigate the impact on OPR measurements of (a) a conversion efficiency lower than 100% (for both types of conversion: NO_2-to-O_3 and O_3-to-NO_2), (b) NO_2 and O_3 losses, as well as HONO production, on the walls of the flow tubes, (c) a possible increase of the temperature in the reference flow tube due to the absorption of solar radiation by the UV filter, (d) the dilution of the sampled air by injecting zero air inside the flow tubes at the periphery of the inlets and (f) reactions of OH with NO_z species leading to additional O_x production in the ambient flow tube. The objective of these sensitivity tests was to estimate the accuracy of the OPR instrument, based on the impacts that each of the above mentioned factors will have on the $P(O_3)$ measurements.

3.2 Selected field campaigns, data and chemical mechanism

As mentioned above, datasets from two intensive field campaigns were used to model the response of the OPR instrument. Specifically, the datasets included measurements performed in (i) a megacity as part of the Mexico City Metropolitan Area (MCMA) during March 2006 (Dusanter et al., 2009a) and (ii) an urban area as part of the California Nexus (CalNex) field campaign during May - June 2010 (Griffith et al., 2016). All times given below are local times, i.e CST (UTC – 6h) for MCMA-2006 and PDT (UTC – 7h) for CalNex-2010.

Mexico City is one of the biggest megacities in the world and is characterized by high emissions of VOCs and NO_x (Dusanter et al., 2009a). Located at subtropical latitude and at an elevated altitude of 2240 m, Mexico city experiences an active photochemistry that leads to high levels of secondary pollutants such as O_3 and secondary organic aerosols. During this field campaign, NO_x, O_3, HONO, HNO_3, SO_2, CO, VOCs, HO_x, and meteorological parameters were measured. Photolysis frequencies (J-values) were directly measured for NO_2, O_3 (dissociation to O^1D), HONO and HCHO (2 photolytic pathways).

The objective of the CalNex campaign was to study air pollution issues in the California region, as it is an area with well-documented air quality issues (Ryerson et al., 2013). In this campaign, measurements were taken from ground sites, a research ship, tall towers, balloon-borne ozone sondes, multiple aircrafts, and satellites. The datasets included gas concentrations, aerosol chemical composition and microphysical properties, cloud microphysics, and meteorological parameters. The CalNex-LA site was located on the campus of the California Institute of Technology in Pasadena, approximately 18 km northeast of downtown Los Angeles. This site often receives air masses from Los Angeles and is also impacted by local emissions of VOCs and NO_x from traffic and other anthropogenic sources. Measurements of HO_x, VOCs, O_3, NO_x, NO_y, SO_2, CO, HONO, PAN, HNO_3, organic acids, total OH reactivity and photolysis frequencies were conducted on this site, along with measurements of aerosol species.

Table 3.1 indicates the range of mixing ratios of NO_x,O_3, total VOCs, peak photolysis frequencies of NO_2 and O_3 (towards O^1D), as well as total OH reactivity during these two field campaigns.

Table 3.1: Range of NO_x, O_3, $J(NO_2)$, $J(O^1D)$, total VOC and OH reactivity during MCMA 2006 and CalNex 2010.

Species	MCMA 2006 (Dusanter et al., 2009a)	CalNex 2010 (*Griffith et al., 2016*)
NO_2	few ppbv – 140 ppbv	few ppbv – 50 ppbv
NO	few ppbv – 400 ppbv	few ppbv – 20 ppbv
O_3	few ppbv – 150 ppbv	few ppbv – 110 ppbv
Total VOCs	109 – 404 ppbv [(a)]	31 – 47 ppbv [(a)]
OH reactivity	17.4 – 70 s^{-1} [(b)]	15 – 30 s^{-1} [(a)]
peak $J(NO_2)$	7.6×10^{-3} – 9.9×10^{-3} s^{-1}	2.8×10^{-3} – 9.1×10^{-3} s^{-1}
peak $J(O^1D)$	3.4×10^{-5} – 5.5×10^{-5} s^{-1}	0.6×10^{-5} – 3.3×10^{-5} s^{-1}

(a) measured diurnal average
(b) calculated diurnal average

It can be seen that NO_x were significantly higher in Mexico City (up to 400 ppbv on specific days). On most days, NO was peaking during morning traffic hours, around 7:00-8:00, and was decreasing to levels lower than 20 ppbv after midday. NO_2 was peaking later in the day, around 10:00, indicating a fast conversion of NO into NO_2 likely due to ozone titration. During nighttime, while NO_2 was near 40 ppbv, NO could reach 100 ppbv on some occasions. During the morning NO peak, ozone was almost fully titrated, remaining at mixing ratios lower than 40 ppbv before 10:00. Later during the day, ozone usually peaked around 14:00, to decrease again at levels lower than 40 ppbv during nighttime. High concentrations of total VOCs were observed, mainly from anthropogenic origin, reaching 400 ppbv during morning hours on some days. Total OH reactivity values calculated for a campaign average ranged from 17 to 70 s^{-1}. High photolysis frequencies were also observed due to the high altitude and the subtropical latitude of Mexico City.

The atmospheric composition in California was characteristic of a typical urban environment in developed countries. NO_x peaked in the late morning without exceeding 70 ppbv, and O_3 peaked near midday, at mixing ratios lower than 110 ppbv. In this environment, clear differences can be seen between weekends and weekdays. On average, NO and NO_2 mixing ratios were greater during the weekdays after 9:00, when the CalNex site began to receive polluted air from other locations in the Los Angeles basin. On the other hand, O_3 had the opposite trend, where average ozone mixing ratios were approximately 20 ppbv higher on the weekends. A lower level of VOCs was observed during CalNex compared to MCMA-2006, as the diurnal average did not exceed 50 ppbv, while measured total OH reactivity was less than 30 s^{-1} on average.

Free radical species (OH and HO_2) were also measured during these campaigns using the Indiana University LIF-FAGE instrument. These measurements were used together with NO measurements to calculate ozone production rates as described in chapter 1 (section 1.4.2). Figure 3.1 shows diurnal average profiles of $P(O_3)$ for the two campaigns.

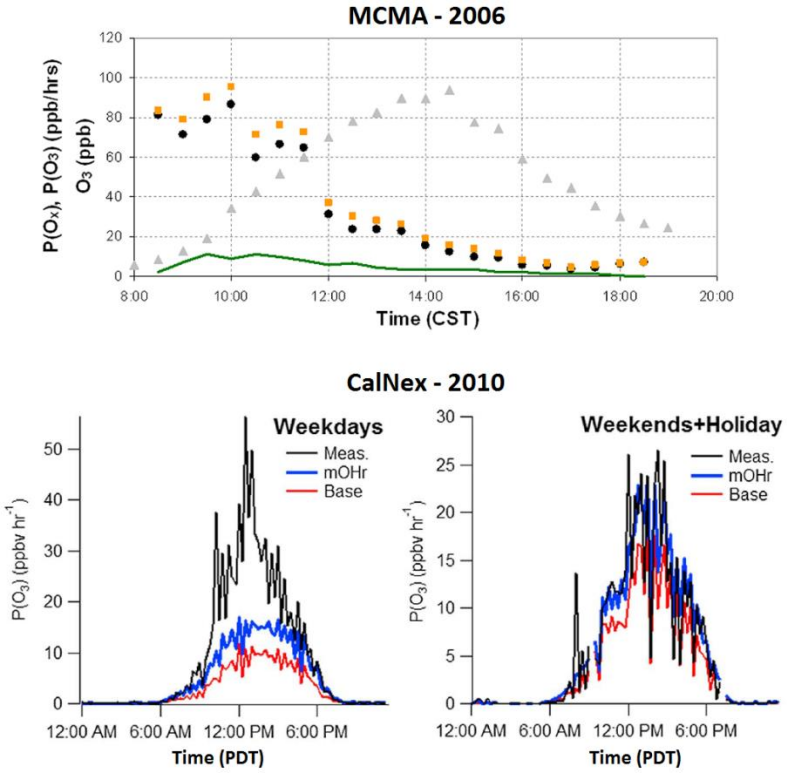

Figure 3.1: Top (Dusanter et al., 2009a): Diurnal average production rates of O_x (orange squares) and O_3 (black circles) due to HO_2+NO during MCMA-2006. Median measurements of surface ozone mixing ratios (grey circles) and reaction rates of OH+NO→HNO_3 (green line) also shown. Bottom (Griffith et al., 2016): Diurnal average ozone production rates of O_3 due to HO_2^*+NO during CalNex-2010 from the radical measurements (black line) and two different models for (a) weekdays and (b) weekends.

For MCMA-2006, $P(O_3)$ values calculated from measured HO_2 radicals were as high as 90 ppbv/h in the early morning, decreasing to 30 ppbv/h around noon and reaching a minimum of 3–4 ppbv/h in the late afternoon. It is worth noting that these values represent upper limits of ozone production rates from HO_2+NO since HO_2 measurements performed during MCMA2006 were prone to interferences from RO_2 species (section 1.5.1.1) that had not been identified at that time (Fuchs et al., 2011). A recent quantification of these interferences on the IU-FAGE instrument (Lew et al., to be submitted) showed a contribution of approximately 30% of RO_2 radicals to the measured HO_2 signal during this campaign. Ozone production rates reported in Fig. 3.1 (Top panel) are therefore from HO_2^*+NO.

For CalNex, the RO_2 interference was identified and quantified, and $P(O_3)$ was calculated from HO_2* measurements. Average $P(O_3)$ values during weekdays reached a maximum of 50 ppbv/h around noon, while it was reduced to approximately half this value during weekends. In this study, the model ("base" in Fig. 3.1) underestimated $P(O_3)$ values calculated from HO_2*, but the total OH reactivity was also underestimated by the model. Constraining the measured OH reactivity ("mOHr" in Fig. 3.1) helped to improve the agreement between measured and modeled $P(O_3)$, especially during weekends and holidays.

Two days characterized by high and low O_3 concentrations were selected for each campaign: 19 and 21 March for MCMA and 30 May and 8 June for CalNex. Ozone production rates were modeled in the OPR instrument for each day from 8:00-9:00 to 18:00-18:30. Average and peaking values of O_3, NO_x, total VOCs, OH reactivity, $J(NO_2)$ and $J(O^1D)$ are presented in Table 3.2 for each of these 4 days, while Fig. 3.2 shows time series of O_3 and NO_x.

For MCMA-2006, O_3 did not exceed 48 ppbv on the low-ozone day (19 March), while on 21 March O_3 reached levels above 110 ppbv two times during the day. The peak of NO_x on both days appeared during traffic hours in the early morning. Average total VOCs and total OH reactivity were about 3 times higher on 21 March. Comparing O_x mixing ratios measured on these days clearly indicates that 21 March was characterized by a higher rate of ozone production on average. For CalNex, the high O_3 day (30 May) is a Sunday, with lower NO_x levels than the low O_3 day (08 June), which is a weekday. During 30 May, O_3 is higher by approximately a factor 2 for most of the day, with a peak exceeding 100 ppbv at 13:45. OH reactivity is similar on the two days, while the total mixing ratio of VOCs during 08 June reaches a maximum values that is about 36% higher than on 30 May.

Additionally, as can be seen from Table 3.2, the differences in NO_x and VOCs between the 2 campaigns on 19 March and 30 May don't correspond to similar differences in the average OH reactivity. This is partly due to the presence of more reactive compounds during CalNex. For example, isoprene was about 4-5 times higher than in MCMA on these two days.

Table 3.2: Average and peak mixing ratios of O_3, NO_2 and NO for the 4 selected days of the MCMA-2006 and CalNex-2010 field campaigns

Species		MCMA – 2006		CalNex – 2010	
		19 March 2006 9:00 – 18:00	**21 March 2006** 8:30 – 18:30	**30 May 2010** 8:00 – 18:30	**08 June 2010** 8:00 – 18:30
O_3 (ppbv)	average	40.9	73	69.8	35.0
	max	47.9	119.7	108.7	46.4
	peak	11:10	16:50	13:45	15:30
NO_2 (ppbv)	average	10.8	24.8	8.0	13.2
	max	36.3	69.9	14.3	20.3
	peak	09:00	09:10	11:45	12:45
NO (ppbv)	average	5.1	10.0	2.1	5.2
	max	18.8	61.5	5.1	13.2
	peak	09:00	8:30	08:15	12:45
Total VOCs (ppbv)	average	56.4	165.0	43.2	47.1
	max	148.5	331.8	49.6	68.0
	peak	09:00	08:30	11:30	13:00
OH reactivity (s^{-1})	average	12.9	35.8	14.6	14.9
	max	35.7	86.3	17.8	22.3
	peak	09:00	08:30	11:30	13:00
$J(NO_2)$ (s^{-1})	average	7.2×10^{-3}	5.2×10^{-3}	6.3×10^{-3}	5.6×10^{-3}
	max	9.8×10^{-3}	9.2×10^{-3}	7.8×10^{-3}	8.4×10^{-3}
	peak	12:40	12:40	13:15	11:15
$J(O^1D)$ (s^{-1})	average	2.7×10^{-5}	1.9×10^{-5}	1.6×10^{-5}	1.6×10^{-5}
	max	4.8×10^{-5}	4.3×10^{-5}	2.7×10^{-5}	2.9×10^{-5}
	peak	12:30	12:40	12:45	12:30

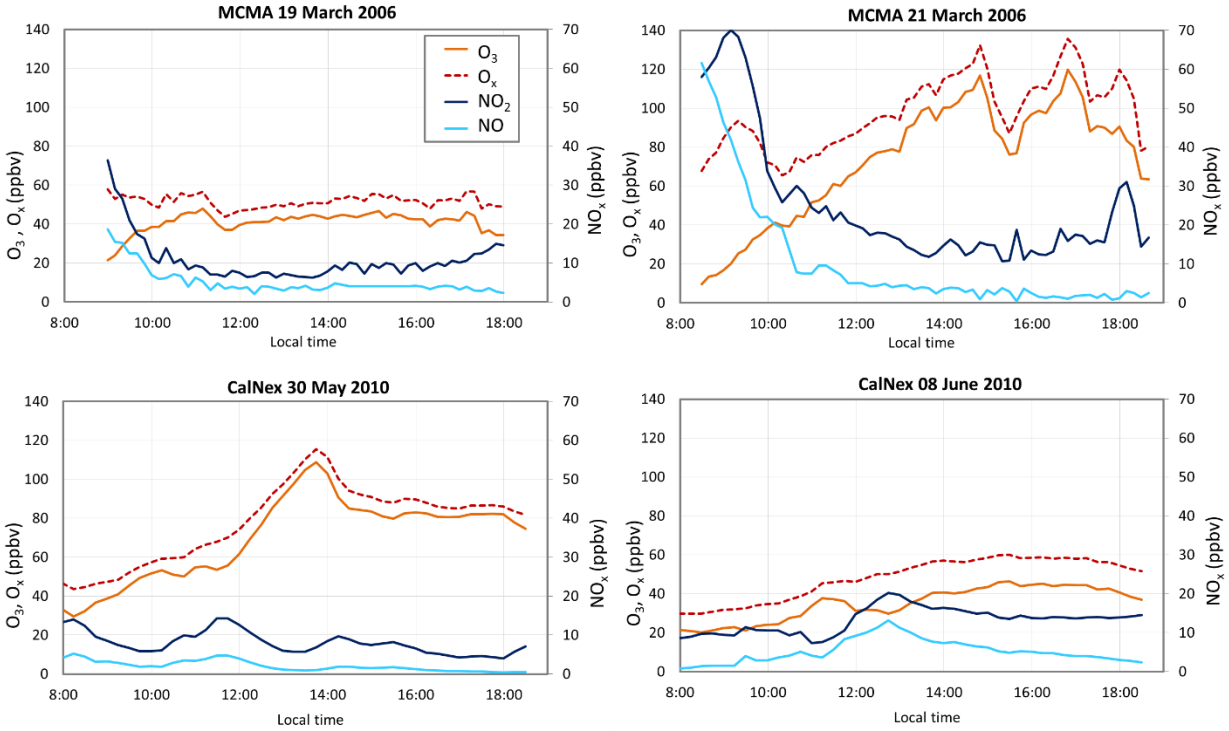

Figure 3.2: Time series of NO_x, O_x and O_3 for the 4 selected days: 19 and 21 March 2006 for MCMA (top) and 30 May and 08 June 2010 for CalNex (bottom).

Modeling four days exhibiting different air compositions, two days from a megacity and two days from a moderately polluted urban environment, should provide a robust assessment of the accuracy of OPR measurements for NO_x-rich environments.

The simulations were performed using a zero-dimensional box model based on the Regional Atmospheric Chemistry Mechanism (RACM) (Stockwell et al., 1997). As previously mentioned in chapter 1 (section 1.5.1.2), RACM is a gas-phase chemical mechanism developed for the modeling of regional atmospheric chemistry and includes 17 stable inorganic species, 4 inorganic intermediates, 32 stable organic species and 24 organic intermediates for a total of 237 chemical reactions. Organic compounds are grouped in surrogates to form a manageable set of compounds. Only 8 organic species are treated explicitly (methane, ethane, ethene, isoprene, formaldehyde, glyoxal, methyl hydrogen peroxide and formic acid) and 24 are surrogates that are grouped based on emission rates, chemical structure and reactivity with the OH radical. Heterogeneous chemistry was not included in the model.

3.3 Modeling methodology

The modeling methodology included 3 steps:

1. ***Modeling atmospheric P(O_3)*** values using the MCMA and CalNex data. The modeled values are referred as $P(O_3)_{atm}$.
2. ***Modeling P(O_3) measurements*** from the OPR instrument by modeling the chemistry that takes place in the two flow tubes. These calculations were performed assuming a conversion efficiency of 100% (either O_3-to-NO_2 or NO_2-to-O_3), and no O_x losses in the flow tubes. The modeled P(O_3) values are referred as "base model", $P(O_3)_{OPR,base}$, and were compared to $P(O_3)_{atm}$.
3. ***Sensitivity tests*** were performed to test the impact of certain factors on the P(O_3) measurements. These factors were:
    - A NO_2-to-O_3 (or O_3-to-NO_2) conversion efficiency lower than 100%,
    - O_3 (or NO_2) losses inside the flow tubes
    - An heterogeneous formation of HONO from the conversion of NO_2 on the walls of the flow tubes
    - An increase of the temperature in the reference flow tube compared to the ambient flow tube due to the UV filter
    - A dilution of the sampled air due to the injection of zero air in the flow tubes at the periphery of the inlets
    - Reactions of OH with NO_z species that lead to additional O_x production

The $P(O_3)$ values modeled during the third step are referred as $P(O_3)_{OPR}$. When a factor is varied in the model, $P(O_3)_{OPR}$ is compared to $P(O_3)_{OPR,base}$ to assess its impact on the measurements. Details on the modeling methodology are given in the following sections.

3.3.1 Modeling atmospheric $P(O_3)$

The model was constrained by 10-min (MCMA) and 15-min (CalNex) average measurements of temperature, pressure, humidity, J-values, and organic and inorganic species, while the differential equation system was integrated by the FACSIMILE solver (MCPA Software Ltd).

For both MCMA-2006 and CalNex-2010, unmeasured J-values were calculated as a function of the solar zenith angle at the coordinates of the measurement site using the Master Chemical Mechanism parameterization, corrected for cloud coverage using two scaling factors. For species photolyzed at wavelengths shorter than 330-nm, the scaling factor was derived from the ratio between measured and calculated $J(O^1D)$ values. For species photolyzed at wavelengths longer than 330-nm, measured and calculated $J(NO_2)$ values were used instead of $J(O^1D)$. In total, 24 photolysis frequencies were used to constrain the model (Table 3.3). Regarding the chemical species, 7 inorganic species and 17 organic species or surrogates were constrained for MCMA (Table 3.4). For CalNex, concentrations of chemical species were obtained from Griffith et al. (2016). In this study, the authors used the 2nd version of the Regional Atmospheric Chemical Mechanism (RACM2), which includes more chemical species and reactions than the first version of RACM (in total 363 reactions and 119 species, 17 stable inorganic species, 4 inorganic intermediates, 55 stable organic species and 43 organic intermediates). Therefore, the concentrations of several species used in RACM2 by Griffith et al. (2016) were added together to build the RACM surrogates (Annex III, Table I). In total, 24 J- values, and 28 species were used to constrain the model.

The integration time used to model steady concentrations of oxidation products that are not constrained, and as a consequence of radicals, was 30-h for each 10 or 15min data point. The concentrations of the constrained species were reinitialized every two seconds during the 30-h integration period to ensure that their concentration does not change.

Table 3.3. Photolytic reactions constrained in the model by J-values for MCMA-2006 and CalNex-2010. Details about the RACM notations can be found in Stockwell et al. (1997).

Photolytic reaction	RACM symbol	Photolytic reaction	RACM symbol
$NO_2 \rightarrow NO+O(^3P)$	JNO2	$CH_3OOH \rightarrow HO_2+OH+HCHO$	JOP1
$O_3 \rightarrow O(^1D)+O_2$	JO1D	$OP_2 \rightarrow HO_2+OH+ALD$	JOP2
$O_3 \rightarrow O(^3P)+O_2$	JO3P	$PAA \rightarrow CH_3O_2+OH$	JPAA
$HONO \rightarrow OH+NO$	JHONO	$KET \rightarrow ETHP+ACO3$	JKET
$HNO_3 \rightarrow OH+NO_2$	JHNO3	$GLY \rightarrow HCHO+CO$	JGLY1
$HO_2NO_2 \rightarrow 0.65HO_2+ 0.65NO_2+0.35OH+0.35NO_3$	JHO2NO2	$GLY \rightarrow CO+H_2$	JGLY2
$NO_3 \rightarrow NO+O_2$	JNO3_NO	$GLY \rightarrow HO_2+HO_2$	JGLY3
$NO_3 \rightarrow NO_2+O(^3P)$	JNO3_NO2	$MGLY \rightarrow HO_2+ACO3+CO$	JMGLY
$H_2O_2 \rightarrow OH+OH$	JH2O2	$DCB \rightarrow TCO3+HO_2$	JDCB
$HCHO \rightarrow HO_2+HO_2+CO$	JHCHO_CO	$ONIT \rightarrow HO_2+NO_2+0.2ALD+0.8KET$	JONIT
$HCHO \rightarrow CO+H_2$	JHCHO_H2	$MACR \rightarrow CO+HO_2+ACO3+HCHO$	JMACR
$ALD \rightarrow CH_3O_2+HO_2+CO$	JALD	$HKET \rightarrow HO_2+ACO3+HCHO$	JHKET

Table 3.4: Chemical compounds and surrogates constrained in the model for MCMA-2006 and CalNex-2010. The species with (*) have been only constrained for the CalNex modeling. Details about the RACM notations can be found in Stockwell et al. (1997).

Species	Definition	Species	Definition
O3	Ozone	HC3	Alkanes, alcohols, esters and alkynes with OH rate constant (298 K, 1 atm) less than 3.4 x 10^{-12} cm^3 s^{-1}
SO2	Sulfur dioxide	HC5	Alkanes, alcohols, esters and alkynes with OH rate constant (298 K, 1 atm) between 3.4 x 10^{-12} $cm^3 s^{-1}$ and 6.8 x 10^{-12} cm^3 s^{-1}
CO	Carbon monoxide	HC8	Alkanes, alcohols, esters and alkynes with OH rate constant (298 K, 1 atm) greater than 6.8 x 10^{-12} cm^3 s^{-1}
H2	Hydrogen	OLT	Terminal alkenes
HONO	Nitrous acid	OLI	Internal alkenes
NO	Nitric oxide	TOL	Toluene and less reactive aromatics
NO2	Nitrogen dioxide	XYL	Xylene and more reactive aromatics
CH4	Methane	HCHO	Formaldehyde
ETH	Ethane	ALD	Acetaldehyde and higher aldehydes
ETE	Ehtene	API	α-pinene and other cyclic terpenes with one double bond
ISO	Isoprene	DIEN	Butadiene and other anthropogenic dienes
GLY	Glyoxal	KET	Ketones
ORA1 (*)	Formic acid	ORA2 (*)	Acetic acid and higher acids
HNO3 (*)	Nitric acid	PAN (*)	Peroxyacetyl nitrate and higher saturated PANs

As explained in section 1.4.2, instantaneous ozone production rates, $p(O_3)$, can be calculated from Eq.1.6 as the sum of the rates of peroxy radical+NO reactions. Instantaneous ozone loss rates, $l(O_3)$, can be calculated using Eq. 1.14, based on reaction rates for ozone photolysis, reactions of O_3 with HO_x and alkenes, and the

reaction of OH with NO_2, since NO_2 is a reservoir molecule for O_3. The net ozone production rate, $P(O_3)$, is then computed as the difference between instantaneous production and loss rates, as shown in Eq. 1.15:

$$p(O_3) = k_{HO_2+NO}[HO_2][NO] + \sum_i (k_{RO_{2,i}+NO}\Phi_i[RO_{2\,i}][NO]) \quad \text{(Eq. 1.6)}$$

$$l(O_3) = k_{O(^1D)+H_2O}[O(^1D)][H_2O] + k_{OH+O_3}[OH][O_3] + k_{HO_2+O_3}[HO_2][O_3] + \sum_i k_{O_3+Alkene_i}[O_3][Alkene_i] + k_{OH+NO_2}[OH][NO_2] \quad \text{(Eq. 1.14)}$$

$$P(O_3) = p(O_3) - l(O_3) \quad \text{(Eq. 1.15)}$$

where the brackets indicate concentrations, $k_{RO2,i}$ the bimolecular rate constant for the reaction of $RO_{2,i}$ with NO, and Φ_i the branching ratio leading to radical propagation.

These calculations were performed using the model outputs to calculate atmospheric $p(O_3)$, $l(O_3)$ and, finally, $P(O_3)_{atm}$ as their difference. For Eq. 1.6, 18 RO_2 species or surrogates were taken into account, while for Eq. 1.14, 10 alkene species or surrogates were used, as shown in Table 3.5.

Table 3.5. Peroxy radical surrogates used for $p(O_3)$ calculations and unsaturated species used for $l(O_3)$ calculations.

	Species	Definition
Peroxy radicals used for $p(O_3)$ calculation	HO2	Hydroperoxy radical
	CH3O2	Methyl peroxy radical
	ETHP	Peroxy radical formed from ETH
	HC3P	Peroxy radical formed from HC3
	HC5P	Peroxy radical formed from HC5
	HC8P	Peroxy radical formed from HC8
	ETEP	Peroxy radical formed from ETE
	OLTP	Peroxy radical formed from OLT
	OLIP	Peroxy radical formed from OLI
	ISOP	Peroxy radical formed from ISO and DIEN
	APIP	Peroxy radical formed from API
	LIMP	Peroxy radical formed from LIM
	TOLP	Peroxy radical formed from TOL
	XYLP	Peroxy radical formed from XYL
	CSLP	Peroxy radical formed from CSL
	ACO3	Acetyl peroxy and higher saturated acyl peroxy radicals
	TCO3	Unsaturated acyl peroxy radicals
	KETP	Peroxy radicals formed from KET
	XO2	Accounts for additional NO to NO_2 conversions
Unsaturated species used for $l(O_3)$ calculation	ETE	Ethene
	OLT	Terminal alkenes
	OLI	Internal alkenes
	DIEN	Butadiene and other anthropogenic dienes
	ISO	Isoprene
	API	α-pinene and other cyclic terpenes with one double bond
	LIM	d-limonene and other cyclic diene-terpenes
	MACR	Methacrolein and other unsaturated monoaldehydes
	DCB	Unsaturated dicarbonyls
	TPAN	Unsaturated PANs

3.3.2 Modeling P(O_3) in the flow tubes

Modeling OPR measurements requires simulating the chemistry inside each flow tube. J-values used to model the chemistry in the ambient flow tube were the same as for atmospheric modeling since the quartz material used to build the flow tubes is transparent to solar irradiation. For the modeling of the reference flow tube, J-values were scaled based on the absorption coefficient of the Ultem film.

The absorption coefficient α of the Ultem film is linked to the light transmission:

$$I(\lambda) = I_0(\lambda)e^{-a(\lambda)x} \quad \text{(Eq. 3.1)}$$

where I(λ) and $I_0(\lambda)$ are the transmitted and incident actinic fluxes at the wavelength λ, respectively, α(λ) is the absorption coefficient, and x is the sample thickness (0.25 mm) (Philipp et al., 1989). The absorption coefficient α(λ) was obtained from Philipp et al. (1989) and the transmission of the Ultem film (I/I_0) was then calculated at different wavelengths from Eq. 3.1. The results are presented in Table 3.6 and Fig. 3.3.

Table 3.6: Absorption coefficients for an Ultem film (Philipp et al., 1989) and calculated transmissions for wavelengths ranging from 360 – 600 nm

λ (nm)	Absorption coefficient (cm^{-1})	Transmission (I/I_0)
600	1.85	95.5%
575	2.4	94.2%
550	3.2	92.3%
525	4.3	89.8%
500	5.7	86.7%
490	6.5	85.0%
480	7.5	82.9%
470	8.6	80. 7%
460	10.5	76.9%
450	12.5	73. 2%
440	16.5	66.2%
430	22	57. 7%
420	34	42.7%
400	113	5.9%
390	305	0.1%
380	1020	0.0%
370	2830	0.0%
360	6070	0.0%

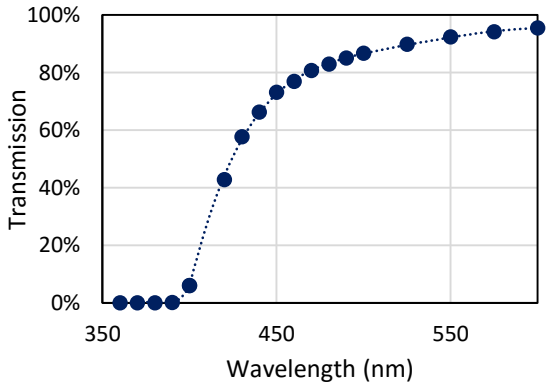

Figure 3.3: Transmission of an Ultem film as a function of wavelength

Photolysis frequencies for NO_2, O_3 ($O(^1D)$ channel) and NO_3 were calculated for clear sky conditions as:

$$J = \int_{\lambda_1}^{\lambda_2} I_0(\lambda)\, \sigma(\lambda)\, \varphi(\lambda)\, d\lambda \qquad \text{(Eq. 3.2)}$$

Where σ(λ) is the absorption cross section and φ(λ) the quantum yield for each species.

The actinic flux $I_0(\lambda)$ was calculated for the selected days of the MCMA-2006 campaign by the Tropospheric Ultraviolet-Visible model (TUV version 5.2) (Madronich and Flocke, 1999). Photolysis frequencies were calculated for the ambient flow tube (ambient J-values) and for the reference flow tube (reference J-values) using the incident (I_0) and transmitted (I) actinic fluxes, respectively. For NO_3, both photolysis channels (producing $NO+O_2$ or NO_2+O) where examined separately. The quantum yields were obtained from Johnston et al. (1996), Gardner et al. (1987) and Shetter et al. (1996) for NO_3, NO_2 and $O(^1D)$, respectively, while absorption cross sections were obtained from Orphal et al. (2003), Harder et al. (1997) and Molina and Molina (1986) for NO_3, NO_2 and O_3, respectively.

The J-values calculated inside the reference flow tube are only presented for 19 March in Fig. 3.4, since similar results were obtained for 21 March. The dark blue line represents the ambient clear sky J-values and the orange line the J-values beneath the UV filter.

The average ratio between the reference J-values and the ambient J-values provides a scaling transmission factor for each of the species NO_2, $O(^1D)$ and NO_3. J-values for chemical species photolyzed at wavelengths shorter than 400 nm (including HONO) were scaled using the $J(O^1D)$ scaling factor. J-values for species photolyzed at wavelengths up to 450 nm (glyoxal, methylglyoxal, other α-carbonyl aldehydes and unsaturated dicarbonyls) were scaled with the $J(NO_2)$ scaling factor. The $J(NO_3)$ scaling factors were used for the photolytic pathway of O_3 leading to $O(^3P)$. Since both channels of NO_3 photolysis lead to a similar scaling factor with a difference lower than 2%, an average value was therefore used. Table 3.7 reports the different scaling factors. It is worth noting that a spectroradiometer (METCON) was used after this study to directly measure the transmission factors of the Ultem film, which were in good agreement with the calculations (within 5%).

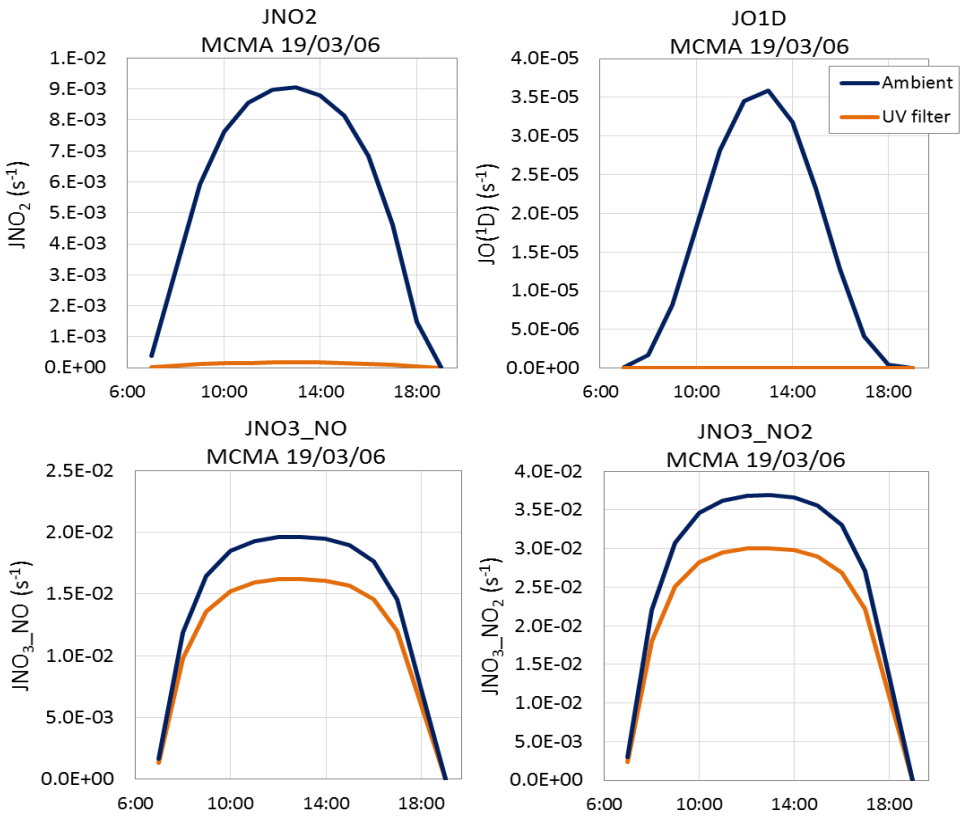

Figure 3.4: J-values calculated under clear sky conditions for the ambient and reference flow tubes (beneath the UV filter).

Table 3.7: Scaling factors used to calculate J-values in the reference flow tube (beneath the UV filter)

J-value	Scaling factor	Value of sc. factor	J-value	Scaling factor	Value of sc. factor
JNO2	JNO2	0.02	**JOP1**	JO1D	0
JO1D	JO1D	0	**JOP2**	JO1D	0
JO3P	JNO3	0.82	**JPAA**	JO1D	0
JHONO	JO1D	0	**JKET**	JO1D	0
JHNO3	JO1D	0	**JGLY1**	JNO2	0.02
JHO2NO2	JO1D	0	**JGLY2**	JNO2	0.02
JNO3_NO	JNO3	0.82	**JGLY3**	JNO2	0.02
JNO3_NO2	JNO3	0.82	**JMGLY**	JNO2	0.02
JH2O2	JO1D	0	**JDCB**	JNO2	0.02
JHCHO_CO	JO1D	0	**JONIT**	JO1D	0
JHCHO_H2	JO1D	0	**JMACR**	JO1D	0
JALD	JO1D	0	**JHKET**	JO1D	0

To simulate the chemistry inside the flow tubes, the model was constrained by the same 10 or 15-min average measurements of meteorological parameters and chemical species as for the modeling of $P(O_3)_{atm}$. In addition, concentrations of oxidation products of primary VOCs and peroxy radicals obtained as model outputs from the modeling of $P(O_3)_{atm}$were also constrained in these simulations, assuming that these species are not lost in the short sampling line. The concentration of OH was set to zero since this species does not survive in a sampling line. Tests were performed to check the impact of a loss of peroxy radicals in the sampling line (see section 3.4). The additional secondary species constrained in the flow tubes simulations are shown in Table 3.8.

Table 3.8. Secondary compounds constrained in the model to simulate the chemistry in the OPR flow tubes.

Species	Definition
N2O5	Dinitrogen pentoxide
H2O2	Hydrogen peroxide
CH3OOH	Methyl hydrogen peroxide
OP2	Higher organic peroxides
MGLY	Methylglyoxal and other α-carbonyl aldehydes
MACR	Methacrolein and other unsaturated monoaldehydes
UDD	Unsaturated dihydroxy dicarbonyl
HKET	Hydroxy ketone
DCB	Unsaturated dicarbonyls
ONIT	Organic nitrate
PAN	Peroxyacetyl nitrate and higher saturated PANs
TPAN	Unsaturated PANs
PAA	Peroxyacetic acid and higher analogs
ORA1	Formic acid
ORA2	Acetic acid and higher acids
HNO3	Nitric acid

The constrained concentrations are initialized once, to mimic what the air mass composition would be at the entrance of the flow tubes, and the simulations are run for a duration that is longer than the residence time in the flow tubes, typically 10-15 minutes. During the integration of the chemistry, the constraints are not reinitialized, so the concentrations of the species are free to change over time. With a model output every 15 s, it is possible to examine how the concentration of each species, as well as of $P(O_3)$, change inside the flow tubes during the residence time τ. The simulations were run separately for each flow tube and $P(O_3)$ was calculated from Eq. 1.15 every 15 sec.

An integrated value of $P(O_3)$ was then computed for each flow tube at a residence time of 4.5 min (determined experimentally in section 2.3.1.1). Figure 3.5 shows how ozone production changes in the ambient flow tube for 19 March 2006. The shaded areas correspond to the periods where $P(O_3)$ is integrated. $P(O_3)$ is calculated by computing the area under the curve using a trapezoidal approximation, which is then divided by the residence time of 4.5 min. These calculations are referred as $P(O_3)_{amb}$ and $P(O_3)_{ref}$ for the ambient and reference flow tubes, respectively.

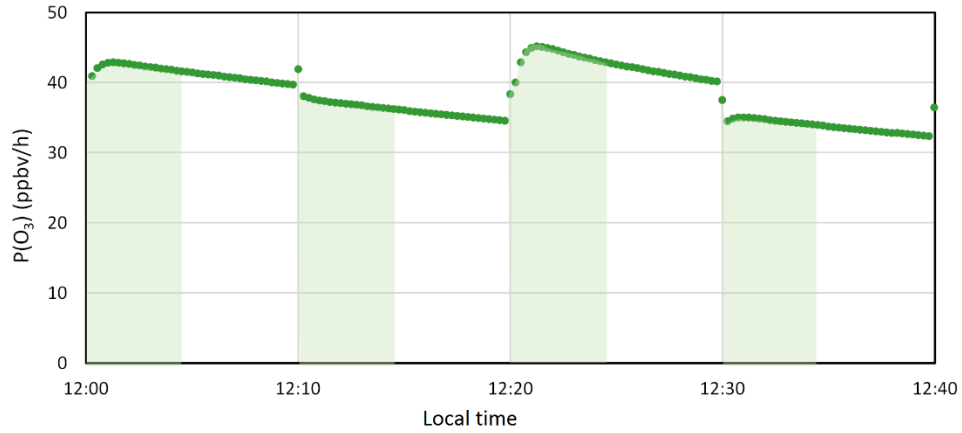

Figure 3.5: Net ozone production inside the ambient flow tube for MCMA, 19 March 2006. The shaded areas indicate the time periods (4.5 min) where P(O_3) is integrated.

$P(O_3)_{amb}$ is then compared to $P(O_3)_{atm}$ to check whether ozone production in the ambient flow tube is similar to ozone production in the atmosphere. $P(O_3)_{ref}$ is also scrutinized to check whether ozone production is negligible in the reference flow tube or whether there is a significant production of peroxy radicals under the Ultem film.

From the modeling, there are two ways of calculating the P(O_3) value that the OPR instrument will measure ($P(O_3)_{OPR}$):

$$P(O_3)_{OPR} = P(O_3)_{amb} - P(O_3)_{ref} \quad \text{(Eq. 3.3)}$$

$$P(O_3)_{OPR} = \frac{\Delta O_x}{\tau} = \frac{O_{x_{amb}} - O_{x_{ref}}}{\tau} \quad \text{(Eq. 3.4)}$$

where $O_{x_{amb}}$ and $O_{x_{ref}}$ are the modeled mixing ratios of O_x at the exit of the ambient and reference flow tubes, respectively, which are obtained from the output of the model at the residence time in the flow tubes (τ = 271 s).

Both ways were examined for the base model simulation, while only the second approach was used for the sensitivity tests since it represents how P(O_3) is derived experimentally, i.e. from O_x measurements at the exit of each flow tube. For the base simulation, the accuracy of OPR measurements is quantified by comparing $P(O_3)_{OPR}$ to $P(O_3)_{atm}$.

The results of the modeling in the flow tubes, along with the comparison with the modeling of the ambient atmosphere, are presented in section 3.4.

3.3.3 Sensitivity tests

a) Conversion efficiency

As mentioned above, both conversion methods were tested. For the NO_2-to-O_3 conversion, the OPR instrument measures O_x in the form of O_3, and O_3 mixing ratios at the exit of the conversion unit are referred as $O_{3_{conv}}$. For the O_3-to-NO_2 conversion, the OPR instrument measures O_x in the form of NO_2, and NO_2 mixing ratios at the exit of the conversion unit are referred as $NO_{2_{conv}}$.

For both cases, the converted O_3 or NO_2 is linked to the mixing ratio of O_x in the flow tubes and the conversion efficiency C as follows:

$$O_{3_{conv}} = O_{3_\tau} + C\, NO_{2_\tau} \quad \text{(Eq. 3.5)}$$

$$\text{or} \quad NO_{2_{conv}} = NO_{2_\tau} + C\, O_{3_\tau} \quad \text{(Eq. 3.6)}$$

where the mixing ratios correspond to the exit of the conversion unit (subscript: *conv*) or the exit of the flow tubes (subscript: *τ)*. The mixing ratios at the exit of the flow tubes are the model outputs for the given residence time τ. Based on Eq. 3.4, the ozone production rate measured by the OPR is then calculated as:

$$P(O_3)_{OPR} = \frac{O_{3_{conv,amb}} - O_{3_{conv,ref}}}{\tau} = \frac{O_{3_{\tau,amb}} - O_{3_{\tau,ref}} + C(NO_{2_{\tau,amb}} - NO_{2_{\tau,ref}})}{\tau} \quad \text{(Eq. 3.7)}$$

$$\text{or } P(O_3)_{OPR} = \frac{NO_{2_{conv,amb}} - NO_{2_{conv,ref}}}{\tau} = \frac{NO_{2_{\tau,amb}} - NO_{2_{\tau,ref}} + C(O_{3_{\tau,amb}} - O_{3_{\tau,ref}})}{\tau} \quad \text{(Eq. 3.8)}$$

where the subscripts *amb* and *ref* indicate the ambient and reference flow tubes, respectively.

To assess the impact of a conversion efficiency lower than 100% on $P(O_3)$ measurements, the parameter C was varied in the above equations from 75% to 100%, and $P(O_3)_{OPR}$ calculated by Eq. 3.7 (or Eq. 3.8) was compared to $P(O_3)_{atm}$. The NO_2-to-O_3 converter exhibits a conversion efficiency in this range (section 2.3.2.1), while the O_3-to-NO_2 converter allows to reach a conversion efficiency higher than 99.9% (section 2.3.2.2).

b) O_x losses and HONO production on the walls of the flow tubes

To account for O_x losses, a sink of O_3 or NO_2 is introduced in the model with a first order loss rate ranging from 1.5×10^{-4} to 1.2×10^{-3} s^{-1}, assuming it equal in the two flow tubes. This range of loss rates corresponds to a relative loss of 4 – 28% for a residence time of 271 s inside the flow tubes, which is similar to the relative losses observed during laboratory and field characterizations of the OPR instrument (section 2.3.1.2). $P(O_3)_{OPR}$ is then calculated by Eq. 3.8 assuming C=100% and is compared to the base simulation. It is

important to note here, that since these tests were made for a conversion efficiency of 100%, both Eqs. 3.7 and 3.8 would give the same results.

Additional sensitivity tests were also performed assuming that the fraction of NO_2 lost on the walls was converted into HONO with the same first order rate as the NO_2 loss. However, experiments presented in section 2.3.1.3 suggest that the presence of NO_2 is not essential for HONO formation, after the use of the OPR instrument in the field. These experiments suggested a production rate of HONO on the order of 10 ppbv/h under dark conditions and up to 60 ppbv/h under irradiated conditions. Photoenhanced HONO production rates, however, were on the order of 20 ppbv/h or less for most experiments. In order to quantify the impact of a photoenhanced HONO production (independent of the NO_2 loss) on the OPR measurements, simulations were performed including HONO production rates of 10 ppbv/h and 20 ppbv/h in the reference and the ambient flow tubes, respectively, without loss of NO_2. These production rates are similar to the experiment performed in the absence of NO_2 (see Fig. 2.23, section 2.3.1.3).

c) Increased temperature in the reference flow tube

Since the UV filter used to cover the reference flow tube absorbs photons below 400 nm, it can release this energy as heat, leading to an increase of the temperature in the reference flow tube. Even though the UV filter is not in direct contact with the quartz surface and the use of fans is expected to reduce this effect, modeling tests with an increased temperature in the reference tube were performed to assess its impact. The temperature of the reference flow tube was increased from 2% to 20% and $P(O_3)_{OPR}$ was again calculated by Eq. 3.8 (C=100%) and compared to the base simulation.

d) Dilution of the sampled air mixture

As explained in section 2.2.1, zero air is injected in the flow tubes at the periphery of the inner inlets to keep the flow going forward, minimizing recirculation eddies. The dilution of ambient air is on the order of 10%. To assess the impact of the dilution on $P(O_3)$ measurements, the concentrations of all the constrained species were lowered by a similar relative fraction in the simulations, testing dilutions ranging from 5%-30%. The O_x model outputs were then corrected for this dilution factor. $P(O_3)_{OPR}$ was calculated by Eq. 3.8 (C=100%) and compared to the base simulation.

e) Reactions of OH with NO_z leading to additional O_x production

Finally, a test was performed in order to check whether reactions of OH with NO_z species, that produce O_x, could impact the change in O_x in the flow tubes. Indeed, this Ox formation is not linked to the definition of ozone production being due to reactions of NO with peroxy radicals (Eq. 1.6). The NO_z species that produce NO_2 or NO_3 (NO_2 reservoir) when reacting with OH are: HONO, HO_2NO_2, NO_3, organic nitrates, HNO_3,

PANs and unsaturated PANs. The NO_2 and NO_3 products of the reactions mentioned above were removed from the mechanism to test whether $P(O_3)_{OPR}$ was significantly different than for the base simulations.

The results of the sensitivity tests are presented in section 3.5.

3.4 OPR base model

As previously mentioned, several days were selected from 2 different field campaigns to model ambient ozone production in urban environments, as well as $P(O_3)$ in both the ambient and reference flow tubes. A detailed analysis of the chemistry occurring in each flow tube is discussed in this section to assess the reliability of OPR measurements.

Figure 3.6 shows time series of modeled RO_x radicals, O_x species, a few selected VOCs, and net $P(O_3)$ inside the two flow tubes from 11:00 to 13:00 for 19 March 2006 during the MCMA-2006 field campaign. This time window was chosen because J-values are high and NO_2 is efficiently photolyzed. Similar results were obtained for the other days.

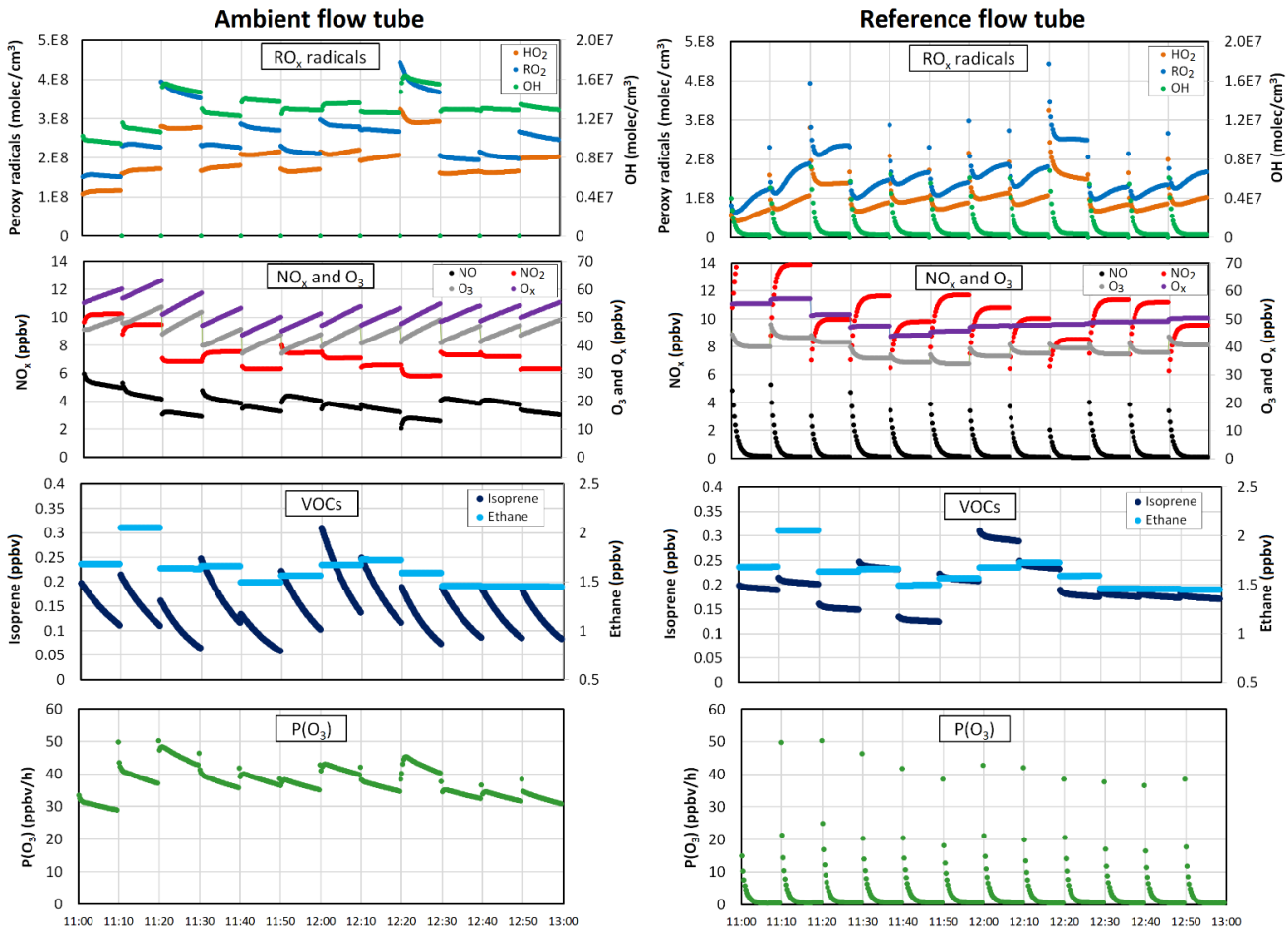

Figure 3.6: Modeled mixing ratios of chemical species in the flow tubes. Time series of RO_x, NO_x, O_x, O_3, isoprene, ethane and net $P(O_3)$ inside the ambient (left) and reference (right) flow tubes for 19 March 2006 during MCMA-2006.

As mentioned in section 3.3.2, peroxy radicals were constrained in these simulations, assuming that these species are not lost in the short sampling line. Therefore, in the ambient flow tube, peroxy radicals are not significantly changing inside the flow tubes (top left panel in Fig. 3.6), with concentrations varying approximately from 6 to 1.4 molecule/cm^3 in the middle of the day. Since peroxy radicals are constrained, the hydroxyl radical builds up in less than 15 s in the ambient flow tube.

On the other hand, since photolytic reactions below 400 nm are almost eliminated in the reference flow tube, most initiation reactions of OH are shut down. With constrained peroxy radicals, OH is generated through propagation reactions involving peroxy radicals and NO, but the OH production rate decreases quickly during the first minute of residence time (top right panel in Fig. 3.6), as NO and peroxy radicals are being consumed. It is interesting to note that peroxy radical concentrations are not reduced to negligible levels in the reference flow tube. During the first minutes of residence time their concentrations decrease, but an increase is observed after 2-3 minutes.

Depending on mixing ratios of O_3, NO and NO_2, as well as photolysis frequencies, NO and NO_2 can either increase or decrease in the ambient flow tubes following the change on the PSS and ozone production. Indeed, an increase in O_3 and O_x is observed in the ambient flow tube due to ozone production (2^{sd} left panel in Fig. 3.6). In the reference flow tube, NO_2 photolysis is reduced to 2% of its ambient value (Table 3.7), and therefore NO_2 mixing ratios increase, while NO is quickly consumed through reactions with ozone and peroxy radicals. Ozone is also decreasing since it reacts with NO and organic compounds and there is no production from NO_2 photolysis. The important thing to note is that, in the reference flow tube, there is almost no change in the O_x mixing ratios.

Looking at how VOCs are processed in the two flow tubes (3rd panel in Fig. 3.6), one can see that reactive VOCs such as isoprene ($k_{isoprene+OH} = 1\times10^{-10}$ cm^3/molecule/s) will be quickly consumed in the ambient flow tube by reacting with OH, while less reactive compounds (e.g. ethane, $k_{ethan+OH} = 2.4\times10^{-13}$ cm^3/molecule/s) will not significantly change over 10 min (less than 0.2% change). In the reference flow tube, with lower OH concentrations, isoprene exhibits a much slower change.

The bottom panel of Fig. 3.6 shows how ozone production changes during the residence time in the flow tubes, as calculated by Eq. 1.15, i.e. by subtracting $l(O_3)$ to $p(O_3)$ for each 15 s datapoint. Since peroxy radicals and NO are constrained, the first 15-s point of $P(O_3)$ is almost equal between the two flow tubes (differences are only due to loss reactions including OH, see Eq. 1.14). Then, the change in $P(O_3)$ follows the change in NO and peroxy radicals. It is interesting to note that, in the reference flow tube, as NO is consumed, $P(O_3)$ values decrease to almost zero after 3-4 min of residence time. However, integrating the $P(O_3)$ values over the residence time as shown in Fig. 3.5, will lead to positive $P(O_3)$ values in this flow tube.

It should be mentioned here that simulations performed without constraining peroxy radicals, i.e. with initial concentrations set at zero at the entrance of the flow tubes, have shown that integrated $P(O_3)$ values in the ambient and reference flow tubes for this day (19 March 2006) would be lower by 9 and 25%, respectively. This is due to a longer time for the radicals to build up to stable levels. For instance, OH and peroxy radicals will take about 2-3 minutes to build up in the ambient flow tube when peroxy radicals are not constrained. However, both flow tubes will be impacted similarly and the measured ozone production, $P(O_3)_{OPR}$, which reflects the difference in $P(O_3)$ between the two flow tubes, will decrease by less than 5%. Similar results were obtained for the other days of the MCMA-2006 and CalNex-2010 campaigns. Therefore, while $P(O_3)$ values presented in this section for the two flow tubes may be considered as upper limits, $P(O_3)_{OPR}$ is not expected to change significantly when peroxy radicals are constrained.

Time series of the peroxy radicals (HO_2 and RO_2) and NO in each flow tube at a residence time of 271 s are shown in Fig. 3.7 for MCMA-2006 and in Fig. 3.8 for CalNex-2010. These figures also include time series of HO_2 and RO_2 lifetimes, as calculated from Eqs. 3.9 -3.10.

$$HO_2\ lifetime = \frac{[HO_2]}{k_{NO+HO_2}[NO][HO_2]} \quad \text{(Eq. 3.9)}$$

$$RO_2\ lifetime = \frac{\sum[RO_2]}{[NO]\sum(k_{NO+RO_{2,i}}[RO_{2,i}])} \quad \text{(Eq. 3.10)}$$

Due to the UV filter, the O_3-NO_x PSS is shifted towards NO_2 in the reference flow tube and both NO and O_3 decrease. As a result, NO mixing ratios in the reference flow tube are lower than in the ambient flow tube for both campaigns, with the difference reaching one order of magnitude sometimes.

It is also interesting to note that peroxy radical mixing ratios in the reference flow tube are on the same order of magnitude as in the ambient flow tube. Especially on 21 March of the MCMA-2006 field campaign, where the pool of organic peroxy radicals (RO_2) increases in the reference flow tube, reaching a higher level than in the ambient flow tube in the late afternoon. This counterintuitive observation is also due to the consumption of NO in the reference flow tube that leads to a longer lifetime for the peroxy radicals.

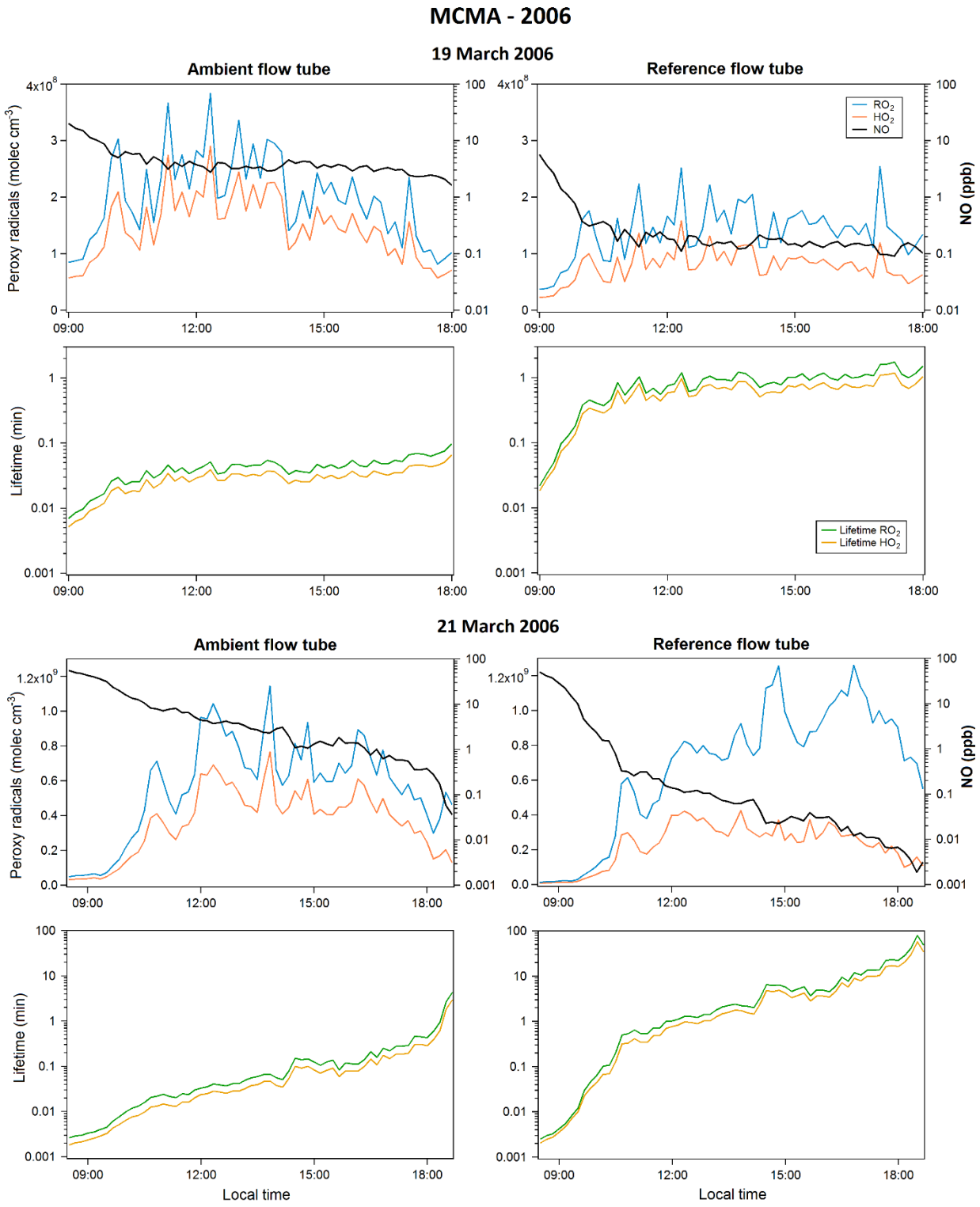

Figure 3.7: Peroxy radical concentrations, NO mixing ratios and lifetimes of HO_2 and RO_2 radicals in the ambient (left) and reference (right) flow tubes for the two selected days of the MCMA-2006 campaign.

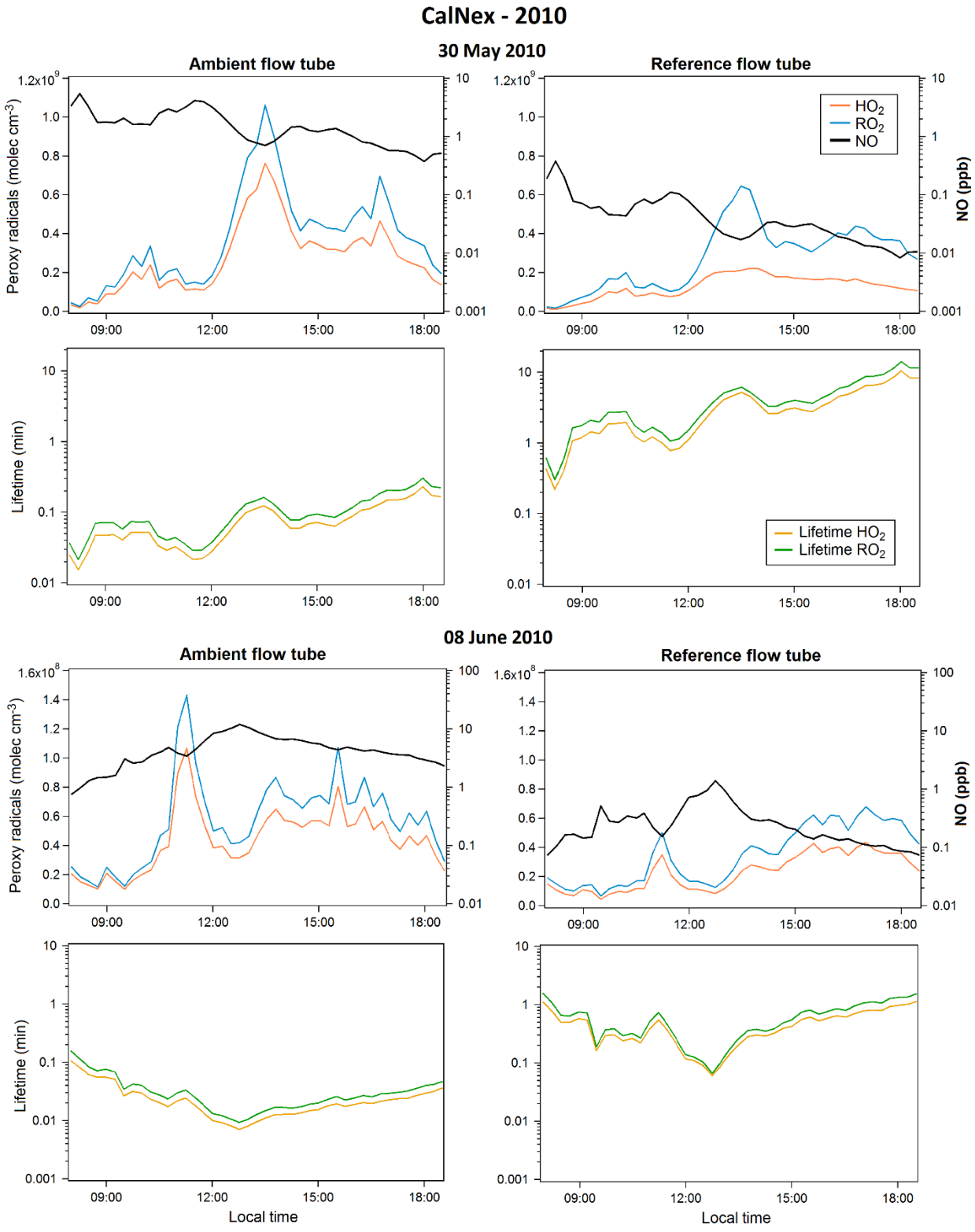

Figure 3.8: Peroxy radical concentrations, NO mixing ratios and lifetimes of HO_2 and RO_2 radicals in the ambient (left) and reference (right) flow tubes for the two selected days of the CalNex campaign.

An analysis of the radical budget was performed to investigate the radical production and loss routes in the two flow tubes. The radical budget analysis was performed using concentrations modeled when the air exits the flow tube, at the residence time of 271 s.

For the radical budget, the production and loss rates of OH and peroxy radicals were calculated taking into account initiation, propagation and termination reactions (section 1.4.1). OH production rates were calculated by adding the rates of photolytic reactions involving closed shell molecules (O_3, HONO, H_2O_2, HNO_3, HO_2NO_2 and organic peroxides), the rate of O_3 reactions with alkenes, and the propagation rate from HO_2+NO. Loss routes of OH include propagation reactions to HO_2 and RO_2 and termination reactions of OH with NO_2 or other species (NO, PANs, HNO_3, HONO, HO_2 and HNO_4). For peroxy radicals, production routes include the photolysis of oxygenated organic species (carbonyls, organic peroxides and organic nitrates), the ozonolysis of alkenes, PAN decomposition, and the propagation of OH from reactions with volatile organic compounds. Loss rates were calculated from reactions of peroxy radicals with NO_x (formation of PAN species or organic nitrates), self or cross reactions between peroxy radicals, and propagation of HO_2 to OH through reactions with O_3 and NO.

Figure 3.9 shows the production and loss rates of OH in each flow tube for the MCMA field campaign on 19 and 21 March 2006. Similarly, Fig. 3.10 shows the production and loss rates of OH for the two selected days of the CalNex campaign. These plots also include the OH chain length, which is calculated as the rate of propagation of HO_2 to OH divided by the total termination of RO_x radicals. The chain length offers useful information over the propagation efficiency of the radical reactions. Figures 3.11 and 3.12 show the production and loss rates of peroxy radicals (HO_2 + RO_2) in each flow tube, for the selected days of the two field campaigns.

It is interesting to note that high ozone days (MCMA 21 March, CalNex 30 May) exhibit higher production rates of radicals for both OH and peroxy radicals compared to low ozone days, showing that ozone production is strongly related to radical production as discussed in chapter 1 (section 1.3).

Figures 3.9 – 3.12 clearly show that the UV filter covering the reference flow tube leads to a decrease of the production rate for all radicals by approximately a factor 30. In the ambient flow tube, photolytic reactions of HONO and OVOCs are the most important initiation routes for OH and peroxy radicals, respectively. In the reference flow tube, the primary route of radical initiation is reactions of O_3 with alkenes since wavelengths below 400nm are blocked by the UV filter. These reactions contribute to both the initiation of OH and peroxy radicals. In addition, species photolyzed at longer wavelengths (glyoxal, methyl glyoxal, dicarbonyls, denoted as “OVOC+hv” in Figs. 3.11-3.12) contribute to approximately 10% of the total initiation of peroxy radicals. These results show that, even though OH and peroxy radical levels are significantly reduced in the reference flow tube, there are still radical initiation processes, with the most

important being O_3–alkene reactions. This initiation route of radicals cannot be suppressed since ozonolysis reactions are not photolytic.

The propagation reactions are important in both flow tubes for the production and loss of radicals. However, the partitioning between initiation and propagation processes is different in the two tubes, which in turn leads to different OH chain lengths. As can be seen from Fig. 3.9 for the MCMA-2006 field campaign, the OH chain length is fairly constant at a value of 3 in the ambient flow tube, while in the reference flow tube it quickly decreases to values lower than 0.5 and 0.05 in the late afternoons of 19 and 21 March, respectively. For the CalNex campaign, a similar decrease in the OH chain length is also observed for the reference flow tube. This decrease is due to the UV filter that almost completely suppresses NO_2 photolysis. Therefore, NO is quickly consumed through its reaction with O_3 and peroxy radicals, which in turn leads to a lower rate of HO_2 propagation to OH. Therefore, in addition to lowering initiation rates of radicals, the UV filter allows to reduce ozone production by lowering the cycling efficiency within the pool of RO_x radicals.

A close inspection of radical termination rates in Figs. 3.9 and 3.10 indicates that the partitioning between OH termination routes is not significantly disturbed in the reference flow tube, while for peroxy radicals, the peroxy-NO_x termination reactions are almost suppressed (Figs. 3.11-3.12). These termination reactions mainly occur through reactions with NO. As indicated for the reduction of the chain length in the reference flow tube, the change in the O_3-NO_x PSS leads to lower NO levels in this flow tube, and as a consequence, lower rates of organic nitrate formation.

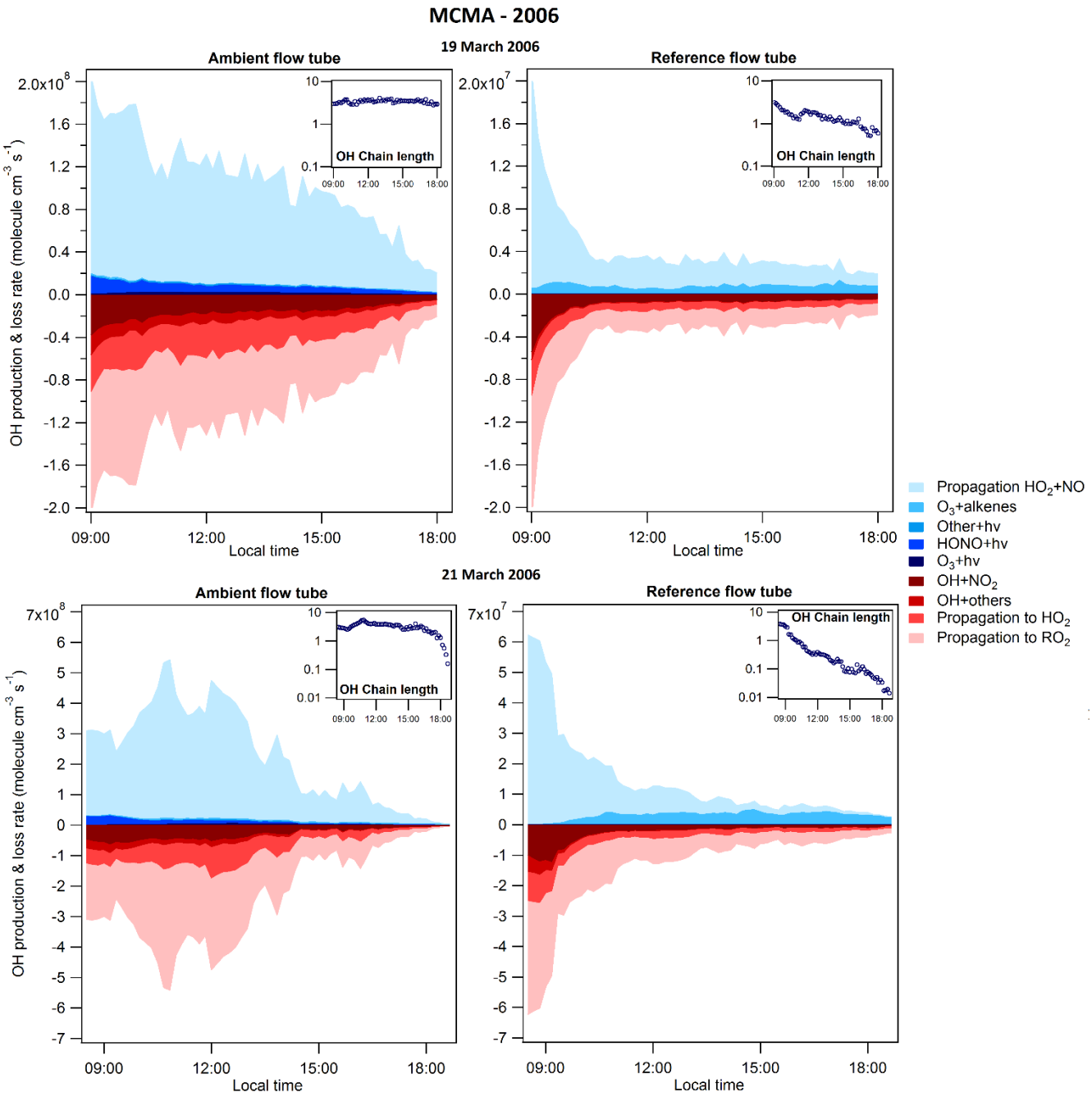

Figure 3.9: Modeled OH radical budget in the ambient (left) and reference (right) flow tubes for the two days of the MCMA-2006 campaign. The OH chain length is also presented as an insert for each flow tube.

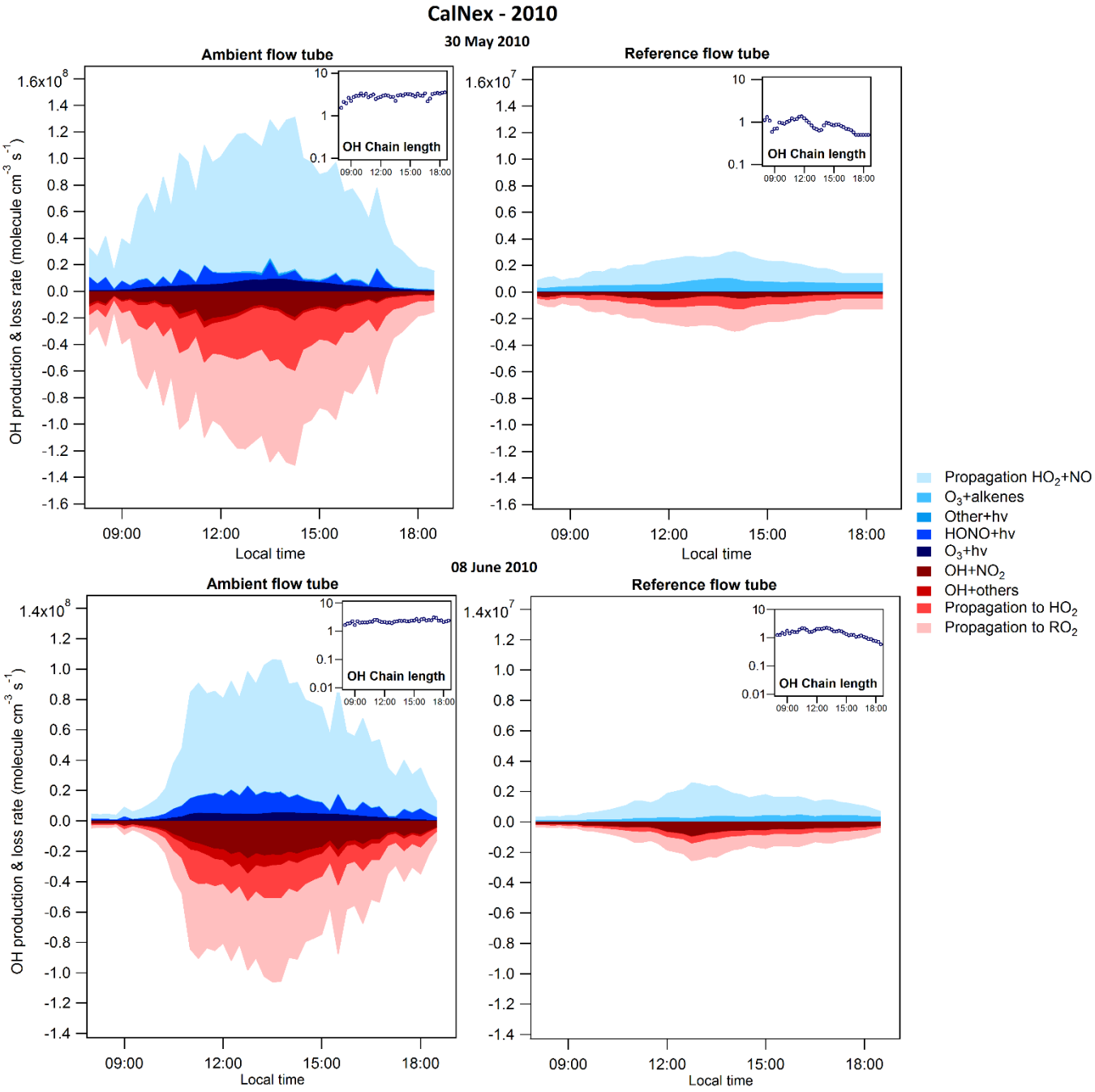

Figure 3.10: Modeled OH radical budget in the ambient (left) and reference (right) flow tubes for the two days of the CalNex campaign. The OH chain length is also presented for each flow tube.

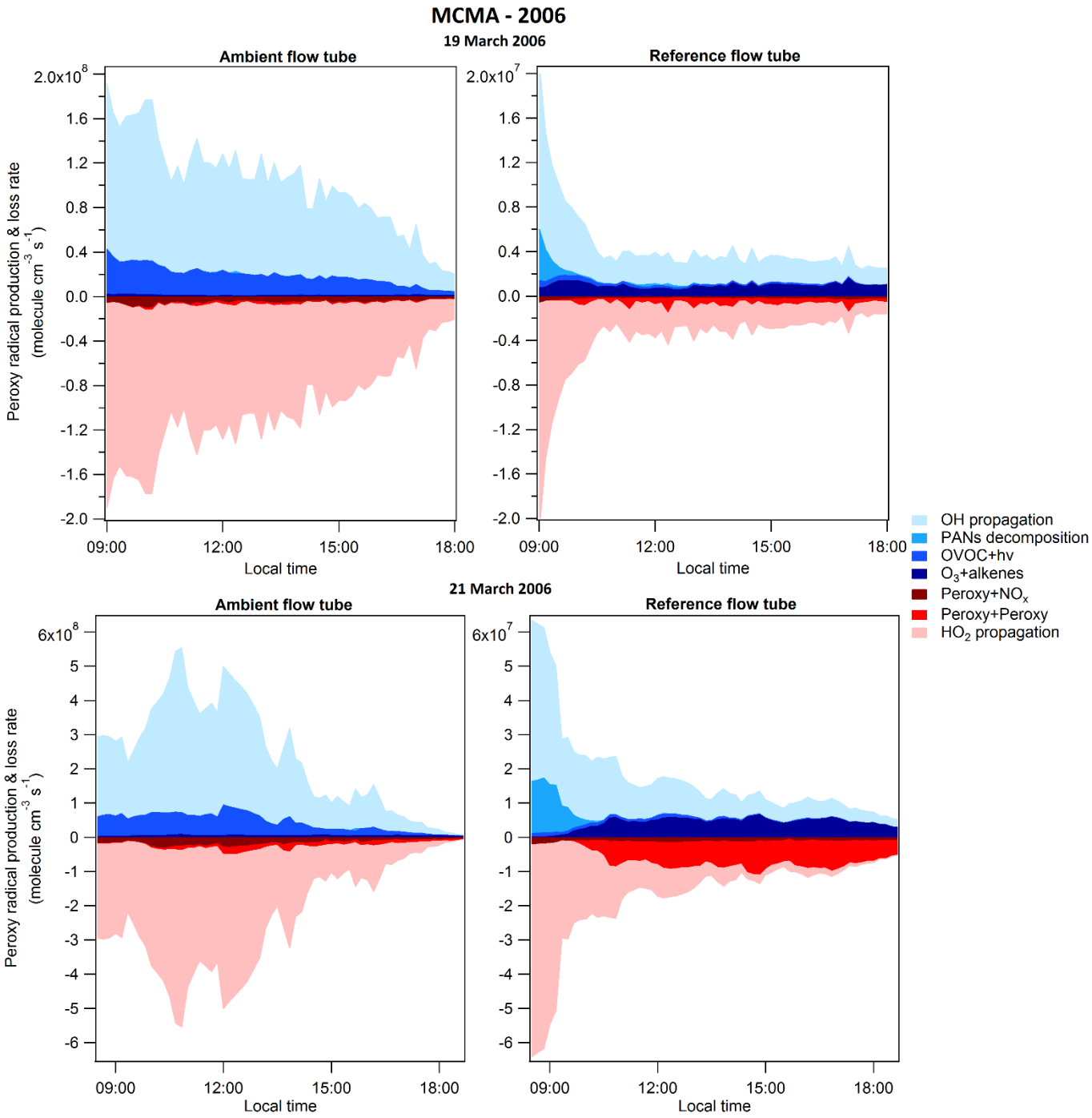

Figure 3.11: Modeled peroxy (HO_2+RO_2) radical budget in the ambient (left) and reference (right) flow tubes for the two days of the MCMA-2006 campaign.

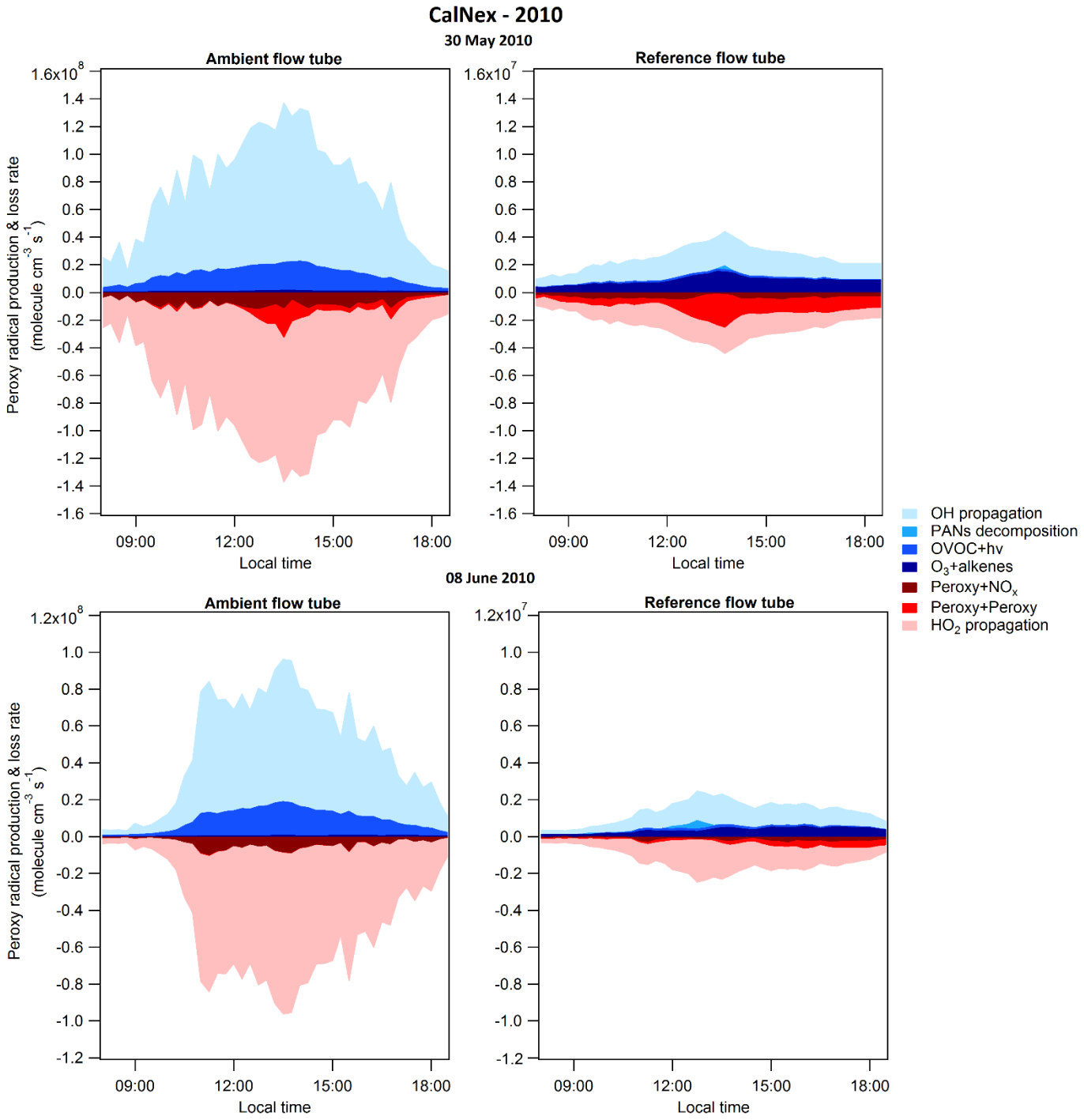

Figure 3.12: Modeled peroxy (HO_2+RO_2) radical budget in the ambient (left) and reference (right) flow tubes for the two days of the CalNex campaign.

Ozone production rates were calculated from the modeled radical concentrations, using Eq. 1.6, Eq. 1.14 and Eq. 1.15, for the modeling in the ambient atmosphere ($P(O_3)_{atm}$), the ambient flow tube ($P(O_3)_{amb}$) and the reference flow tube ($P(O_3)_{ref}$). The results of these $P(O_3)$ calculations are shown in Fig. 3.13 for MCMA-2006 and Fig 3.14 for CalNex-2010. These scatter plots show the agreement between $P(O_3)_{amb}$ (y axis) and $P(O_3)_{atm}$ (x axis) to determine whether the assumption that the chemistry in the ambient flow tube mimics the chemistry in the atmosphere is valid. Additional panels also show the ratio of $P(O_3)_{ref}$ over $P(O_3)_{amb}$ to assess the impact of the residual production of radicals in the reference flow tube on OPR measurements.

Figures 3.13 and 3.14 show that ozone production rates in the ambient flow tube, $P(O_3)_{amb}$, are in very good agreement with the modeled $P(O_3)_{atm}$ for the two low ozone days, 19 March (MCMA-2006) and 8 June (CalNex-2010), and in relatively good agreement for the two high ozone days, with a systematic underestimation of 10 ppbv/h on average on 21 March (MCMA-2006), and a relative difference of 10% on 30 May (CalNex-2010), as shown from the scatter plots. However, significant ozone production rates are also observed in the reference flow tube, which can reach up to 35 ppbv/h in the morning of the high ozone day for MCMA-2006 (21 March), when NO is still high. Ozone production in the reference flow tube is about 20% of the ozone production in the ambient flow tube for most of the day during MCMA-2006, and 10-15% during CalNex-2010. The ratio of $P(O_3)_{ref}$ over $P(O_3)_{amb}$ is generally higher during morning or late afternoon hours when ozone-alkene reactions contribute the most to radical initiation (lower photolysis frequencies, higher concentrations of alkenes during traffic hours).

It is important to note, however, that this ozone production in the reference flow tube is in reality O_x ($=O_3+NO_2$) production, since NO_2 is not photolyzed in the reference flow tube. These results indicate that the assumptions initially made for the principle of direct $P(O_3)$ measurements, i.e that (i) $P(O_3)$ in the ambient flow tube mimics $P(O_3)$ in the atmosphere and (ii) $P(O_3)$ in the reference flow tube is not significant, are not completely fulfilled. Based on the modeling results discussed above, the accuracy of the measurements will be mainly impacted by O_x production in the reference flow tube.

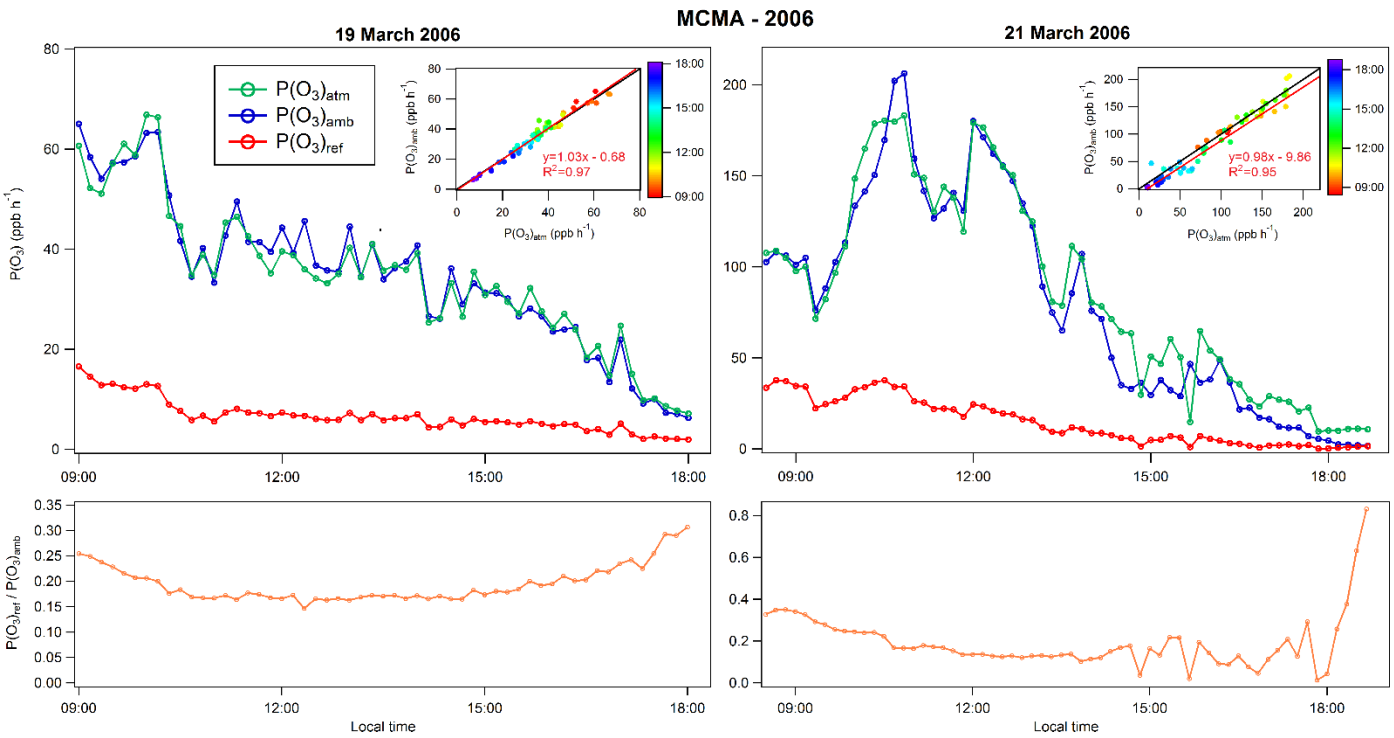

Figure 3.13: Comparison of modeled ozone production rates in the ambient atmosphere, $P(O_3)_{atm}$, in the ambient flow tube, $P(O_3)_{amb}$, and in the reference flow tube, $P(O_3)_{ref}$, for the two selected days of the MCMA-2006 campaign. The inserts show the correlation between $P(O_3)_{amb}$ and $P(O_3)_{atm}$, color-coded with the time of day. The black line at the inserts is the y=x line, with the red line is the linear fit on the data. The lower panels show time series of $P(O_3)_{ref}$ / $P(O_3)_{amb}$.

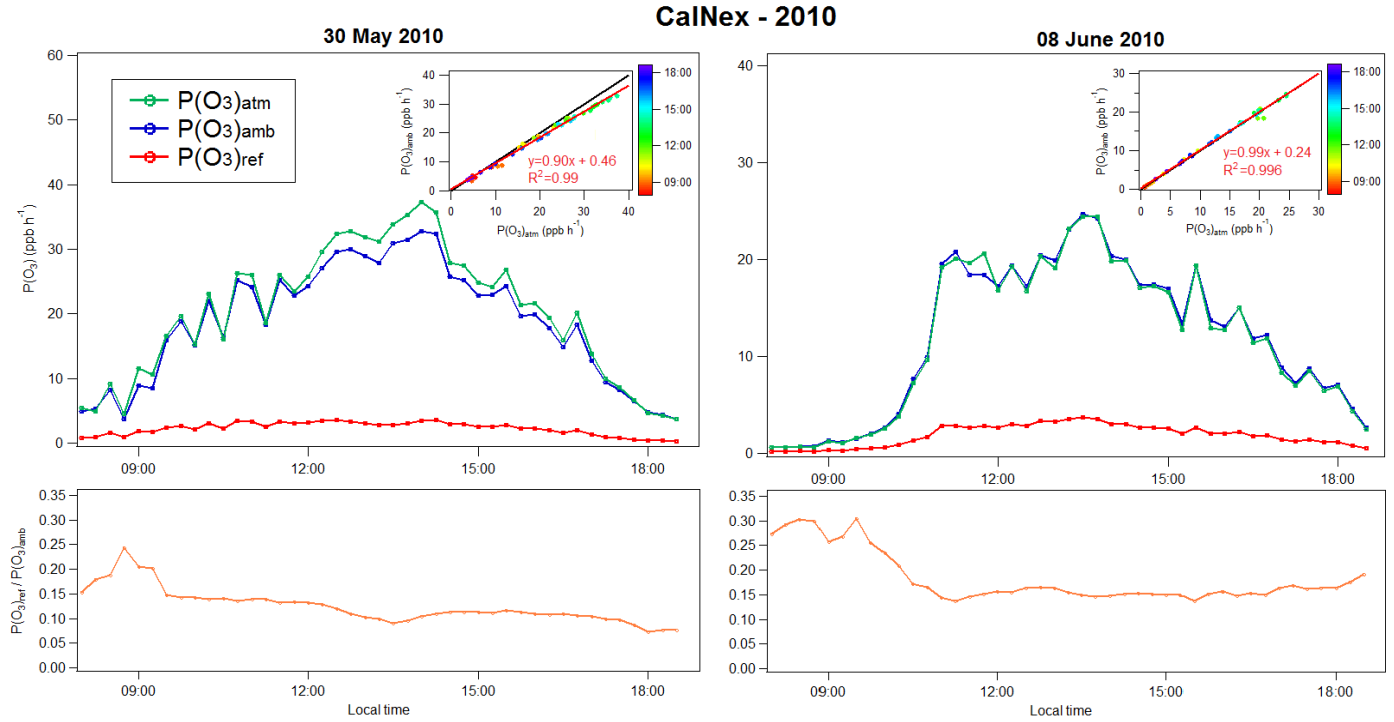

Figure 3.14: Comparison of modeled ozone production rates in the ambient atmosphere, $P(O_3)_{atm}$, in the ambient flow tube, $P(O_3)_{amb}$, and in the reference flow tube, $P(O_3)_{ref}$ for the two selected days of the CalNex-2010 campaign. The inserts show the correlation between $P(O_3)_{amb}$ and $P(O_3)_{atm}$, color-coded with the time of day. The black line at the inserts is the y=x line, with the red line is the linear fit on the data. The lower panels show time series of $P(O_3)_{ref}$ / $P(O_3)_{amb}$.

As mentioned in section 3.3.2, the ozone production that is measured by the OPR instrument can be calculated from (a) the difference between $P(O_3)_{amb}$ and $P(O_3)_{ref}$ or (b) the model O_x outputs and the mean residence time τ, as $\frac{O_{x_{amb}} - O_{x_{ref}}}{\tau}$. The latter (b) represents more accurately the OPR instrument, as O_x is measured by the CAPS monitor at the exit of each flow tube, and was chosen to calculate the modeled $P(O_3)_{OPR}$. The former (a) was also tested and was found to be in agreement with (b) within ±5% for most of the day, but exceeding ±10% when the $P(O_3)$ values were lower than 10 ppbv/h. In most cases, the absolute disagreement was less than 1.5 ppbv/h and was only higher for 21 March of the MCMA-2006 campaign (very high $P(O_3)$ day) when it reached 4 ppbv/h.

Figures 3.15 and 3.16 show the modeled $P(O_3)_{OPR,base}$ calculated using approach (b) and compared to $P(O_3)_{atm}$. These scatter plots show the agreement between $P(O_3)_{OPR,base}$ (y axis) and $P(O_3)_{atm}$ (x axis). Additional panels also show the relative difference between the two quantities calculated as: ($P(O_3)_{atm}$- $P(O_3)_{OPR,base}$)/ $P(O_3)_{atm}$. As discussed above, $P(O_3)_{OPR,base}$ underestimates $P(O_3)_{atm}$, mainly because of the significant O_x production in the reference flow tube. The scatter plots indicate that a negative bias on the order of 20% on average could be observed on $P(O_3)$ measurements performed by the OPR technique.

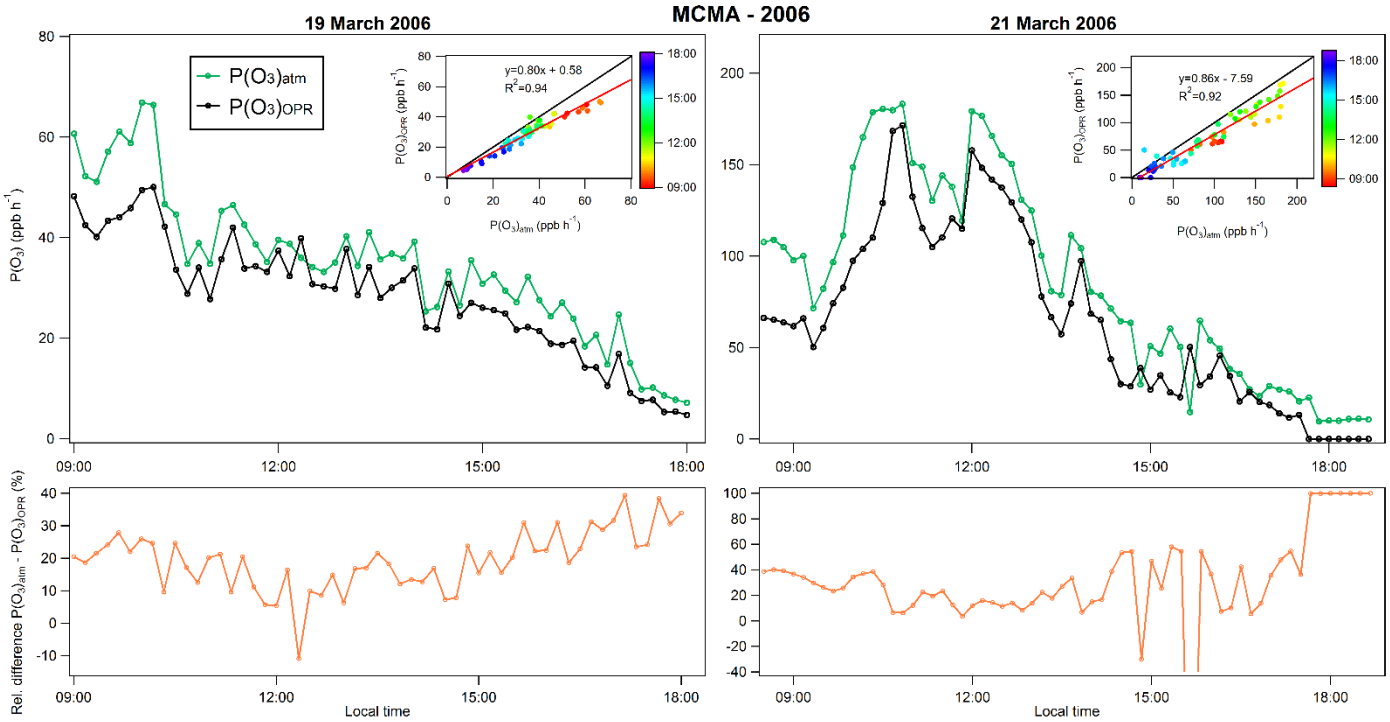

Figure 3.15: Comparison of $P(O_3)_{OPR}$ to $P(O_3)_{atm}$ for the two selected days of the MCMA–2006 campaign. The inserts show the correlation between $P(O_3)_{OPR}$ and $P(O_3)_{atm}$, color-coded with the time of day. The black line at the inserts is the y=x line, with the red line is the linear fit on the data. The lower panels show time series of the relative difference between these 2 quantities.

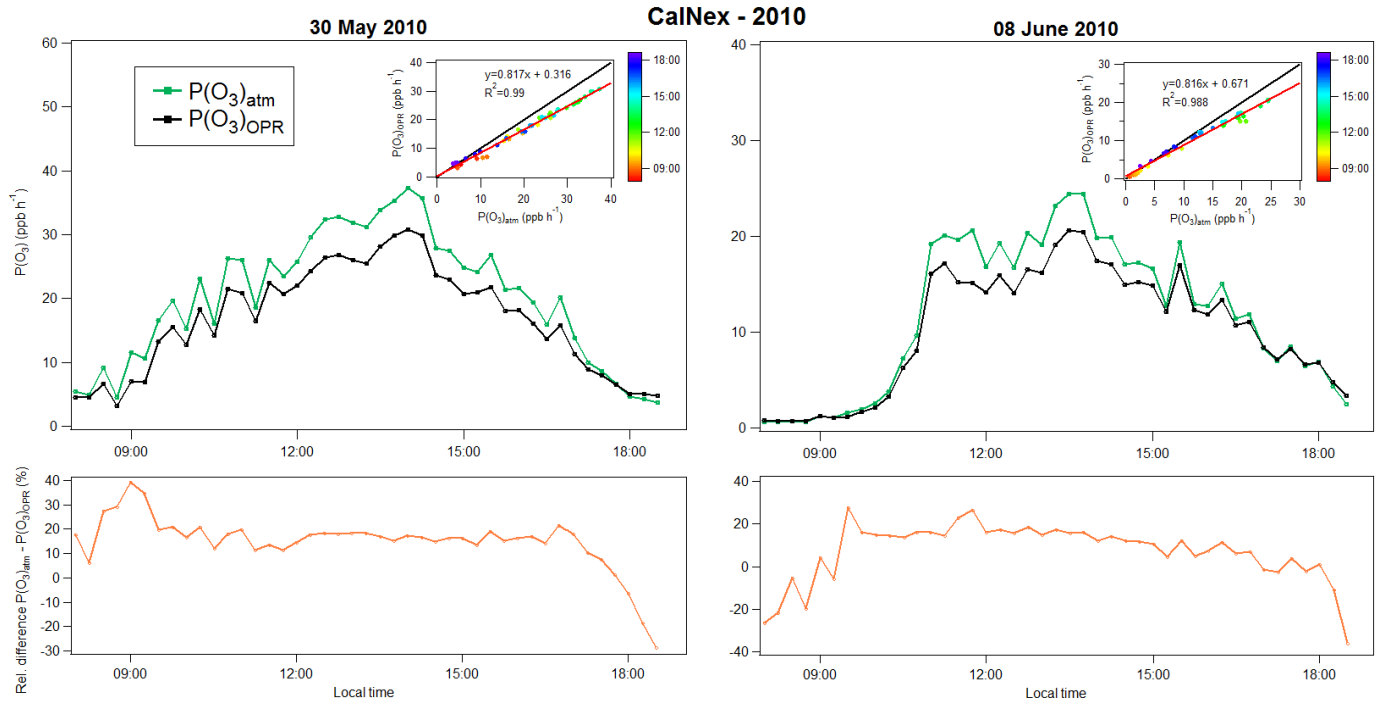

Figure 3.16: Comparison of $P(O_3)_{OPR}$ to $P(O_3)_{atm}$ for the two selected days of the CalNex-2010 campaign. The inserts show the correlation between $P(O_3)_{OPR}$ and $P(O_3)_{atm}$, color-coded with the time of day. The black line at the inserts is the y=x line, with the red line is the linear fit on the data. The lower panels show time series of the relative difference between these 2 quantities.

3.5 Sensitivity tests

Several factors were identified as potential sources of error for $P(O_3)$ measurements. These factors include a conversion efficiency lower than 100%, O_x losses and HONO production on the walls of the flow tubes, a temperature increase in the reference flow tube due to the UV filter, the dilution of the sampled air mixture, and reactions of OH with NO_z species leading to additional O_x production. Sensitivity tests are presented below to assess the impact of each of these factors on the $P(O_3)$ measurements.

3.5.1 Conversion efficiency

As explained in section 2.2.2, two methods can be used to measure O_x on the OPR instrument:

- Convert NO_2 to O_3 through NO_2 photolysis and quantify ozone with an O_3 monitor
- Convert O_3 to NO_2 through an addition of NO and quantify NO_2

The impact of a lower than 100% conversion efficiency was tested for both methods. For the NO_2-to-O_3 converter, $P(O_3)_{OPR}$ was calculated from Eq. 3.7, while for the O_3-to-NO_2 converter, $P(O_3)_{OPR}$ was calculated from Eq. 3.8.

3.5.1.1 NO_2-to-O_3 conversion

Figure 3.17 compares $P(O_3)_{OPR}$ values calculated using a conversion efficiency of 75% (Eq. 3.7) to values calculated with a conversion efficiency of 100% ($P(O_3)_{OPR\,base}$) for each campaign. The plots are color coded with the constrained NO_2 mixing ratios. From this figure, it is clear that a conversion efficiency lower than 100% will lead to an overestimation of $P(O_3)$. In some cases, such as for the lowest $P(O_3)$ values of 21 March (MCMA-2006), the overestimation can be negligible. In other cases, however, such as on 8 June, the overestimation can reach a factor of 2.5.

The overestimation of ambient $P(O_3)$ values can be understood from Eq. 3.7. In most cases, NO_2 in the reference flow tube is higher than NO_2 in the ambient flow tube during daytime, due to the lack of NO_2 photolysis in the former. Therefore, the second part of Eq. 3.7, ($NO_{2_{\tau,amb}} - NO_{2_{\tau,ref}}$), is negative. By decreasing the conversion efficiency C, the calculated $P(O_3)_{OPR}$ will increase.

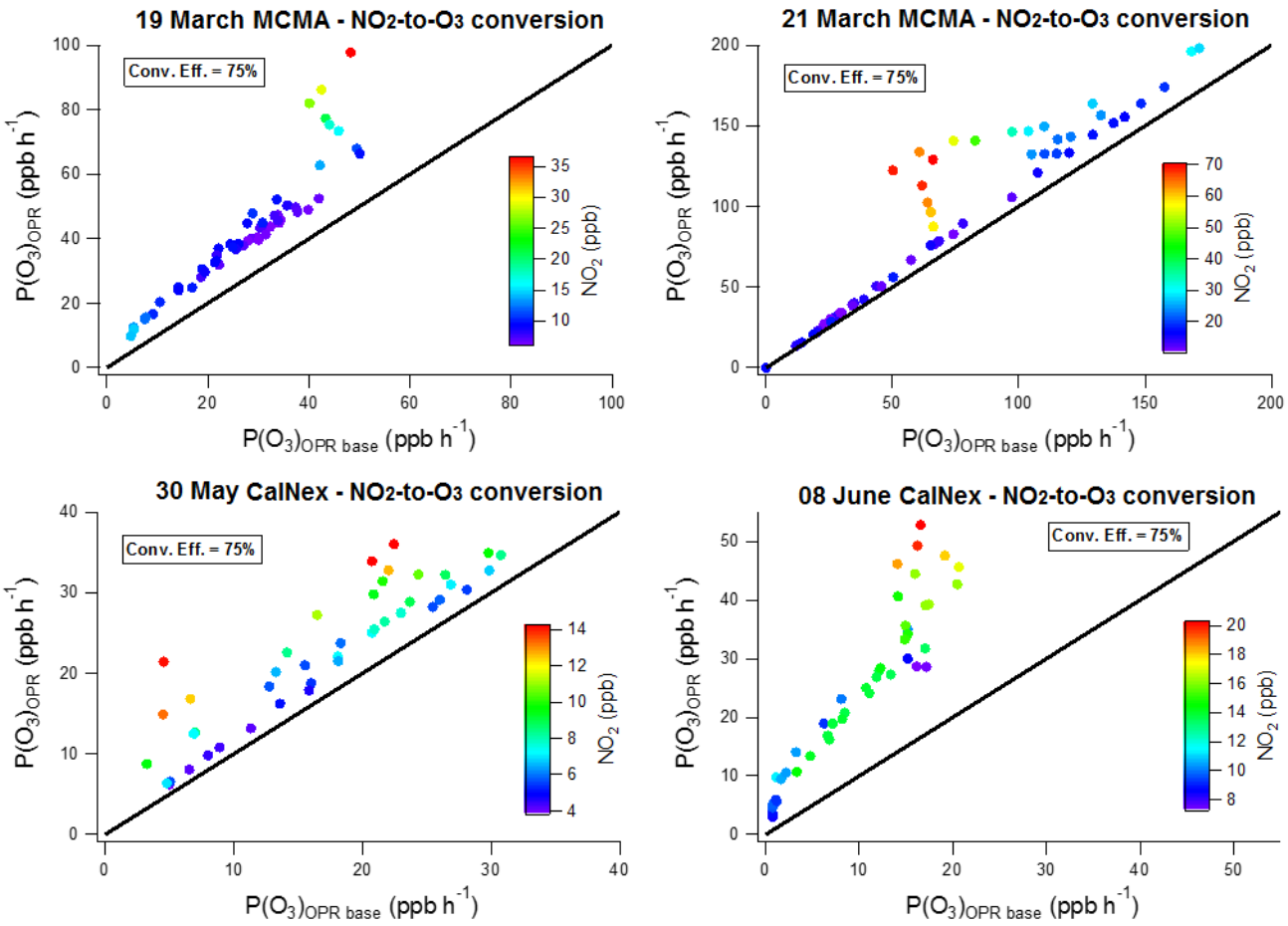

Figure 3.17: Comparison of $P(O_3)_{OPR}$ calculated at a NO_2-to-O_3 conversion efficiency of 75% to $P(O_3)_{OPR\ base}$, which assumes a conversion efficiency of 100%. The black lines represent "1:1" lines.

Several parameters were investigated to identify those enhancing the impact of the conversion efficiency on $P(O_3)$ measurements. These parameters were the concentrations of O_3, NO_2, NO, as well as the O_3/O_x and NO_2/O_x ratios. NO_2 was found to correlate well with the observed overestimations. As seen from the color coded scatter plots (Fig. 3.17), the impact of a low conversion efficiency on the $P(O_3)$ measurements is higher for high NO_2 mixing ratios. In addition, the impact of NO_2 is higher at low $P(O_3)$ values, since they correspond to lower values of $(O_{3_{\tau,amb}} - O_{3_{\tau,ref}})$ in Eq. 3.7. For instance, a high impact of the conversion efficiency is observed for 08 June (CalNex-2010), when $P(O_3)$ is relatively low, below 20 ppbv/h for most of the day, and NO_2 is high compared to other days exhibiting similar $P(O_3)$ values.

As can be seen from Eq. 3.7, measured $P(O_3)$ values depend on absolute NO_2 and O_3 differences between the two flow tubes and the impact of the conversion efficiency on $P(O_3)$ measurements will therefore depend on the O_3-NO_x partitioning, which is different between the two flow tubes. For this reason, there is not a single parameter that drives the impact of the conversion efficiency on the $P(O_3)$ measurements, but it strongly depends on the chemical composition of each sampled air mass. However, it is possible to provide

a rough estimate of how a low conversion efficiency will impact the $P(O_3)$ measurements using the $P(O_3)_{OPR}/P(O_3)_{OPR\ base}$ ratio.

Figure 3.18 shows how $P(O_3)$ measurements would change depending on the NO_2-to-O_3 conversion efficiency for each day of the two field campaigns. For this purpose, the conversion efficiency was varied between 70 and 100% as described in section 3.3.3. The $P(O_3)_{OPR}/P(O_3)_{OPR\ base}$ ratio is displayed for two different times of the day (9:00 and 13:30) that have been identified as the times when the highest and lowest impacts of the conversion efficiency are observed. For 08 June (CalNex-2010), the highest impact was found at 10:30, because $P(O_3)$ was too low (< 3 ppbv/h) before this time.

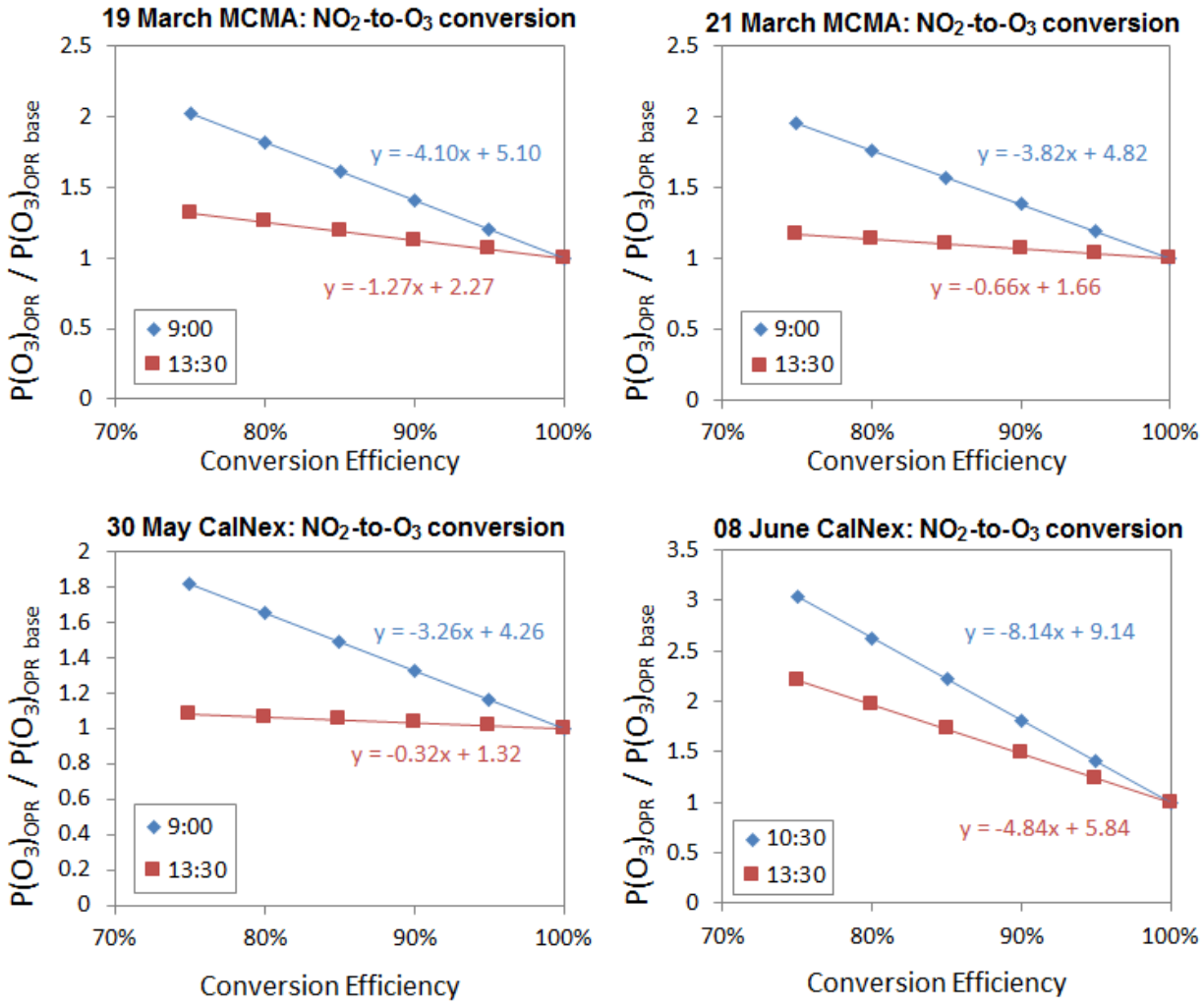

Figure 3.18: Impact of the NO_2-to-O_3 conversion efficiency on $P(O_3)$ measurements. $P(O_3)_{OPR}/P(O_3)_{OPR\ base}$ ratios are plotted as a function of the conversion efficiency for 2 different times of the day (see text).

Fig 3.18 confirms that $P(O_3)_{OPR}$ is sensitive to the conversion efficiency during all days, especially during 08 June (CalNex-2010), which was a weekday characterized by high NO_x mixing ratios and low ozone production rates. For this day, lower and upper limits of the measurement bias introduced by a conversion efficiency of 75% are overestimations by a factor 2 and 3 (morning hours), respectively. For the other three days, a conversion efficiency of 75% would lead to an overestimation of ambient $P(O_3)$ by a factor 2 at most during morning hours and less than a factor 1.3 for the rest of the day.

It is interesting to see that the $P(O_3)_{OPR}/P(O_3)_{OPR\,base}$ ratio changes linearly with the conversion efficiency. The slope of the straight line can be used to gauge the impact of the conversion efficiency on the $P(O_3)$ measurements throughout the day. The steeper the slope, the higher the impact on the $P(O_3)$ measurements.

The NO_2-to-O_3 converter developed in Mines Douai has a maximum conversion efficiency of 75%-80% (section 2.3.2.1). For the modeled days, it was found that a 75% conversion efficiency would lead to a large overestimation of the $P(O_3)$ measurements, ranging from a factor 1.1 to 3, which is not suitable for ambient measurements. It is however interesting to note that this error could, to some extent, be cancelled out by the underestimation expected from ozone production in the reference flow tube (section 3.4).

3.5.1.2 O_3-to-NO_2 conversion

Similarly to the previous section, Fig. 3.19 shows $P(O_3)_{OPR}$ values calculated with an O_3-to-NO_2 conversion efficiency of 75% using Eq. 3.8. These values are compared to the values derived using a conversion efficiency of 100%, i.e. $P(O_3)_{OPR\,base}$. The plots are again color coded with the constrained NO_2 mixing ratios. From this figure, it is clear that a lower than 100% conversion efficiency would cause an underestimation of $P(O_3)$. This underestimation can again be explained from Eq. 3.8 using the same reasoning than above. O_3 in the ambient flow tube is higher than in the reference flow tube due to NO_2 photolysis, leading to positive values of $(O_{3_{\tau,amb}} - O_{3_{\tau,ref}})$. Therefore, a decrease of the conversion efficiency C will lead to a concomitant decrease of the calculated $P(O_3)_{OPR}$. Similarly to the NO_2-to-O_3 converter, a higher impact is observed for elevated NO_2 mixing ratios.

However, $P(O_3)_{OPR}$ is much more sensitive to lower conversion efficiency values than what was observed for the NO_2-to-O_3 converter (section 3.5.1.1). It can be seen from Fig. 3.19 that, during the first three days (19 and 21 March 2006, and 30 May 2010), the underestimation of ambient $P(O_3)$ values is on the order of 60%. For 8 June 2010, the underestimation is on the order of 170%. This can be explained from Eq. 3.8. As mentioned before, the term $(O_{3_{\tau,amb}} - O_{3_{\tau,ref}})$ is positive, while the term $(NO_{2_{\tau,amb}} - NO_{2_{\tau,ref}})$ is

negative. For positive $P(O_3)$ values and a conversion efficiency of 100%, the term $C\left|O_{3_{\tau,amb}} - O_{3_{\tau,ref}}\right|$ is higher than $\left|NO_{2_{\tau,amb}} - NO_{2_{\tau,ref}}\right|$ by a few ppbv (e.g. 3 ppbv of difference correspond to 40 ppbv/h of ozone production). By decreasing the conversion efficiency, the absolute decrease in $P(O_3)_{OPR}$ is higher that what it was for the NO_2-to-O_3 conversion, as the conversion efficiency is multiplied with the larger term, i.e $\left|O_{3_{\tau,amb}} - O_{3_{\tau,ref}}\right|$.

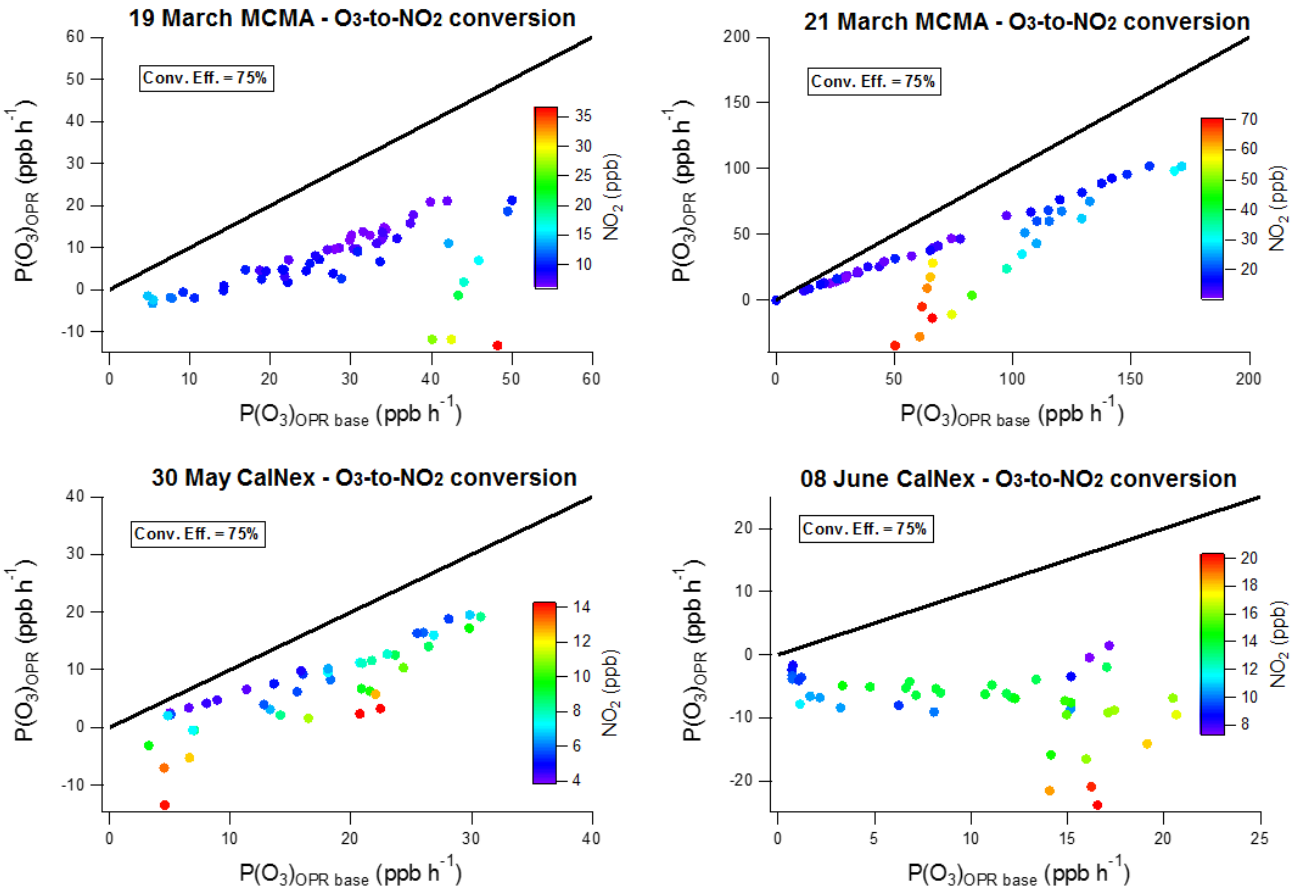

Figure 3.19: Comparison of $P(O_3)_{OPR}$ values calculated at an O_3-to-NO_2 conversion efficiency of 75% to $P(O_3)_{OPR\ base}$, which assumes a conversion efficiency of 100%. The black lines represent the "1:1" lines.

Figure 3.20 shows how the $P(O_3)$ measurements would be impacted by the O_3-to-NO_2 conversion efficiency for each day. As in the previous section, the results are displayed for a range of conversion efficiencies and two different times of the day, exhibiting the highest and lowest impacts on the $P(O_3)$ measurements.

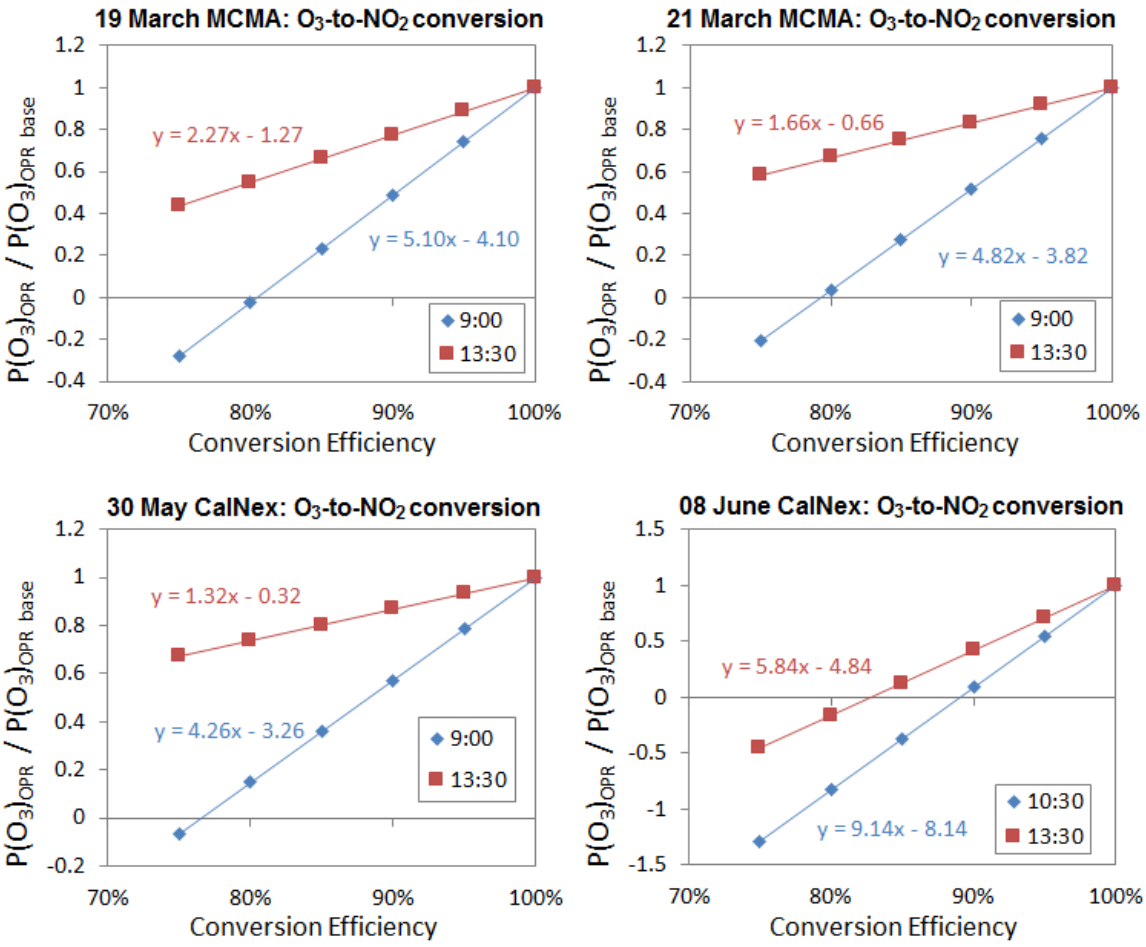

Figure 3.20: Impact of the O_3-to-NO_2 conversion efficiency on $P(O_3)$ measurements. $P(O_3)_{OPR}/P(O_3)_{OPR\ base}$ ratios are plotted as a function of the conversion efficiency for 2 different times of the day (see text).

The first three days (19 and 21 March 2006, and 30 May 2010) exhibit similar impacts of the O_3-to-NO_2 conversion efficiency on the $P(O_3)$ measurements. For instance, during these three days, a conversion efficiency of 75% would lead to an underestimation of the $P(O_3)$ measurements by 35-60% at 13:30, and by 105-130% during morning hours. However, a conversion efficiency of 75% on 08 June 2010 would lead to an underestimation of 150-225%.

These results indicate the strong sensitivity of $P(O_3)$ measurements to the O_3-to-NO_2 conversion efficiency, as well as the need to reach a conversion efficiency better than 99% to keep this artifact below 5%. The O_3-to-NO_2 converter of the OPR instrument exhibits a conversion efficiency of 99.9% (see section 2.3.2.2) and is therefore suitable for ambient $P(O_3)$ measurements.

3.5.2 O_x losses on the walls of the flow tubes

As explained in section 3.3.3, in order to assess the impact of O_3 and NO_2 surface-losses in the flow tubes on the $P(O_3)$ measurements, an O_3 or NO_2 sink was introduced in the model with constant loss rate ranging from 1.5×10^{-4} to 1.2×10^{-3} s^{-1}, which corresponds to relative losses of 4% – 28% for a residence time of 271 s. $P(O_3)_{OPR}$ was then calculated by Eq. 3.8 for a conversion efficiency of 100%, and was compared to $P(O_3)_{OPR\ base}$.

Figures 3.21 and 3.22 show the change in $P(O_3)_{OPR}/\ P(O_3)_{OPR\ base}$ as a function of the relative O_3 and NO_2 loss, respectively, for each day of the two field campaigns and times windows identified for the highest and lowest impacts on the $P(O_3)$ measurements.

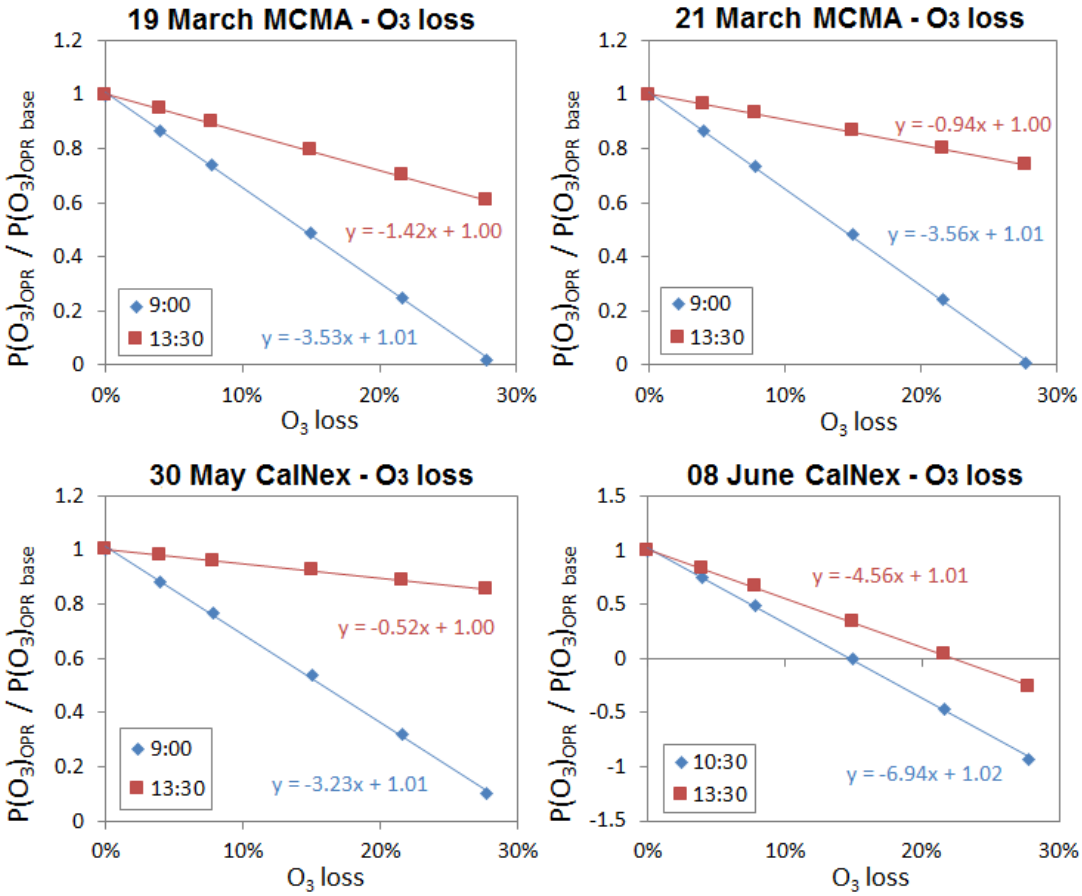

Figure 3.21: Impact of O_3 surface-losses on $P(O_3)$ measurements. $P(O_3)_{OPR}/P(O_3)_{OPR\ base}$ ratios are plotted as a function of O_3 loss for 2 different times of the day (see text).

Figure 3.21 shows that an ozone loss on the quartz tubes can lead to a significant underestimation of the $P(O_3)$ measurements. On the other hand, an NO_2 loss leads to an overestimation of the $P(O_3)$ measurements (Fig. 3.22). As for the conversion efficiency, $P(O_3)$ measurements are more sensitive to the losses during 8

June (CalNex-2010), which is a result of the combination of low $P(O_3)$ values and high NO_2 mixing ratios observed on this day.

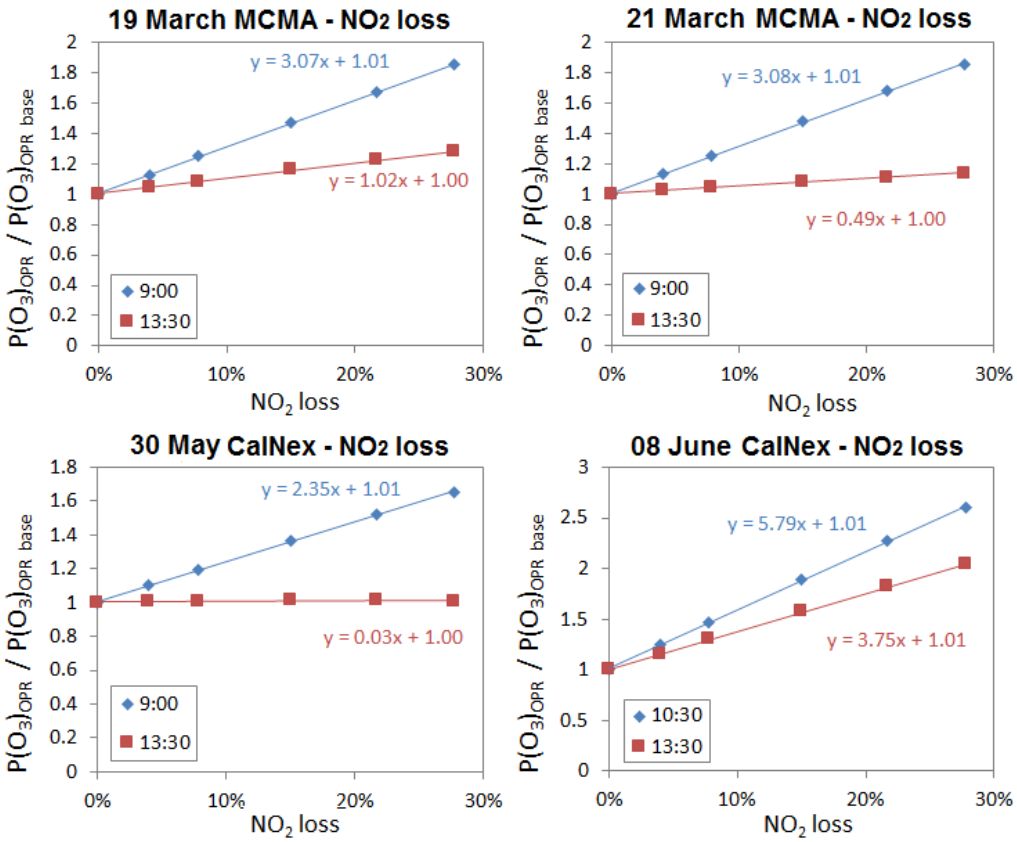

Figure 3.22: Impact of NO_2 surface-losses on $P(O_3)$ measurements. $P(O_3)_{OPR}/P(O_3)_{OPR\ base}$ ratios are plotted as a function of NO_2 loss for 2 different times of the day (see text).

During the first three days (19 March 2006, 21 March 2006, 30 May 2010), a 5% ozone loss, as observed during the laboratory testing of the instrument and during field measurements (section 2.3.1.2), can lead to an underestimation of the measurements by 5-13%. On the other hand, a 3% NO_2 loss, upper value estimated by the characterization tests (section 2.3.1.2), can lead to an opposite impact with a 1-9% overestimation of the $P(O_3)$ measurements. On 08 June (CalNex-2010), a 5% O_3 loss can lead to a $P(O_3)$ underestimation on the order of 25%, and a 3% NO_2 loss to a $P(O_3)$ overestimation of approximately 15%.

These antagonistic effects between O_3 and NO_2 losses can be explained as follows: ozone in the reference flow tube is lower than in the ambient flow tube, due to the conjunction of a lower production rate of ozone and a shift of the O_3-NO_x PSS towards NO_2. An heterogeneous loss of ozone will therefore lead to a larger absolute loss of O_x species in the ambient flow tube, which in turn will lead to a measurement underestimation of $P(O_3)$ (Eq. (3.8)). In contrast, NO_2 is higher in the reference flow tube and an heterogeneous loss of NO_2 will lead to a larger absolute loss of O_x species in the reference flow tube, and as a consequence, to an overprediction of $P(O_3)$.

It should be noted, however, that the O_3 loss sensitivity tests were applied assuming similar losses in the two flow tubes. For this reason, the above discussion represents more accurately an impact associated to the dark ozone loss and not the photoenhanced loss (section 2.3.1.2). Since the photoenhanced loss mainly takes place in the ambient flow tube, it is expected to further increase the negative bias on the measurements. This aspect of the measurements is discussed in more details in chapter 4.

NO_2 loss sensitivity tests were then modified, assuming that all the NO_2 that is lost on the quartz tubes is equally converted into HONO in both flow tubes. Figure 3.23 shows how the NO_2 loss combined with production of HONO would impact the $P(O_3)$ measurements. The impact is again much stronger during 8 June (CalNex-2010). These results indicate that HONO production may cause an additional overestimation of ambient $P(O_3)$, on top of the impact of an NO_2 loss. This overestimation results from HONO photolysis in the ambient tube, which leads to additional OH production and an enhancement of the radical cycling and ozone production. During the first three days (19 March 2006, 21 March 2006, 30 May 2010), a relative loss of 3% would lead to an overestimation of up to 24% throughout the day while on 8 June 2010 the overestimation may reach approximately 35%.

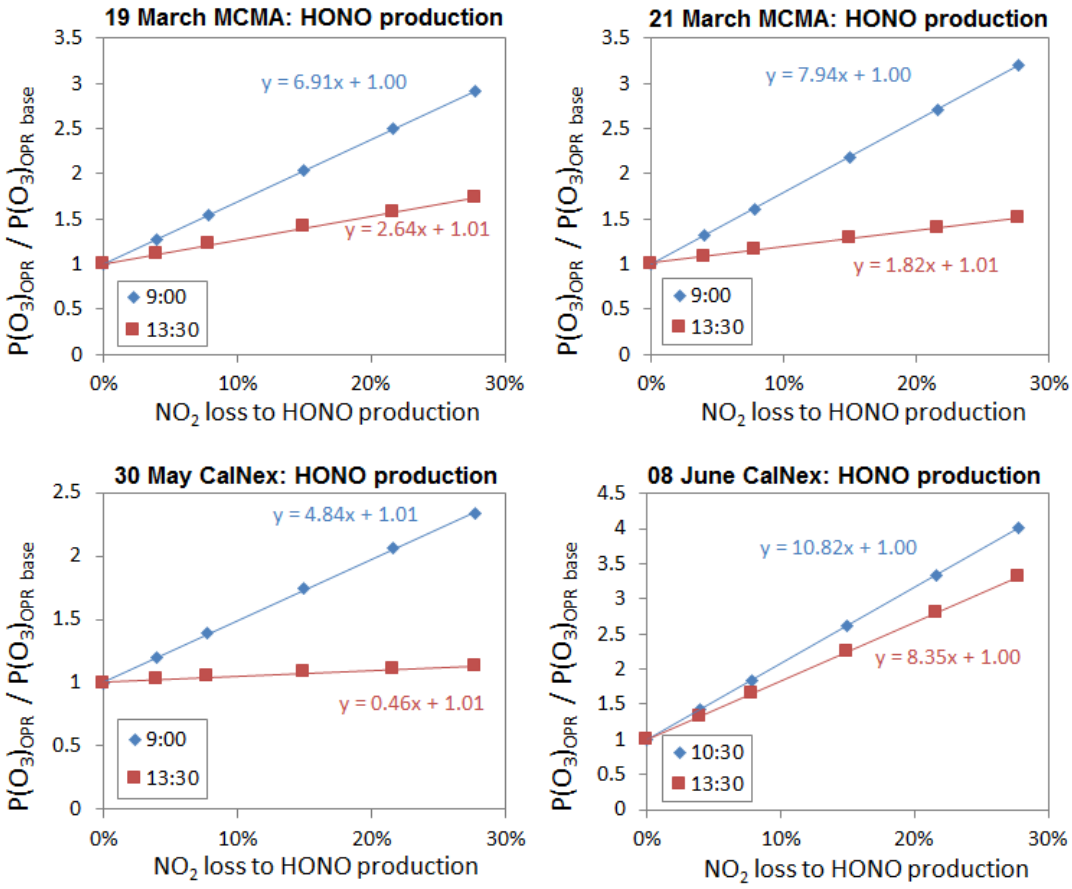

Figure 3.23: Impact of HONO production on $P(O_3)$ measurements. $P(O_3)_{OPR}/P(O_3)_{OPR\ base}$ ratios are plotted as a function of an NO_2 loss leading to HONO production for 2 different times of the day (see text).

The simulations presented above were performed assuming equal NO_2 losses in both flow tubes towards HONO formation. As explained in section 3.3.3, simulations were also performed to check the impact of a HONO production that is independent of the NO_2 loss, including HONO production rates of 10 ppbv/h and 20 ppbv/h in the reference and ambient flow tubes, respectively. These simulations showed that the $P(O_3)_{OPR}$ values can be overestimated by up to 30% due to this photoenhanced HONO production in the ambient flow tube, which can be further photolyzed and act as a source of OH. It is interesting to note, however, that this error could, to some extent, cancel out the error caused by the O_x production in the reference flow tube.

3.5.3 Other sensitivity tests

As discussed in section 3.3.3, a few additional tests were also performed to assess the accuracy of $P(O_3)$ measurements: a temperature increase in the reference flow tube, the dilution of the sampled air mixture, and the removal of O_x production from reactions of OH with NO_z species.

Figure 3.24 shows how $P(O_3)$ would change if the temperature was increased by 2–25% in the reference flow tube. A temperature increase of 5% in this flow tube (1^o C increase at 20^o C) can lead to an underestimation of $P(O_3)$ values by less than 5%. Generally, a higher impact is observed during the early morning or the late afternoon. The temperature difference between the two flow tubes that was observed during the field testing of the instrument was less 1^o C, and therefore, the OPR instrument is not thought to be significantly affected by this issue.

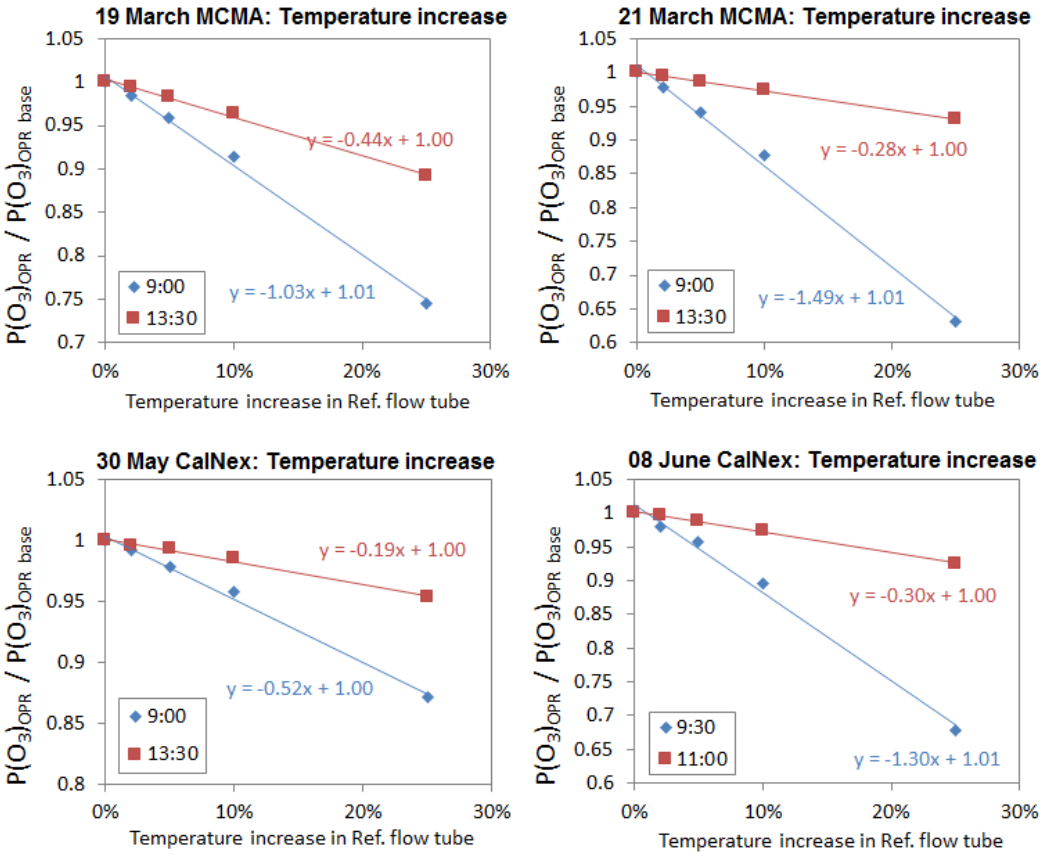

Figure 3.24: Impact of a temperature increase of the reference flow tube on $P(O_3)$ measurements. $P(O_3)_{OPR}/P(O_3)_{OPR\ base}$ ratios are plotted as a function of a relative temperature increase in the reference flow tube for 2 different times of the day (see text).

Figure 3.25 displays how the injection of zero air inside the flow tubes at the periphery of the Teflon inlets impacts $P(O_3)$ measurements by diluting the sampled air. As can be seen from this figure, a 10% dilution only leads to a ±4% change in the measured $P(O_3)$. The dilution causes a systematic 3-4% overprediction of the measurements for most of the day. The impact decreases in the early morning or late afternoon when J-values are low, where it can lead to a small underprediction of the measurements on the order of 2-3%.

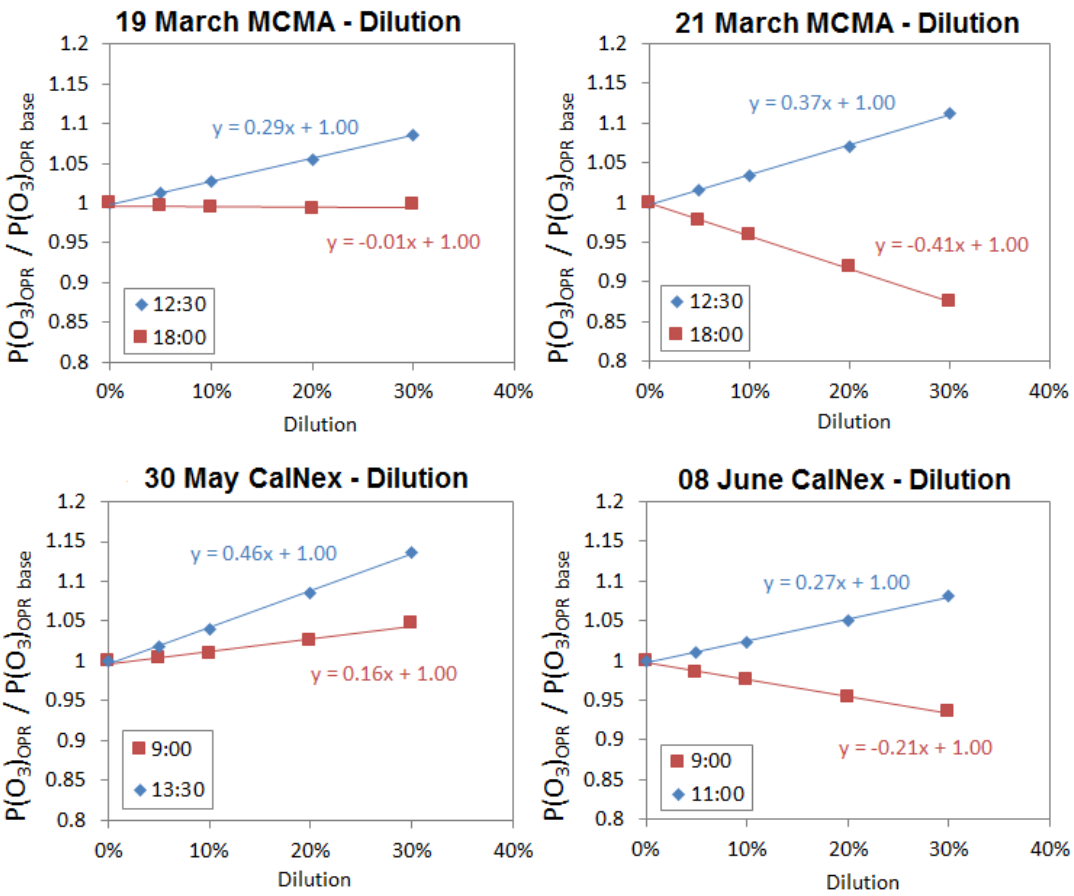

Figure 3.25: Impact of diluting ambient air on $P(O_3)$ measurements. $P(O_3)_{OPR}/P(O_3)_{OPR\ base}$ ratios are plotted as a function of the relative dilution for 2 different times of the day (see text).

Finally, the last test was performed to check whether reactions of OH with NO_z species (HONO, HO_2NO_2, NO_3, organic nitrates, HNO_3, PANs and unsaturated PANs) that produce O_x could impact the $P(O_3)$ measurements. The NO_2 and NO_3 products of these reactions were removed from the chemical mechanism to test whether the model output is significantly different that of the base simulation. The results showed that this O_x production can lead to an overestimation of 3% at most, for all examined days.

3.6 Conclusions on the accuracy of $P(O_3)$ measurements

In this chapter, we conducted an extensive modeling exercise to investigate the reliability of $P(O_3)$ measurements in moderately and heavily polluted urban areas. The modeling was performed using field data from 2 different campaigns, the Mexico City Metropolitan Area (2006) and the California Nexus (2010) field campaigns. We first investigated whether the assumptions made to demonstrate the principle of OPR measurements are valid, i.e. (i) $P(O_3)$ in the ambient flow tube is similar to $P(O_3)$ in the atmosphere and (ii) no significant production of ozone occurs in the reference flow tube. We then investigated how field operating conditions could impact $P(O_3)$ measurements, the idea being to estimate the accuracy of the measurements.

The modeling has shown that $P(O_3)$ is indeed similar between the atmosphere and the ambient flow tube, but that a significant amount of O_x can be produced in the reference flow tube (approximately 15% of the ambient $P(O_3)$). This is one of the main sources of errors in the OPR technique. The production of O_x in the reference flow tube is mainly caused radicals formed through O_3-alkene reactions. This artifact can lead to a 10-20% underestimation of ambient $P(O_3)$ for the conditions observed during the MCMA-2006 and the CalNex-2010 field campaigns.

The conversion efficiency of the NO_2-to-O_3 and O_3-to-NO_2 converters were also found to cause significant errors on the $P(O_3)$ measurements. With the NO_2-to-O_3 converter, the conversion efficiency of 75% achieved experimentally would lead to an overestimation of the $P(O_3)$ measurements by 10 – 200%. The O_3-to-NO_2 conversion was found to cause higher errors at the same conversion efficiency of 75%, with an underestimation of the measurements on the order of 35-225%. However, an O_3-to-NO_2 conversion efficiency of 99.9% was achieved experimentally for the OPR instrument. This level of conversion leads a negligible bias in the $P(O_3)$ measurements and the OPR instrument built in this study is therefore not affected by an O_x conversion issue.

Additional sources of error associated to the flow tubes come from a 5% dark ozone loss, a 3% NO_2 loss, a 60 ppbv/h HONO production in the ambient flow tube, the dilution by 10% of ambient air, a 5% temperature increase in the reference flow tube, and O_x production from reactions of OH with NO_z species. In addition to these errors, there is also a statistical uncertainty on the residence time in the flow tubes, which was quantified experimentally at ±4.9% (section 2.3.1.1).

Upper limits of errors associated to each factor impacting $P(O_3)$ measurements are reported in Table 3.9, with a direct sum of the negative or positive bias, calculated by grouping together the negative or positive errors, respectively.

Table 3.9: Sources of errors and their contribution to a systematic error on $P(O_3)$ measurements.

Error sources	Lab tests	Negative bias (upper limit)	Positive bias (upper limit)
Residence time (s)	271 ± 13	-4.9%	+4.9%
$P(O_x)$ in reference flow tube	20%	-20%	
O_3 loss	5%	-25%	
NO_2 loss	2%		+15%
HONO production	1%		+30%
Dilution of sampled air	10%	-3%	+4%
Temperature increase in ref. flow tube	5%	-5%	
O_x production from $OH+NO_z$			+3%
Sum of errors		-58%	+57%

The total accuracy of $P(O_3)$ measurements is estimated to be between -58% and +57%, with these numbers representing upper limits. These errors will always depend on the atmospheric composition of the sampled air mass and indeed, the positive errors will cancel out to some extent with the negative errors. Their combination should lead to a lower absolute value for the systematic error.

The estimation of the total accuracy is based on ambient conditions observed in two different environments, with different air compositions for 4 different days. Therefore, it is safe to assume that similar uncertainty values would be observed in other urban environments. However, the impact of each separate source of errors can significantly vary depending on the chemical composition of the sampled air mass, as seen from 08 June 2010. For this reason, it will be necessary to perform a similar analysis for each environment where the OPR instrument is deployed in the future.

Chapter 4. IRRONIC field campaign

4.1 Introduction

This chapter describes the field deployment of the OPR instrument during the Indiana Radical, Reactivity and Ozone Production Intercomparison (IRRONIC) field campaign. The field testing of the instrument showed that losses of O_3 in the flow tubes are an issue for field measurements, and this chapter presents how surface reactions in the flow tubes affect the zero of the instrument. A strategy is proposed to derive the sensitivity of O_3 formation to NO_x, accounting for artifacts generated by these surface reactions. This strategy implies to model the chemistry occurring inside the flow tubes including the surface reactions to infer ozone production rates. In the end of this chapter, the results from the IRRONIC campaign are compared to results observed during other campaigns.

4.2 Overview of the field campaign

The Indiana Radical, Reactivity and Ozone Production Intercomparison (IRRONIC) took place in Bloomington, Indiana, during summer 2015 during 1– 31 July. This was a joint project involving Indiana University, University of Massachusets, Mines Douai, Yale University, University of Houston and University of Montana. The goals of the study included: (a) an informal intercomparison of peroxy radical measurements by two different techniques, (b) a comparison of total OH radical reactivity measurements to values calculated from measured trace gases, (c) a comparison of measured OH, HO_2, RO_2 radicals, and ozone production rates with model predictions, and (d) an analysis of ozone production sensitivity at this site.

4.2.1 Description of the field site

The measurements were taken at the Indiana University Research and Teaching Preserve (IURTP) field laboratory (39.1908N, 86.502W), located 2.5 km east from the Bloomington University Campus. A map is shown in Fig. 4.1.

Figure 4.1: Location of the IRRONIC measuring site (red circle), northeast of Bloomington, IN (maps.google.com)

This site is located 3.5 km from the city center. Bloomington is the seventh largest city in Indiana, located 75 km southwest of Indianapolis, and has a population of 80,405 inhabitants according to the 2010 census. A highway (E Matlock Rd 45) is located 1 km from the site, and therefore the site can be impacted by anthropogenic emissions. The measurement facility was located within a mixed deciduous forest containing northern red oaks and big-tooth aspens, which are known to be strong emitters of isoprene and monoterpenes (Isebrands et al., 1999;Funk et al., 2005).

The instruments and the sampling lines were located at the northwest side of the IURTP laboratory. Two scaffolding towers were used on the side of the building (Fig. 4.2) to expose the instruments to the sunlight for the entire day. The OPR instrument was placed on one of the scaffolding towers as shown in Fig. 4.2.

Figure 4.2: The IURTP field laboratory (left) and the OPR instrument during the IRRONIC field campaign (right)

4.2.2 Description of the collocated measurements

The OPR instrument was deployed in the field from 25 June to 06 August 2006. Collocated measurements during IRRONIC included OH, HO_2*, total peroxy radicals (HO_2+RO_2), total OH radical reactivity, NO, NO_2, O_3, anthropogenic and biogenic VOCs, radiation and meteorological data.

OH radicals were measured with the Indiana University Laser - Induced Fluorescence with Fluorescence Assay by Gas Expansion (IU-FAGE) instrument (Lew et al., 2015;Dusanter et al., 2009a). HO_2* (HO_2+ αRO_2, section 1.3.1.1) radicals were measured with the same instrument, by chemical conversion to OH by reacting HO_2 with NO in the sampling inlet. Total OH reactivity was measured using the Indiana University - Total OH Loss Measurement (IU-TOHLM) instrument coupling a turbulent flow reactor with the LIF-FAGE detection technique (Sigler et al., 2015;Hansen et al., 2014). Measurements of HONO were made using the Laser Photofragmentation/Laser-induced Fluorescence (LP/LIF) instrument from Indiana University (Bottorff et al., 2015).

Total peroxy radicals (HO_2+RO_2) were measured using the UMASS Chemical Amplification – Cavity Attenuated Phase Shift Spectroscopy (CA-CAPS) instrument (Wood and Charest, 2014). The instrument employed a new chemical amplification scheme using ethane (instead of CO) and NO, while cavity attenuated phase-shift (CAPS) spectroscopy was used to detect the NO_2 amplification product.

Nonmethane hydrocarbons, including C2-C10 alkanes and alkenes, butadiene, aromatic compounds, isoprene, α- and β-pinene were measured by Mines Douai using an online TD-GC/FID at a time resolution of 1.5-h. Oxygenated VOCs, including acetone, acetaldehyde, ethanol and isopropanol were also measured by TD-GC/FID-MS at the same time resolution. Details about these instruments, including operating conditions, can be found elsewhere (Badol et al., 2004;Roukos et al., 2009).

Offline sampling was also performed by Mines Douai, focusing on measurements of oxygenated VOCs, including formaldehyde and C2-C6 aldehydes, acetone, methylethylketone (MEK), glyoxal and methylglyoxal, using DiNitroPhenylHydrazine (DNPH) cartridges (Waters Sep-Pak) and chemical desorption/HPLC-UV analysis (Waters 2695). C6-C16 VOCs including α- and β-pinene, limonene, camphene, heptane-hexadecane, methylpentene-pentadecene were measured using Sorbent cartridges (Carbopack B/Carbopack C) and thermo-desorption/GC-MS analysis (GC/ATD 650 Perkin Elmer).

Additionally, offline sampling performed by Yale University also took place to characterize un-oxidized biogenic and anthropogenic hydrocarbons from C6 to C25 by carbon number and chemical class (e.g. alkane, cyclic alkane, monoterpene, sesquiterpene, aromatic, PAH), with isomer-level resolution as appropriate, and their first and second generation oxidation products. These organic compounds were collected on multi-bed adsorbent traps and analyzed via thermal desorption with tandem MS (Q-TOF) aided by gas chromatographic

separation. These measurements were not available at the time the manuscript was written and are not included in this chapter.

Measurements of NO (chemiluminescence, Thermo model 42i-TL), NO_2 (cavity attenuated phase shift spectroscopy, Aerodyne Research), and ozone (UV absorption, API model 400A) were also conducted. Measurements of $J(NO_2)$ were performed using a scanning actinic flux spectroradiometer (SAFS, METCON) by the University of Houston. Finally, meteorological data, including temperature, relative humidity, wind speed and wind direction were measured with a meteorological station from Montana University.

These measurements are summarized in Table 4.1 and a list of the measured VOCs is given in Table 4.2.

Table 4.1: Summary of measurements performed during the IRRONIC field campaign

Species	Technique	Time resolution / LoD	Institution
OH, HO2*	Indiana University Laser - Induced Fluorescence with Fluorescence Assay by Gas Expansion (IU-FAGE)	OH: 15-min / 2×10^5 cm^{-3} (1σ) HO_2: 30-s / 2×10^6 cm^{-3} (1σ)	Indiana University
OH reactivity	Indiana University - Total OH Loss Measurement (IU-TOHLM)	10-min / 0.7 s^{-1} (1σ)	Indiana University
HONO	Laser Photofragmentation/Laser-induced Fluorescence (LP/LIF)	30-min / 18 pptv (1σ)	Indiana University
HO_2+ RO_2	Chemical Amplification – Cavity Attenuated Phase Shift Spectroscopy (CA-CAPS)	1-min / 0.6 pptv (2σ)	University of Massachusets
NMHCs	Online TD-GC/FID	1.5-h / 10–20 pptv (3σ)	Mines Douai
OVOCs	Online TD-GC/FID-MS	1.5-h / 80-140 pptv (3σ)	Mines Douai
OVOCs	Offline DinitroPhenylHydrazine (DNPH) cartridges HPLC-UV analysis	3-h / 20 pptv (3σ)	Mines Douai
C6-C16	Offline Sorbent cartridges (Carbopack B/Carbopack C) GC-MS analysis	3-h / 2–10 pptv (3σ)	Mines Douai
C6 – C25	Adsorbent traps MS (Q-TOF) analysis	3-h / –	Yale University
NO	Chemiluminescence Thermo model 42i-TL	60-s / 50 pptv (1σ)	University of Massachusets
NO_2	Cavity Attenuated Phase Shift spectroscopy (CAPS) Aerodyne Research	10-s / 100 pptv (3σ)	University of Massachusets
O_3	UV absorption API model 400A	10-s / 400 pptv (2σ)	University of Massachusets
$J(NO_2)$	SAFS	1-min / –	University of Houston
Meteorological data	Campbell Scientific WINDSONIC4 Vaisala HMP45C	1-s / –	University of Montana

Table 4.2: VOC measurements performed during the IRRONIC field campaign

VOC type	Species	Min (pptv)	Max (pptv)	24-h average (pptv)	Method
NMHCs	Ethane	1066	18301	4171	online GC HCNM
	Propane	158	2785	827	online GC HCNM
	Butane	70	1485	433	online GC HCNM
	Isobutane	42	536	187	online GC HCNM
	Pentane	55	1478	298	online GC HCNM
	Isopentane	80	2090	410	online GC HCNM
	Neopentane	< LOD (LOD=20 ppt)	18	10	online GC HCNM
	2,2-Dimethylbutane	< LOD (LOD=10 ppt)	81	16	online GC HCNM
	Cyclopentane + 2,3-Dimethylbutane	< LOD (LOD=10 ppt)	136	19	online GC HCNM
	2-Methylpentane	< LOD (LOD=10 ppt)	385	80	online GC HCNM
	3-Methylpentane	< LOD (LOD=10 ppt)	174	39	online GC HCNM
	Hexane	< LOD (LOD=10 ppt)	207	53	online GC HCNM
	2,2-Dimethylpentane	< LOD (LOD=10 ppt)	6	5	online GC HCNM
	2,4-Dimethylpentane	< LOD (LOD=10 ppt)	85	23	online GC HCNM
	2,2,3-Trimethylbutane	< LOD (LOD=10 ppt)	11	5	online GC HCNM
	3,3-Dimethylpentane	< LOD (LOD=10 ppt)	13	5	online GC HCNM
	2,3-Dimethylpentane	< LOD (LOD=10 ppt)	25	6	online GC HCNM
	Cyclohexane	< LOD (LOD=10 ppt)	45	11	online GC HCNM
	2-Methylhexane	< LOD (LOD=10 ppt)	52	9	online GC HCNM
	Isooctane	< LOD (LOD=10 ppt)	47	15	online GC HCNM
	Heptane	< LOD (LOD=10 ppt)	71	14	online GC HCNM
	Octane	< LOD (LOD=10 ppt)	18	6	online GC HCNM
	Nonane	< LOD (LOD=10 ppt)	40	6	online GC HCNM
	Decane	< LOD (LOD=2 ppt)	10	4	Absorbent cartridges
	Alkane nC11	< LOD (LOD=10 ppt)	119	11	online GC HCNM
	Alkane nC12	< LOD (LOD=10 ppt)	52	6	online GC HCNM
	Alkane nC13	< LOD (LOD=2 ppt)	24	4	Absorbent cartridges
	Alkane nC14	< LOD (LOD=2 ppt)	57	6	Absorbent cartridges
	Alkane nC15	< LOD (LOD=2 ppt)	106	8	Absorbent cartridges
	Alkane nC16	< LOD (LOD=2 ppt)	79	11	Absorbent cartridges
	Ethylene	30	920	217	online GC HCNM
	Propene	< LOD (LOD=20 ppt)	404	30	online GC HCNM
	trans-2-Butene	< LOD (LOD=20 ppt)	103	27	online GC HCNM
	1-Butene	106	207	146	online GC HCNM
	Isobutene	156	375	243	online GC HCNM
	cis-2-Butene	< LOD (LOD=20 ppt)	86	14	online GC HCNM
	3-Methyl-1-butene	< LOD (LOD=20 ppt)	18	10	online GC HCNM
	trans-2-Pentene	< LOD (LOD=20 ppt)	82	17	online GC HCNM
	2-Methyl-2-butene	10	161	51	online GC HCNM
	1-pentene	< LOD (LOD=20 ppt)	55	15	online GC HCNM
	2-Methyl-1-butene	< LOD (LOD=20 ppt)	39	11	online GC HCNM
	cis-2-Pentene	< LOD (LOD=20 ppt)	40	12	online GC HCNM
	Hexene	< LOD (LOD=10 ppt)	27	10	online GC HCNM
	1,3-Butadiene	27	156	66	online GC HCNM
	3-Methyl-1,4-pentadiene	< LOD (LOD=10 ppt)	303	77	online GC HCNM
	Acetylene	27	658	218	online GC HCNM
	Propyne	18	102	50	online GC HCNM
	Butyne	< LOD (LOD=20 ppt)	51	16	online GC HCNM
	Benzene	12	204	79	online GC HCNM
	Toluene	75	535	157	online GC HCNM
	Chlorobenzene	< LOD (LOD=10 ppt)	21	5	online GC HCNM
	Ethylbenzene	< LOD (LOD=10 ppt)	62	10	online GC HCNM
	Styrene	< LOD (LOD=4 ppt)	18	5	Absorbent cartridges
	m + p-Xylene	5	215	33	online GC HCNM
	o-Xylene	< LOD (LOD=10 ppt)	80	16	online GC HCNM
	Isopropylbenzene	< LOD (LOD=10 ppt)	12	5	online GC HCNM
	n-Propylbenzene	< LOD (LOD=10 ppt)	27	5	online GC HCNM
	3-Ethyltoluene	< LOD (LOD=10 ppt)	107	8	online GC HCNM
	4-Ethyltoluene	< LOD (LOD=10 ppt)	48	5	online GC HCNM
	1,3,5-Trimethylbenzene	< LOD (LOD=10 ppt)	103	19	online GC HCNM
	2-Ethyltoluene	< LOD (LOD=10 ppt)	65	23	online GC HCNM
	1,2,4-Trimethylbenzene	< LOD (LOD=4 ppt)	100	14	Absorbent cartridges
	1,2,3-Trimethylbenzene	< LOD (LOD=4 ppt)	34	5	Absorbent cartridges
	n-Butylbenzene	5	75	38	online GC HCNM
BVOCs	Isoprene	15	11133	2490	online GC HCNM
	α-Pinene	< LOD (LOD=10 ppt)	153	51	online GC OVOC
	β-Pinene	9	231	41	Absorbent cartridges
	α-Terpinene	< LOD (LOD=2 ppt)	8	1	Absorbent cartridges
	Limonene	12	114	35	Absorbent cartridges
	α-Ocimene	< LOD (LOD=2 ppt)	13	3	Absorbent cartridges
	γ-terpinene	< LOD (LOD=2 ppt)	7	2	Absorbent cartridges
	Terpinolene	< LOD (LOD=2 ppt)	9	2	Absorbent cartridges
	Camphene	< LOD (LOD=6 ppt)	65	15	Absorbent cartridges
	Myrcene	2	5	2	Absorbent cartridges
	Borneol	< LOD (LOD=2 ppt)	137	8	Absorbent cartridges
	Camphor	< LOD (LOD=2 ppt)	137	7	Absorbent cartridges
	3-Carene	5	209	20	online GC OVOC
	Cumene	< LOD (LOD=2 ppt)	8	2	Absorbent cartridges
OVOCs	Formaldehyde	273	5164	1897	DNPH cartridges
	Acetaldehyde	32	1573	674	DNPH cartridges
	Propanal	< LOD (LOD = 20 ppt)			DNPH cartridges
	Butanal	< LOD (LOD = 20 ppt)			DNPH cartridges
	Isobutanal	< LOD (LOD = 20 ppt)			DNPH cartridges
	isopentanal	< LOD (LOD = 20 ppt)			DNPH cartridges
	Pentanal	< LOD (LOD = 20 ppt)			DNPH cartridges
	Hexanal	< LOD (LOD=8 ppt)	213	23	Absorbent cartridges
	Heptanal	2	86	33	Absorbent cartridges
	Octanal	2	69	21	Absorbent cartridges
	Nonanal	5	179	44	Absorbent cartridges
	Decanal	2	106	21	Absorbent cartridges
	Undecanal	1	35	7	Absorbent cartridges
	Benzaldehyde	< LOD (LOD=4 ppt)			Absorbent cartridges
	o-Tolualdehyde	< LOD (LOD = 20 ppt)			DNPH cartridges
	m + p-Tolualdehyde	< LOD (LOD = 20 ppt)			DNPH cartridges
	Propenal	< LOD (LOD = 20 ppt)			DNPH cartridges
	2-methylpropenal	< LOD (LOD = 20 ppt)			DNPH cartridges
	Butenal	< LOD (LOD = 20 ppt)			DNPH cartridges
	Glyoxal	< LOD (LOD = 20 ppt)			DNPH cartridges
	Methylglyoxal	< LOD (LOD = 20 ppt)			DNPH cartridges
	Acetone	261	3634	1354	DNPH cartridges
	2-Pentanone	48	573	225	online GC OVOC
	MEK	5	257	58	Absorbent cartridges
	MVK	< LOD (LOD=10 ppt)	192	27	Absorbent cartridges
	Nopinone	2	6	2	Absorbent cartridges
	Ethanol	1397	68480	8108	online GC OVOC
	Isopropanol	18	188	76	online GC OVOC

4.2.3 Chemical composition of air masses

Figures 4.3 and 4.4 show time series of temperature, relative humidity, NO_x, O_3, $J(NO_2)$, a few VOCs and OH reactivity for 16 days of the IRRONIC field campaign (10 July – 26 July), which is the period identified with less missing measurements. Figure 4.5 shows averaged diurnal profiles of these parameters. Isoprene was chosen as a tracer of BVOC emissions since the trees present on-site were mainly isoprene emitters. The other VOCs were chosen as tracers of anthropogenic emissions, with acetylene and aromatics being good tracers of vehicular emissions. Oxygenated VOCs are shown as tracers of the photochemical activity. While these VOCs can also be directly emitted by primary sources, a significant fraction of these compounds is usually due to the oxidation of primary VOCs.

Meteorological conditions varied widely from day to day, including cloudy rainy days (e.g. 10 July), storms (e.g.13 July), and sunny days (e.g. 22 July). Temperature varied from 14 to 34 ºC, showing a clear diurnal profile. On most days, the peak temperature was between 25 and 30 °C. Relative humidity was close to 90% during most nights, while it decreased to 55%-65% during the day. The relative humidity values hardly dropped below 50%, revealing a generally humid environment.

Anthropogenic VOCs were found to be at relatively low levels, indicating a small impact of human activities. Toluene and acetylene were lower than 500 pptv on most days and benzene was lower than 200 pptv, while in urban environments, acetylene and aromatics are usually observed at levels of 0.4 – 7 ppbv and 1 – 50 ppbv, respectively (Williams and Koppmann, 2007). On the other hand, high levels of biogenic VOCs were observed, with an isoprene peak exceeding 4 ppbv most of the days, and reaching levels of more than 10 ppbv near the end of the campaign (25 July).

Additionally, higher levels of oxygenated VOCs (formaldehyde, acetone, acetaldehyde) were observed during 17 – 19 July and 24 – 25 July compared to the other days of the campaign. This increase correlates with an increase in temperature, suggesting higher photochemical activity for these periods.

Interesting correlations between several species can be observed in the diurnal profiles shown in Fig. 4.5. Indeed, isoprene exhibits a clear diurnal profile well correlated with temperature and $J(NO_2)$, peaking in the afternoon, between 15:00 and 20:00, when temperatures are higher. Similarly, oxygenated VOCs and OH reactivity follow the changes in temperature and J-values. Regarding the anthropogenic VOCs and NO_x, a morning peak between 8:00 – 11:00 appears in the diurnal profile of NO, NO_2, toluene and acetylene. This observation indicates increased traffic emissions during these hours, but with a low impact on the measurement site.

OH reactivity data during IRRONIC were reported by Sigler et al. (2015). In general, the observed reactivity increased with increasing temperature and isoprene was the dominant contributor to the measured OH

reactivity. During daytime, from 11:00 to 17:00, approximately 70% of the total OH reactivity was due to isoprene. Contributions of other species were 8.2 % from aromatics, 6.4% from CO, 6.2 % from OVOCs, 4.2 % from alkanes/alkenes, 3.5 % from inorganic species and 0.7% from monoterpenes (Sigler et al., 2015). The measured and calculated OH reactivity were found to be within 20% of agreement (Sigler et al., 2015), indicating that the most important VOCs were measured during IRRONIC. The diurnally averaged OH reactivity peaked at approximately 14 s^{-1} during the day, while individual values higher than 30 s^{-1} were reported, especially when isoprene was high (> 6 ppbv).

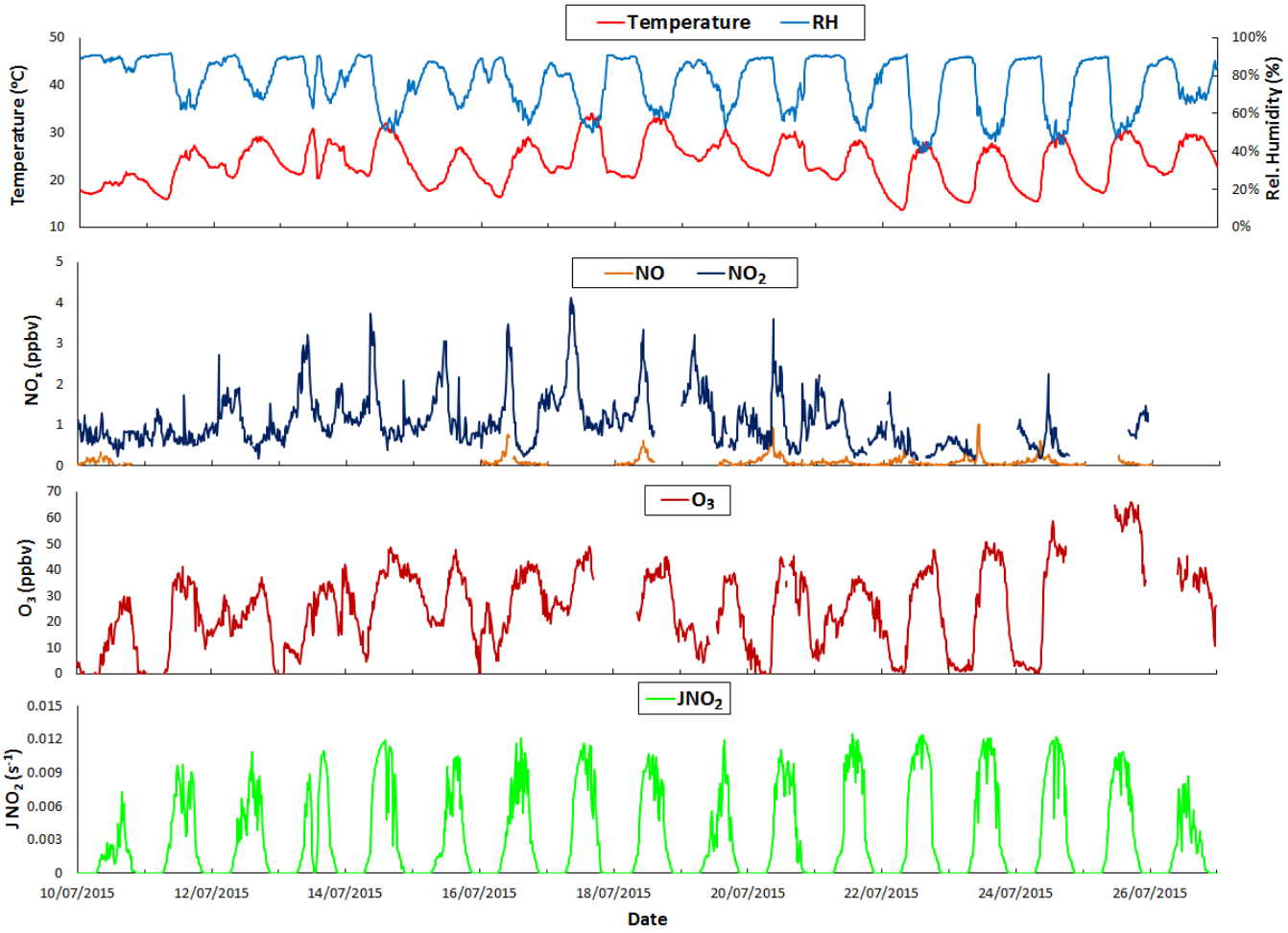

Figure 4.3: Time series of J(NO_2) values, O_3, NO_2, NO, temperature and relative humidity for the IRRONIC field campaign.

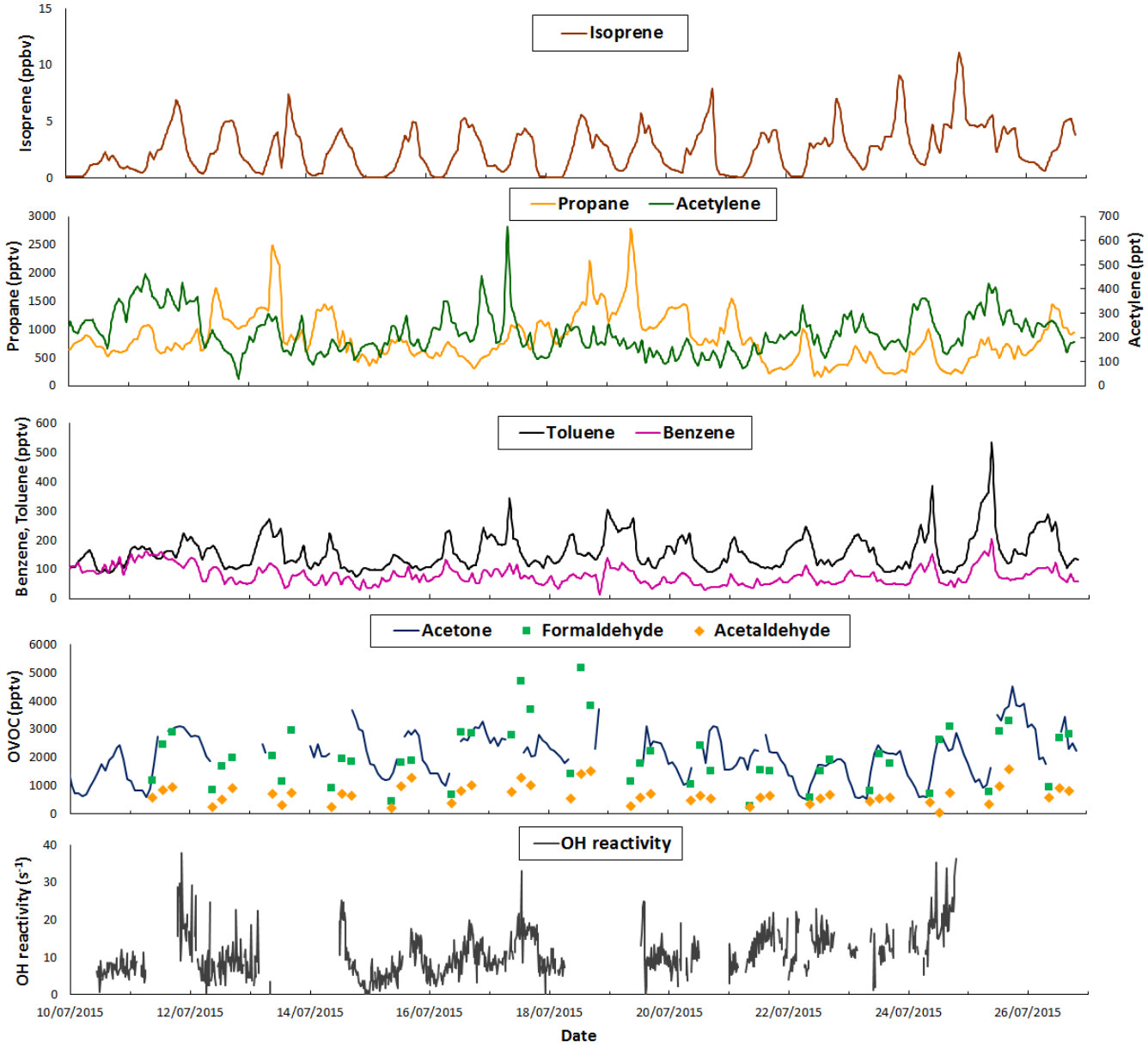

Figure 4.4: Time series of isoprene, propane, acetylene, toluene, benzene, formaldehyde, acetone, acetaldehyde and OH reactivity for the IRRONIC field campaign.

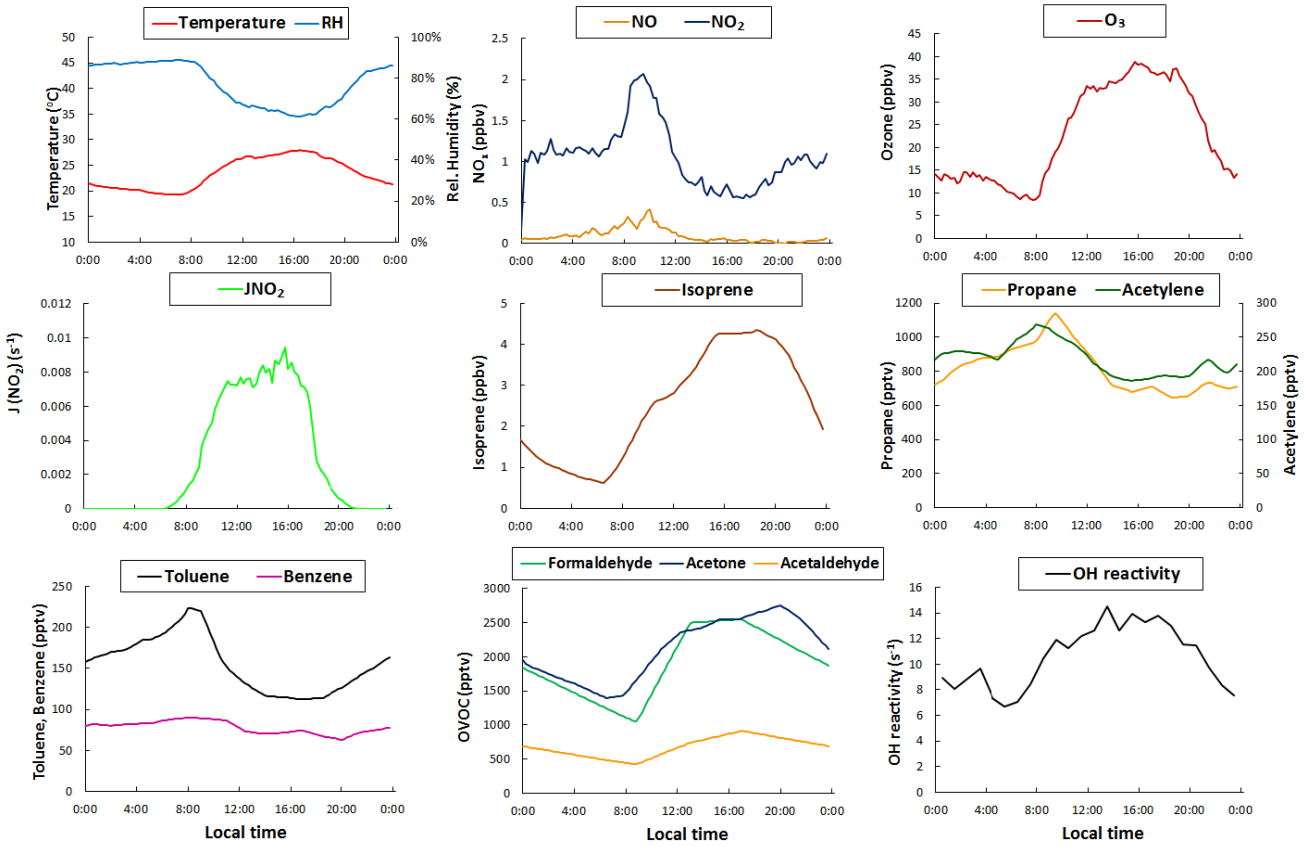

Figure 4.5: Diurnal mean values of several meteorological parameters and chemical species measured during the IRRONIC field campaign.

The low impact of anthropogenic emissions was confirmed by low levels of NO_x species (<5 ppbv). NO_2 was lower than 4 ppbv most of the days while NO hardly exceeded 1 ppbv. These observations are surprising since the site is located next to major traffic roads and the university campus. However, there is less traffic during the summer compared to the winter, when college students are in town, which could possibly explain the low measured NO_x. Additionally, as shown in Fig. 4.1, the east side of the site is free of major urban areas and air masses coming from this sector are relatively clean and not polluted by anthropogenic emissions. Figure 4.5 shows a wind rose diagram from the wind measurements during IRRONIC. Indeed, 100% of the wind measured on-site comes from north-east-south directions, with approximately 42% of the winds coming from the northeastern sector (NNE, NE, ENE). Additionally, wind speeds were very low, below 1 m/s at most cases. This analysis confirms the fact that the site is mainly affected by BVOC emissions, either emitted on-site or transferred by the north-eastern region.

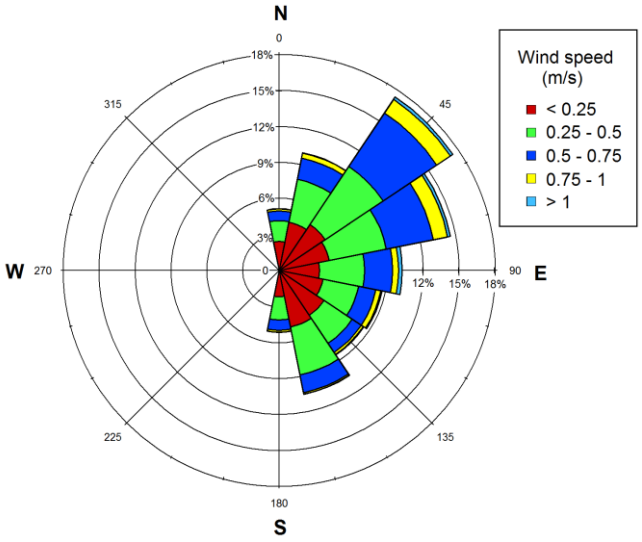

Figure 4.6: Wind speed and directions during the IRRONIC field campaign.

On the other hand, ozone mixing ratios ranged from 3 – 65 ppbv and did not exceed 60 ppbv on most days. Taking into account the low NO_x mixing ratios in this environment, simple calculations (Eq. 1.6, Chapter 1) based on measurements of HO_2+RO_2 (not shown) and NO showed that ambient $P(O_3)$ values were lower than 5 ppbv/h for most of the days and ozone was therefore mainly adverted to the site.

The observations discussed above indicate that the photochemistry in this environment was mainly driven by the oxidation of biogenic VOCs under low NO_x conditions, similar to that observed in other forested areas (Zannoni et al., 2016;Hens et al., 2014;Griffith et al., 2013). Biogenic VOCs such as isoprene are very reactive with the hydroxyl radical, leading to a large range of OH reactivity. The conjunction of the latter with low levels of NO_x makes this site of particular interest to study the sensitivity of ozone formation to NO_x by perturbing the sampled air masses through an addition of NO_x species, which is easily performed with the OPR instrument.

4.3 OPR measurements

4.3.1 Zeroing tests performed during the IRRONIC campaign

It should be reminded that the OPR instrument records ΔO_x values, which result as the O_x difference between the two flow tubes:

$$\Delta O_x = O_{x_{amb}} - O_{x_{ref}} \qquad \text{(Eq. 4.1)}$$

When there is no ozone production, the difference in O_x observed between the two flow tubes should be zero within the measurement precision. However, as highlighted in chapter 2, inhomogeneous losses of O_x

species on the walls of the flow tubes (both dark and photoenhanced losses) could lead to a measurement artifact. For ambient $P(O_3)$ measurements, zeroing the instrument is therefore necessary to record a reference value of ΔO_x, which may be used as a zero.

Theoretically, the zero of the OPR instrument could be recorded when the two flow tubes are operated under the same conditions: either both flow tubes covered by the UV filter or both flow tubes equally exposed to sunlight. These tests were mainly performed during the first 7 days of the field deployment of the instrument (28 June – 4 July) and one of them were selected to be presented below.

Figure 4.7 shows a test performed on 04 July, zeroing the instrument by covering both flow tubes with a UV filter. The two flow tubes are covered by the UV filter to record a "zero" during one hour, then the ambient flow tube is exposed to the light for another hour to perform $P(O_3)$ measurements. The blue and orange lines display the "zero" and ozone production measurement, respectively. $J(NO_2)$ is also shown as a green line.

During nighttime, the flow tubes were covered by a plastic tarp to protect them from possible rain or water condensation. On this day, the tarp was removed at 7:45 am. A close inspection of this figure shows that ΔO_x slowly decreases during the "$P(O_3)$ measurement" period, while ΔO_x slowly increases during the "zero" period. These slow changes in ΔO_x were observed on other days when the same test was repeated, and is in the order of 1.5 ppbv, which would translate into negative values of ozone production since ΔO_x is lower for the $P(O_3)$ measurement configuration.

Since the reference flow tube is always covered by the UV filter, processes occurring in the ambient tube drive the change in ΔO_x. Figure 4.7 shows that, while exposed to the light, O_x in the ambient flow tube decreases, causing a decrease in ΔO_x. This observation is in agreement with the photoenhanced O_3 loss previously observed in this flow tube (section 2.3.1.2). It is interesting to note, however, that even when both flow tubes are covered by the UV filter and are operated under the same conditions, one hour is not enough to bring the ΔO_x level at zero, as they were during nighttime.

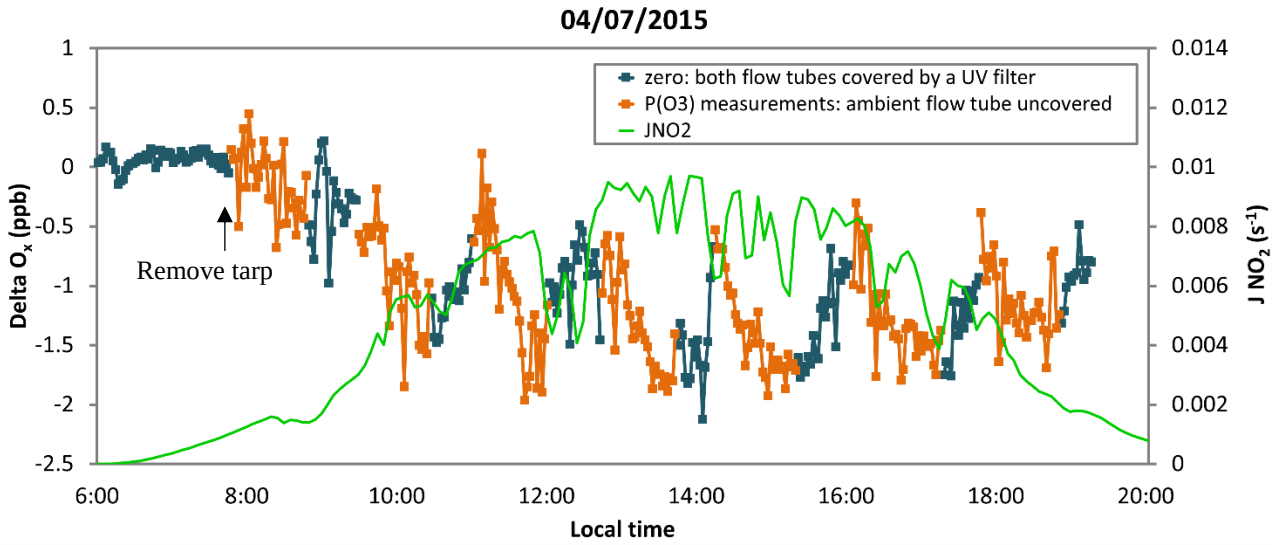

Figure 4.7: Zeroing test of the OPR instrument on 4 July 2015. ΔO_x signal observed when both flow tubes are covered by the UV filter (blue line) and when the ambient flow tube is uncovered (orange line). The green line shows $J(NO_2)$.

As a result, this method is not suitable to zero the instrument, as the change in the radiation conditions leads to a change in surface-O_3 losses for the ambient flow tube. Zeroing tests performed by exposing both flow tubes equally to sunlight showed similar artifacts, which are caused by disturbing the O_3 loss rate in the flow tubes when the light conditions change.

These results indicate that photoenhanced processes taking place in the flow tubes have a very strong impact on the ΔO_x measurements and there is clearly a need to thoroughly investigate the physicochemical processes taking place in the flow tubes to improve the reliability of $P(O_3)$ measurements with this instrument. For this version of the OPR instrument, we cannot perform reliable zeros and this prevent its use for ambient $P(O_3)$ measurements. For this reason, the OPR measurements were focused on investigating the sensitivity of $P(O_3)$ to NO, where zeroing the instrument is not necessary (see below).

4.3.2 Methodology designed for investigating the sensitivity of $P(O_3)$ to NO

Investigating the sensitivity of $P(O_3)$ to NO requires to disturb the air sample by adding NO inside the OPR instrument. This was achieved by introducing a certain mixing ratio of NO (3-170 ppbv) inside the OPR sampling line for 40 minutes, and then stopping the NO addition for another 40 minutes. This pattern was repeated continuously, keeping the NO mixing ratio constant for several days. For each measurement step, the OPR instrument was run in the "$P(O_3)$ measurement" mode, i.e. the ambient flow tube was exposed to sunlight and the reference flow tube was covered with the UV filter. This methodology ensured that the irradiation in each flow tube was not disturbed, which in turn should ensure that O_3–surface losses do not change.

The measurements of ΔO_x performed without NO addition was considered a representative of ambient $P(O_3)$, although it was not possible to extract ambient $P(O_3)$ values since the measured ΔO_x is a combination of ambient ozone production and surface-losses in the ambient flow tube. This measurement is referred as "baseline" and is denoted ΔO_x^{zero} in the following. The ΔO_x measurement performed with addition of NO is assumed to deviate from ΔO_x^{zero} due to a change in ozone production in the ambient flow tube, while the surface loss of ozone is assumed to be unchanged. This measurement step is referred as "NO addition" and is denoted ΔO_x^{NO}. The difference between ΔO_x^{zero} and ΔO_x^{NO} should therefore provide a quantification of the change in $P(O_3)$ due to the addition of NO. The validity of assuming that the O_3 loss is not disturbed by the addition of NO is discussed in section 4.4.3.

A schematic of how NO is added into the OPR instrument is shown in Fig. 4.8. The addition was made using a NO cylinder (3.75 ppmv in N_2) and a mass flow controller to regulate flow rates ranging from 4 to 90 SCCM. In total, 6 different mixing ratios of NO were used: 3.3, 6.0, 13.5, 29.5, 77.6 and 167.1 ppbv. The NO addition was performed through a 1/8"-OD stainless steel tube into a 1/2"-OD Teflon line. The later was used as a sampling line. After the connection point, a length of 10 m of 1/2"-OD Teflon tube was used to ensure a good mixing of NO with the sampled air, leading to a residence time of approximately 10 s in the line at a total flow rate of 4 L/min.

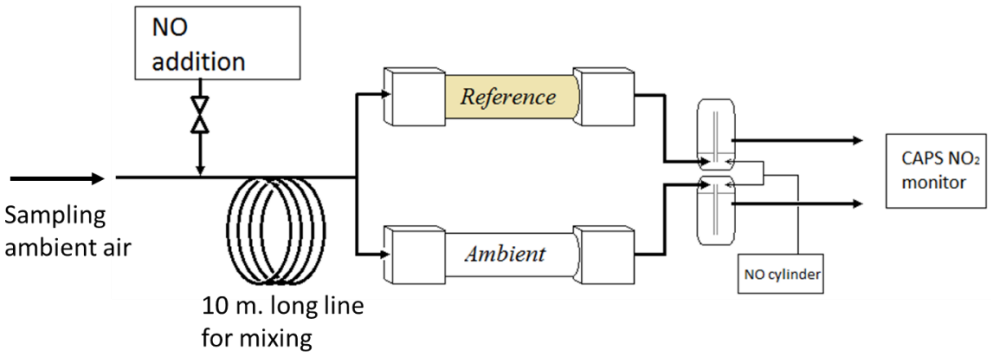

Figure 4.8: Schematic of the sampling setup of the OPR instrument during the IRRONIC campaign

The first 20 minutes of each 40-minutes ΔO_x^{zero} and ΔO_x^{NO} measurements were removed since they correspond to a transient regime between the two measurements due to the long residence time of air in the flow tubes. As mentioned above, the change in $P(O_3)$ due to the addition of NO was calculated by subtracting the differential O_x measurement observed without NO addition (ΔO_x^{zero}) from the differential O_x measurement observed during the NO addition (ΔO_x^{NO}). The change in $P(O_3)$, defined as ozone sensitivity and denoted OS in the following, resulted from Eq. 4.2, where τ is the residence time in the flow tubes (271 s, section 2.3.1.1).

$$OS = \frac{\Delta O_x{}^{NO} - \Delta O_x{}^{zero}}{\tau} \quad \text{(Eq. 4.2)}$$

It should be reminded here that the solenoid valves before the CAPS monitor alternate the sampling between the two flow tubes every minute, so each ΔO_x measurement is a 2-min data point. In order to apply Eq. 4.2, the $\Delta O_x{}^{zero}$ value was interpolated during a NO addition step from the two surrounding $\Delta O_x{}^{zero}$ measurements, and the interpolated value was subtracted from $\Delta O_x{}^{NO}$. This method led to ten 2-min $P(O_3)$ data points, for a duration of 20 min, with a gap of 60 min between each OP measurement. The 20-min period can be further averaged resulting into one OS value every 80 minutes.

4.3.3 Limits of detection

The detection limit for OS measurements was quantified from the scattering of nighttime values. Figure 4.9 shows nighttime OS measurements from 5 July until 25 July. The time window that corresponds to nighttime measurements is from 22:00 to 05:00. Figure 4.9 displays 2-min OS measurements (pink circles), as well as averaged single-night OS values (red diamonds). Error bars correspond to 3-σ of the single-night scattering.

The limit of detection for this instrument and the selected methodology is calculated as 3 times the standard deviation (3σ) of the scattered OS measurements. It is interesting to note that the standard deviation can change from day to day. Lower limits of 3σ are 2.5 ppbv/h (10 July), while upper limits reach 10 ppbv/h (6, 12, 14 and 15 July). An average of the observed scatter indicated a detection limit of 6.2 ppbv/h for the OPR instrument.

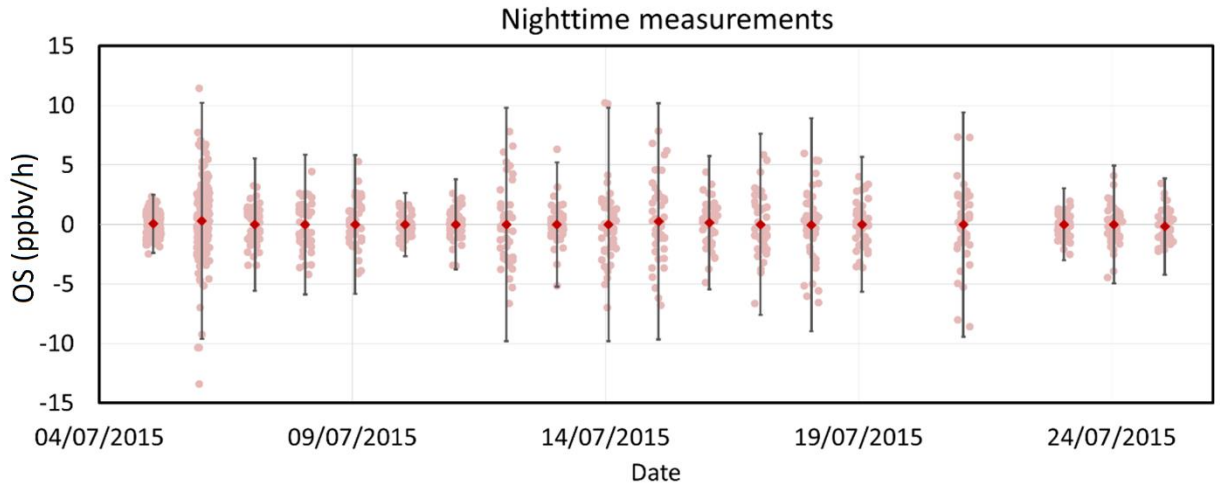

Figure 4.9: Nighttime OS measurements for the quantification of the OPR detection limit. Pink circles are 2-min OS measurements and dark red diamonds are OS values averaged over one night. Error bars represent 3σ of the measurement scatter for each night.

It is interesting to note that the OS values are equal to zero during nighttime, while, as will be shown in the next section, $\Delta O_x{}^{NO}$ and $\Delta O_x{}^{zero}$ can systematically deviate from zero during nighttime, due to different O_x losses in the two flow tubes. Finally, it is important to note that the limit of detection identified here for the complete OPR sequence is much higher than the limit of detection calculated from the CAPS monitor in section 2.3.3.2 (0.64 ppbv/h). This is due to the fact that the scatter in the final OS measurements does not only depend on the precision of the CAPS monitor, but also depends on how fast each flow tube responds to variations of O_x, and could also be linked to possible changes in temperature of humidity that can affect the O_x losses in the flow tubes.

4.3.4 Field results

Measurements of ozone sensitivity made with the methodology described in section 4.3.2 were performed for 19 days (05-18 July, 21 July, 23-25 July). Additional field testing was performed during 15 more days (O_3 and NO_2 loss tests presented in chapter 2, conversion efficiency tests also presented in chapter 2, and zeroing tests presented in section 4.3.1).

Figure 4.10 shows how $\Delta O_x{}^{zero}$ and $\Delta O_x{}^{NO}$ change from 9 July to 26 July 2015, along with the different NO addition steps (colored bars at the top of the figure). Time series of ambient O_3, NO_2, relative and absolute humidity, temperature, and $J(NO_2)$ are also displayed for this period.

This figure shows that $\Delta O_x{}^{zero}$ is scattered around zero during nighttime, with measured values usually lower than 0.4 ppbv (equivalent to 5.8 ppbv/h of ozone production), showing no systematic deviations from zero. However, the baseline described by $\Delta O_x{}^{zero}$ exhibits systematic negative values during the day. On most of these days, $\Delta O_x{}^{zero}$ ranges between -2 and -4 ppbv during daytime, with the lowest values at approximately -5 ppbv (e.g. 25 July).

A negative $\Delta O_x{}^{zero}$ value indicates that the O_x mixing ratio is higher in the reference flow tube compared to the ambient flow tube. As explained for the zero tests in sections 4.3.1 and 2.3.1.2, a significant photoenhanced ozone loss was found to take place in the ambient flow tube under the presence of sunlight. The negative values of ΔOx^{zero} observed all along the campaign are consistent with this photoenhanced loss, which is well correlated with $J(NO_2)$. It is interesting to note that for ambient O_3 mixing ratios close to 50 ppbv, values that were often measured during the IRRONIC campaign, a $\Delta O_x{}^{zero}$ of -3 ppbv would correspond to a 6% difference in the losses between the flow tubes, which is consistent with the range of photoenhanced losses observed during characterization experiments discussed in chapter 2 (Figs. 2.18-2.20).

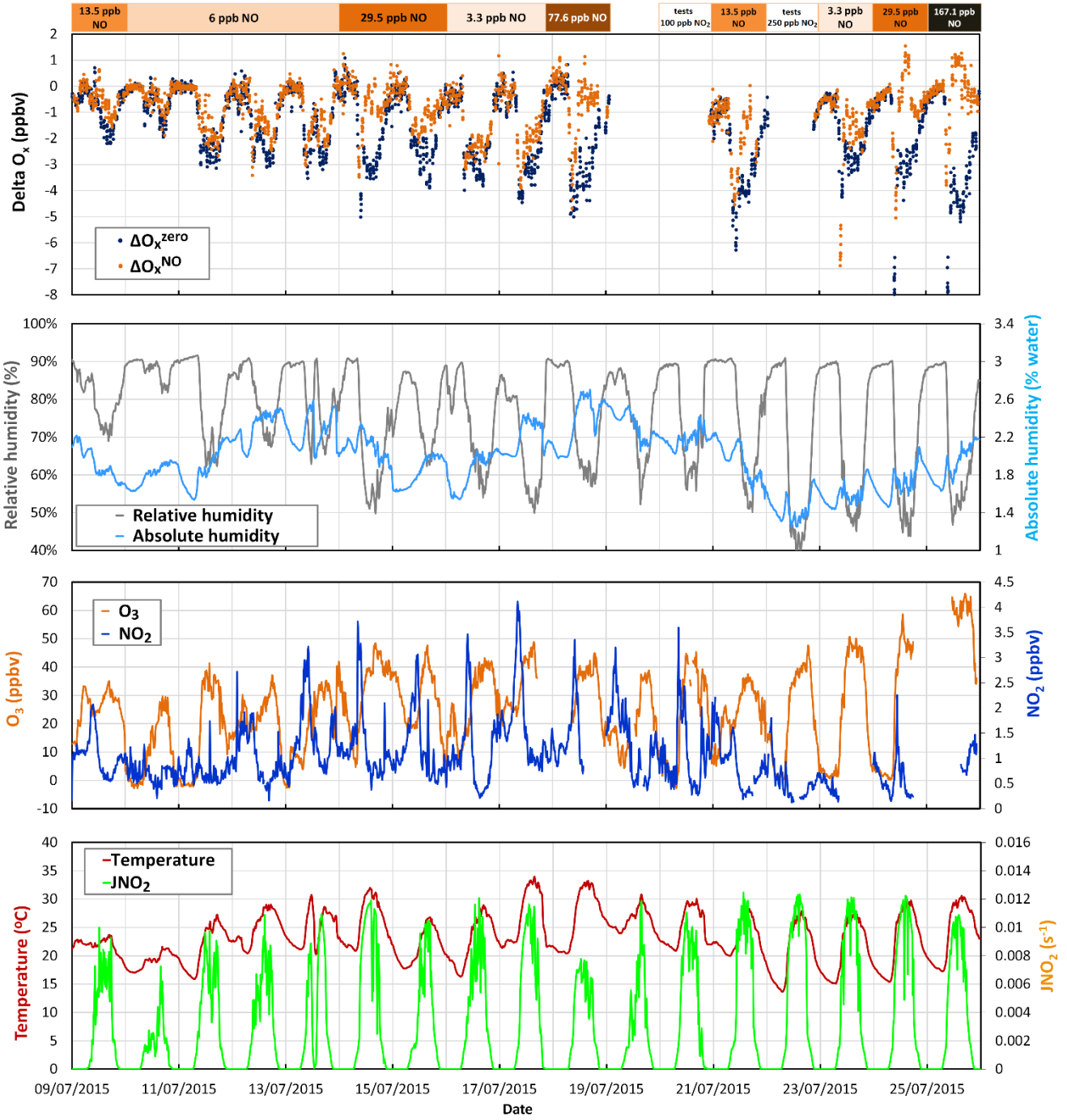

Figure 4.10: Time series of measured ΔO_x^{zero} and ΔO_x^{NO}, relative and absolute humidity, O_3, NO_2, temperature and $J(NO_2)$ during the IRRONIC field campaign.

The photoenhanced ozone loss, as shown in the characterization section 2.3.1.2, depends on several factors:

a) Solar irradiation: As mentioned above, the negative ΔO_x^{zero} shown in Fig. 4.10 seems well correlated with $J(NO_2)$ during the 14 days of measurements. For example, ΔO_x^{zero} is on the order of -1 ppbv during

low-J(NO_2) days such as 10 July, while it is on the order -3 ppbv during high-J(NO_2) days such as 14 July.

b) Ozone mixing ratio: For a constant relative difference in O_3 losses between the two flow tubes, the absolute value of ΔO_x^{zero} increases with the ozone mixing ratio. For example, J values were similar on 16 July and 25 July, but O_3 mixing ratios were higher on 25 July by about 35% (80 ppbv vs 50 ppbv). A close look at these days in Fig. 4.10 indicates that there is also an approximate 35% difference in ΔO_x^{zero} between these two days (-4.5 vs -3 ppbv).

c) Absolute humidity: the dependence on absolute humidity was shown during the characterization experiments described in section 2.3.1.2. For example, 16 July and 18 July are two days with similar O_3 mixing ratios and J(NO_2) values that are only slightly different. However, the absolute humidity is higher by a factor 1.5 on 18 July. Fig. 4.10 shows that ΔO_x^{zero} is more negative on the high humidity day, indicating enhanced ozone losses.

It is interesting to note that a ΔO_x^{zero} value of 1 ppbv is equivalent to 13.3 ppbv/h of ozone production. Therefore, a ΔO_x^{zero} value of -3 ppbv would correspond to an ozone loss rate of 40 ppbv/h. Additionally, there is a large negative spike in ΔO_x^{zero} on most days, which can reach -8 ppbv during the last days of the campaign. This behavior is thought to come from higher ozone losses in the ambient flow tube during sunrise, when the first photons reach the flow tubes, and under the presence of early morning water condensation, which can drive additional heterogeneous chemistry involving ozone.

Regarding the measurement of ΔO_x^{NO}, when NO was added in the sampling line, it can be seen that ΔO_x^{NO} is similar to ΔO_x^{zero} during nighttime, indicating that the addition of NO under dark conditions has no impact on the O_x measurement. Indeed, adding NO under dark conditions only converts O_3 into NO_2 and therefore the amount of O_x does not change. Even for the last day, where 167 ppbv of NO were added in the flow tubes, there is no significant difference between ΔO_x^{NO} and ΔO_x^{zero} during nighttime.

During daytime, ΔO_x^{NO} is greater than ΔO_x^{zero}, which may indicate additional ozone production when NO is added. The difference between ΔO_x^{NO} and ΔO_x^{zero}, divided by the residence time τ of 271 s as shown in Eq. 4.2, yields the measured ozone sensitivity (OS_{meas}). These results are shown in Fig. 4.11, along with the different NO addition steps. The 2-min OS_{meas} data points are displayed by pink circles and the 20-min averaged values by red diamonds. J(NO_2) values are also displayed in green for this period.

During nighttime, the measurements are scattered around zero, with values usually below ±5 ppbv/h. During daytime, there is a clear diurnal profile, while during the early morning, there are occasional positive or negative spikes, which are the result of the sudden negative drop observed in the ΔO_x^{zero} measurements as discussed above.

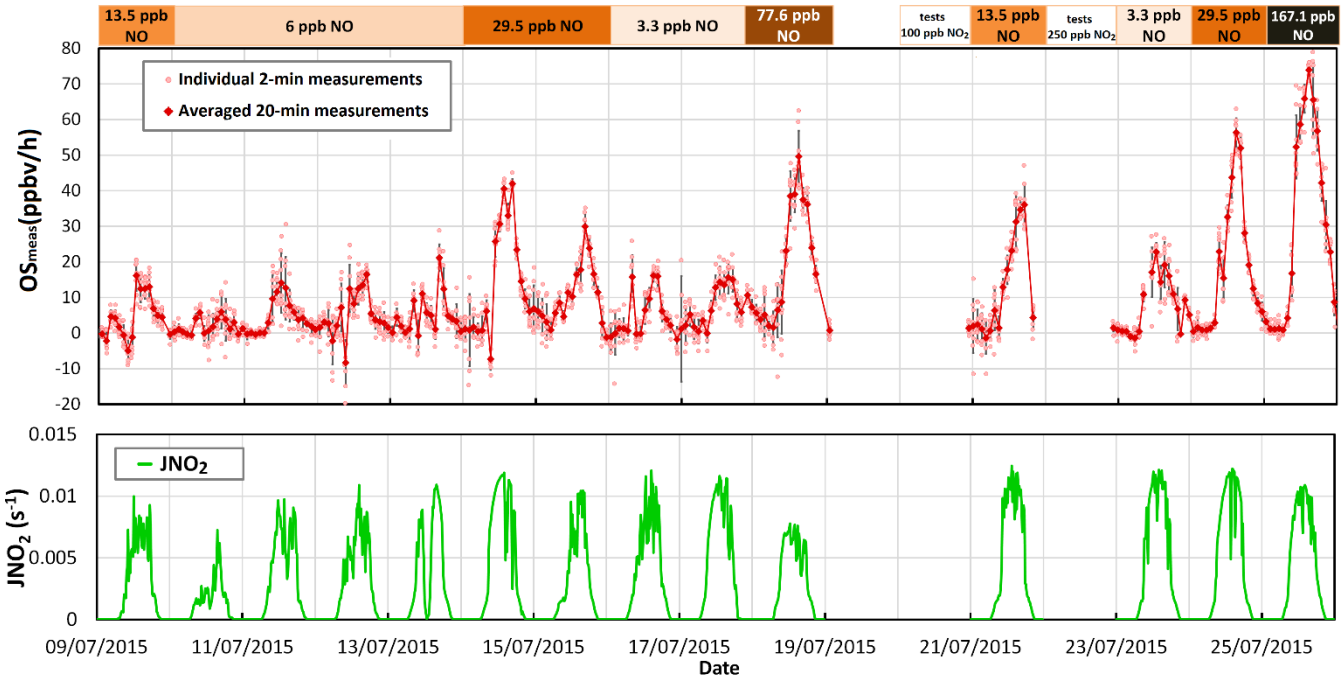

Figure 4.11: Ozone sensitivity measurements during IRRONIC. The pink circles represent 2-min OS_{meas} values, in groups of 20 min measurements, while the red diamonds represent 20-min averaged values. Error bars are 1σ of the mean on the averaged values. J(NO_2) values are displayed in the bottom panel.

The ozone formation chemistry indicates that the rate of ozone production increases with NO in a NO_x-limited regime, and decreases with NO in a NO_x saturated regime. The turnover point between the two regimes is usually on the order of a few ppbv of NO_x. However, for the OS measurements made during IRRONIC, there is no indication of a turnover point. The measured OS is on the order of 15 ppbv/h for additions of 3.3 and 6 ppbv of NO, increases to 35 ppbv/h when 13.5 ppbv of NO is added, and keeps increasing at even higher NO mixing ratios, reaching 75 ppb/h at 167 ppbv of NO. This observation is an indication that there are measurement errors, especially at high NO mixing ratios.

This error may come from a change in the amount of ozone lost in the flow tubes when NO is added. As explained before, the negative ΔO_x^{zero} values are mainly due to O_3 losses in the ambient flow tube during daytime and its magnitude depends, among others, on the O_3 mixing ratio. When an elevated NO mixing ratio is added in the flow tubes, a large fraction of O_3 is converted into NO_2 and the O_3 mixing ratio is reduced. This, in turn, impacts the amount of O_3 lost since the absolute loss scales with the O_3 mixing ratio. With a lower ozone mixing ratio in the ambient flow tube, the ΔO_x^{zero} value that should be subtracted from ΔO_x^{NO} should be higher (closer to zero), and the difference between ΔO_x^{NO} and ΔO_x^{zero} lower, leading to lower OS_{meas} values. As a result, OS_{meas} does not only represent the change in ozone production, but a combination of the change in ozone production and the change in the absolute loss of O_3 when NO is added in the flow tubes.

To extract the change in ozone production rates from OS_{meas}, it is therefore necessary to model the chemistry in the flow tubes to separate the two contributions. Including ozone losses in the model and simulating ΔO_x with and without NO addition, one can calculate a modelled value of OS (OS_{model}). The comparison between OS_{meas} and OS_{model}, as well as the comparison of measured and modeled $O_{x_{amb}}$, $O_{x_{ref}}$ and ΔO_x with and without NO addition, is expected to give valuable information on the magnitude of the error due to ozone losses and on the $P(O_3)$ sensitivity for the IRRONIC campaign. These results will provide a better understanding of the operating conditions of the OPR instrument.

4.4 $P(O_3)$ and Ozone Sensitivity modeling

The Regional Atmospheric Chemistry Mechanism version 2 (RACM2) (Goliff et al., 2013) was chosen to model the ozone formation chemistry in ambient air and inside the OPR flow tubes. Compared to the RACM mechanism used in chapter 3, this mechanism includes additional chemical species and chemical reactions that are important to better describe the radical chemistry in an environment impacted by biogenic emissions such as the type of air masses observed during the IRRONIC field campaign.

4.4.1 Modeling methodology

A 0-D box model similar to that described in chapter 3 but including RACM2 was constrained by measured concentrations of long-lived species. The differential equations were integrated using the FACSIMILE solver. As in chapter 3, the modeling was performed both for the ambient atmosphere and in each flow tube. Measurements of organic and inorganic species, temperature and humidity made during IRRONIC were averaged into 15-min data points and used to constrain the model. Table 4.3 shows the different chemical species and surrogates that were constrained in the model, while Table 4.4 reports the species that were grouped together to generate the RACM2 surrogates. In total, 33 species and surrogates were constrained in the model.

Table 4.3: Chemical species constrained in RACM2 for the IRRONIC modeling. Details about the RACM notation can be found in (Goliff et al., 2013).

Species	Definition	Species	Definition
HONO	Nitrous acid	ACT	acetone
NO	Nitric oxide	HC3	Alkanes, esters and alkynes with OH rate constant (298 K, 1 atm) less than 3.4×10^{-12} cm^3 s^{-1}
NO2	Nitrogen dioxide	HC5	Alkanes, esters and alkynes with OH rate constant (298 K, 1 atm) between 3.4×10^{-12} $cm^3 s^{-1}$ and 6.8×10^{-12} cm^3 s^{-1}
O3	Ozone	HC8	Alkanes, esters and alkynes with OH rate constant (298 K, 1 atm) greater than 6.8×10^{-12} cm^3 s^{-1}
H2	Hydrogen	DIEN	Butadiene and other anthropogenic dienes
CO	Carbon monoxide	ISO	Isoprene
GLY	Glyoxal	CH4	Methane
HCHO	Formaldehyde	TOL	Toluene and less reactive aromatics
BEN	Benzene	MEK	Methyl ethyl ketone
OLT	Terminal alkenes	MVK	Methyl vinyl ketone
OLI	Internal alkenes	XYM / XYP	M-xylene and P-xylene
ACE	Acetylene	XYO	o-xylene
ETE	Ethene	MGLY	Methylglyoxal and other alpha-carbonyl aldehydes
ALD	C3 and higher aldehydes	API	α-pinene and other cyclic terpenes with one double bond
ETH	Ethane	BALD	Benzaldehyde and other aromatic aldehydes
ACD	Acetaldehyde	KET	Ketones other than acetone

Due to technical issues with the LP/LIF instrument that led to many missing values through the campaign, but also given the low HONO mixing ratios that were measured (10 – 50 pptv), a campaign averaged diurnal profile of HONO measurements was used to constrain each day in the model. Hydrogen was constrained at 0.55 ppmv, based on NASA's terrestrial atmosphere factsheet (available at nssdc.gsfc.nasa.gov/planetary/ factsheet). Methane was constrained at a constant mixing ratio of 1832 ppbv, based on data presented in IPCC (2013b). CO was scaled on benzene measurements, with a scaling factor (=1250) calculated as the average ratio between measured CO and benzene during the CalNex campaign (Griffith et al., 2016). Finally, species below the limit of detection of DNPH or absorbent cartridges, including glyoxal, methylglyoxal, benzaldehyde, o-tolualdehyde, m-tolualdehyde, p-tolualdehyde, 2,5-dibenzaldehyde, propanal, butanal, isobutanal, pentanal, isopentanal, propenal and butenal (Table 4.2), were constrained at a value equal to LOD/2.

Table 4.4: Chemical species grouped in each RACM2 surrogate for the IRRONIC modeling

Surrogate	Species included	Method
API	α-pinene, β-pinene, α-terpinene, 3-carene	Absorbent Cartridge
BALD	benzaldehyde,	Absorbent Cartridge
	o-tolualdehyde, m-tolualdehyde, p-tolualdehyde, 2,5-dibenzaldehyde	DNPH Cartridge
BEN	benzene	GC-NMHC
OLT	propene, 1-butene, isobutene, 3-methyl-1-butene, 1-pentene, 2-methyl-1-butene, hexene	GC-NMHC
OLI	trans-2-butene, cis-2-butene, trans-2-pentene, 2-methyl-2-butene, cis-2-pentene, cyclopentene	GC-NMHC
ALD	hexanal, heptanal, octanal, nonanal, decanal, undecanal,	Absorbent Cartridge
	propanal, butanal, isobutanal, pentanal, isopentanal, propenal, butenal	DNPH Cartridge
HC3	propane, butane, isobutane, neopentane, 2,2-dimethylbutane, 2,2dimethylpentane	GC-NMHC
HC5	pentane, isopentane, propyne, 2-methylpentane, 3-methylpentane, hexane, 2,4-dimethylpentane, 2,2,3-trimethylbutane, 3,3-dimethylpentane, 2,3-dimethylpentane, isooctane	GC-NMHC
HC8	butyne, cyclopentane, 2,3-dimethylbutane, cyclohexane, 2-methylhexane, heptane, octane, nonane, undecane, dodecane, nC13, nC14	GC-NMHC
DIEN	1,3-butadiene	GC-NMHC
TOL	toluene, ethylbenzene, styrene, isopropylbenzene, n-propylbenzene, 2-ethyltoluene, 3-ethyltoluene, 4-ethyltoluene, 1,3,5-trimethylbenzene, 1,2,4,-trimethylbenzene n-butylbenzene, chlorobenzene	GC-NMHC
ROH	borneol	Absorbent Cartridge
	isopropanol	GC-OVOC
KET	2-pentanone	GC-OVOC

In addition to modeling ambient $P(O_3)$, the model was used to compare measured and modeled O_x mixing ratios at the exit of each flow tube, with the goal to assess how ozone losses in the flow tubes impact the OS measurements discussed above (OS_{meas}). The emphasis was put on evaluating the amplitude of the measurement bias introduced by these losses. For modeling O_x mixing ratios at the exit of each flow tube, it is important to constrain the model with O_3 and NO_2 mixing ratios (measured by UV absorption and CAPS, respectively) that are consistent with O_x (O_3+NO_2) measurements from the CAPS monitor coupled to the OPR flow tubes. A small bias in the calibration of one of the instruments could spoil the comparison since small differences in O_x are equivalent to large $P(O_3)$ values (1 ppbv ≈ 13.3 ppbv/h). To constrain the model with ambient measurements of O_3 and NO_2 that are consistent with O_x measurements performed at the exit of each flow tube, we scaled the O_3 measurements to remove differences due to calibration or zeroing issues on the monitors. Assuming that the ambient NO_2 measurements are correct, subtracting NO_2 from the OPR O_x measurements results in O_3, as measured by the OPR. The measurements performed by

the O_3 monitor were compared to the calculated OPR O_3 values, taking into account measurements from the reference flow tube during nighttime, when NO was not added. This analysis, included in Annex IV, showed that the two sets of ozone measurements were well correlated (R^2=0.97) and the adjustment of the measured O_3 mixing ratios was in the order of 20% (corrected mixing ratio = 1.196×measured mixing ratio + 2.977). This set of scaled O_3 measurements was then used to constrain the model.

Table 4.5: Photolytic reactions constrained by J-values in RACM2 for the IRRONIC modeling. Details about the RACM notation can be found in (Goliff et al., 2013).

Photolytic reaction	RACM2 symbol	Reference flow tube scaling factor	Photolytic reaction	RACM symbol	Reference flow tube scaling factor
$O_3 \rightarrow O(3P)$	JO3P	0.82	HKET → HO_2 + ACO_3 + HCHO	JHKET	0
$O_3 \rightarrow O(1D)$	JO1D	0	PAN → ACO_3 + NO_2	JPAN_ACO3	0
$H_2O_2 \rightarrow$ OH + OH	JH2O2	0	PAN → MO_2 + NO_3 + CO_2	JPAN_MO2	0
$NO_2 \rightarrow$ NO + O	JNO2	0.02	GLY → 2CO + H_2	JGLY1	0.02
$NO_3 \rightarrow$ NO + O2	JNO3_NO	0.82	GLY → HCHO + 2CO	JGLY2	0.02
$NO_3 \rightarrow NO_2$ + O	JNO3_NO2	0.82	GLY → HO_2 + HO_2 + CO + CO	JGLY3	0.02
HONO → HO + NO	JHONO	0	MGLY → HO2 + ACO_3 + CO	JMGLY	0.02
$HNO_3 \rightarrow$ OH + NO2	JHNO3	0	DCB1 → 1.5 HO_2 + 0.5 ACO_3 + 2XO_2 + CO + 0.5 GLY + 0.5 MGLY	JDCB1	0.02
$HO_2NO_2 \rightarrow$ 0.2OH + 0.8HO_2 + 0.8 NO_2 + 0.2 NO_3	JHO2NO2	0	DCB2 → 1.5 HO_2 + 0.5 ACO_3 + 2XO_2 + CO + 0.5 GLY + 0.5 MGLY	JDCB2	0.02
HCHO → CO + H_2	JHCHO_CO	0	BALD → CHO + HO_2 + CO	JBALD	0
HCHO → HO_2 + HO_2 + CO	JHCHO_HO2	0	OP1 → OH + HO_2 + HCHO	JOP1	0
ACD → HO_2 + MO_2 + CO	JACD	0	OP2 → OH + HO_2 + ALD	JOP2	0
ALD → HO_2 + ETHP + CO	JALD	0	PAA → MO_2 (CH_3O_2) + OH	JPAA	0
ACT → MO_2 + ACO_3	JACT	0	ONIT → HO_2 + NO_2 + 0.2ALD + 0.80KET	JONIT	0
UALD → 1.22 HO_2 + 0.784 ACO_3 + 1.22 CO + 0.35 HCHO + 0.434 ALD + 0.216 KET	JUALD	0	MACR → 0.67CO + 0.66HO_2 + 0.67ACO_3+0.67HCHO+0.34OH+ 0.33MACP+0.34XO_2	JMACR	0
MEK → 0.5 MO_2 + 0.5 ETHP + ACO_3	JMEK	0	MVK → 0.3 MO_2 + 0.3 MACP + 0.7 CO + 0.7 UALD	JMVK	0
KET → ETHP + ACO_3	JKET	0			

Since only J(NO_2) was measured during IRRONIC, all other J-values were calculated as a function of the solar zenith angle at the coordinates of the measuring site (39.1908N, 86.502W) using the Master Chemical Mechanism parametrization as in Dusanter et al. (2009b). As this parameterization relies on the calculation of J-values for clear sky conditions, the calculated J-values were corrected for cloud coverage using a scaling factor, derived from the ratio between measured and calculated J(NO_2) values. For the modeling in the ambient flow tube, ambient J-values were used, while for the reference flow tube, the J-values were

scaled based on the absorption properties of the UV film (section 3.3.2). Table 4.5 shows the J-values that were constrained in the model, along with the J-values scaling factors for the UV filter.

The modeling of ambient $P(O_3)$ was first performed using a 5-day spin-up procedure to build up the concentrations of unmeasured secondary species (Michoud et al., 2012). During the spin-up procedure, the model constraints were reinitialized every 10 seconds to ensure constant concentrations over the integration time for these species. Unconstrained oxidation products that were generated as outputs from the ambient modeling were used as constrained inputs for the flow tubes modeling. Peroxy radicals were not constrained in the flow tubes as in chapter 3, as they would be lost in the 10 m line used for mixing NO with the sampled air. In the end, $P(O_3)$ values of the ambient atmosphere are derived from the model-calculated peroxy radical concentrations using Eq. 1.6 (chapter 1).

It should be noted here that modeling the ambient atmosphere serves mainly the purpose of constraining the unmeasured oxidation products in the flow tubes model. Therefore, the focus in this section is on the modeling in the flow tubes and the comparison with the OPR measurements.

Table 4.6 lists the oxidation products that were extracted from the ambient modeling and used as constraints for the modeling in the flow tubes. The concentrations of the constrained species (measured inorganic and organic species, as well as unmeasured oxidation products derived from the ambient modeling) were initialized only once at the entrance of the flow tubes, and the simulations were run for 271 s, i.e. the residence time in the flow tubes, with an output value every 15 sec. The O_3 and NO_2 concentrations simulated at 271 s were used to perform the model-measurement comparison.

Table 4.6. Secondary compounds and unmeasured species constrained in RACM2 for the flow tubes modeling.

Species	Definition
N2O5	Dinitrogen pentoxide
H2O2	Hydrogen peroxide
HNO3	Nitric acid
HO2NO2	Peroxynitric acid
CSL	Cresol and other hydroxy substituted aromatics
DCB1	Unsaturated dicarbonyls, carbon # 4.5, MW 91
DCB2	Unsaturated dicarbonyls, carbon # 7, MW 110
DCB3	Unsaturated dicarbonyls, carbon # 4, MW 84
EPX	Epoxide formed in TOL, XYL and XYO reactions
ETEG	Ethylene glycol
HKET	Hydroxy ketone
ISHP	Beta-hydroxy hydroperoxides from ISOP+HO2
ISON	Beta-hydroxyalkylnitrates from ISOP+NO, alkylnitrates from ISO+NO3
MAHP	Hydroperoxides from MACP+HO2
MACR	methacrolein
MPAN	Peroxymethacryloylnitrate and other higher peroxyacylnitrates from isoprene oxidation
NALD	nitrooxyacetaldehyde
ONIT	Organic nitrates
OP1	Methyl hydrogen peroxide
OP2	Higher organic peroxides
ORA1	Formic acid
ORA2	Acetic acid and higher acids
PAA	Peroxyacetic acids and higher analogs
PAN	Peroxyacetyl nitrate and higher saturated PANs
PHEN	Phenol
PPN	Peroxypropionyl nitrate
UALD	Unsaturated aldehydes

It should be reminded here, that the addition of NO takes place in a long line before the inlet of the flow tubes, leading to a residence time of 10 s. As a consequence, the partitioning between NO, NO_2 and O_3 at the exit of the sampling line (entrance of the flow tubes) is different than at the entrance of the line when NO is added. The chemistry in the sampling line was simulated by running the model for 10 s (J-values set at zero and constraints initialized only once at the entrance of the line) for each NO addition step. The NO, NO_2 and O_3 outputs of these simulations were used to constrain the modeling for the flow tubes during the NO addition step. A schematic presented in Fig. 4.12 summarizes the different steps of the modeling procedure.

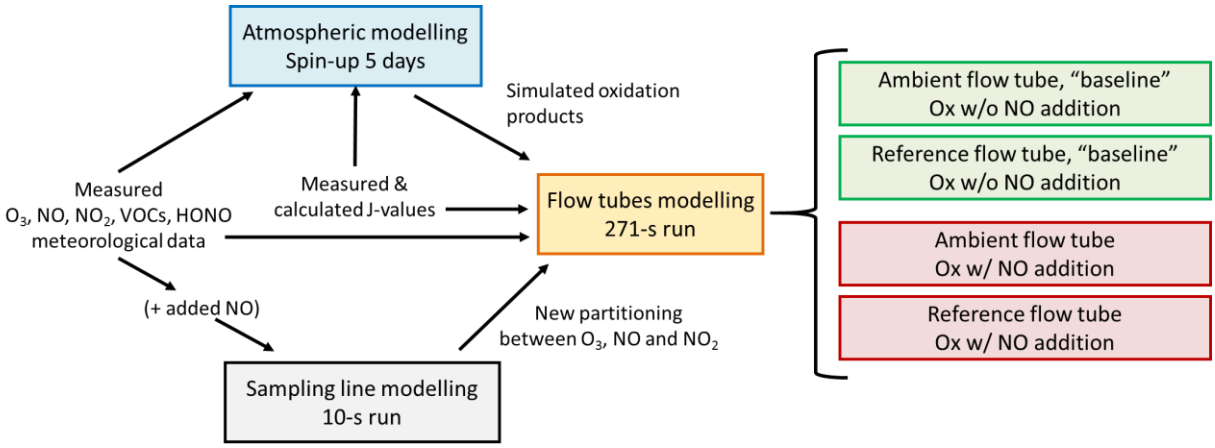

Figure 4.12: Schematic of the modeling methodology

The modeling in the flow tubes includes 3 main steps:

- **Baseline modeling:** The chemistry is modeled separately in the ambient and reference flow tubes to reproduce the ΔO_x^{zero}. The latter is calculated by the model O_x outputs (ambient and reference flow tubes) for a residence time τ of 271 s, as shown in Eq. 4.3:

  $$\Delta O_{x\ model}^{\ zero} = O_{x_{amb,\,model}}^{\ zero} - O_{x_{ref,\,model}}^{\ zero} \quad \text{(Eq. 4.3)}$$

  where the subscripts "amb, model" and "ref, model" indicate the model output for the ambient and reference flow tubes, respectively.

- **NO addition modeling:** The chemistry is also modeled separately in the ambient and reference flow tubes to reproduce the "NO addition" step. The partitioning between O_3 and NO_x was adjusted as described above to account for the reaction between ambient O_3 and NO in the sampling line. ΔO_x^{NO} is calculated by the two model O_x outputs (ambient and reference flow tubes) at a residence time τ of 271 s, as shown in Eq. 4.4:

  $$\Delta O_{x\ model}^{\ NO} = O_{x_{amb,\,model}}^{\ NO} - O_{x_{ref,\,model}}^{\ NO} \quad \text{(Eq. 4.4)}$$

- ***OS* calculation:** The modeled ozone sensitivity is calculated as follows:

  $$OS_{model} = \frac{\Delta O_{x\,model}^{\ NO} - \Delta O_{x\,model}^{\ zero}}{\tau} \quad \text{(Eq. 4.5)}$$

Comparisons will be performed between measured and modelled $O_{x,amb}$, $O_{x,ref}$, ΔO_x and OS with and without NO addition, as shown in the schematic of Fig. 4.13.

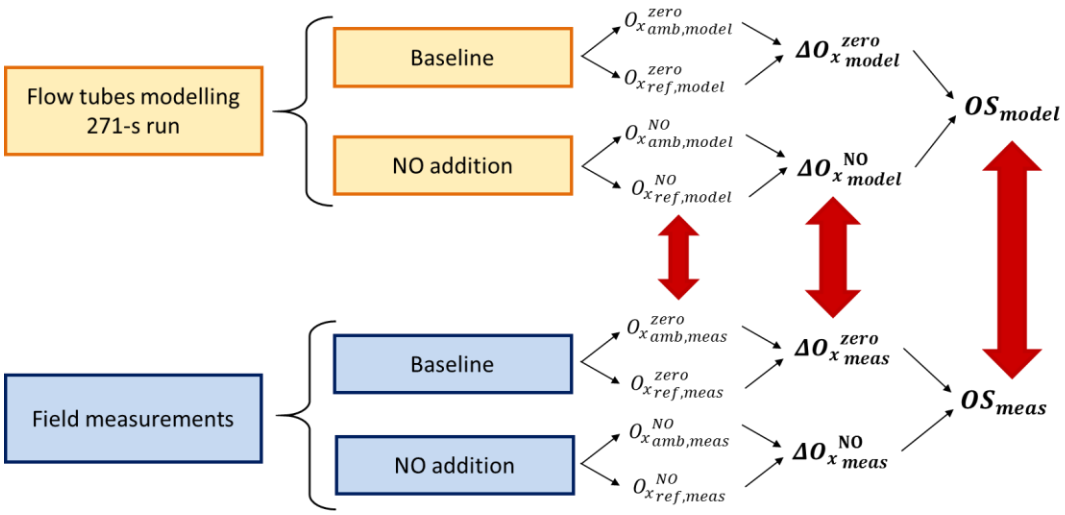

Figure 4.13: Schematic of the different modeled and measured parameters that can be compared

As explained previously, negative ΔO_x values are the result of higher O_3 losses in the ambient flow tube compared to the reference flow tube. For this reason, the simulations were first performed without including any ozone losses in the model to see what the OS measurements should look like, and then introducing dark and photoenhanced O_3 losses (identified and discussed in chapter 2) to reproduce the field measurements.

4.4.2 Flow tubes modeling exempt of wall losses

The modeling of the chemistry without wall losses cannot be used for comparison with the measurements since it doesn't represent the complete chemistry that takes place in the flow tubes. However, as it was shown in section 3.4, comparing ozone production rates modelled in the flow tubes and in ambient air allows to discuss the validity of the OPR principle. In addition, as it will be shown in this section, this modelling provides a useful theoretical description of the $P(O_3)$ sensitivity to NO_x and VOCs for this environment.

Figure 4.14 shows the net ozone production as modeled in the ambient atmosphere ($P(O_3)_{atm}$), in the ambient flow tube ($P(O_3)_{amb}$) and in the reference flow tube ($P(O_3)_{ref}$), as well as the modeled ozone production as would be measured by the OPR instrument $P(O_3)_{OPR}$ for 18 July. These calculations have been done as described in sections 3.3 and 3.4.

The modelled $P(O_3)$ in the atmosphere is in the range of 0–5 ppbv/h. One can see that $P(O_3)_{amb}$ exhibits the same profile than $P(O_3)_{atm}$, although it overestimates it by approximately 2 ppbv/h during daytime. This difference, although small, corresponds to more than a factor 2 disagreement during the afternoon, when $P(O_3)$ is lower than 3 ppbv/h. The modelling has shown that this disagreement is caused by a difference in the mixing ratios of NO, that are higher in the ambient flow tube compared to the atmosphere, as shown in Fig. 4.15. As described above, NO mixing ratios are constrained at the measured values for the modelling

in the atmosphere and are kept constant during the 5-day spin up integration. For the modelling in the flow tubes, constrained species are initialized only once at the beginning of the simulation (entrance of the flow tubes) and are left free to change during the 271 s residence time. As a consequence, NO increases by more than a factor 2 during daytime in the ambient flow tube, due to NO_2 photolysis. It should be noted here, however, that with the low NO_x levels observed during IRRONIC, a factor 2 of change in the NO mixing ratio corresponds to a change lower than 1 ppbv.

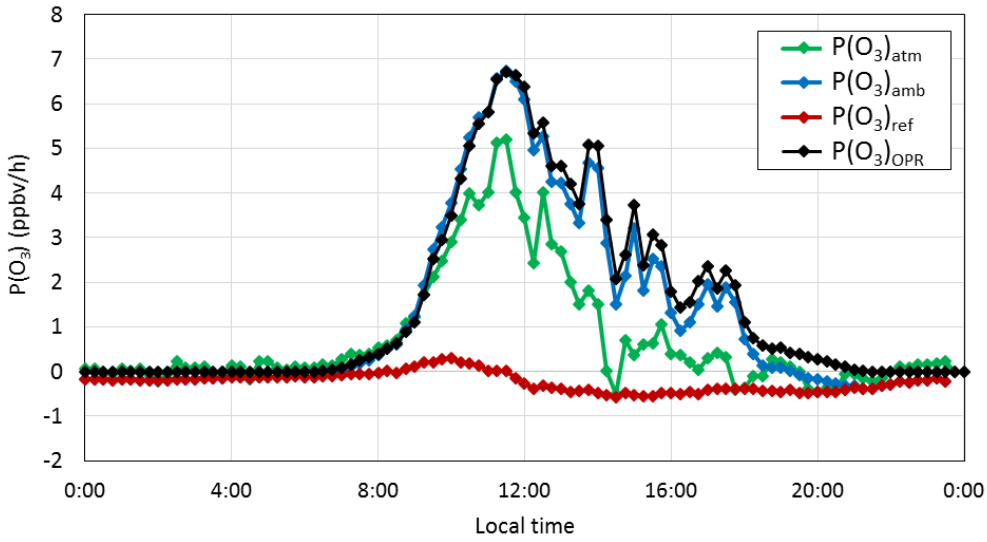

Figure 4.14: Net ozone production as modeled for 18 July in the ambient atmosphere ($P(O_3)_{atm}$), in the ambient flow tube ($P(O_3)_{amb}$), in the reference flow tube ($P(O_3)_{ref}$) and for the OPR instrument ($P(O_3)_{OPR}$).

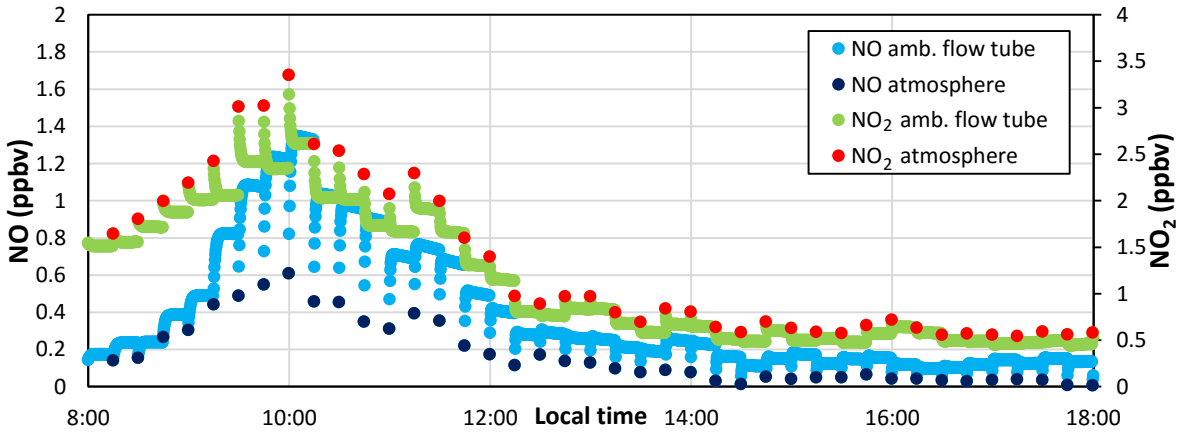

Figure 4.15: NO_x partitioning in the atmosphere and in the ambient flow tube during daytime on 18 July.

Regarding the net ozone production (or better, O_x production) in the reference flow tube, one can see that $P(O_3)_{ref}$ exhibits negative values of approximately 0.5 ppbv/h in the afternoon, while it is only slightly

positive during the morning. This behaviour is due to the low NO mixing ratios in this environment, where the loss rate of O_3 (gas-phase processes) become larger than the ozone production rate. Therefore, in contrast with the urban environments presented in chapter 3, when NO is lower than 0.5 ppbv, O_x production in the reference flow tube is slightly negative, contributing to an overestimation of ambient $P(O_3)$.

To conclude, it seems difficult to compare $P(O_3)_{atm}$ and $P(O_3)_{amb}$ for ozone production rates lower than 3 ppbv/h, due to small but significant differences in NO levels. Overall, however, $P(O_3)_{atm}$ and $P(O_3)_{amb}$ exhibit similar profiles and we could consider the modelled $P(O_3)$ presented in this chapter as an upper limit of the ozone production in the ambient air.

The ΔO_x values modelled with ($\Delta O_x{}^{NO}{}_{model}$) and without ($\Delta O_x{}^{zero}{}_{model}$) NO addition are presented in Fig. 4.16 with black and green colours (top panel), respectively. Dividing ΔO_x by the residence time τ, we can calculate ozone production rates associated to different NO_x conditions, as shown on the right axis. When NO is not added (baseline), $P(O_3)$ represents the ambient ozone production. When NO is added, $P(O_3)$ represents how the ozone production rate would change due to the increase of NO, for the same VOC composition and same irradiation. Figure 4.16 also presents $OS_{no\ losses}$ (difference between $P(O_3)$ values with and without NO addition) on the middle panel, as well as measured $J(NO_2)$ on the bottom panel.

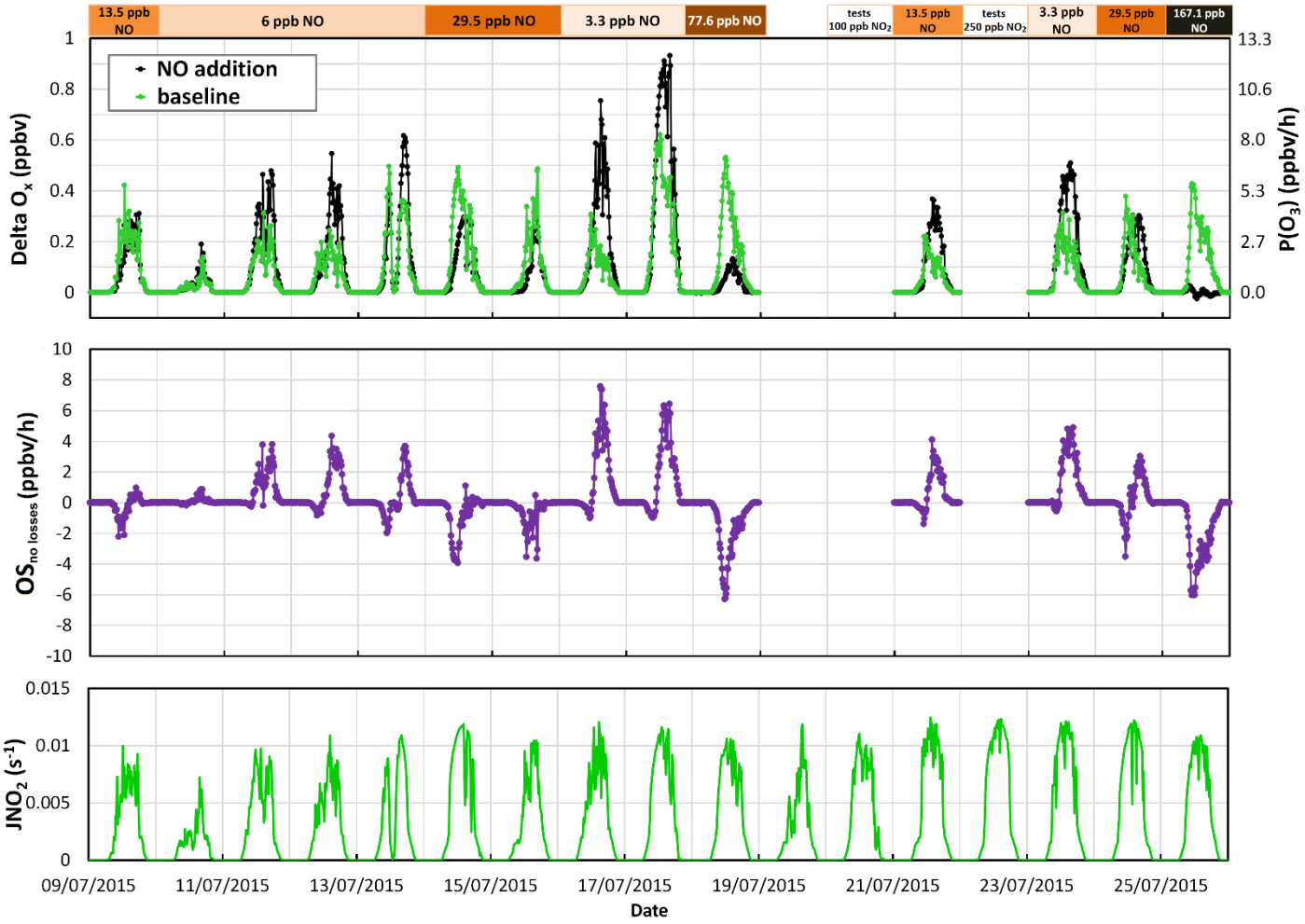

Figure 4.16: Modeled ΔO_x values with and without NO addition (top panel, left axis), equivalent ozone production rates (top panel, right axis), $OS_{no\ losses}$ (middle panel) and measured $J(NO_2)$ values (bottom panel).

As can be seen from Fig. 4.16, modeled ΔO_x values are always positive, indicating higher O_x mixing ratios in the ambient flow tube than in the reference flow tube. The baseline indicates low $P(O_3)$ values in the ambient atmosphere, on the order of 5 ppbv/h on most days, that are well correlated with J-values. Therefore, the ambient $P(O_3)$ values were indeed near or below the instrument's detection limit as stated in section 4.3.3, confirming the difficulty to measure ozone production rates in this type of environment.

ΔO_x^{NO} can be either higher, close to or lower than ΔO_x^{zero}. The difference between the two, as expressed by $OS_{no\ losses}$, indicates the theoretical predictions for the ozone production sensitivity to NO, if there were no O_3 losses in the flow tubes. When ΔO_x^{NO} is higher than ΔO_x^{zero}, the amount of NO added in the sampling line leads to higher ozone production rates than in the ambient atmosphere. In the opposite case, the added NO leads to lower ozone production rates than in ambient air. In the case that ΔO_x^{NO} is equal to ΔO_x^{zero}, the added NO doesn't cause any change to the ambient ozone production.

One could assume, therefore, that the sign of $OS_{no\ losses}$ expresses the ozone production regime: positive for NO_x-limited and negative for VOC-limited. It is important to make clear, however, that the sign of $OS_{no\ losses}$ is not linked to the ozone production regime. This is clearly illustrated by Fig. 4.17, where $P(O_3)$ has been averaged from 13:00 – 15:00 for every NO addition step, showing the change of $P(O_3)$ for the different NO levels. The ambient $P(O_3)$ is shown by the green circle and the black dashed straight line, at approximately 3 ppbv/h for 0.1 ppbv of NO, which is the average ambient mixing ratio of NO from 13:00 to 15:00 during IRRONIC. During the NO addition, $P(O_3)$ can reach various levels ranging from approximately 0 to 7 ppbv/h, depending on how much NO is added. It can easily be seen that a VOC-limited regime is observed when more than 3 ppbv of NO are added, while the turnover point should be between 0.5 and 3 ppbv of NO. Taking the 6 ppbv level of NO as an example (10 – 13 July), a higher ozone production is observed compared to the ambient level but, at this NO mixing ratio, this is a VOC-limited regime since $P(O_3)$ keeps decreasing when increasing NO. Therefore, an increase in $P(O_3)$ by adding a certain amount of NO does not necessarily indicate that ozone production is NO_x-limited at this NO level. It does indicate, however, that ozone production was NO_x-limited without the NO addition; for a VOC-limited regime ozone production would not increase with increasing NO (see section 1.4.3).

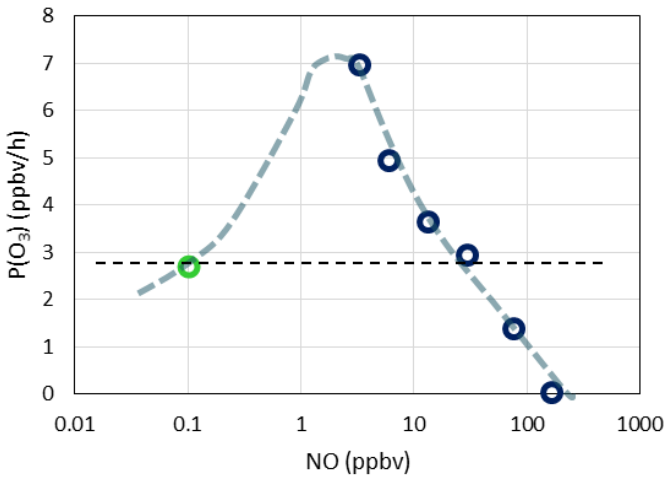

Figure 4.17: Modeled ozone production rates ($P(O_3)_{OPR}$) as a function of NO.

Figure 4.18 shows the modelled ozone production as a function of NO. $P(O_3)$ values reported in these figures for NO levels higher than 2 ppbv and lower than 1 ppbv correspond to ozone production rates modelled with and without NO addition, respectively. The different panels of this figure are color-coded with $J(NO_2)$, the hour of the day, and the measured isoprene mixing ratios. As mentioned in section 4.2.3, isoprene accounted for approximately 70% of the measured total OH reactivity during the IRRONIC field campaign (Sigler et al., 2015) and therefore isoprene was chosen as a metric of the total OH reactivity in the following, especially because there were gaps in the OH reactivity measurements due to technical issues with the instrument.

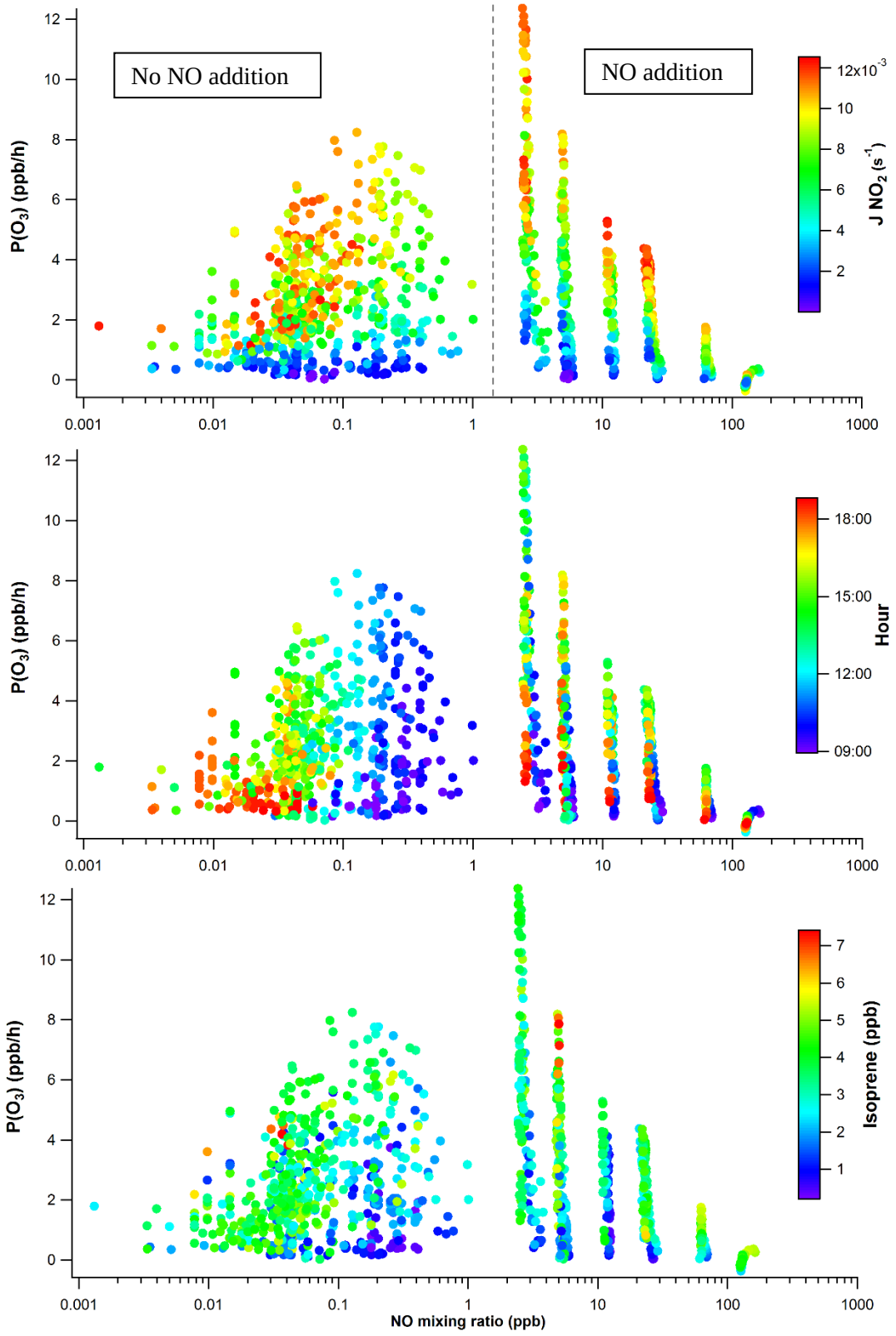

Figure 4.18: Modeled ozone production rates ($P(O_3)_{OPR}$) as a function of NO. The color coding corresponds to measured J-values (top), the hour of the day (middle) or measured isoprene mixing ratios (bottom).

For the different NO addition levels, the NO mixing ratio displayed on the x-axis of Fig. 4.18 corresponds to the NO mixing ratio that enters in the flow tubes, after the long mixing line at the inlet. For this reason, the points are scattered within a certain range of NO mixing ratios for each addition and they are not all located on the same vertical line. NO mixing ratios after the long mixing line depend on ambient O_3 levels since for higher O_3 mixing ratios, more NO is converted into NO_2. This approach for plotting $P(O_3)$ was chosen for better visibility.

The general shape of the points in these figures suggests that the transition from a NO_x-limited to a VOC-limited regime occurs for NO mixing ratios between 1 and 3 ppbv as discussed for Fig. 4.17. The highest ozone production rates are on the order of 12 ppbv/h and occur at NO mixing ratios close to 3 ppbv. Lower ozone production rates are observed for ambient NO levels, on the order of 0-8 ppbv/h at most, while $P(O_3)$ values also decrease for NO levels higher than 5 ppbv. For NO levels near 100 ppbv, ozone production rates are practically equal to zero due to the enhancement of the total radical termination rate through radical-NO_x reactions and the conversion of O_3 (important OH precursor) into NO_2.

For all NO levels, low $J(NO_2)$ values ($< 0.002\ s^{-1}$) lead to ozone production rates close to zero (< 1 ppbv/h). It can be seen from Fig. 4.18 that, for NO levels higher than 2 ppbv, likely characteristic of a VOC-limited regime, the highest ozone production rates are found at the highest J-values. Indeed, higher J-values lead to an increase of the total radical production rate and ozone production increases. In contrast, for NO levels lower than 1 ppbv, the highest ozone production rates do not occur at the highest J-values. The highest J-values are observed for ambient NO levels lower than 0.1 ppbv, which lead to ozone production rates on the order of 2-6 ppbv/h. However, higher ozone production rates (6-8 ppbv/h) are observed for NO mixing ratios ranging from 0.1-1.0 ppbv when J-values are lower, indicating that $P(O_3)$ is enhanced when NO increases, consistent with a NO_x-limited regime,.

For the middle panel of Fig. 4.18, looking at the ambient NO levels ($NO \leq 1$ ppbv), NO is generally higher during morning hours. NO usually ranges from 0.2 – 1 ppbv from 9:00 to 11:00, decreases to 0.08 – 0.2 ppbv around noon, and keeps decreasing to 0.03 ppbv until 16:00, reaching even lower levels around 18:00. The highest ozone production rates occur between 11:00 and 13:00. During this time window, NO is around 0.1 ppbv, $J(NO_2)$ has increased to about $0.009\ s^{-1}$, and BVOC emissions are significant, leading to isoprene mixing ratios higher than 3 ppbv. These conditions lead to an increase of ozone production from 9:00 to 11:00, reaches its maximum around noon, which then decreases in the afternoon.

A similar behaviour is observed during the NO addition step. NO is generally higher during morning hours, which can be explained by morning NO_x emissions in this area (leading to a peak of a few ppbv) and a large variability of O_3 levels throughout the day. For example, during 25 July, O_3 mixing ratios were on the order of a few ppbv during morning hours while it reached approximately 70 ppbv in the afternoon. For an

addition of 167 ppbv of NO on this day, only a few ppbv of NO were converted into NO_2 in the morning while several tens of ppbv of NO were converted later in the day when O_3 increased. As can be seen from the middle panel in Fig. 4.18, ozone production rates for NO levels higher than 2 ppbv increase during morning hours and peak later in the day, between 14:00 to 17:00, when isoprene mixing ratios and OH reactivity are at their highest values.

These observations illustrate that while ozone production is always radical dependent (see section 1.4.3), there is a complex interplay between the different parameters involved in the ozone formation chemistry, i.e J-values, VOC reactivity, and NO_x. For this environment, the model predicts that the turnover from a NO_x-limited to a VOC-limited regime occurs between 1 and 3 ppbv of NO_x. Addition of NO mixing ratios lower than 3 ppbv (e.g. 0.5 ppbv, 1 ppbv, 2 ppbv) would have been better to identify the turnover point between the NO_x- and VOC-limited regimes. For all the NO addition steps, the model predicts that ozone production is close to or beyond the turnover point. These results are compared to ozone production rates derived from the OPR measurements in section 4.4.4 to test the model-measurement agreement.

4.4.3 Flow tubes modeling including wall losses

For this modeling exercise, O_3 losses were included in the chemical mechanism with the objective to reproduce the observed negative ΔO_x values. The goal was to reproduce the measured "baseline", ΔO_x^{zero}, by parameterizing the O_3 losses in the two flow tubes based on the characterization experiments discussed in section 2.3.1.2. Applying the same parametrization when NO is added in the flow tubes should allow checking whether the model can successfully reproduce ΔO_x^{NO}, and thus OS_{meas}. This modelling exercise should also allow investigating how the addition of NO impacts the total amount of ozone lost on the walls of the flow tubes (because of the conversion of O_3 into NO_2), and as a consequence, to quantify the resulting bias in OS_{meas}. This analysis was then used to infer ozone production sensitivity values from the OPR measurements.

A close inspection of Fig. 4.10 indicates that negative ΔO_x^{zero} values have been measured during nighttime, often down to -0.5 ppbv. During nighttime, in the absence of sunlight, these negative values can only be caused by different dark O_x losses in the two flow tubes, with higher losses in the ambient tube. For this reason, a dark ozone loss has been added in the parametrisation of the losses in the ambient flow tube model to express the difference in O_3 losses between the two flow tubes. The dark loss rate was adjusted to reproduce the nighttime measurements. Specifically, the dark loss rate was determined for 21:00 and 6:00 of for each day, interpolating for nighttime and daytime. Usually the dark loss was higher at the end of the day, when different photolytic processes had taken place in the two tubes, likely due to different compounds

adsorbed on the walls. Interestingly, a lower dark loss had to be introduced when similar processes had occurred in the two flow tubes during the night. The adjusted dark loss rate coefficient was on the order of 1×10^{-4} s^{-1} on average throughout the campaign, which corresponds to a 2.7% difference in O_3 losses between the two flow tubes.

Additionally, the photoenhanced O_3 loss rate in the ambient flow tube was parameterized as a function of the O_3 mixing ratio, $J(NO_2)$ and absolute humidity, as a dependence on these parameters was identified during the characterization experiments performed on the OPR instrument (section 2.3.1.2). The product of these three parameters was used to calculate the photoenhanced O_3 loss rate, adding a multiplicative factor to reproduce the daytime measured O_x mixing ratios at the exit of the ambient flow tube. This multiplicative factor was determined for one day (17 July), and the same factor was then applied for the other days of the campaign. The multiplicative factor was determined at 0.018. As shown below, using the parameterization adjusted on one day of the campaign successfully reproduce the day to day variations, which give confidence in this parameterization. For an ambient $J(NO_2)$ value of 0.01 s^{-1} and an absolute humidity of 2%, the photoenhanced ozone loss would be 9.3%, which is consistent with the results of the characterization experiments performed on the flow tubes (section 2.3.1.2).

Combining the photoenhanced and dark losses for the ambient flow tube, the O_3 loss rate was parameterized as described by Eqs. 4.6 – 4.7. For simplicity, no product was assumed for the loss reaction included in the mechanism.

$$O_3\ Amb.loss\ rate = \left(k_{O_3\ phot.\ loss\ amb} + k_{dark\ loss}\right) \times [O_3] \quad \text{(Eq. 4.6)}$$

where $k_{O_3\ phot.\ loss\ amb} = 0.018 \times AH \times J(NO_2)$ (Eq. 4.7)

and $9\times10^{-6}\ s^{-1} < k_{dark\ loss} < 2.8\times10^{-4}\ s^{-1}$

For the reference flow tube, the first modelling tests were also performed with a photolytic O_3 loss rate equal to 2% of the ambient flow tube's loss rate since $J(NO_2)$ in the reference tube under the UV filter was scaled at 2% of the ambient values (see Table 4.5). However, a comparison between the modelled and measured O_x mixing ratios for the reference flow tube showed that, while nighttime measurements were successfully reproduced, the measured daytime mixing ratios were overestimated by up to 5%. While this systematic error looks small, it can have a large impact on the simulated ΔO_x values; for example, with ozone levels around 50 ppbv, a 5% error would lead to an increase of ΔO_x by 2.5 ppbv, which would translate to 33 ppbv/h of ozone production. As a consequence, it was decided to include an additional O_x loss in the reference flow tube during daytime. As was discussed in section 2.3.1.2, there is experimental evidence that a photoenhanced ozone loss may be present in the reference flow tube. The mechanism underlying the surface ozone loss in the flow tubes being very uncertain, it is possible that this additional

loss is not necessarily photoenhanced, as it could arise from an amplified dark loss due to temperature variations or a VOC coating on the surface that are correlated with J-values during daytime. These aspects would deserve to be further investigated.

Similarly to the approach used for the ambient flow tube, a multiplicative factor was determined to parameterize the photoenhanced ozone loss in the reference flow tube as a function of O_3, AH and $J(NO_2)$. This multiplicative factor was adjusted to get a good agreement between the modelled and measured O_x mixing ratios during one day (17 July) and the same multiplicative factor was used for the whole campaign (Eqs. 4.8-4.9). Based on the value of this scaling factor (0.09), it can be seen that the ozone loss rate of in the reference flow tube will be half the value for the ambient flow tube.

Therefore, the O_3 loss rate parameterized in the reference flow tube is given by Eqs. 4.8 – 4.9.

$$O_3\ Ref.loss\ rate = k_{O_3\ loss\ ref} \times [O_3] \quad \text{(Eq. 4.8)}$$

where $k_{O_3\ loss\ ref} = 0.09 \times AH \times JNO_2$ (Eq. 4.9)

The results of the modeling are shown in Fig. 4.19 for the baseline and in Fig. 4.20 for the NO addition, where modeled values of $O_{x_{amb}}$, $O_{x_{ref}}$ and ΔO_x, are compared to the constrained O_x mixing ratios and the measured values of each parameter. Note that the measurements are presented in groups of 20 min every 80 min (see section 4.3.2), while O_x measurements may differ from the values presented in Fig. 4.3 due to the scaling of the O_3 measurements as presented in section 4.4.1

As can be seen from the top two panels of Fig. 4.19, a good agreement between measured and modelled O_x mixing ratios is observed for the two flow tubes. The daytime O_x losses can be seen by comparing measured and constrained O_x mixing ratios. The losses are higher in the ambient flow tube, as determined by the loss rate coefficients included in the model for the two flow tubes. The approach used to parameterize the ozone loss in the flow tubes for one day of the campaign (17 July) is able to successfully reproduce the change in O_x mixing ratios from day-to-day, giving confidence in this parameterization. The ozone loss corresponds to 9.3% and 4.8% of the sampled O_3 for a $J(NO_2)$ value of 0.01 s^{-1} and an absolute humidity of 2% (ambient conditions leading to the largest ozone loss rate) for the ambient and reference flow tubes, respectively.

Less good agreement is observed during 23 and 24 of July. During 22 of July, tests with high mixing ratios of NO_2 (e.g. 250 ppbv) had been performed in the flow tubes, which is thought to have altered the surface coating of the flow tubes, affecting the processes that take place on the walls during the next days.

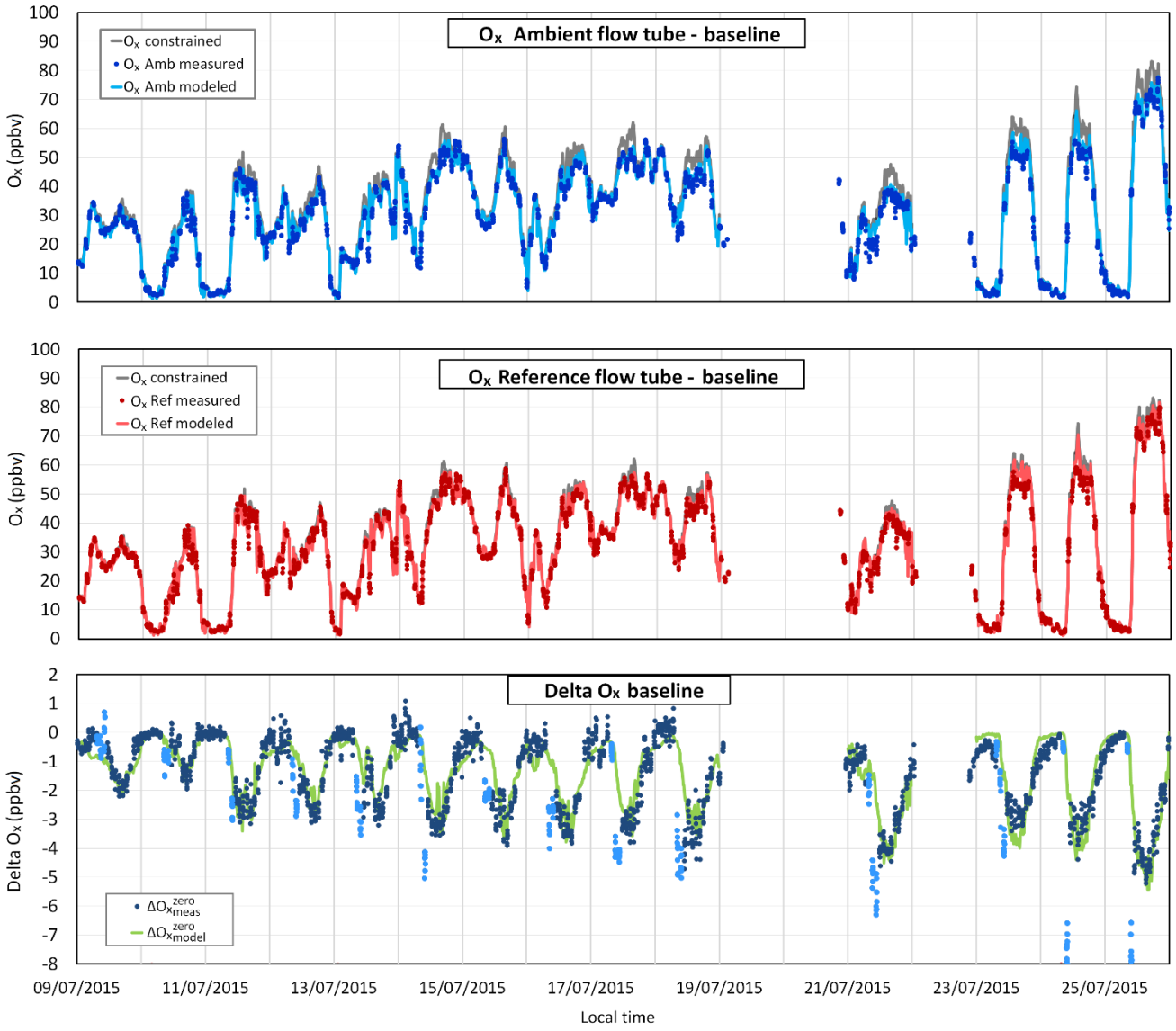

Figure 4.19: Comparison between measured and modeled O_x in the ambient flow tube (top panel), O_x in the reference flow tube (middle panel), and ΔO_x (bottom panel) during the baseline measurement step. The top and middle panels also display the model-constrained O_x mixing ratios. The light blue points in the bottom panel are ΔO_x measurements between 07:30 and 11:00.

The bottom panel of Fig. 4.19 also shows that ΔO_x^{zero} is well described by the model, following the variation of the J-values and exhibiting slightly negative values at night on most days. However, the sharp negative spikes observed during morning hours (7:30-11:00) cannot be reproduced (light blue circles). These negative spikes are thought to be linked to a physical or chemical surface-process leading to additional O_x losses in the ambient flow tube, which is initiated at sunrise when the solar irradiation reaches the flow tubes. This effect lasts for a 2-3 hours and may be due to the photolysis of chemical species adsorbed on the wall during nighttime. It is interesting to note that water condensation was usually observed on the walls of the flow tubes during this time window and some aqueous chemistry may be involved. Sensitivity tests

such as the release of HONO were performed to reproduce this feature but were unsuccessful. The morning data has therefore been discarded from further analyses.

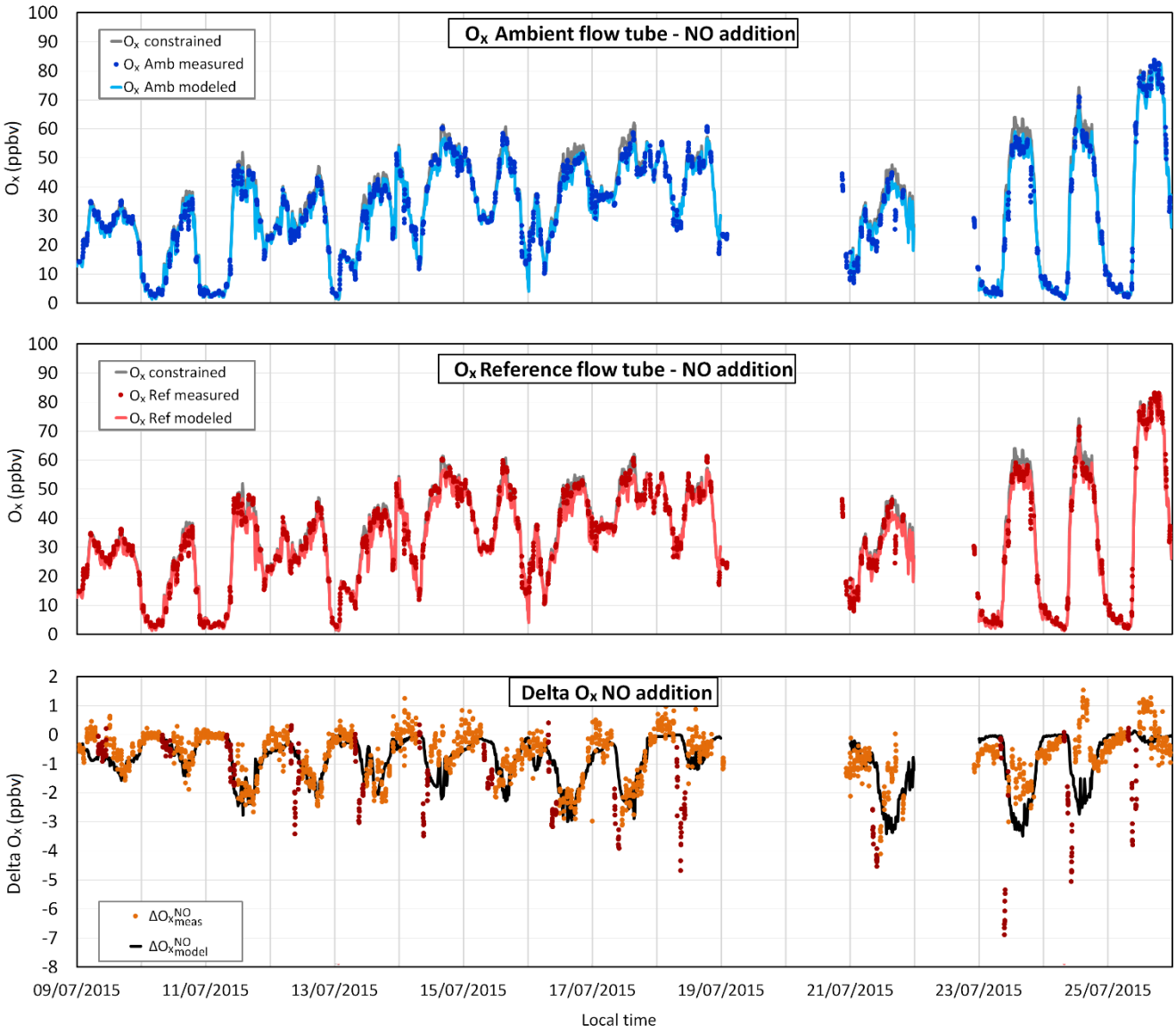

Figure 4.20: Comparison between measured and modeled O_x in the ambient flow tube (top panel), O_x in the reference flow tube (middle panel), and ΔO_x (bottom panel) during the NO addition measurement step. The top and middle panels also display the model-constrained O_x mixing ratios. The dark red points in the bottom panel are ΔO_x measurements between 07:30 and 11:00.

Regarding the NO addition step, modelled and measured O_x mixing ratios are also in good agreement, both for the ambient and reference flow tubes. For ΔO_x, however, despite the large level of scatter in the measured values, the model often underestimates the measurements by less than 1 ppbv in most cases.

Subtracting $\Delta O_{x_{model}}^{zero}$ from $\Delta O_{x_{model}}^{NO}$ and dividing by the residence time τ, one can calculate OS_{model} using Eq. 4.5. As explained in the previous section, OS_{model} is a combination of ozone production that

takes place in the ambient flow tube and a change in the amount of ozone lost on the walls of the flow tubes when NO is added. OS_{model}, along with OS_{meas} and $OS_{no\ losses}$ are presented in Fig. 4.21, together with the difference between OS_{model} and $OS_{no\ losses}$. It should be reminded here that OS_{meas} are the measured values, $OS_{no\ losses}$ shows what the OPR instrument should have measured if there were no losses in the flow tubes, and OS_{model} is the modeled values, including surface-O_3 losses in the model.

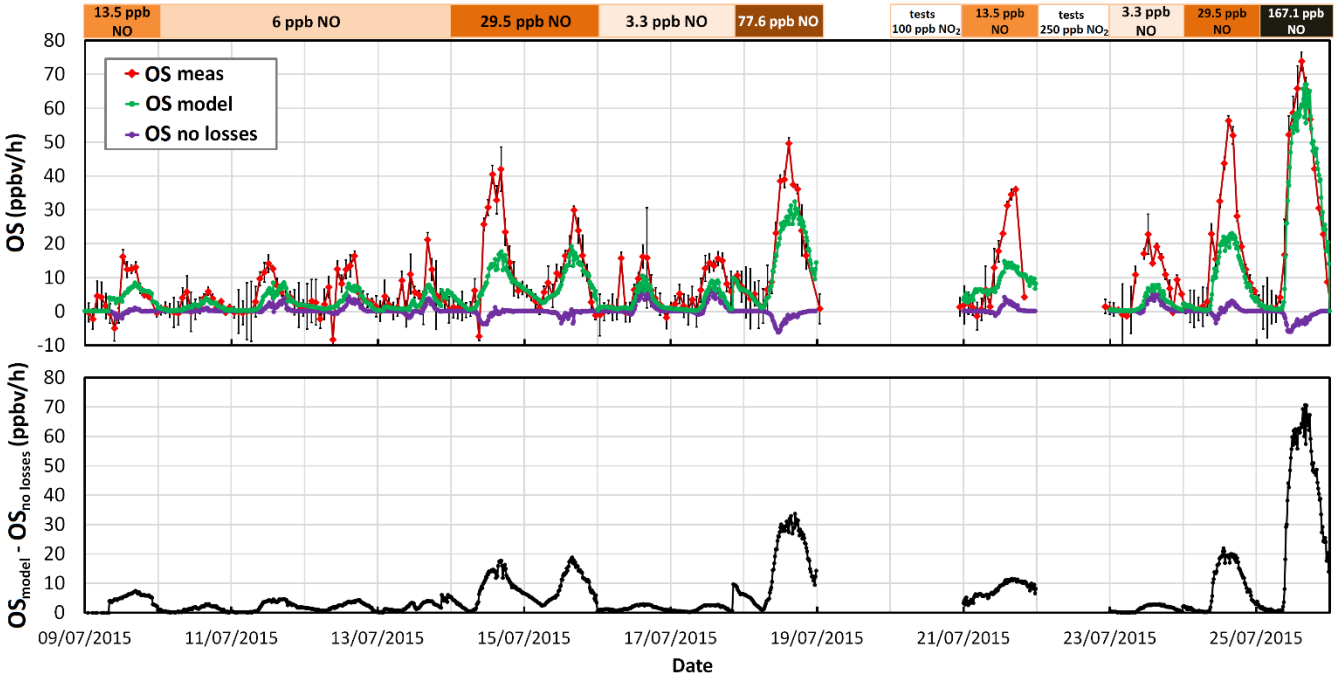

Figure 4.21: Comparison between OS_{meas}, OS_{model} and $OS_{no\ losses}$. The bottom panel displays the difference between OS_{model} and $OS_{no\ losses}$. Error bars are 1σ of the mean on the averaged 20-min measurements.

Figure 4.21 shows that OS_{model} is higher than $OS_{no\ losses}$, and in many cases close to the measured values (OS_{meas}). The difference between OS_{model} and $OS_{no\ losses}$, presented in the lower panel of Fig. 4.21, expresses the magnitude of the bias caused by a change in surface-O_3 losses when NO is added. As mentioned previously, NO converts a fraction of O_3 into NO_2, resulting in lower O_3 mixing ratios in the flow tubes and as a consequence, lower absolute ozone losses. The magnitude of this error varies significantly with the amount of NO added in the flow tubes. For additions of NO at 3.3 and 6 ppbv, the bias is lower than 3 and 5 ppbv/h, respectively. We can safely conclude that for low addition of NO (mixing ratios < 6 ppbv) the error on ozone sensitivity measurements will be lower than 5 ppbv/h.

However, while an absolute error of 5 ppbv/h seems low, it is on the order of the change in $P(O_3)$ that is expected in this environment when NO is added in the flow tubes. This error can even reach 10, 20 and up to 70 ppbv/h for additions of 13.5, 29.5 and 167 ppbv of NO, respectively, accounting almost completely

for OS_{meas}. At high NO mixing ratios, almost all the ozone is converted into NO_2 in the flow tubes and therefore, no O_3 is left to be lost on the walls of the flow tubes, shifting the baseline to almost zero. For example, the large value of OS_{meas} observed at 167 ppbv of NO is caused by a bias when subtracting the ΔO_x^{zero} baseline (Eq. 4.2).

Regarding the agreement between OS_{model} and OS_{meas}, one can see that the model underestimates the measurements. Since the ΔO_x^{zero} baseline is generally well reproduced by the model (Fig. 4.19), this underestimation is directly linked to the difference between $\Delta O_x^{NO}{}_{meas}$ and $\Delta O_x^{NO}{}_{model}$, as shown in Fig. 4.20. Assuming that the parameterization of O_x losses in the flow tubes is valid when NO is added, there seems to be a "missing $p(O_3)$" component that takes place in the ambient flow tube of the OPR instrument. The "missing $p(O_3)$" though, cannot be calculated only by the difference between OS_{meas} and OS_{model}; the additional ozone produced will further lead to a change in the O_3 mixing ratio in the ambient flow tube and as a consequence, to a change in surface-O_3 losses, impacting the measurement artifact. A procedure was developed to calculate the missing $p(O_3)$ and is described in the following section.

4.4.4 Missing P(O_3) modeling

The mechanism including ozone losses was modified to include an additional source of ozone in the ambient flow tube when NO is added. This methodology is based on the observation that O_x mixing ratios in the two flow tubes are well reproduced by the model during the baseline measurement step and that O_x mixing ratios in the reference flow tube are well reproduced during the NO addition step. The only missing component comes from the modeling of O_x in the ambient flow tube during NO addition.

The objective was to calculate the missing $p(O_3)$ by adjusting the strength of this additional source to get a good agreement between OS_{model} and OS_{meas}. The methodology is described below.

- The gross $p(O_3)$ in the ambient flow tube when NO is added was calculated as the rate of reaction between NO and peroxy radicals and is referred as $p(O_3)_{amb}^{NO}$.
- The "missing $p(O_3)$" was calculated from the difference between measured and modeled ΔO_x when NO is added, for a time window ranging from 11:00 to 18:00. This time window was chosen to skip the negative morning spike that was usually observed from 8:00-11:00 (see section 4.3.4). Additionally, the "missing $p(O_3)$" was calculated only when the measured ΔO_x was higher than the modelled one, and when their difference was quantifiable with the CAPS monitor, i.e. 0.1 ppbv. The missing $p(O_3)$ is calculated as:

$$p(O_3)_{missing} = \frac{\Delta O_{x_{meas}}^{NO} - \Delta O_{x_{model}}^{NO}}{\tau} \quad \text{(Eq. 4.10)}$$

- A factor F was calculated for each 15 min datapoint as the ratio between the additional ozone production rate needed and the rate modelled in the ambient flow tube:

$$F = \frac{p(O_3)_{missing}}{p(O_3)^{NO}_{amb}} \quad \text{(Eq. 4.11)}$$

This factor F is therefore zero for hours earlier than 11:00 and later than 18:00. It can also be zero if the difference between $\Delta O_{x\,meas}^{NO}$ and $\Delta O_{x\,model}^{NO}$ is lower than 0.1 ppbv.

- The model was run for the ambient flow tube when NO is added, including an additional gross ozone production, $p(O_3)_F$, with a rate calculated using Eq. 4.12:

$$p(O_3)_F = F\left(k_{HO_2+NO}[HO_2][NO] + \sum_i (k_{RO_{2,i}+NO}\Phi_i[RO_{2\,i}][NO])\right) \quad \text{(Eq. 4.12)}$$

- After running the model, the total net ozone production is calculated from Eq. 4.15, taking into account the additional production of ozone, as shown in Eq. 4.13.

$$p(O_3) = k_{HO_2+NO}[HO_2][NO] + \sum_i \left(k_{RO_{2,i}+NO}\Phi_i[RO_{2\,i}][NO]\right) + p(O_3)_F \quad \text{(Eq. 4.13)}$$

$$l(O_3) = k_{O(^1D)+H_2O}[O(^1D)][H_2O] + k_{OH+O_3}[OH][O_3] + k_{HO_2+O_3}[HO_2][O_3] + \sum_i k_{O_3+Alkene_i}[O_3][Alkene_i] + k_{OH+NO_2}[OH][NO_2] \quad \text{(Eq. 4.14)}$$

$$P(O_3)_{tot} = p(O_3) - l(O_3) \quad \text{(Eq. 4.15)}$$

- The final step of this procedure is to compare $OS_{model\,F}$ to OS_{meas}. If $OS_{model\,F}$ was found to be significantly higher than OS_{meas}, an iterative loop would be applied, refining F from the new $p(O_3)$ values generated by the model. In our case, it was seen that this step could be skipped.

Using the output of this model, we can calculate $\Delta O_{x\,model\,F}^{NO}$, and therefore $OS_{model\,F}$ using similar equations than Eqs. 4.4 and 4.5. Figure 4.22 presents measured and modelled $\Delta O_x{}^{NO}$, a comparison of $OS_{model\,F}$ to OS_{meas} and OS_{model}, as well as $P(O_3)_{tot}$ and $p(O_3)_F$. It should be noted here that $P(O_3)_{tot}$ as calculated from Eq. 4.15 is the final measured ozone production extracted by the model from OS_{meas}, while $p(O_3)_F$ expresses the missing ozone production. Additionally, since the missing ozone production was calculated only from 11:00 to 18:00, results of $OS_{model\,F}$, $P(O_3)_{tot}$ and $p(O_3)_F$ are only presented for this timeframe.

It can be seen that the agreement between measured and modeled $\Delta O_x{}^{NO}$ is improved compared to Fig. 4.20 and $OS_{model\,F}$ successfully describes OS_{meas} most of the time. However, although $\Delta O_{x\,meas}^{NO}$ is well reproduced by the model on 12 and 17 July, $OS_{model\,F}$ tends to be significantly lower than OS_{meas} on these days. This disagreement is due to a small overestimation of $\Delta O_{x\,meas}^{zero}$ by the model (Fig. 4.19). This overestimation is approximately 0.5 ppbv on average, which correspond to 1 – 1.5% of the ambient concentration of O_x (35-50 ppbv). It is unlikely that the parameterization introduced in the model to account

for surface-ozone losses could perform well enough to avoid such a small error in the modelling. The missing $p(O_3)$ values extracted from this analysis are therefore very uncertain and should be interpreted with caution.

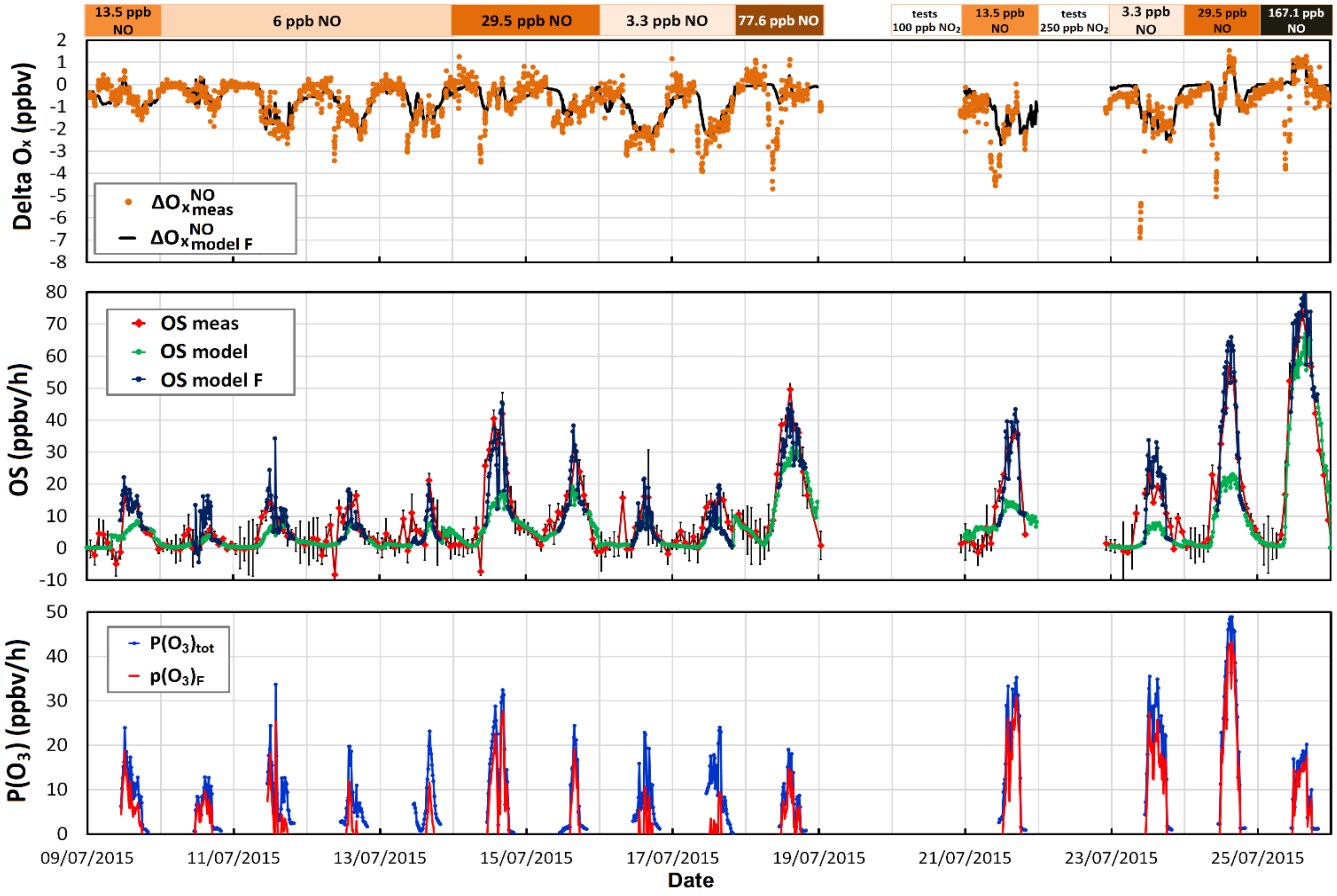

Figure 4.22: Time series of measured and modeled ΔO_x, OS and $P(O_3)$ values, including an additional ozone source in the model. Top panel: ΔO_x. Middle panel: OS_{meas}, OS_{model} and $OS_{model\ F}$. Bottom panel: missing ozone production rate inferred by the model, $p(O_3)_F$, and total ozone production rate inferred from the model, $P(O_3)_{tot}$.

The bottom panel of Fig. 4.22 shows the additional "missing $P(O_3)$", $p(O_3)_F$, that is needed to explain OP_{meas}, as well as the total ozone production rates, $P(O_3)_{tot}$, extracted from the model (Eq. 4.15). For NO addition levels up to 6 ppbv, $p(O_3)_F$ is lower than 10 ppbv/h on most days. For higher NO levels, $p(O_3)_F$ increases up to approximately 30 ppbv/h (14 and 21 July). On 23 July though, with a low NO mixing ratio of 3.3 ppbv, $p(O_3)_F$ is up to 30 ppbv/h and decreases to 15 ppb/h for a NO level of 78 ppbv.

During the last days of the campaign (21-25 July) unexpected high $p(O_3)_F$ are observed. As mentioned before, tests with high NO_2 levels had been performed on 20 and 22 of July (100 ppbv and 250 ppbv of NO_2 respectively), that are thought to have altered the wall coating of the flow tubes. For this reason, these

last four days have been excluded from further analysis. Additionally, 12 and 17 July are also discarded because of the disagreement between $OP_{model\,F}$ and OP_{meas} discussed above.

One objective of this campaign was to investigate the ozone production sensitivity to NO_x in this forested environment and to compare it to theoretical predictions, based on the modeling presented in section 4.4.2. Fig. 4.23 shows ozone production as a function of NO to investigate whether the model predicts a location of the turnover point between the NO_x and VOC-limited regimes that is consistent with the field observations. Note that NO mixing ratios indicated in Fig. 4.23 correspond to mixing ratios entering the flow tubes, after mixing in the sampling line. The model outputs have been averaged from 12:00 to 17:00 for each day and the three panels correspond to:

- the modeled theoretical ozone production: $P(O_3)_{th}$ (section 4.4.2)
- the missing gross ozone production: $p(O_3)_F$ (section 4.4.4, Eq. 4.13)
- the total ozone production: $P(O_3)_{tot}$, including $p(O_3)_F$ (section 4.4.4, Eq. 4.15)

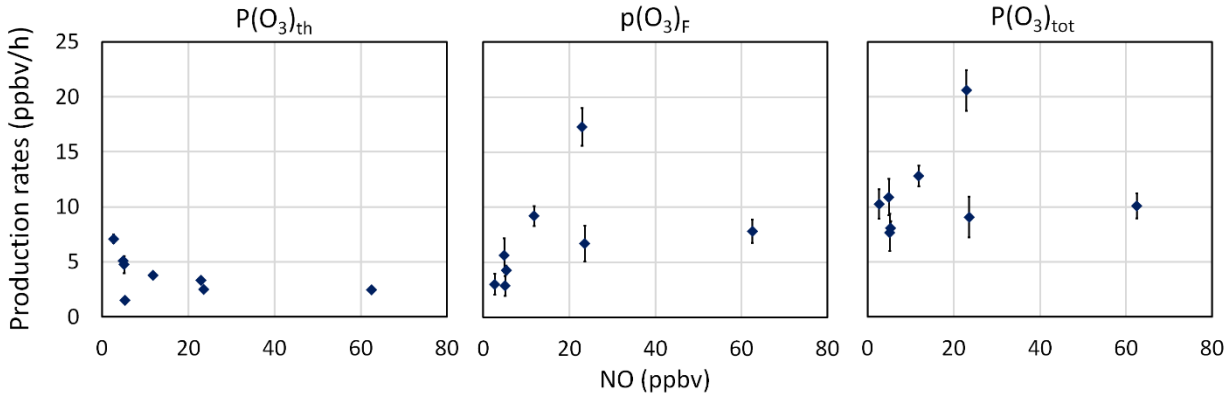

Figure 4.23: Ozone production as a function of NO: $P(O_3)_{th}$, $p(O_3)_F$ and $P(O_3)_{tot}$.

According to the base model (left panel in Fig. 4.23), the highest ozone production rates should occur around 3 ppbv of NO. After this point, ozone production decreases, indicating a VOC-limited regime. In addition, the highest ozone production rate should be close to 7.5 ppbv/h at approximately 3 ppbv of NO, while there is less than 3 ppbv/h of ozone production at 65 ppbv of NO.

The measurements (middle panel in Fig. 4.23), however, suggest that there is a missing gross ozone production of up to 18 ppbv/h. For NO mixing ratios lower than 10 ppbv, the missing $p(O_3)$ is low, e.g. less than 5 ppbv/h. While this production rate seems low, it would however significantly increase the total amount of ozone produced since the base model predicts ambient ozone production rates of only 5-10 ppbv/h. The highest missing $p(O_3)$ occurs between 10 and 20 ppbv of NO, while it drops for higher NO mixing ratios. For 65 ppbv of NO, the missing $p(O_3)$ is approximately 8 ppbv/h.

Including the missing $p(O_3)$ in the calculations of ozone production rates (Eqs. 4.13, 4.14, 4.15), the total production rate of O_3 (right panel in Fig. 4.23) suggests that ozone production in this environment can reach

up to 22 ppbv/h for NO levels near 20 ppbv, while there is a $P(O_3)_{tot}$ value of 9 ppbv/h at the same NO mixing ratio. Ozone production rates for lower or higher NO mixing ratios range between 7.5 – 13 ppbv/h. Therefore, there is no clear turnover point from a NO_x-limited to a NO_x-saturated regime, although it seems to be located between 5-30 ppbv of NO. Therefore, the model seems to underestimate the magnitude of ozone production by at least a factor 2 for NO mixing ratios higher than 6ppbv, as well as the NO level at which the turnover point occurs.

This disagreement between the model predictions and the field observations is consistent with other studies (Griffith et al., 2016;Brune et al., 2016;Ren et al., 2013;Spencer et al., 2009;Ren et al., 2003;Sheehy et al., 2010), showing that the turnover point for model-calculated $P(O_3)$ values is at lower NO levels than for $P(O_3)$ values calculated from peroxy radical measurements.

Sheehy et al. (2010) showed that $P(O_3)$ values calculated from measured peroxy radical concentrations during the MCMA-2003 field campaign were underestimated (factor 2) by the model (MCMv3.1) during morning hours, when NO_x were high (NO_x>25 ppbv),. Spencer et al. (2009) reached similar conclusions from an analysis of peroxynitric acid measurements performed during the MILAGRO 2006 field campaign for NO mixing ratios lower than 10 ppbv.. The authors reported lower measured-to-model $P(O_3)$ ratios, of less than a factor 2 in most cases. Their observations did not show a turnover point in contrast to the model.

In New York City (Ren et al., 2003), ozone production rates calculated from measured radical concentrations were higher than the modeled values by a factor 3 on average, for a NO mixing ratio of approximately 90 ppbv. This disagreement could reach almost a factor 10 at high radical production rates ($P(HO_x)$>4.7cm^3s^{-1}) and was still about a factor 2 at low radical production rates ($P(HO_x)$< 1.5cm^3s^{-1}). These authors highlighted the importance of the radical production rates for the agreement between model and measurement calculated $P(O_3)$. For a NO mixing ratio of approximately 10 ppbv, the measured-to-modeled $P(O_3)$ ratio was ranging from 2 to 4.

During the SHARP field campaign in Houston (Ren et al., 2013), the MOPS instrument was deployed to measure ozone production rates (Cazorla et al., 2012) and to compare the measurements with $P(O_3)$ values calculated from modeled and measured peroxy radicals. At a level of 10 ppbv of NO, $P(O_3)$ values calculated from measured radicals were higher than the modeled values by a factor 5, while the MOPS measurements were higher by only a factor 2. While there were differences between the direct MOPS measurements and the $P(O_3)$ calculations from radical measurements, both methods suggested that the models underpredict $P(O_3)$ at high NO levels.

Brune et al. (2016) compared modelled $P(O_3)$ with $P(O_3)$ values derived from measured HO_2 radicals and found a good agreement for NO mixing ratios lower than 1.5ppbv, but almost a factor 4 of disagreement

for NO mixing rations close to 10 ppbv with the models underestimating the measurements. Higher NO mixing ratios were not measured in this study. Additionally, almost 50% missing OH reactivity was reported during daytime. The authors suggested a missing chemical mechanism as described by reactions R 4.1–4.3 to explain a missing production of ozone in the models

$$OH + NO \rightarrow HONO^* \quad \text{(R 4.1)}$$

$$HONO^* + N_2 \rightarrow HONO \quad \text{(R 4.2)}$$

$$HONO^* + O_2 \rightarrow HO_2 + NO_2 \quad \text{(R 4.3)}$$

However, extensive laboratory study is needed to test the validity of this suggestion.

Finally, Griffith et al. (2016) used RACM2 to model the photochemistry during the CalNex campaign, where measured NO_x mixing ratios were lower than 40 ppbv. The authors showed that for OH reactivity values higher than 15 s^{-1} and NO_x mixing ratios higher than 10-15 ppbv, $P(O_3)$ values calculated from peroxy radical measurements were about 2 times higher than modeled values, even when the measured OH reactivity was constrained in the model to account for the missing OH reactivity observed during this campaign.

While large uncertainties are associated to the results presented in this chapter due to O_3-surface reactions in the current version of the OPR instrument and the use of a parameterization to account for wall losses in the model, these results together with previously published studies tend to suggest that atmospheric models underestimate ozone production rates and that the radical propagation chemistry, especially under high NO_x conditions, is not well understood. Future work could include the implementation of an explicit chemical mechanism (e.g. MCM) to test whether it can better reproduce the measured ozone production rates.

4.5 Conclusions on the field deployment of the OPR instrument

The OPR instrument was deployed in a forested environment near Bloomington, IN, as a part of the IRRONIC field campaign during July 2015. Tests performed at the beginning of the campaign revealed the difficulty to zero the instrument for ambient measurements. These tests highlighted a large photoenhanced surface-loss of ozone in the flow tubes, which disturbed the $P(O_3)$ measurements. No simple solution was found to zero the instrument and it was decided to focus the OPR measurements on investigating the $P(O_3)$ sensitivity to NO. This was achieved by introducing various amounts of NO into the sampling line of the OPR instrument.

Collocated measurements of meteorological parameters, organic and inorganic species, and J-values were used to constrain a box model. This model was used to calculate ozone production rates in ambient air and

in the two flow tubes of the OPR instrument. Simulations were also performed by adding the photoenhanced surface-loss of ozone in the flow tubes to help assess its impact on the OPR measurements. The loss of ozone was found to be dependent on J-values, ambient ozone and humidity and a parameterization including these variables was successfully used to model the OPR measurements. The simulations showed that adding NO in the flow tubes would lead to a significant bias in the measurements due to a change in the amount of ozone lost in the flow tubes. While the OPR measurements performed by adding NO were not directly usable to derive ozone production rates, it was however possible to infer the ozone production rates under different NO levels, as well as the change in ozone production due to the increase of NO, by combining the OPR measurements with a suitable modeling approach.

While it was possible to extract some information from the field observations of the OPR instrument, the derived values are highly uncertain. This work showed that the current version of the OPR instrument needs to be optimized to remove (or reduce to a negligible level) the photoenhanced surface-loss of ozone in the flow tubes. This represents a prerequisite to get an instrument capable of accurate and precise measurements of ozone production rates. Hints towards the optimization of the OPR instruments are given in the general conclusion of the manuscript.

Comparisons between the measured and modeled ambient $P(O_3)$ values showed two main disagreements; (i) the magnitude of $P(O_3)$ and (ii) the turnover point characterizing the NO_x-VOC sensitivity. The measured ozone production rates were at least two times higher than the modeled rates for NO mixing ratios higher than 6 ppbv, suggesting a "missing $p(O_3)$" component in the chemical mechanism. Additionally, the model predicted that the turnover point would occur at a NO mixing ratio lower than 3 ppbv, while the measurements did not exhibit a clear turnover point. These disagreements are consistent with previous studies, questioning our ability to successfully model ozone production rates and indicating that there are still unknowns in the chemistry of ozone formation. The results presented in this analysis will need to be confirmed when an optimized version of the OPR instrument is available.

Conclusions & Perspectives

Conclusions

An OPR instrument was developed in Mines Douai, in collaboration with the School of Public and Environmental Affairs from Indiana University. The objective was to (i) advance the technological understanding of direct ozone production rate measurements and (ii) improve our knowledge on the ozone formation chemistry. The OPR instrument was designed and characterized through both laboratory and modelling experiments, and was deployed in the field to evaluate its performances. This instrument differs significantly from the other two instruments of its kind, as it includes quartz flow tubes instead of Teflon sampling chambers, and uses an O_3-to-NO_2 conversion unit coupled to a NO_2 detection instead of a NO_2-to-O_3 conversion unit equipped with an ozone analyser.

The two sampling flow tubes were designed to minimize surface reactions that could disturb the $P(O_3)$ measurements. These flow tubes were characterized in the laboratory under specific field operating conditions leading to a residence time of 271 ± 13 (1σ) s, whose uncertainty will contribute to an error of 4.9% on the $P(O_3)$ measurements. Additionally, it was found that an air exchange time of approximately 20 min was necessary to observe a change in the measurements when the air composition varies at the inlet. This indicates that OPR measurements should be averaged on 20 min at least to be considered independent.

The quantification of O_x (O_3 and NO_2) surface-losses in the flow tubes revealed an O_3 loss under dark conditions in both flow tubes. This dark loss was lower than 5% when the flow tubes were clean (flushed with high O_3 mixing ratios under high humidity for a few days), but could increase to 10%-15% after a long use in the field. For this reason, periodic flushing periods with humid air and ozone during nighttime are suggested to keep the flow tubes clean. Regarding NO_2, losses lower than 3% were found in both flow tubes. A photoenhanced O_3 loss was also observed in the ambient flow tube, especially at wavelengths near 312 nm, which can be as high as 15%-20% of the ambient ozone. This photoenhanced loss was found to be dependent on J-values, O_3 concentrations and absolute humidity levels.

Laboratory tests were also performed to quantify HONO production rates in the flow tubes since it has been shown that NO_2 or other nitrogen-containing compounds can be converted to HONO on surfaces. A large production of HONO in the flow tubes could disturb the $P(O_3)$ measurements by increasing the oxidative capacity of the sampled air masses since HONO is a precursor of the hydroxyl radical. These tests showed HONO production rates in the ambient flow tube on the order of 10 and 60 ppbv/h under dark and irradiated conditions, respectively. In the reference flow tube, only dark HONO production was observed, at similar

levels than in the ambient flow tube. The HONO production rate was enhanced under UV radiation, but the magnitude of the rate was strongly dependent on the flow tube contamination (adsorbed compounds on the inner surface).

Two types of conversion unit/detection systems were built and characterized in the laboratory. The NO_2-to-O_3 conversion unit coupled to an ozone monitor exhibited an average conversion efficiency of approximately 70%. The conversion efficiency was found to be independent on relative humidity up to 75% RH. However, it was found that the NO_2-to-O_3 conversion efficiency depends on NO_2 levels and varies between 60 and 80% for an atmospheric relevant range of NO_2 mixing ratios (10-100 ppbv). In addition, it was found that the ozone monitor was significantly impacted by ambient humidity, with a change of up to 30% on the ozone reading when relative humidity was varied from 0 to 75%. On the other hand, a conversion efficiency of 99.9% was achieved for the O_3-to-NO_2 converter coupled to a NO_2 monitor (CAPS) by titrating O_3 with NO. The O_3-to-NO_2 conversion efficiency is independent of O_3 mixing ratios and humidity. The only issue with this converter is the addition of NO_2 impurities together with NO, which was on the order of a few ppbv. The later leads to a higher background NO_2 measurement from the CAPS monitor and as a consequence, to a small degradation of the measurement precision. Overall, it was shown that the O_3-to-NO_2 conversion scheme proposed in this work presents significant advantages compared to the O_3-to-NO_2 scheme. This new method was chosen to be used on the Mines Douai OPR instrument in contrast to the other ozone production rate instruments.

A modelling study was carried out to assess the accuracy of $P(O_3)$ measurements using field measurements from two previous urban field campaigns performed in Mexico City (MCMA-2006) and in Pasadena (CalNex-2010). The principle of the OPR instrument was tested, i.e. (i) checking that $P(O_3)$ in the ambient flow tube is equal to $P(O_3)$ in the ambient atmosphere, and (ii) $P(O_3)$ in the reference flow tube is not significant. It was found that a significant underestimation of ambient $P(O_3)$ values (10-20%) by the instrument could be due to a non-zero O_x production in the reference flow tube, which is mainly caused by radical initiation through O_3-alkene reactions. Sensitivity tests were also carried out in this modelling study to assess the impact of possible sources of errors on the $P(O_3)$ measurements. These tests were based on the results of the laboratory characterization discussed above. The sensitivity tests showed that a lower-than-100% conversion efficiency for the O_3-to-NO_2 conversion unit can have a strong impact on $P(O_3)$ measurements, leading to an overestimation of ambient $P(O_3)$ values. On the other hand, it was shown that the NO_2-to-O_3 conversion unit exhibits a 99.9% conversion efficiency, which is more suitable for the OPR instrument since it will not lead a bias on the measurement. The ozone surface-loss in the flow tubes and a possible temperature increase of the reference flow tube were found to cause an underestimation of the measurements, while a NO_2 surface-loss in the flow tubes, a production of HONO on surfaces and the

dilution of the sampled air masses could cause an overestimation of the measurements. Combining the different sources of errors, upper limits of approximately -58% and +57% were quantified for the underestimations and overestimations discussed above. The positive and negative errors will cancel out to some extent and the total accuracy is likely better than the two bounds given above.

The OPR instrument was deployed in the field during July 2015 in Bloomington, IN, as a part of the IRRONIC field campaign. This field deployment allowed investigating the limits of the OPR instrument. It was found that the surface-losses of O_3 (dark and photoenhanced) in the flow tubes lead to a non-zero baseline for the measurements and the photoenhanced surface-loss makes difficult to zero the instrument. No reliable method was found to zero the instrument and there is a need to develop such a method.

As a consequence of our inability to zero the instrument the OPR measurements were focused on investigating the $P(O_3)$ sensitivity to NO by adding various amounts of NO into the sampling line of the instrument. The instrument sampled ambient air without NO addition for 40 minutes and NO was then added for another 40 minutes measurement period. This pattern was repeated all along the campaign measuring ΔO_x for each step and changing the level of NO every one or two days. Changes in ozone production rates were quantified from the difference in ΔO_x between these two steps. Once again, it was shown that the photoenhanced surface-loss of O_3 in the flow tubes was disturbing the measurements since the consumption of O_3 by NO during its addition was altering the O_3 concentration in the flow tubes and, as a consequence, the total amount of ozone lost in the tubes. A modelling methodology was developed to extract changes in ozone production rates due to the addition of NO from the disturbed OPR measurements. For this purpose, ozone production was modelled in the two flow tubes to reproduce the OPR measurements, including O_x surface-loss terms in the model. It was shown that the model was not capable to reproduce the measurements when NO was added, indicating a potential "missing $p(O_3)$" component taking place under higher-than ambient NO mixing ratios. Measured ozone production rates were peaking at approximately 20 ppbv/h, which is higher than the model predictions by at least a factor 2 for NO mixing ratios higher than 6 ppbv. Additionally, the measurements suggested that the transition from a NO_x-limited to a VOC-limited regime takes place between 10 and 20 ppbv of NO, while the model indicated a turnover at a few ppbv of NO (<3 ppbv).

We cannot rule out the possibility that the measured changes in ozone production presented in chapter 4 are not due to a wrong parameterization of the O_3 loss in the model or an unknown artifact. However, even if the methodology used in chapter 4 leads to a high level of uncertainty, these results are consistent with recent studies of atmospheric radical measurements performed in urban environments suggesting that ozone production rates are not well reproduced by current atmospheric chemical mechanisms.

To sum up, the new OPR instrument constructed at Mines Douai was successfully characterized and used in the field, showing promising results for direct ozone production measurements. The O_3-to-NO_2 conversion system and the CAPS monitor are thought to be more suitable for $P(O_3)$ measurements. As every new instrument, there are still technical issues to be resolved, but this study definitely contributed to expand our knowledge on ozone production measurements, suggesting several improvements for this technique and broadening the opportunities of $P(O_3)$ measurements intercomparisons.

Perspectives

This work has shown the current performances and limitations of the Mines Douai OPR instrument, which can now be further improved.

First of all, the characterization experiments and the field results highlighted the impact of photoenhanced wall reactions on the OPR measurements. Therefore, a new flow tube design should be implemented in order to minimize these wall effects. A suggestion would be a wide opening in the flow tubes that can be even as large as the diameter of the tube, including a honeycomb to achieve a laminar flow. Recirculation eddies would be avoided and a laminar plug flow would be achieved in the flow tubes. It should be noted that a honeycomb is currently used on the Birmingham OPR instrument (William Bloss'group) and smoke tests have shown that a uniform laminar flow can be achieved. Additionally, the diameter of the flow tube can be increased in order to decrease the total surface-to-volume ratio, and the length of the flow tubes can be decreased together with an increase of the total flow rate to reduce the contact-time between trace gases and the walls. A shorter residence time would also decrease the air-exchange-time necessary to produce independent measurements of $P(O_3)$.

However, attention should be payed to keep a minimum residence time that enables radical species to build-up in the flow tubes. Even if the inlet is wide open, radical species can still be lost on the surface of the honeycomb and will need time to build-up to their initial atmospheric levels. It should be reminded that, as shown from the modelling performed in chapter 3 when initial radical concentrations were set at zero, a stable concentration of radicals can be achieved after approximately 2 min of residence time in the flow tubes.

There is definitely more work to be done with the fluid dynamics simulations. Star CCM+ is a powerful tool that can be used to design an optimized geometry, with the goal to further decrease gas-surface interactions. For example, the percentage of molecules at the center of the flow tubes that have been in contact with the walls could be quantified to help identifying the best geometry. More importantly, a chemical mechanism including surface reactions should be included in the STAR CCM+ simulations to

quantify how the concentrations of various chemical species would change along the flow tube on both the radical and axial dimensions.

Regarding the deployment of the instrument in the field, this work has shown that the instrument can be used to study the sensitivity of $P(O_3)$ to NO. However, a method to zero the instrument needs to be developed for ambient $P(O_3)$ measurements (even if the future version of the OPR is less sensitive to surface reactions). One way would be to introduce a radical scavenger in the flow tubes to stop ozone production, but we were not able to find a suitable compound so far.

An important novelty of the Mines Douai OPR instrument is the lamp cover. This cover allows extending the use of the OPR instrument to well characterized synthetic air mixtures of O_3, NO_x, VOCs and water. Comparing the OPR measurements performed on these synthetic mixtures with modelling results will allow checking our understanding of ozone formation in simple chemical systems.

Finally, the OPR instrument was also used during the PROPHET-AMOS (Program for Research on Oxidants: Photochemistry, Emissions and Transport – Atmospheric Oxidants in Summer) field campaign performed in a forested environment in northern Michigan during July 2016. As for the IRRONIC field campaign, NO_x levels in this environment were low and the OPR measurements focused on investigating the $P(O_3)$ sensitivity to NO. Five different levels of NO were used from 0.5 ppbv to 10 ppbv, which is a range were low artifacts are expected. An important difference with the IRRONIC campaign was that the flow tubes were placed inside the laboratory and were constantly irradiated by the UV lamps, leading to constant J-values and constant NO levels. Therefore, any change observed in $P(O_3)$ should be directly linked to VOC concentrations and OH reactivity. The results from this campaign will be contrasted to that observed during the IRRONIC campaign.

References

Akimoto, H.: Global Air Quality and Pollution, Science, 302, 1716-1719, 2003.

Aksoyoglu, S., Keller, J., Oderbolz, D. C., Barmpadimos, I., Prévôt, A. S. H., and Baltensperger, U.: Sensitivity of ozone and aerosols to precursor emissions in Europe, International Journal of Environment and Pollution, 50, 451-459, 2012.

Ashmore, M. R.: Assessing the future global impacts of ozone on vegetation, Plant, Cell & Environment, 28, 949-964, 2005.

Atkinson, R., Baulch, D. L., Cox, R. A., Crowley, J. N., Hampson, R. F., Hynes, R. G., Jenkin, M. E., Rossi, M. J., and Troe, J.: Evaluated kinetic and photochemical data for atmospheric chemistry: Volume I - gas phase reactions of O_x, HO_x, NO_x and SO_x species, Atmos. Chem. Phys., 4, 1461-1738, 2004.

Atkinson, R. B., D.L.; Cox, R.A.; Hampson Jr., R.F.; Kerr, J.A.; Troe, J.: Evaluated Kinetic and Photochemical Data for Atmospheric Chemistry: Supplement III, J. Phys. Chem. Ref. Data, 18, 881 - 1097, 1989.

Aumont, B.: Modélisation de la chimie troposphérique, Diplome d'habilitation à diriger les recherches, Université Paris 12 – Val de Marne UFR de Sciences et Technologie, 2005.

Australian Gov.: National standards for criteria air pollutants in Australia, Air quality fact sheet, Australian Government, Department of the Environment and Heritage, http://www.environment.gov.au/protection/publications/factsheet-national-standards-criteria-airpollutants-australia, 2005.

Avnery, S., Mauzerall, D. L., Liu, J., and Horowitz, L. W.: Global crop yield reductions due to surface ozone exposure: 2. Year 2030 potential crop production losses and economic damage under two scenarios of O_3 pollution, Atmospheric Environment, 45, 2297-2309, 2011.

Badol, C., Borbon, A., Locoge, N., Léonardis, T., and Galloo, J.-C.: An automated monitoring system for VOC ozone precursors in ambient air: development, implementation and data analysis, Analytical and Bioanalytical Chemistry, 378, 1815-1827, 2004.

Baier, B. C., Brune, W. H., Lefer, B. L., Miller, D. O., and Martins, D. K.: Direct ozone production rate measurements and their use in assessing ozone source and receptor regions for Houston in 2013, Atmospheric Environment, 114, 83-91, 2015.

Beekmann, M., Ancellet, G., Blonsky, S., De Muer, D., Ebel, A., Elbern, H., Hendricks, J., Kowol, J., Mancier, C., Sladkovic, R., Smit, H. G. J., Speth, P., Trickl, T., and Van Haver, P.: Regional and Global Tropopause Fold Occurrence and Related Ozone Flux Across the Tropopause, J Atmos Chem, 28, 29-44, 1997.

Biswas, G., Breuer, M., and Durst, F.: Backward-Facing Step Flows for Various Expansion Ratios at Low and Moderate Reynolds Numbers, Journal of Fluids Engineering, 126, 362-374, 10.1115/1.1760532, 2004.

Bojkov, R. D.: Surface Ozone During the Second Half of the Nineteenth Century, Journal of Climate and Applied Meteorology, 25, 343-352, 1986.

Bottorff, B., Stevens, P. S., Lew, M., Sigler, P. R., and Dusanter, S.: Measurements of Nitrous Acid (HONO) in an Indiana Forest by Laser Photofragmentation/Laser-induced Flourescence (LP/LIF), Poster, AGU Fall meeting, American Geophysical Union, 2015.

Brune, W. H., Stevens, P. S., and Mather, J. H.: Measuring OH and HO_2 in the Troposphere by Laser-Induced Fluorescence at Low Pressure, Journal of the Atmospheric Sciences, 52, 3328-3336, 1995.

Brune, W. H., Baier, B. C., Thomas, J., Ren, X., Cohen, R. C., Pusede, S. E., Browne, E. C., Goldstein, A. H., Gentner, D. R., Keutsch, F. N., Thornton, J. A., Harrold, S., Lopez-Hilfiker, F. D., and Wennberg, P. O.: Ozone production chemistry in the presence of urban plumes, Faraday Discussions, 189, 169-189, 2016.

Byun, D., and Schere, K. L.: Review of the Governing Equations, Computational Algorithms, and Other Components of the Models-3 Community Multiscale Air Quality (CMAQ) Modeling System, Applied Mechanics Reviews, 59, 51-77, 10.1115/1.2128636, 2006.

CAI-Asia: Air Quality in Asia: Status and Trends - 2010 Edition, Clean Air Initiative for Asian Cities Center, Pasig City, Philippines, 2010.

Carter, W. P. L.: Documentation of the SAPRC-99 chemical mechanism for VOC reactivity assessment, Final Report to California Air Resources Board, Air Pollution Research Center and College of Engineering, 1999.

Carter, W. P. L.: Development of the SAPRC-07 chemical mechanism and updated ozone reactiviy scales, Final Report to the California Air Resources Board Contract No. 03-318, College of Engineering, University of California, 2007.

Cazorla, M., and Brune, W. H.: Measurement of Ozone Production Sensor, Atmos. Meas. Tech., 3, 545-555, 2010.

Cazorla, M., Brune, W. H., Ren, X., and Lefer, B.: Direct measurement of ozone production rates in Houston in 2009 and comparison with two estimation methods, Atmos. Chem. Phys., 12, 1203-1212, 10.5194/acp-12-1203-2012, 2012.

CCME: 2013: Progress Report on the Canada-Wide Standards for Particulate Matter and Ozone, PN1495, Canadian Council of Ministers of the Environment, 2013.

Chang, R. Y. W., Sullivan, R. C., and Abbatt, J. P. D.: Initial uptake of ozone on Saharan dust at atmospheric relative humidities, Geophysical Research Letters, 32, 2005.

Chen, H., Stanier, C. O., Young, M. A., and Grassian, V. H.: A Kinetic Study of Ozone Decomposition on Illuminated Oxide Surfaces, The Journal of Physical Chemistry A, 115, 11979-11987, 2011.

Chen, S., Ren, X., Mao, J., Chen, Z., Brune, W. H., Lefer, B., Rappenglück, B., Flynn, J., Olson, J., and Crawford, J. H.: A comparison of chemical mechanisms based on TRAMP-2006 field data, Atmospheric Environment, 44, 4116-4125, 2010.

Crawford, J., Davis, D., Olson, J., Chen, G., Liu, S., Gregory, G., Barrick, J., Sachse, G., Sandholm, S., Heikes, B., Singh, H., and Blake, D.: Assessment of upper tropospheric HO_x sources over the tropical Pacific based on NASA GTE/PEM data: Net effect on HO_x and other photochemical parameters, Journal of Geophysical Research: Atmospheres, 104, 16255-16273, 1999.

Daum, P. H., Kleinman, L., Imre, D. G., Nunnermacker, L. J., Lee, Y. N., Springston, S. R., Newman, L., and Weinstein-Lloyd, J.: Analysis of the processing of Nashville urban emissions on July 3 and July 18, 1995, Journal of Geophysical Research: Atmospheres, 105, 9155-9164, 2000.

Davis, D. D., Chen, G., Chameides, W., Bradshaw, J., Sandholm, S., Rodgers, M., Schendal, J., Madronich, S., Sachse, G., Gregory, G., Anderson, B., Barrick, J., Shipham, M., Collins, J., Wade, L., and Blake, D.: A photostationary state analysis of the NO_2-NO system based on airborne observations from the subtropical/tropical North and South Atlantic, Journal of Geophysical Research: Atmospheres, 98, 23501-23523, 1993.

Dolgorouky, C., Gros, V., Sarda-Esteve, R., Sinha, V., Williams, J., Marchand, N., Sauvage, S., Poulain, L., Sciare, J., and Bonsang, B.: Total OH reactivity measurements in Paris during the 2010 MEGAPOLI winter campaign, Atmos. Chem. Phys., 12, 9593-9612, 2012.

Dorn, H.-P., Brandenburger, U., Brauers, T., and Hausmann, M.: A New In Situ Laser Long-Path Absorption Instrument for the Measurement of Tropospheric OH Radicals, Journal of the Atmospheric Sciences, 52, 3373-3380, 1995.

Dusanter, S., Vimal, D., Stevens, P. S., Volkamer, R., and Molina, L. T.: Measurements of OH and HO_2 concentrations during the MCMA-2006 field campaign – Part 1: Deployment of the Indiana University laser-induced fluorescence instrument, Atmos. Chem. Phys., 9, 1665-1685, 2009a.

Dusanter, S., Vimal, D., Stevens, P. S., Volkamer, R., Molina, L. T., Baker, A., Meinardi, S., Blake, D., Sheehy, P., Merten, A., Zhang, R., Zheng, J., Fortner, E. C., Junkermann, W., Dubey, M., Rahn, T., Eichinger, B., Lewandowski, P., Prueger, J., and Holder, H.: Measurements of OH and HO_2 concentrations during the MCMA-2006 field campaign – Part 2: Model comparison and radical budget, Atmos. Chem. Phys., 9, 6655-6675, 2009b.

Dusanter, S., and Stevens, P. S.: Recent Advances in the Chemistry of OH and HO_2 Radicals in the Atmosphere: Field and Laboratory Measurements, Book chapter, to be published, 2016.

Ebeling, D., Patel, V., Findlay, M., and Stetter, J.: Electrochemical ozone sensor and instrument with characterization of the electrode and gas flow effects, Sensors and Actuators B: Chemical, 137, 129-133, 2009.

Edwards, G. D., Cantrell, C. A., Stephens, S., Hill, B., Goyea, O., Shetter, R. E., Mauldin, R. L., 3rd, Kosciuch, E., Tanner, D. J., and Eisele, F. L.: Chemical ionization mass spectrometer instrument for the measurement of tropospheric HO_2 and RO_2, Analytical chemistry, 75, 5317-5327, 2003.

EEA: 2007: Air Pollution in Europe 1990–2004, EEA Report No 2/2007, European Environment Agency, Copenhagen, 2007.

EEA: 2013: Air quality in Europe, EEA Report No 9/2013, European Environment Agency, Copenhagen, 2013.

EEA: 2015: Air quality in Europe, EEA Report No 5/2015, European Environment Agency, Copenhagen, 2015.

Ehhalt, D. H.: Radical Ideas, Science, 279, 1002-1003, 1998.

Eisele, F. L., and Tanner, D. J.: Ion-assisted tropospheric OH measurements, Journal of Geophysical Research: Atmospheres, 96, 9295-9308, 1991.

ENVIRON: User's Guide to the Comprehensive Air Quality Modeling System with Extensions (CAMx), Version 3.10, 2002.

EPA: 2006: Air Quality Criteria for Ozone and Related Photochemical Oxidants (Final Report), United States Environmental Protection Agency, Washington, DC, 2006.

EPA: 2012: Health Effects of Ozone in the General Population, United States Environmental Protection Agency, http://www3.epa.gov/apti/ozonehealth/population.html, 2012.

EPA: 2015 National Ambient Air Quality Standards (NAAQS) for Ozone, United States Environmental Protection Agency, http://www.epa.gov/ozone-pollution/2015-national-ambient-air-quality-standards-naaqs-ozone, 2015a.

EPA: 2015 Ozone Standards, United States Environmental Protection Agency, ozoneairqualitystandards.epa.gov/OAR_OAQPS/OzoneSliderApp/index.html, 2015b.

EU: 2008: Air Quality Standards, Directive 2008/50/EC of the European Parliament and of the Council of 21 May 2008 on ambient air quality and cleaner air for Europe, http://ec.europa.eu/environment/air/quality/standards.htm, 2008.

Fast, J. D., Zaveri, R. A., Bian, X., Chapman, E. G., and Easter, R. C.: Effect of regional-scale transport on oxidants in the vicinity of Philadelphia during the 1999 NE-OPS field campaign, Journal of Geophysical Research: Atmospheres, 107, 13-11 - 13-22, 2002.

Filleul, L., Cassadou, S., Medina, S., Fabres, P., Lefranc, A., Eilstein, D., Le Tertre, A., Pascal, L., Chardon, B., Blanchard, M., Declercq, C., Jusot, J. F., Prouvost, H., and Ledrans, M.: The relation between temperature, ozone, and mortality in nine French cities during the heat wave of 2003, Environmental health perspectives, 114, 1344-1347, 2006.

Finlayson-Pitts, B. J., and Pitts, J. N.: Chemistry of the upper and lower atmosphere; Theory, Experiments, and Applications, Academic Press, ISBN: 978-970-912-257060-257065, 1999.

Finlayson-Pitts, B. J., Wingen, L. M., Sumner, A. L., Syomin, D., and Ramazan, K. A.: The heterogeneous hydrolysis of NO_2 in laboratory systems and in outdoor and indoor atmospheres: An integrated mechanism, Physical Chemistry Chemical Physics, 5, 223-242, 2003.

Fowler, D., Flechard, C., Skiba, U. T. E., Coyle, M., and Cape, J. N.: The atmospheric budget of oxidized nitrogen and its role in ozone formation and deposition, New Phytologist, 139, 11-23, 1998.

Fowler, D., Amann, M., Anderson, R., Ashmore, M., Cox, P., Depledge, M., Derwent, D., Grennfelt, P., Hewitt, N., Hov, O., Jenkin, M., Kelly, F., Liss, P., Pilling, M., Pyle, J., Slingo, J., and Stevenson, D.: Ground-level ozone in the 21st century: future trends, impacts and policy implications, Royal Society Policy Document 15/08, The Royal Society, 2008.

Fuchs, H., Holland, F., and Hofzumahaus, A.: Measurement of tropospheric RO_2 and HO_2 radicals by a laser-induced fluorescence instrument, The Review of scientific instruments, 79, 084104, 2008.

Fuchs, H., Ball, S. M., Bohn, B., Brauers, T., Cohen, R. C., Dorn, H. P., Dubé, W. P., Fry, J. L., Häseler, R., Heitmann, U., Jones, R. L., Kleffmann, J., Mentel, T. F., Müsgen, P., Rohrer, F., Rollins, A. W., Ruth, A. A., Kiendler-Scharr, A., Schlosser, E., Shillings, A. J. L., Tillmann, R., Varma, R. M., Venables, D. S., Villena Tapia, G., Wahner, A., Wegener, R., Wooldridge, P. J., and Brown, S. S.: Intercomparison of measurements of NO_2 concentrations in the atmosphere simulation chamber SAPHIR during the NO_3 Comp campaign, Atmos. Meas. Tech., 3, 21-37, 2010.

Fuchs, H., Bohn, B., Hofzumahaus, A., Holland, F., Lu, K. D., Nehr, S., Rohrer, F., and Wahner, A.: Detection of HO_2 by laser-induced fluorescence: calibration and interferences from RO_2 radicals, Atmos. Meas. Tech., 4, 1209-1225, 2011.

Fuchs, H., Dorn, H. P., Bachner, M., Bohn, B., Brauers, T., Gomm, S., Hofzumahaus, A., Holland, F., Nehr, S., Rohrer, F., Tillmann, R., and Wahner, A.: Comparison of OH concentration measurements by DOAS and LIF during SAPHIR chamber experiments at high OH reactivity and low NO concentration, Atmos. Meas. Tech., 5, 1611-1626, 2012.

Funk, J. L., Jones, C. G., Gray, D. W., Throop, H. L., Hyatt, L. A., and Lerdau, M. T.: Variation in isoprene emission from Quercus rubra: Sources, causes, and consequences for estimating fluxes, Journal of Geophysical Research: Atmospheres, 110, 2005.

Gao, R. S., Ballard, J., Watts, L. A., Thornberry, T. D., Ciciora, S. J., McLaughlin, R. J., and Fahey, D. W.: A compact, fast UV photometer for measurement of ozone from research aircraft, Atmos. Meas. Tech., 5, 2201-2210, 2012.

Gardner, E. P., Sperry, P. D., and Calvert, J. G.: Primary quantum yields of NO_2 photodissociation, Journal of Geophysical Research: Atmospheres, 92, 6642-6652, 1987.

Garnica, R. M., Appel, M. F., Eagan, L., McKeachie, J. R., and Benter, T.: A REMPI Method for the Ultrasensitive Detection of NO and NO_2 Using Atmospheric Pressure Laser Ionization Mass Spectrometry, Analytical chemistry, 72, 5639-5646, 2000.

Geng, F., Tie, X., Guenther, A., Li, G., Cao, J., and Harley, P.: Effect of isoprene emissions from major forests on ozone formation in the city of Shanghai, China, Atmos. Chem. Phys., 11, 10449-10459, 2011.

Goliff, W. S., Stockwell, W. R., and Lawson, C. V.: The regional atmospheric chemistry mechanism, version 2, Atmospheric Environment, 68, 174-185, 2013.

Gregory, G. L., Hoell, J. M., Carroll, M. A., Ridley, B. A., Davis, D. D., Bradshaw, J., Rodgers, M. O., Sandholm, S. T., Schiff, H. I., Hastie, D. R., Karecki, D. R., Mackay, G. I., Harris, G. W., Torres, A. L., and Fried, A.: An intercomparison of airborne nitrogen dioxide instruments, Journal of Geophysical Research: Atmospheres, 95, 10103-10127, 1990.

Griffith, S. M., Hansen, R. F., Dusanter, S., Stevens, P. S., Alaghmand, M., Bertman, S. B., Carroll, M. A., Erickson, M., Galloway, M., Grossberg, N., Hottle, J., Hou, J., Jobson, B. T., Kammrath, A., Keutsch, F. N., Lefer, B. L., Mielke, L. H., O'Brien, A., Shepson, P. B., Thurlow, M., Wallace, W., Zhang, N., and Zhou, X. L.: OH and HO_2 radical chemistry during PROPHET 2008 and CABINEX 2009 - Part 1: Measurements and model comparison, Atmos. Chem. Phys., 13, 5403-5423, 2013.

Griffith, S. M., Hansen, R. F., Dusanter, S., Michoud, V., Gilman, J. B., Kuster, W. C., Veres, P. R., Graus, M., de Gouw, J. A., Roberts, J., Young, C., Washenfelder, R., Brown, S. S., Thalman, R., Waxman, E., Volkamer, R., Tsai, C., Stutz, J., Flynn, J. H., Grossberg, N., Lefer, B., Alvarez, S. L., Rappenglueck, B., Mielke, L. H., Osthoff, H. D., and Stevens, P. S.: Measurements of hydroxyl and hydroperoxy radicals during CalNex-LA: Model comparisons and radical budgets, Journal of Geophysical Research: Atmospheres, 121, 4211-4232, 2016.

Guerreiro, C. B. B., Foltescu, V., and de Leeuw, F.: Air quality status and trends in Europe, Atmospheric Environment, 98, 376-384, 2014.

Hanisch, F., and Crowley, J. N.: Ozone decomposition on Saharan dust: an experimental investigation, Atmos. Chem. Phys., 3, 119-130, 2003.

Hanke, M., Uecker, J., Reiner, T., and Arnold, F.: Atmospheric peroxy radicals: ROXMAS, a new mass-spectrometric methodology for speciated measurements of HO_2 and ΣRO_2 and first results, International Journal of Mass Spectrometry, 213, 91-99, 2002.

Hansen, R. F., Griffith, S. M., Dusanter, S., Rickly, P. S., Stevens, P. S., Bertman, S. B., Carroll, M. A., Erickson, M. H., Flynn, J. H., Grossberg, N., Jobson, B. T., Lefer, B. L., and Wallace, H. W.: Measurements of total hydroxyl radical reactivity during CABINEX 2009 - Part 1: field measurements, Atmos. Chem. Phys., 14, 2923-2937, 2014.

Hansen, R. F., Blocquet, M., Schoemaecker, C., Léonardis, T., Locoge, N., Fittschen, C., Hanoune, B., Stevens, P. S., Sinha, V., and Dusanter, S.: Intercomparison of the comparative reactivity method (CRM) and pump–probe technique for measuring total OH reactivity in an urban environment, Atmos. Meas. Tech., 8, 4243-4264, 2015.

Hard, T. M., George, L. A., and O'Brien, R. J.: FAGE Determination of Tropospheric HO and HO_2, Journal of the Atmospheric Sciences, 52, 3354-3372, 1995.

Harder, J. W., Brault, J. W., Johnston, P. V., and Mount, G. H.: Temperature dependent NO_2 cross sections at high spectral resolution, Journal of Geophysical Research: Atmospheres, 102, 3861-3879, 1997.

Hausmann, M., Brandenburger, U., Brauers, T., and Dorn, H. P.: Detection of tropospheric OH radicals by long-path differential-optical-absorption spectroscopy: Experimental setup, accuracy, and precision, Journal of Geophysical Research: Atmospheres, 102, 16011-16022, 1997.

Heard, D.: Analytical Techniques for Atmospheric Measurement, Wiley-Blackwell, ISBN: 978-1-4051-2357-0, 2006.

Hens, K., Novelli, A., Martinez, M., Auld, J., Axinte, R., Bohn, B., Fischer, H., Keronen, P., Kubistin, D., Nölscher, A. C., Oswald, R., Paasonen, P., Petäjä, T., Regelin, E., Sander, R., Sinha, V., Sipilä, M., Taraborrelli, D., Tatum Ernest, C., Williams, J., Lelieveld, J., and Harder, H.: Observation and modelling of HO_x radicals in a boreal forest, Atmos. Chem. Phys., 14, 8723-8747, 2014.

Hornbrook, R. S., Crawford, J. H., Edwards, G. D., Goyea, O., Mauldin Iii, R. L., Olson, J. S., and Cantrell, C. A.: Measurements of tropospheric HO_2 and RO_2 by oxygen dilution modulation and chemical ionization mass spectrometry, Atmos. Meas. Tech., 4, 735-756, 2011.

Ianni, J. C.: Kintecus, Windows Version 5.20, www.kintecus.com, 2014.

INECC: Normas Mexicanas de Calidad del Aire, Instituto Nacional de Ecología y Cambio Climático, NOM-020-SSA1-1993, 2002.

Ingham, T., Goddard, A., Whalley, L. K., Furneaux, K. L., Edwards, P. M., Seal, C. P., Self, D. E., Johnson, G. P., Read, K. A., Lee, J. D., and Heard, D. E.: A flow-tube based laser-induced fluorescence instrument to measure OH reactivity in the troposphere, Atmos. Meas. Tech., 2, 465-477, 2009.

IPCC: Summary for Policymakers, Climate Change 2013: The Physical Science Basis., Contribution of Working Group I to the Fifth Assessment Report of the Intergovernmental Panel on Climate Change, Cambridge University Press, Cambridge, United Kingdom and New York, NY, USA, 2013a.

IPCC: Working Group I contribution to the IPCC Fifth Assessment Report "Climate Change 2013: The Physical Science Basis", Final Draft Underlying Scientific-Technical Assessment, Intergovernmental Panel on Climate Change, 2013b.

Isebrands, J. G., Guenther, A. B., Harley, P., Helmig, D., Klinger, L., Vierling, L., Zimmerman, P., and Geron, C.: Volatile organic compound emission rates from mixed deciduous and coniferous forests in Northern Wisconsin, USA, Atmospheric Environment, 33, 2527-2536, 1999.

Jacob, D. J., and Winner, D. A.: Effect of climate change on air quality, Atmospheric Environment, 43, 51-63, 2009.

Jaeglé, L., Jacob, D. J., Brune, W. H., and Wennberg, P. O.: Chemistry of HO_x radicals in the upper troposphere, Atmospheric Environment, 35, 469-489, 2001.

Jeffries, H. E.: An experimental method for measuring the rate of synthesis, destruction, and transport of ozone in the lower atmosphere, E.S.E. Publication No. 285, Ph.D. Thesis, Department of Environmental Science and Engineering, 1971.

Jenkin, M. E., Saunders, S. M., and Pilling, M. J.: The tropospheric degradation of volatile organic compounds: a protocol for mechanism development, Atmospheric Environment, 31, 81-104, 1997.

Jenkin, M. E., Saunders, S. M., Wagner, V., and Pilling, M. J.: Protocol for the development of the Master Chemical Mechanism, MCM v3 (Part B): tropospheric degradation of aromatic volatile organic compounds, Atmos. Chem. Phys., 3, 181-193, 2003.

Jerrett , M., Burnett , R. T., Pope , C. A. I., Ito , K., Thurston , G., Krewski , D., Shi , Y., Calle , E., and Thun , M.: Long-Term Ozone Exposure and Mortality, New England Journal of Medicine, 360, 1085-1095, 2009.

Johnston, H. S., Davis, H. F., and Lee, Y. T.: NO_3 Photolysis Product Channels: Quantum Yields from Observed Energy Thresholds, The Journal of Physical Chemistry, 100, 4713-4723, 1996.

Kahan, T. F., Kwamena, N. O. A., and Donaldson, D. J.: Heterogeneous ozonation kinetics of polycyclic aromatic hydrocarbons on organic films, Atmospheric Environment, 40, 3448-3459, 2006.

Kanaya, Y., Sadanaga, Y., Hirokawa, J., Kajii, Y., and Akimoto, H.: Development of a Ground-Based LIF Instrument for Measuring HO_x Radicals: Instrumentation and Calibrations, Journal of Atmospheric Chemistry, 38, 73-110, 2001.

Kanaya, Y., and Akimoto, H.: Direct Measurements of HO_x Radicals in the Marine Boundary Layer: Testing the Current Tropospheric Chemistry Mechanism, The Chemical Record, 2, 199-211, 2002.

Kanaya, Y., Cao, R., Akimoto, H., Fukuda, M., Komazaki, Y., Yokouchi, Y., Koike, M., Tanimoto, H., Takegawa, N., and Kondo, Y.: Urban photochemistry in central Tokyo: 1. Observed and modeled OH and HO_2 radical concentrations during the winter and summer of 2004, Journal of Geophysical Research: Atmospheres, 112, 2007.

Kebabian, P. L., Herndon, S. C., and Freedman, A.: Detection of nitrogen dioxide by cavity attenuated phase shift spectroscopy, Anal. Chem., 77, 724-728, 2005.

Kebabian, P. L., Wood, E. C., Herndon, S. C., and Freedman, A.: A practical alternative to chemiluminescence-based detection of nitrogen dioxide: cavity attenuated phase shift spectroscopy, Environ Sci. Technol., 42, 6040-6045, 2008.

Keywood, M., Kanakidou, M., Stohl, A., Dentener, F., Grassi, G., Meyer, C. P., Torseth, K., Edwards, D., Thompson, A. M., Lohmann, U., and Burrows, J.: Fire in the Air: Biomass Burning Impacts in a Changing Climate, Critical Reviews in Environmental Science and Technology, 43, 40-83, 2013.

Kim, S.-R., Hong, H.-K., Kwon, C. H., Yun, D. H., Lee, K., and Sung, Y. K.: Ozone sensing properties of In_2O_3-based semiconductor thick films, Sensors and Actuators B: Chemical, 66, 59-62, 2000.

Kim, S., Guenther, A., Karl, T., and Greenberg, J.: Contributions of primary and secondary biogenic VOC tototal OH reactivity during the CABINEX (Community Atmosphere-Biosphere INteractions Experiments)-09 field campaign, Atmos. Chem. Phys., 11, 8613-8623, 2011.

Kleinman, L. I.: Low and high NOx tropospheric photochemistry, Journal of Geophysical Research: Atmospheres, 99, 16831-16838, 1994.

Kleinman, L. I., Daum, P. H., Imre, D. G., Lee, J. H., Lee, Y.-N., Nunnermacker, L. J., Springston, S. R., Weinstein-Lloyd, J., and Newman, L.: Ozone production in the New York City urban plume, Journal of Geophysical Research: Atmospheres, 105, 14495-14511, 2000.

Kleinman, L. I., Daum, P. H., Lee, Y.-N., Nunnermacker, L. J., Springston, S. R., Weinstein-Lloyd, J., and Rudolph, J.: Sensitivity of ozone production rate to ozone precursors, Geophysical Research Letters, 28, 2903-2906, 2001.

Kleinman, L. I., Daum, P. H., Imre, D., Lee, Y. N., Nunnermacker, L. J., Springston, S. R., Weinstein-Lloyd, J., and Rudolph, J.: Ozone production rate and hydrocarbon reactivity in 5 urban areas: A cause of high ozone concentration in Houston, Geophysical Research Letters, 29, 105-101-105-104, 2002.

Kleinman, L. I.: The dependence of tropospheric ozone production rate on ozone precursors, Atmospheric Environment, 39, 575-586, 2005.

Kley, D., and McFarland, M.: Chemiluminescence detector for NO and NO_2, Atmos. Tech., 12, 63-69, 1980.

Kovacs, T. A., and Brune, W. H.: Total OH Loss Rate Measurement, J Atmos Chem, 39, 105-122, 2001.

Kukui, A., Ancellet, G., and Le Bras, G.: Chemical ionisation mass spectrometer for measurements of OH and Peroxy radical concentrations in moderately polluted atmospheres, Journal of Atmospheric Chemistry, 61, 133-154, 2009.

Kumar, V., and Sinha, V.: VOC–OHM: A new technique for rapid measurements of ambient total OH reactivity and volatile organic compounds using a single proton transfer reaction mass spectrometer, International Journal of Mass Spectrometry, 374, 55-63, 2014.

Kwamena, N.-O. A., Earp, M. E., Young, C. J., and Abbatt, J. P. D.: Kinetic and Product Yield Study of the Heterogeneous Gas−Surface Reaction of Anthracene and Ozone, The Journal of Physical Chemistry A, 110, 3638-3646, 2006.

Laufs, S., and Kleffmann, J.: Investigations on HONO formation from photolysis of adsorbed HNO3 on quartz glass surfaces, Physical Chemistry Chemical Physics, 18, 9616-9625, 2016.

Leighton, P. A.: Photochemistry of Air Pollution, Elsevier, New York, 1961.

Lelieveld, J., Butler, T. M., Crowley, J. N., Dillon, T. J., Fischer, H., Ganzeveld, L., Harder, H., Lawrence, M. G., Martinez, M., Taraborrelli, D., and Williams, J.: Atmospheric oxidation capacity sustained by a tropical forest, Nature, 452, 737-740, 2008.

Leston, A. R., Ollison, W. M., Spicer, C. W., and Satola, J.: Potential interference bias in ozone standard compliance monitoring, Journal of the Air & Waste Management Association (1995), 55, 1464-1472, 2005.

Lew, M., Dusanter, S., Liljegren, J. A., Bottorff, B., and Stevens, P. S.: Measurement of interferences associated with the detection of the hydroperoxy radical in the atmosphere using laser-induced fluorescence, Abstract A13D-0243, presented at 2013 Fall Meeting, AGU, San Francisco, Calif., 2013.

Lew, M., Bottorff, B., Sigler, P. R., Stevens, P. S., Sklaveniti, S., Leonardis, T., Locoge, N., Dusanter, S., Kundu, S., Deming, B., Wood, E. C. D., and Gentner, D. R.: HOx Radical Chemistry in an Indiana Forest Environment: Measurement and Model Comparison, Conference talk, AGU Fall meeting, American Geophysical Union, 2015.

Lew, M. M., Dusanter, S., and Stevens, P. S.: Measurement of interferences associated with the detection of the hydroperoxy radical in the atmosphere using laser-induced fluorescence, to be submitted.

Li, Y. Q., Demerjian, K. L., Zahniser, M. S., Nelson, D. D., McManus, J. B., and Herndon, S. C.: Measurement of formaldehyde, nitrogen dioxide, and sulfur dioxide at Whiteface Mountain using a dual tunable diode laser system, Journal of Geophysical Research: Atmospheres, 109, 2004.

Liu, Y., Morales-Cueto, R., Hargrove, J., Medina, D., and Zhang, J.: Measurements of peroxy radicals using chemical amplification-cavity ringdown spectroscopy, Environmental science & technology, 43, 7791-7796, 2009.

Lou, S., Holland, F., Rohrer, F., Lu, K., Bohn, B., Brauers, T., Chang, C. C., Fuchs, H., Häseler, R., Kita, K., Kondo, Y., Li, X., Shao, M., Zeng, L., Wahner, A., Zhang, Y., Wang, W., and Hofzumahaus, A.: Atmospheric OH reactivities in the Pearl River Delta – China in summer 2006: measurement and model results, Atmos. Chem. Phys., 10, 11243-11260, 2010.

Lu, K. D., Hofzumahaus, A., Holland, F., Bohn, B., Brauers, T., Fuchs, H., Hu, M., Häseler, R., Kita, K., Kondo, Y., Li, X., Lou, S. R., Oebel, A., Shao, M., Zeng, L. M., Wahner, A., Zhu, T., Zhang, Y. H., and Rohrer, F.: Missing OH source in a suburban environment near Beijing: observed and modelled OH and HO_2 concentrations in summer 2006, Atmos. Chem. Phys., 13, 1057-1080, 2013.

Madronich, S., and Flocke, S.: The Role of Solar Radiation in Atmospheric Chemistry, in: Environmental Photochemistry, edited by: Boule, P., The Handbook of Environmental Chemistry, Springer Berlin Heidelberg, 1-26, 1999.

Manion, J. A., Huie, R. E., Levin, R. D., Jr., D. R. B., Orkin, V. L., Tsang, W., McGivern, W. S., Hudgens, J. W., Knyazev, V. D., Atkinson, D. B., Chai, E., Tereza, A. M., Lin, C. Y., Allison, T. C., Mallard, W. G., Westley, F., Herron, J. T., Hampson, R. F., and Frizzell, D. H.: NIST Chemical Kinetics Database, NIST

Standard Reference Database 17, Version 7.0 (Web Version), Release 1.6.8, Data version 2015.12, 20899-28320, 2015.

Mao, J., Ren, X., Chen, S., Brune, W. H., Chen, Z., Martinez, M., Harder, H., Lefer, B., Rappenglück, B., Flynn, J., and Leuchner, M.: Atmospheric oxidation capacity in the summer of Houston 2006: Comparison with summer measurements in other metropolitan studies, Atmospheric Environment, 44, 4107-4115, 2010.

Mao, J., Ren, X., Zhang, L., Van Duin, D. M., Cohen, R. C., Park, J. H., Goldstein, A. H., Paulot, F., Beaver, M. R., Crounse, J. D., Wennberg, P. O., DiGangi, J. P., Henry, S. B., Keutsch, F. N., Park, C., Schade, G. W., Wolfe, G. M., Thornton, J. A., and Brune, W. H.: Insights into hydroxyl measurements and atmospheric oxidation in a California forest, Atmos. Chem. Phys., 12, 8009-8020, 2012.

Martinez, M., Harder, H., Kovacs, T. A., Simpas, J. B., Bassis, J., Lesher, R., Brune, W. H., Frost, G. J., Williams, E. J., Stroud, C. A., Jobson, B. T., Roberts, J. M., Hall, S. R., Shetter, R. E., Wert, B., Fried, A., Alicke, B., Stutz, J., Young, V. L., White, A. B., and Zamora, R. J.: OH and HO_2 concentrations, sources, and loss rates during the Southern Oxidants Study in Nashville, Tennessee, summer 1999, Journal of Geophysical Research: Atmospheres, 108, 2003.

Mazzuca, G. M., Ren, X., Loughner, C. P., Estes, M., Crawford, J. H., Pickering, K. E., Weinheimer, A. J., and Dickerson, R. R.: Ozone Production and Its Sensitivity to NO_x and VOCs: Results from the DISCOVER-AQ Field Experiment, Houston 2013, Atmos. Chem. Phys. Discuss., 2016, 1-27, 2016.

McKeachie, J. R., van der Veer, W. E., Short, L. C., Garnica, R. M., Appel, M. F., and Benter, T.: Selective ultra-trace detection of NO and NO in complex gas mixtures using broad-bandwidth REMPI mass spectrometry, Analyst, 126, 1221-1228, 2001.

Mebust, A. K., Russell, A. R., Hudman, R. C., Valin, L. C., and Cohen, R. C.: Characterization of wildfire NO_x emissions using MODIS fire radiative power and OMI tropospheric NO_2 columns, Atmos. Chem. Phys., 11, 5839-5851, 2011.

Michel, A. E., Usher, C. R., and Grassian, V. H.: Heterogeneous and catalytic uptake of ozone on mineral oxides and dusts: A Knudsen cell investigation, Geophysical Research Letters, 29, 10-11-10-14, 2002.

Michoud, V., Kukui, A., Camredon, M., Colomb, A., Borbon, A., Miet, K., Aumont, B., Beekmann, M., Durand-Jolibois, R., Perrier, S., Zapf, P., Siour, G., Ait-Helal, W., Locoge, N., Sauvage, S., Afif, C., Gros, V., Furger, M., Ancellet, G., and Doussin, J. F.: Radical budget analysis in a suburban European site during the MEGAPOLI summer field campaign, Atmos. Chem. Phys., 12, 11951-11974, 2012.

Mills, G., and Harmens, H.: Impacts of ozone pollution on food security in Europe, Working Group on Effects of the Convention on Long-range Transboundary Air Pollution, Centre for Ecology & Hydrology, Bangor, UK, 2012.

Miyazaki, K., Eskes, H. J., Sudo, K., and Zhang, C.: Global lightning NO_x production estimated by an assimilation of multiple satellite data sets, Atmos. Chem. Phys., 14, 3277-3305, 2014.

Molina, L. T., and Molina, M. J.: Absolute absorption cross sections of ozone in the 185- to 350-nm wavelength range, Journal of Geophysical Research: Atmospheres, 91, 14501-14508, 1986.

Monks, P. S.: Gas-phase radical chemistry in the troposphere, Chemical Society Reviews, 34, 376-395, 2005.

Mount, G. H., and Harder, J. W.: The Measurement of Tropospheric Trace Gases at Fritz Peak Observatory, Colorado, by Long-Path Absorption: OH and Ancillary Gases, Journal of the Atmospheric Sciences, 52, 3342-3353, 1995.

Ndour, M., D'Anna, B., George, C., Ka, O., Balkanski, Y., Kleffmann, J., Stemmler, K., and Ammann, M.: Photoenhanced uptake of NO_2 on mineral dust: Laboratory experiments and model simulations, Geophysical Research Letters, 35, 2008.

Nicolas, M., Ndour, M., Ka, O., D'Anna, B., and George, C.: Photochemistry of Atmospheric Dust: Ozone Decomposition on Illuminated Titanium Dioxide, Environmental science & technology, 43, 7437-7442, 2009.

Nölscher, A. C., Sinha, V., Bockisch, S., Klüpfel, T., and Williams, J.: Total OH reactivity measurements using a new fast Gas Chromatographic Photo-Ionization Detector (GC-PID), Atmos. Meas. Tech., 5, 2981-2992, 10.5194/amt-5-2981-2012, 2012a.

Nölscher, A. C., Williams, J., Sinha, V., Custer, T., Song, W., Johnson, A. M., Axinte, R., Bozem, H., Fischer, H., Pouvesle, N., Phillips, G., Crowley, J. N., Rantala, P., Rinne, J., Kulmala, M., Gonzales, D., Valverde-Canossa, J., Vogel, A., Hoffmann, T., Ouwersloot, H. G., Vilà-Guerau de Arellano, J., and Lelieveld, J.: Summertime total OH reactivity measurements from boreal forest during HUMPPA-COPEC 2010, Atmos. Chem. Phys., 12, 8257-8270, 2012b.

Ollison, W. M., Crow, W., and Spicer, C. W.: Field testing of new-technology ambient air ozone monitors, Journal of the Air & Waste Management Association (1995), 63, 855-863, 2013.

Orlando, J. J., and Tyndall, G. S.: Laboratory studies of organic peroxy radical chemistry: an overview with emphasis on recent issues of atmospheric significance, Chemical Society reviews, 41, 6294-6317, 2012.

Orphal, J., Fellows, C. E., and Flaud, P. M.: The visible absorption spectrum of NO_3 measured by high-resolution Fourier transform spectroscopy, Journal of Geophysical Research: Atmospheres, 108, 2003.

Parker, A. E., Amédro, D., Schoemaecker, C., and Fittschen, C.: OH Radical Reactivity Measurements by FAGE, Environmental Engineering Management, 10, 107-114, 2011.

Philipp, H. R., Le Grand, D. G., Cole, H. S., and Liu, Y. S.: The optical properties of a polyetherimide, Polymer Engineering & Science, 29, 1574-1578, 1989.

Platt, U., Perner, D., and Pätz, H. W.: Simultaneous measurement of atmospheric CH_2O, O_3, and NO_2 by differential optical absorption, Journal of Geophysical Research: Oceans, 84, 6329-6335, 1979.

Prinn, R. G.: Ozone, Hydroxyl Radical, and Oxidative Capacity, Book Chapter, Treatise on Geochemistry, 1-19, 2003.

Proffitt, M. H., and McLaughlin, R. J.: Fast-response dual-beam UV-absorption ozone photometer suitable for use on stratospheric balloons, Review of Scientific Instruments, 54, 1719-1728, 1983.

Pugh, T. A. M., MacKenzie, A. R., Hewitt, C. N., Langford, B., Edwards, P. M., Furneaux, K. L., Heard, D. E., Hopkins, J. R., Jones, C. E., Karunaharan, A., Lee, J., Mills, G., Misztal, P., Moller, S., Monks, P. S., and Whalley, L. K.: Simulating atmospheric composition over a South-East Asian tropical rainforest: performance of a chemistry box model, Atmos. Chem. Phys., 10, 279-298, 2010.

Ramazan, K. A., Syomin, D., and Finlayson-Pitts, B. J.: The photochemical production of HONO during the heterogeneous hydrolysis of NO_2, Physical Chemistry Chemical Physics, 6, 3836-3843, 2004.

Reid, N., Yap, D., and Bloxam, R.: The potential role of background ozone on current and emerging air issues: An overview, Air Quality, Atmosphere & Health, 1, 19-29, 2008.

Ren, X., Harder, H., Martinez, M., Lesher, R. L., Oliger, A., Simpas, J. B., Brune, W. H., Schwab, J. J., Demerjian, K. L., He, Y., Zhou, X., and Gao, H.: OH and HO_2 Chemistry in the urban atmosphere of New York City, Atmospheric Environment, 37, 3639-3651, 2003.

Ren, X., Mao, J., Brune, W. H., Cantrell, C. A., Mauldin Iii, R. L., Hornbrook, R. S., Kosciuch, E., Olson, J. R., Crawford, J. H., Chen, G., and Singh, H. B.: Airborne intercomparison of HOx measurements using laser-induced fluorescence and chemical ionization mass spectrometry during ARCTAS, Atmos. Meas. Tech., 5, 2025-2037, 2012.

Ren, X., van Duin, D., Cazorla, M., Chen, S., Mao, J., Zhang, L., Brune, W. H., Flynn, J. H., Grossberg, N., Lefer, B. L., Rappenglück, B., Wong, K. W., Tsai, C., Stutz, J., Dibb, J. E., Thomas Jobson, B., Luke, W. T., and Kelley, P.: Atmospheric oxidation chemistry and ozone production: Results from SHARP 2009 in Houston, Texas, Journal of Geophysical Research: Atmospheres, 118, 5770-5780, 2013.

Ridley, B. A., Grahek, F. E., and Walega, J. G.: A Small High-Sensitivity, Medium-Response Ozone Detector Suitable for Measurements from Light Aircraft, Journal of Atmospheric and Oceanic Technology, 9, 142-148, 1992.

Rohrer, F., Bohn, B., Brauers, T., Brüning, D., Johnen, F. J., Wahner, A., and Kleffmann, J.: Characterisation of the photolytic HONO-source in the atmosphere simulation chamber SAPHIR, Atmos. Chem. Phys., 5, 2189-2201, 2005.

Roukos, J., Plaisance, H., Leonardis, T., Bates, M., and Locoge, N.: Development and validation of an automated monitoring system for oxygenated volatile organic compounds and nitrile compounds in ambient air, J. Chromatogr. A., 1216, 8642-8651, 2009.

Ryerson, T. B., Williams, E. J., and Fehsenfeld, F. C.: An efficient photolysis system for fast-response NO_2 measurements, Journal of Geophysical Research: Atmospheres, 105, 26447-26461, 2000.

Ryerson, T. B., Andrews, A. E., Angevine, W. M., Bates, T. S., Brock, C. A., Cairns, B., Cohen, R. C., Cooper, O. R., de Gouw, J. A., Fehsenfeld, F. C., Ferrare, R. A., Fischer, M. L., Flagan, R. C., Goldstein, A. H., Hair, J. W., Hardesty, R. M., Hostetler, C. A., Jimenez, J. L., Langford, A. O., McCauley, E., McKeen, S. A., Molina, L. T., Nenes, A., Oltmans, S. J., Parrish, D. D., Pederson, J. R., Pierce, R. B., Prather, K., Quinn, P. K., Seinfeld, J. H., Senff, C. J., Sorooshian, A., Stutz, J., Surratt, J. D., Trainer, M., Volkamer, R., Williams, E. J., and Wofsy, S. C.: The 2010 California Research at the Nexus of Air Quality and Climate Change (CalNex) field study, Journal of Geophysical Research: Atmospheres, 118, 5830-5866, 2013.

Sadanaga, Y., Matsumoto, J., Sakurai, K.-i., Isozaki, R., Kato, S., Nomaguchi, T., Bandow, H., and Kajii, Y.: Development of a measurement system of peroxy radicals using a chemical amplification/laser-induced fluorescence technique, Review of Scientific Instruments, 75, 864-872, 2004a.

Sadanaga, Y., Yoshino, A., Watanabe, K., Yoshioka, A., Wakazono, Y., Kanaya, Y., and Kajii, Y.: Development of a measurement system of OH reactivity in the atmosphere by using a laser-induced pump and probe technique, Review of Scientific Instruments, 75, 2648-2655, 2004b.

Saunders, S. M., Jenkin, M. E., Derwent, R. G., and Pilling, M. J.: Protocol for the development of the Master Chemical Mechanism, MCM v3 (Part A): tropospheric degradation of non-aromatic volatile organic compounds, Atmos. Chem. Phys., 3, 161-180, 2003.

Scharko, N. K., Berke, A. E., and Raff, J. D.: Release of Nitrous Acid and Nitrogen Dioxide from Nitrate Photolysis in Acidic Aqueous Solutions, Environmental science & technology, 48, 11991-12001, 2014.

Schlosser, E., Brauers, T., Dorn, H. P., Fuchs, H., Häseler, R., Hofzumahaus, A., Holland, F., Wahner, A., Kanaya, Y., Kajii, Y., Miyamoto, K., Nishida, S., Watanabe, K., Yoshino, A., Kubistin, D., Martinez, M., Rudolf, M., Harder, H., Berresheim, H., Elste, T., Plass-Dülmer, C., Stange, G., and Schurath, U.: Technical Note: Formal blind intercomparison of OH measurements: results from the international campaign HOxComp, Atmos. Chem. Phys., 9, 7923-7948, 2009.

Seinfeld, J. H., and Pandis, S. N.: Atmospheric Chemistry and Physics: From Air Pollution to Climate Change, Wiley, 2006.

Sheehy, P. M., Volkamer, R., Molina, L. T., and Molina, M. J.: Oxidative capacity of the Mexico City atmosphere – Part 2: A RO_x radical cycling perspective, Atmos. Chem. Phys., 10, 6993-7008, 2010.

Shetter, R. E., Cantrell, C. A., Lantz, K. O., Flocke, S. J., Orlando, J. J., Tyndall, G. S., Gilpin, T. M., Fischer, C. A., Madronich, S., Calvert, J. G., and Junkermann, W.: Actinometric and radiometric

measurement and modeling of the photolysis rate coefficient of ozone to $O(^1D)$ during Mauna Loa Observatory Photochemistry Experiment 2, Journal of Geophysical Research: Atmospheres, 101, 14631-14642, 1996.

Shirley, T. R., Brune, W. H., Ren, X., Mao, J., Lesher, R., Cardenas, B., Volkamer, R., Molina, L. T., Molina, M. J., Lamb, B., Velasco, E., Jobson, T., and Alexander, M.: Atmospheric oxidation in the Mexico City Metropolitan Area (MCMA) during April 2003, Atmos. Chem. Phys., 6, 2753-2765, 2006.

Sigler, P. R., Bottorff, B., Lew, M., Stevens, P., Léonardis, T., Locoge, N., Dusanter, S., Kundu, S., Deming, B., Wood, E., and Gentner, D.: OH radical reactivity in an Indiana Forest: Measurements and model comparisons, Poster, AGU Fall meeting, American Geophysical Union, 2015.

Sillman, S., Logan, J. A., and Wofsy, S. C.: The sensitivity of ozone to nitrogen oxides and hydrocarbons in regional ozone episodes, Journal of Geophysical Research: Atmospheres, 95, 1837-1851, 1990.

Sillman, S.: Tropospheric Ozone: The Debate over Control Strategies, Annual Review of Energy and the Environment, 18, 31-56, 1993.

Sillman, S.: The use of NO_y, H_2O_2 and HNO_3 as indicators for O_3-NO_x-VOC sensitivity in urban locations, J. Geophys. Res., 100, 175 - 114, 1995.

Sillman, S., He, D., Cardelino, C., and Imhoff, R. E.: The Use of Photochemical Indicators to Evaluate Ozone-NO_x-Hydrocarbon Sensitivity: Case Studies from Atlanta, New York, and Los Angeles, Journal of The Air & Waste Management Association, 47, 1030-1040, 1997.

Sillman, S., He, D., Pippin, M. R., Daum, P. H., Imre, D. G., Kleinman, L. I., Lee, J. H., and Weinstein-Lloyd, J.: Model correlations for ozone, reactive nitrogen, and peroxides for Nashville in comparison with measurements: Implications for O3-NO x -hydrocarbon chemistry, Journal of Geophysical Research: Atmospheres, 103, 22629-22644, 10.1029/98JD00349, 1998.

Sillman, S., Vautard, R., Menut, L., and Kley, D.: O_3-NO_x-VOC sensitivity and NO_x-VOC indicators in Paris: Results from models and Atmospheric Pollution Over the Paris Area (ESQUIF) measurements, Journal of Geophysical Research: Atmospheres, 108, 2003.

Silva, R. A., West, J. J., Zhang, Y., Anenberg, S. C., Lamarque, J.-F., Shindell, D. T., Collins, W. J., Dalsoren, S., Faluvegi, G., Folberth, G., Horowitz, L. W., Nagashima, T., Naik, V., Rumbold, S., Skeie, R., Sudo, K., Takemura, T., Bergmann, D., Cameron-Smith, P., Cionni, I., Doherty, R. M., Eyring, V., Josse, B., MacKenzie, I. A., Plummer, D., Righi, M., Stevenson, D. S., Strode, S., Szopa, S., and Zeng, G.: Global premature mortality due to anthropogenic outdoor air pollution and the contribution of past climate change, Environmental Research Letters, 8, 034005, 2013.

Singhal, A., and Parveen, M.: Air Flow Optimization via a Venturi Type Air Restrictor, Proceedings of the World Congress on Engineering, Vol III, London, U.K, 2013.

Sinha, B., Singh Sangwan, K., Maurya, Y., Kumar, V., Sarkar, C., Chandra, B. P., and Sinha, V.: Assessment of crop yield losses in Punjab and Haryana using 2 years of continuous in situ ozone measurements, Atmos. Chem. Phys., 15, 9555-9576, 2015.

Sinha, V., Williams, J., Crowley, J. N., and Lelieveld, J.: The Comparative Reactivity Method - a new tool to measure total OH Reactivity in ambient air, Atmos. Chem. Phys., 8, 2213-2227, 2008.

Spencer, K. M., McCabe, D. C., Crounse, J. D., Olson, J. R., Crawford, J. H., Weinheimer, A. J., Knapp, D. J., Montzka, D. D., Cantrell, C. A., Hornbrook, R. S., Mauldin Iii, R. L., and Wennberg, P. O.: Inferring ozone production in an urban atmosphere using measurements of peroxynitric acid, Atmos. Chem. Phys., 9, 3697-3707, 2009.

Spicer, C. W., Joseph, D. W., and Ollison, W. M.: A re-examination of ambient air ozone monitor interferences, Journal of the Air & Waste Management Association (1995), 60, 1353-1364, 2010.

Stemmler, K., Ammann, M., Donders, C., Kleffmann, J., and George, C.: Photosensitized reduction of nitrogen dioxide on humic acid as a source of nitrous acid, Nature, 440, 195-198, 2006.

Stemmler, K., Ndour, M., Elshorbany, Y., Kleffmann, J., D'Anna, B., George, C., Bohn, B., and Ammann, M.: Light induced conversion of nitrogen dioxide into nitrous acid on submicron humic acid aerosol, Atmos. Chem. Phys., 7, 4237-4248, 2007.

Stevenson, D. S., Dentener, F. J., Schultz, M. G., Ellingsen, K., van Noije, T. P. C., Wild, O., Zeng, G., Amann, M., Atherton, C. S., Bell, N., Bergmann, D. J., Bey, I., Butler, T., Cofala, J., Collins, W. J., Derwent, R. G., Doherty, R. M., Drevet, J., Eskes, H. J., Fiore, A. M., Gauss, M., Hauglustaine, D. A., Horowitz, L. W., Isaksen, I. S. A., Krol, M. C., Lamarque, J. F., Lawrence, M. G., Montanaro, V., Müller, J. F., Pitari, G., Prather, M. J., Pyle, J. A., Rast, S., Rodriguez, J. M., Sanderson, M. G., Savage, N. H., Shindell, D. T., Strahan, S. E., Sudo, K., and Szopa, S.: Multimodel ensemble simulations of present-day and near-future tropospheric ozone, Journal of Geophysical Research: Atmospheres, 111, 2006.

Stockwell, W. R., Kirchner, F., Kuhn, M., and Seefeld, S.: A new mechanism for regional atmospheric chemistry modeling, Journal of Geophysical Research: Atmospheres, 102, 25847-25879, 1997.

Stone, D., Whalley, L. K., Ingham, T., Edwards, P. M., Cryer, D. R., Brumby, C. A., Seakins, P. W., and Heard, D. E.: Measurement of OH reactivity by laser flash photolysis coupled with laser-induced fluorescence spectroscopy, Atmos. Meas. Tech., 9, 2827-2844, 2016.

Sullivan, R. C., Thornberry, T., and Abbatt, J. P. D.: Ozone decomposition kinetics on alumina: effects of ozone partial pressure, relative humidity and repeated oxidation cycles, Atmos. Chem. Phys., 4, 1301-1310, 2004.

Thornton, J. A., Wooldridge, P. J., and Cohen, R. C.: Atmospheric NO_2: in situ laser-induced fluorescence detection at parts per trillion mixing ratios, Analytical chemistry, 72, 528-539, 2000.

Thornton, J. A., Wooldridge, P. J., Cohen, R. C., Martinez, M., Harder, H., Brune, W. H., Williams, E. J., Roberts, J. M., Fehsenfeld, F. C., Hall, S. R., Shetter, R. E., Wert, B. P., and Fried, A.: Ozone production rates as a function of NO_x abundances and HO_x production rates in the Nashville urban plume, Journal of Geophysical Research: Atmospheres, 107, ACH 7-1-ACH 7-17, 2002.

Thornton, J. A., Wooldridge, P. J., Cohen, R. C., Williams, E. J., Hereid, D., Fehsenfeld, F. C., Stutz, J., and Alicke, B.: Comparisons of in situ and long path measurements of NO_2 in urban plumes, Journal of Geophysical Research: Atmospheres, 108, ACH 5-1 - ACH 5-12, 2003.

Tonnesen, G. S., and Dennis, R. L.: Analysis of radical propagation efficiency to assess ozone sensitivity to hydrocarbons and NO x : 2. Long-lived species as indicators of ozone concentration sensitivity, Journal of Geophysical Research: Atmospheres, 105, 9227-9241, 2000.

Tutty, O. R.: Nonlinear development of flow in channels with non-parallel walls, Journal of Fluid Mechanics, 326, 265-284, 1996.

Varotsos, C., and Cartalis, C.: Re-evaluation of surface ozone over Athens, Greece, for the period 1901–1940, Atmospheric Research, 26, 303-310, 1991.

Vingarzan, R.: A review of surface ozone background levels and trends, Atmospheric Environment, 38, 3431-3442, 2004.

Wainman, T., Weschler, C. J., Lioy, P. J., and Zhang, J.: Effects of surface type and relative humidity on the production and concentration of nitrous acid in a model indoor environment, Environmental science & technology, 35, 2201-2206, 2001.

Wei, W., Cheng, S., Li, G., Wang, G., and Wang, H.: Characteristics of volatile organic compounds (VOCs) emitted from a petroleum refinery in Beijing, China, Atmospheric Environment, 89, 358-366, 2014.

Whalley, L. K., Edwards, P. M., Furneaux, K. L., Goddard, A., Ingham, T., Evans, M. J., Stone, D., Hopkins, J. R., Jones, C. E., Karunaharan, A., Lee, J. D., Lewis, A. C., Monks, P. S., Moller, S. J., and Heard, D. E.: Quantifying the magnitude of a missing hydroxyl radical source in a tropical rainforest, Atmos. Chem. Phys., 11, 7223-7233, 2011.

Whalley, L. K., Blitz, M. A., Desservettaz, M., Seakins, P. W., and Heard, D. E.: Reporting the sensitivity of laser-induced fluorescence instruments used for HO_2 detection to an interference from RO_2 radicals and introducing a novel approach that enables HO_2 and certain RO_2 types to be selectively measured, Atmos. Meas. Tech., 6, 3425-3440, 2013.

WHO: 2006: Air quality guidelines: global update 2005, particulate matter, ozone, nitrogen dioxide and sulphur dioxide, World Health Organization, Regional Office for Europe, Copenhagen, Denmark, 2006.

WHO: 2008: Global tuberculosis control – surveillance, planning, financing, WHO report, World Health Organization, Regional Office for Europe, Copenhagen, Denmark, 2008.

WHO: 2013: Review of evidence on health aspects of air pollution – REVIHAAP Project Technical report, World Health Organization, Regional Office for Europe, Copenhagen, Denmark, 2013.

Williams, J., and Koppmann, R.: Volatile Organic Compounds in the Atmosphere: An Overview, in: Volatile Organic Compounds in the Atmosphere, Blackwell Publishing Ltd, 1-32, 2007.

Wilson, K. L., and Birks, J. W.: Mechanism and elimination of a water vapor interference in the measurement of ozone by UV absorbance, Environ. Sci. Technol., 40, 6361-6367, 2006.

WMO: 1998: World Meteorological Organization/United Nations Environment Programme report, Scientific Assessment of Ozone Depletion, WMO Global Ozone Research and Monitoring Project, Report No. 44, 1998.

Wood, E. C., and Charest, J. R.: Chemical Amplification - Cavity Attenuated Phase Shift Spectroscopy Measurements of Atmospheric Peroxy Radicals, Analytical chemistry, 86, 10266-10273, 2014.

Xing, J., Wang, S. X., Jang, C., Zhu, Y., and Hao, J. M.: Nonlinear response of ozone to precursor emission changes in China: a modeling study using response surface methodology, Atmos. Chem. Phys., 11, 5027-5044, 2011.

Xue, L. K., Wang, T., Gao, J., Ding, A. J., Zhou, X. H., Blake, D. R., Wang, X. F., Saunders, S. M., Fan, S. J., Zuo, H. C., Zhang, Q. Z., and Wang, W. X.: Ground-level ozone in four Chinese cities: precursors, regional transport and heterogeneous processes, Atmos. Chem. Phys., 14, 13175-13188, 2014.

Yarwood, G., Rao, S., Yocke, M., and Whitten, G. Z.: Updates to the Carbon Bond Mechanism: CB05, Final Report to the US EPA, RT-0400675, December 8, 2005.

Yarwood, G., Whitten, G. Z., Jung, J., Heo, G., and Allen, D. T.: Development, Evaluation and Testing of Version 6 of the Carbon Bond Chemical Mechanism (CB6) Final Report, prepared for Texas Commission on Environmental Quality, Work Order No. 582-587-84005-FY84010-84026, 2010.

Zahn, A., Weppner, J., Widmann, H., Schlote-Holubek, K., Burger, B., Kühner, T., and Franke, H.: A fast and precise chemiluminescence ozone detector for eddy flux and airborne application, Atmos. Meas. Tech., 5, 363-375, 2012.

Zannoni, N., Gros, V., Lanza, M., Sarda, R., Bonsang, B., Kalogridis, C., Preunkert, S., Legrand, M., Jambert, C., Boissard, C., and Lathiere, J.: OH reactivity and concentrations of biogenic volatile organic compounds in a Mediterranean forest of downy oak trees, Atmos. Chem. Phys., 16, 1619-1636, 2016.

Zaripov, R. B., Konovalov, I. B., Kuznetsova, I. N., Belikov, I. B., and Zvyagintsev, A. M.: WRF ARW and CHIMERE models for numerical forecasting of surface ozone concentration, Russian Meteorology and Hydrology, 36, 249-257, 2011.

Zhou, X., Gao, H., He, Y., Huang, G., Bertman, S. B., Civerolo, K., and Schwab, J.: Nitric acid photolysis on surfaces in low-NO_x environments: Significant atmospheric implications, Geophysical Research Letters, 30, 2003.

Zhou, X., Zhang, N., TerAvest, M., Tang, D., Hou, J., Bertman, S., Alaghmand, M., Shepson, P. B., Carroll, M. A., Griffith, S., Dusanter, S., and Stevens, P. S.: Nitric acid photolysis on forest canopy surface as a source for tropospheric nitrous acid, Nature Geosci, 4, 440-443, 2011.

Annex I

Schematics of the inlet and outlet flange of the flow tubes

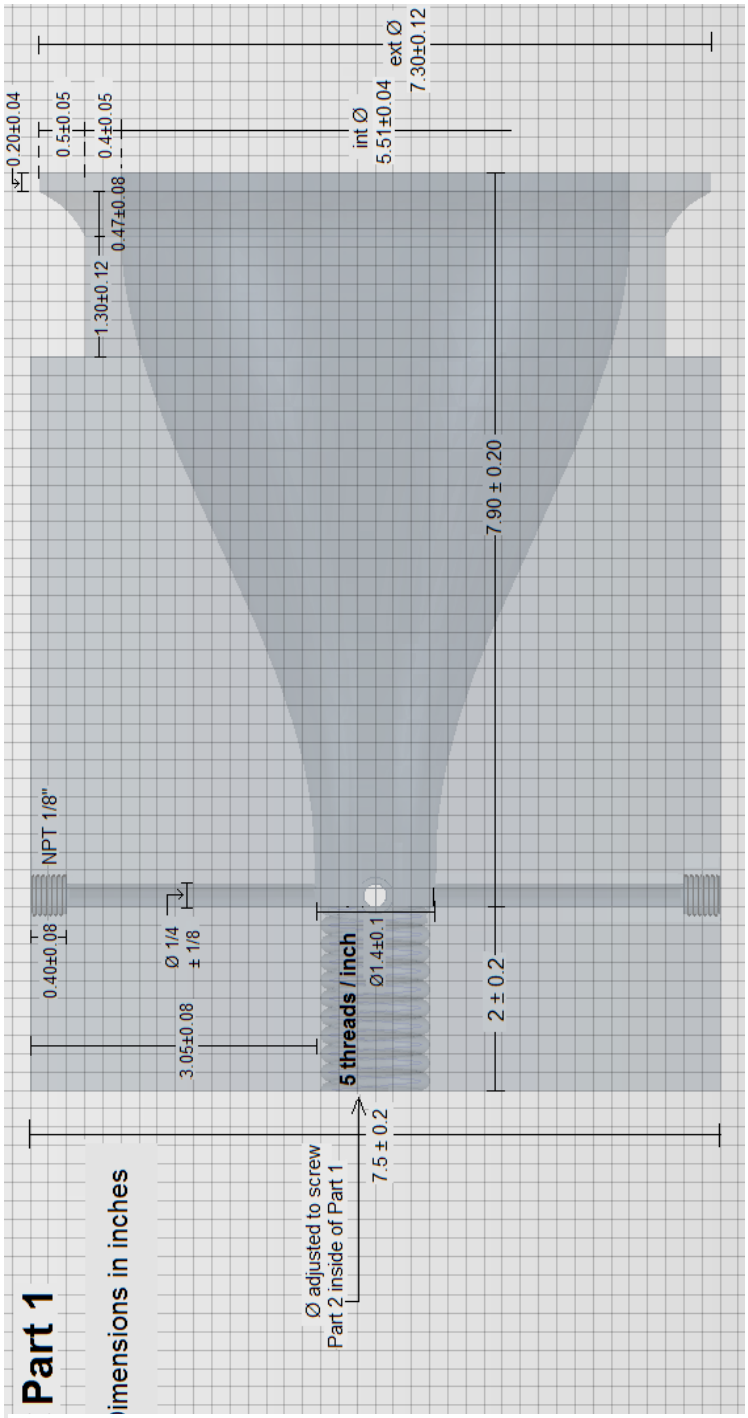

Figure I: Plane section Part 1 – dimensions

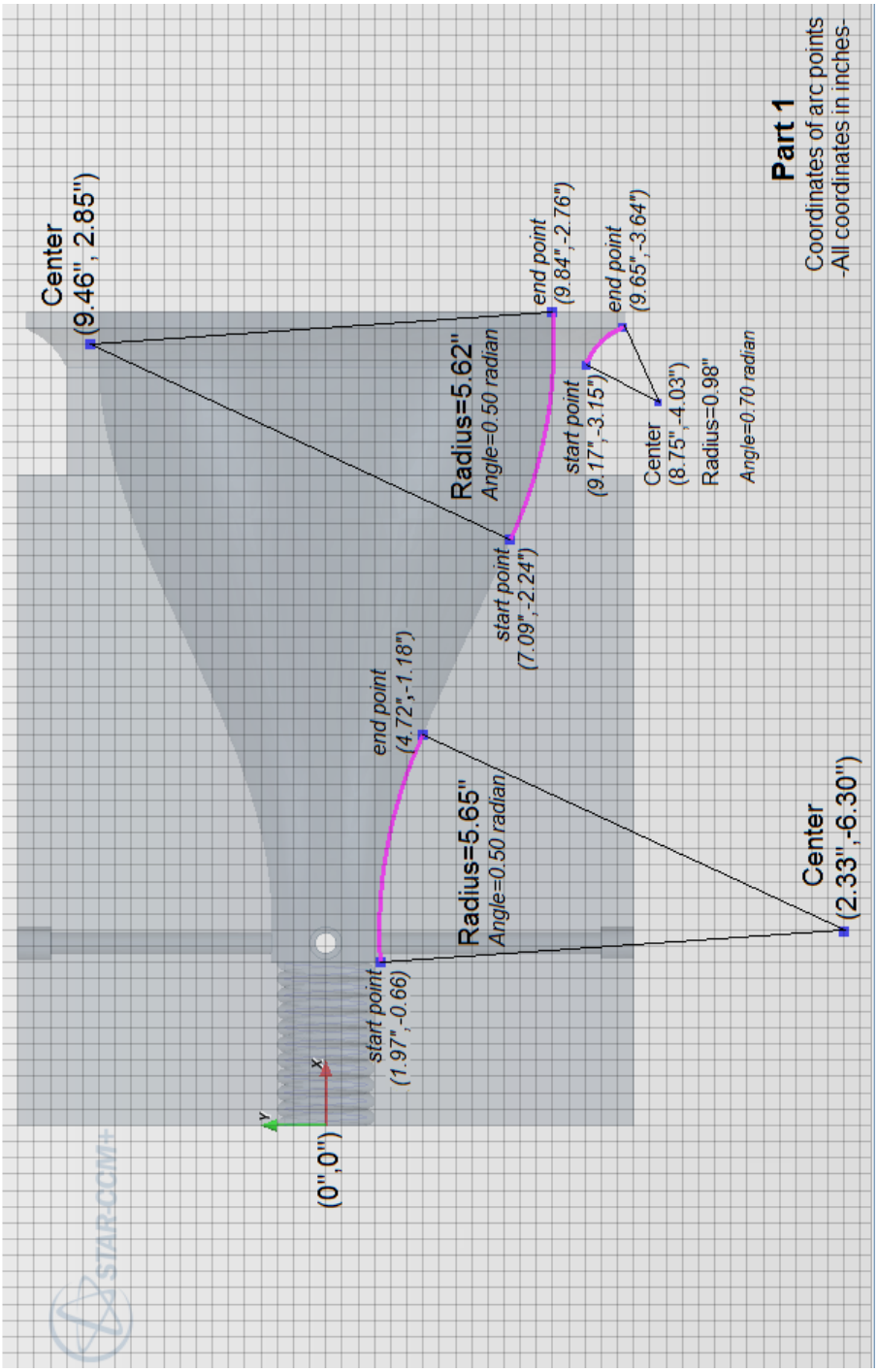

Figure II: Plane section Part 1 – curved parts

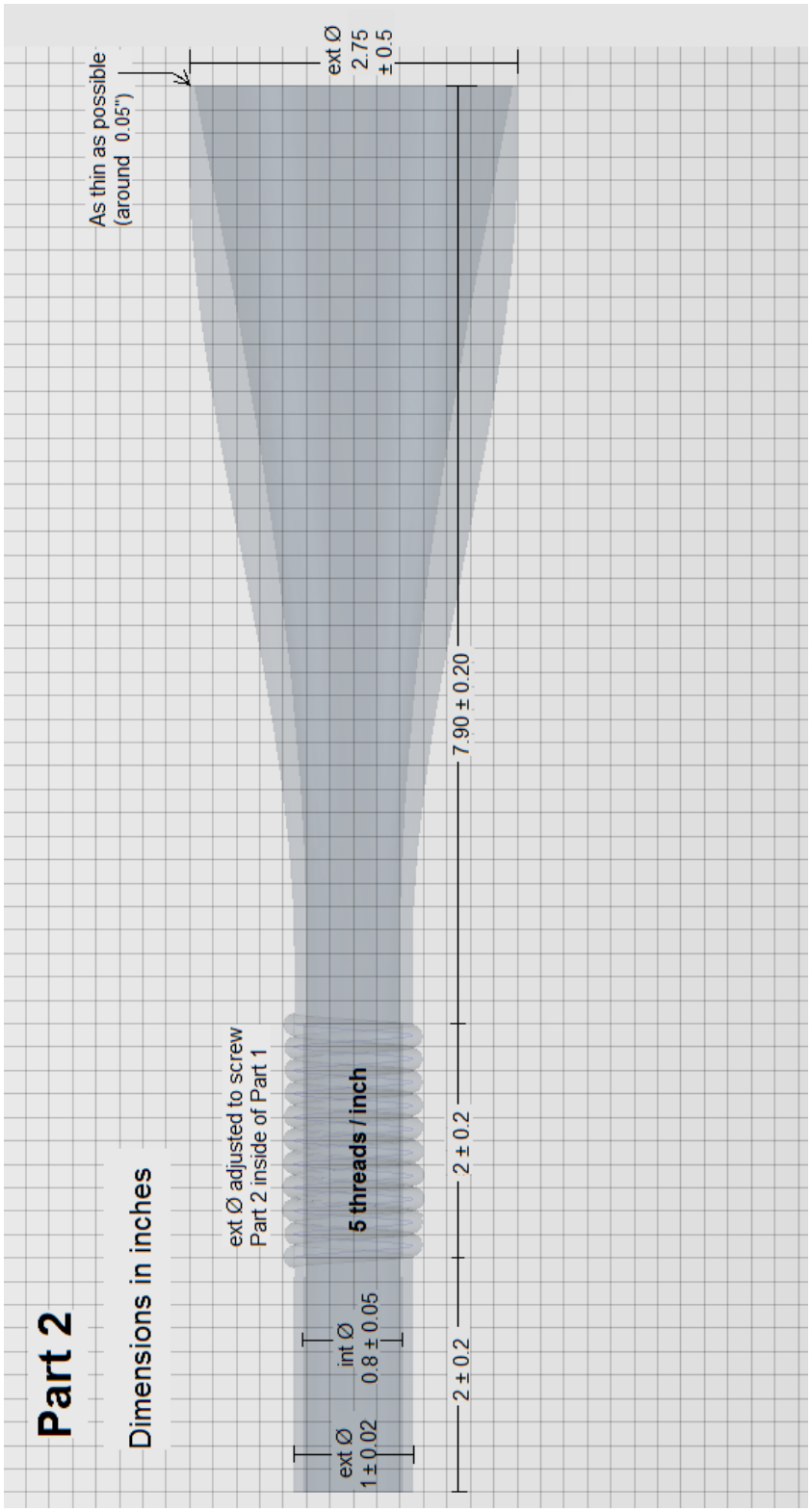

Figure III: Plane section Part 2 – dimensions

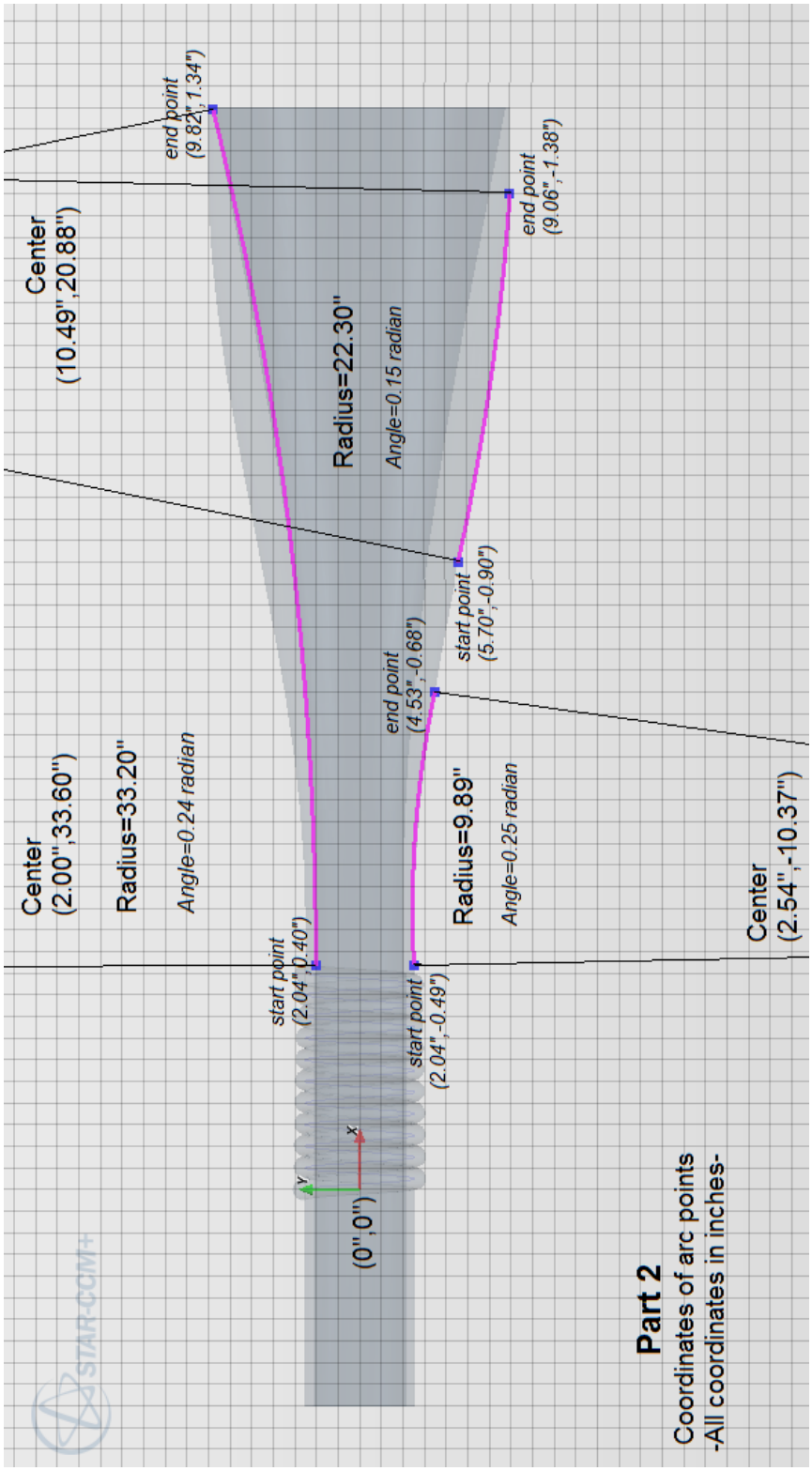

Figure IV:Plane section Part 2 – curved parts

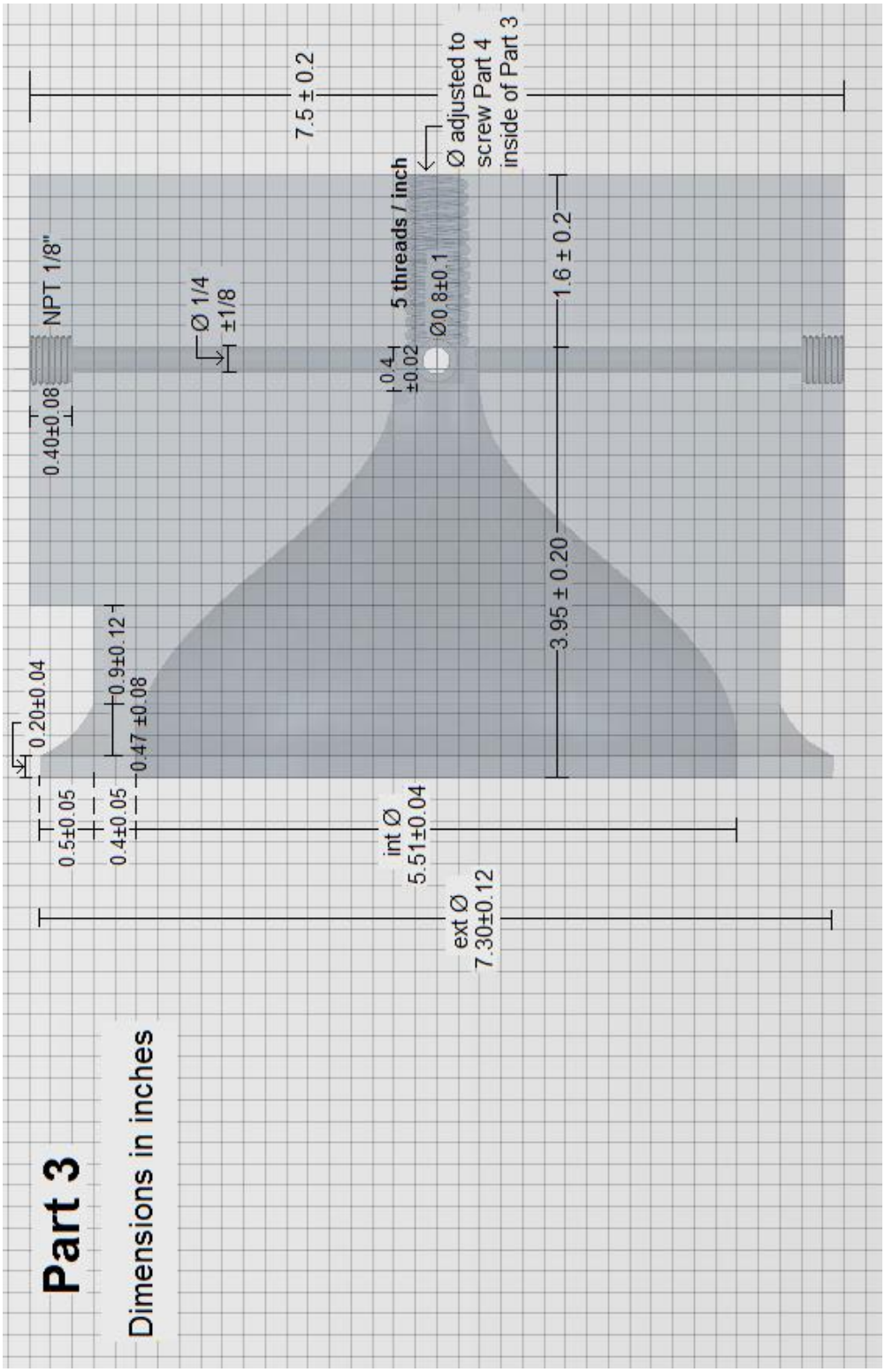

Figure V:Plane section Part 3 – dimensions

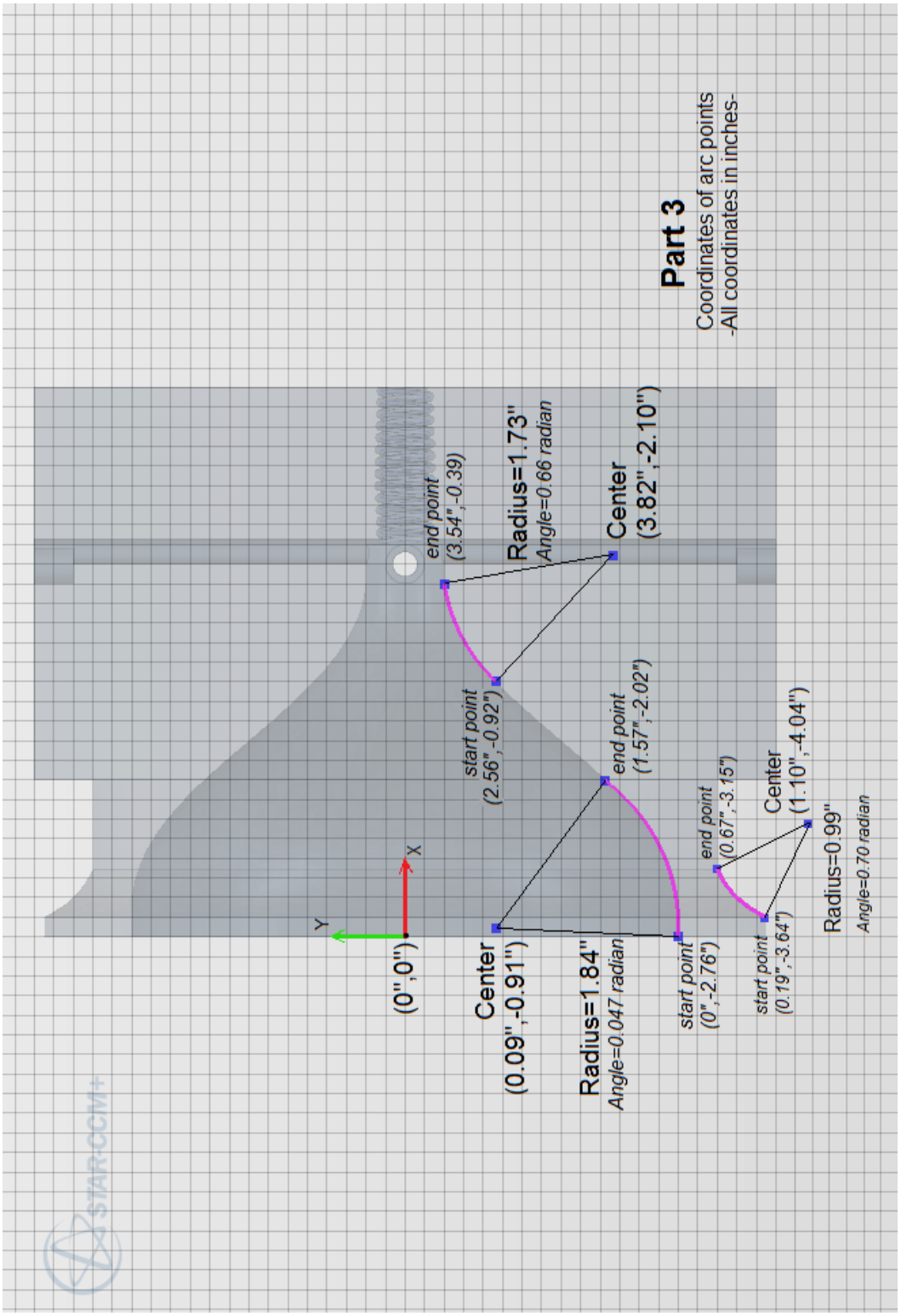

Figure VI:Plane section Part 3 – curved parts

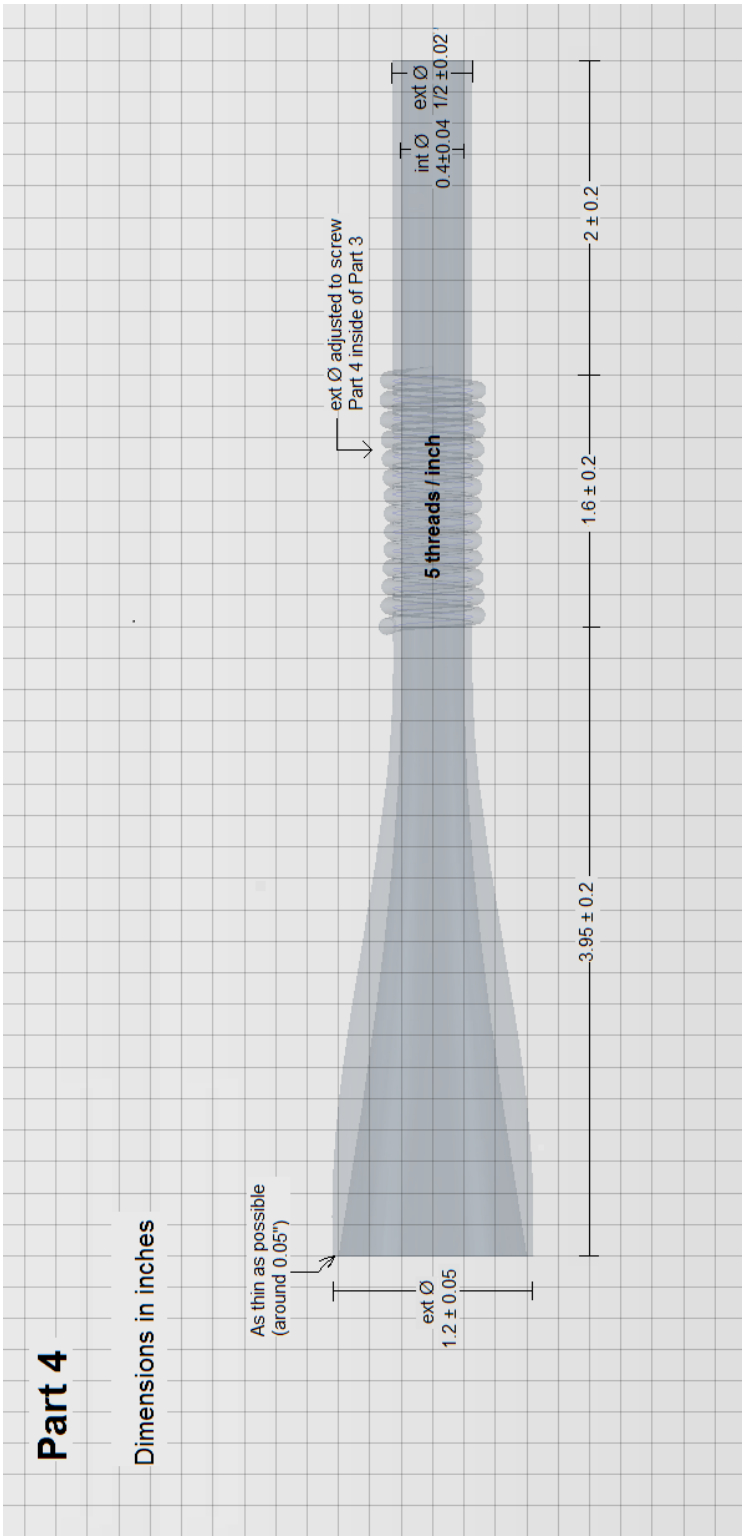

Figure VII:Plane section Part 4 – dimensions

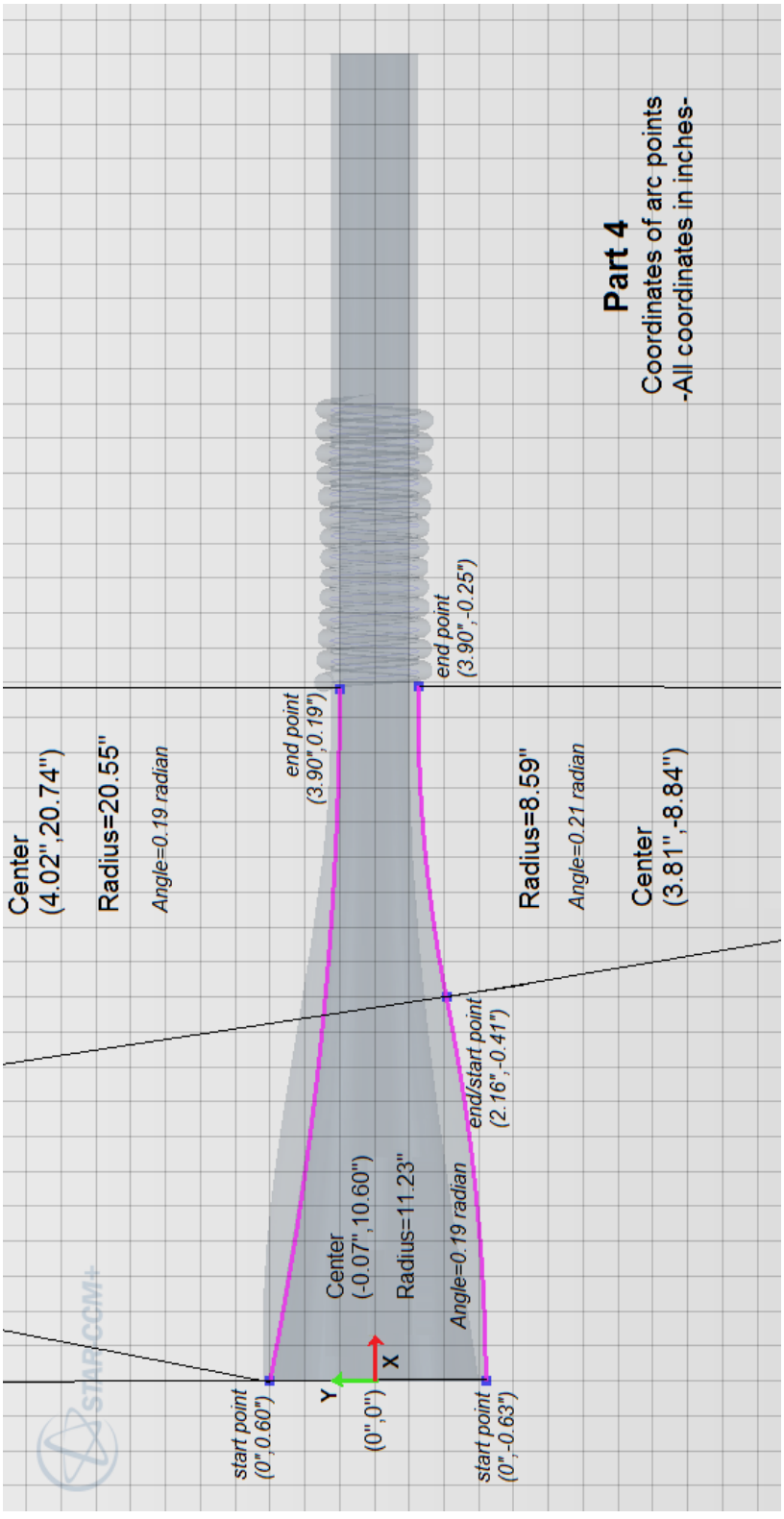

Figure VIII:Plane section Part 4 – curved parts

Annex II

Kintecus simulations

In order to verify that the experimental values of NO_2-to-O_3 conversion efficiency are consistent with our understanding of the NO_2-to-O_3 conversion process, the results of the 2-cell converter presented in Fig. 2.25, Chapter 2, were compared to simulations made using a simple chemical model in the simulation software Kintecus (Ianni, 2014).

Reactions that were introduced in the model are characteristic of the NO_x-O_3 photostationary state:

$$NO_2 \rightarrow NO + O \qquad (R1)$$

$$O + O_2 \rightarrow O_3 \qquad (R2)$$

$$O_3 + NO \rightarrow NO_2 + O_2 \qquad (R3)$$

The rate constants of R2 and R3 were determined from the literature, using the NIST (National Institute of Standards and Technology) Chemical Kinetics Database (Manion et al., 2015). The rate constant used were $2.81 \cdot 10^{-12}$ $cm^3 molecule^{-1} s^{-1}$ (Atkinson, 1989) and for $1.8 \cdot 10^{-14}$ $cm^3 molecule^{-1} s^{-1}$ (Atkinson et al., 2004) for R2 and R3 respectively. The photolysis rate of NO_2 due to exposure to the UV light was determined by adjusting its value in the model to reproduce the conversion efficiency observed for one particular experiment. The experimental data point used to determine the J-value was NO_2 mixing ratio of 75 ppb, where a conversion efficiency of 68.1% was measured at a flow rate of 1 L/min. A J-value of 0.128 s^{-1} was determined from this measurement and was used to model all the other measurements. The initial concentration of O_2 was set at $4.80 \cdot 10^{18}$ molecules/cm^3, equivalent to a mixing ratio of 20% at atmospheric pressure and 20°C, while the concentration of NO_2 was set according to experimental values. The simulations were then run for 1 min for each NO_2 mixing ratio, and the output was examined for different residence times to match with the 0.6, 1.0 and 1.3 L/min flow rates used in the experiments.

Figure IX shows the comparison of the experimental and the theoretical (simulated) values. The decrease of the conversion efficiency with the increase of the NO_2 mixing ratio is also shown by the simulations, as well as the increase of the conversion efficiency with the residence time. However, the simulations revealed larger relative differences between the different flow rates compared to the experiments.

A possible reason is that the residence time in the cells was not measured experimentally, but only determined by the geometrical characteristics of the cells and the measured flow rates. Since the different residence times differ only by a few seconds, an error of one or two seconds could have a large impact on the simulations, as shown by the dashed lines in Fig. IX.

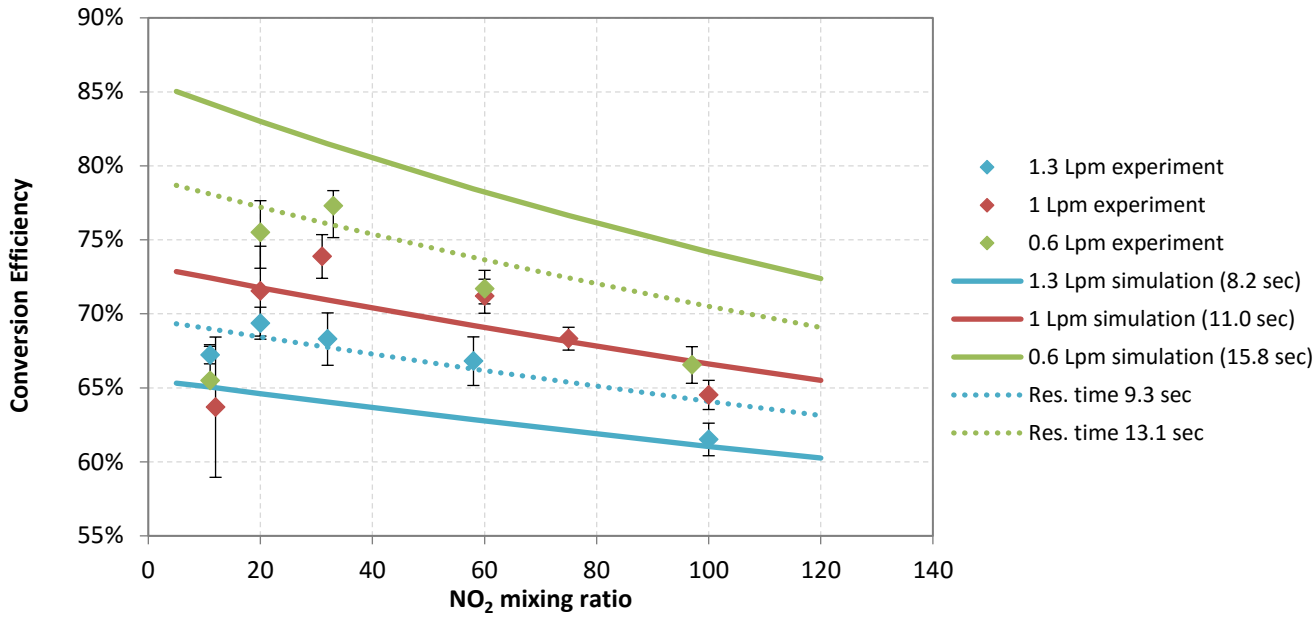

Figure IX: Comparison of the experimental data points with theoretical ones, obtained by Kintecus simulations for different residence times in the converter cells.

Annex III

RACM and RACM2 surrogates

Table I: RACM 2 species and surrogates from Griffith et al. (2016) that have been grouped to RACM surrogates for the CalNex modeling.

RACM surrogates	RACM 2 species	Definition
HC3	HC3	Alkanes, esters and alkynes with HO rate constant (298 K, 1 atm) less than $3.4x10^{-12}$ cm^3 s^{-1}
	EOH	Ethanol
	MOH	Methanol
	ACE	Acetylene
HC5	HC5	Alkanes, esters and alkynes with HO rate constant (298 K, 1 atm) between $3.4x10^{-12}$ and $6.8x10^{-12}$ cm^3 s^{-1}
	ROH	C3 and higher alcohols
TOL	TOL	Toluene and less reactive aromatics
	BEN	Benzene
XYL	XYM	M-xylene
	XYP	P-xylene
	XYO	o-xylene
ALD	ACD	Acetaldehyde
	ALD	C3 and higher aldehydes
	BALD	Benzaldehyde and other aromatic aldehydes
KET	ACT	Acetone
	MEK	Methyl ethyl ketone
	MVK	Methyl vinyl ketone

Annex IV

O_x scaling analysis

As mentioned in section 4.4.1, the O_3 measurements during IRRONIC were scaled to the O_x measurements of the CAPS in order to remove differences due to calibration or zeroing issues on the monitors and allow a direct comparison of the modeled O_x to the O_x measurments.

Assuming that the NO_2 measurements were correct, the measured O_3 in the reference flow tube was calculated as

$$O_{3_{ref.flow\ tube}} = O_{x_{ref.flow\ tube}} - NO_{2_{monitor}}$$

Then, the O_3 measured with the O_3 monitor was calibrated with the O_3 of the reference flow tube, as shown in Fig. X.

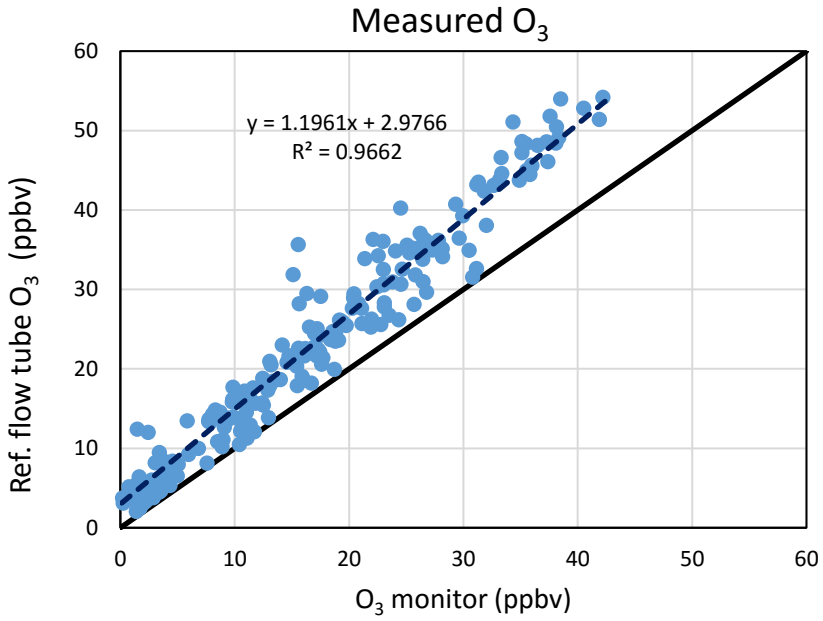

Figure X: Calibration curve of O_3 measured from the O_3 monitor

The calibrated O_3 values (O_3 calibrated = 1.196 × O_3 measured + 2.9766) were used to constrain the model during IRRONIC, in order to ensure better comparison with the O_x measured by the CAPS monitor.

Développement et déploiement sur le terrain d'un analyseur pour la mesure de la vitesse de formation d'ozone dans la troposphère

Résumé

L'ozone (O_3) troposphérique représente un enjeu environnemental majeur en raison de ses effets préjudiciables sur la santé humaine, la végétation et le climat. La formation photochimique de l'O_3 suit une chimie non linéaire complexe, qui rend la mise en œuvre de mesures de réduction difficile. Les pouvoirs publics s'appuient sur la modélisation afin d'élaborer des stratégies de réduction des précurseurs d'O_3, mais il existe encore des incertitudes importantes associées aux mécanismes chimiques utilisés dans les modèles. Une mesure directe de la vitesse de production de l'ozone, $P(O_3)$, permettrait de valider les mécanismes chimiques et de fournir des données en temps réel pour la réglementation.

L'objectif principal de cette thèse a été (i) de développer nos connaissances sur la mesure de $P(O_3)$ et (ii) d'étudier la chimie de l'ozone en air ambiant. Dans ce contexte, un instrument a été développé pour la mesure de $P(O_3)$, caractérisé en laboratoire et déployé sur le terrain. Le principe de l'instrument est basé sur une mesure différentielle de O_x (O_3+NO_2) entre deux réacteurs d'échantillonnage, le premier opérant comme un réacteur "de référence", sans production d'ozone, et le second reproduisant la chimie de formation d'ozone de l'air ambiant. La caractérisation de l'instrument a impliqué des expériences de laboratoire et de modélisation afin d'évaluer la justesse des mesures. L'instrument a également été déployé lors de la campagne IRRONIC afin d'étudier la sensibilité de $P(O_3)$ avec NO. La comparaison des mesures de terrain avec des valeurs modélisées a permis d'évaluer les performances et les limites de cet instrument et d'évaluer la faisabilité de la mesure de $P(O_3)$.

Mots-clés: chimie atmosphérique, ozone, sensibilité de la production d'ozone, développement instrumental, mesures in-situ, campagne de mesures, modèle de boite, qualité de l'air

Development and field deployment of an instrument to measure ozone production rates in the troposphere

Abstract

Ground level ozone (O_3) is a major environmental concern due to its detrimental impacts on human health, vegetation and climate. The photochemical formation of ozone follows a complex nonlinear chemistry that makes strategies for ozone reduction difficult to implement. Governments rely on atmospheric chemistry models to develop emission regulations, but there are still uncertainties associated with the chemical mechanisms used in these models. Direct measurements of ozone production rates, $P(O_3)$, is a new technique that can help validating current atmospheric chemical mechanisms and provide real-time data for emission regulations of ozone precursors.

The main objective of this thesis was (i) to advance the understanding of $P(O_3)$ measurements and (ii) to investigate the ozone production chemistry in ambient air. In this context, an instrument capable of $P(O_3)$ measurements was developed, characterized in the laboratory and deployed in the field. The principle of the instrument is based on differential O_x (=O_3+NO_2) measurements between two sampling reactors, one acting as a "reference" reactor with no O_3 production, and the other one reproducing the same O_3 production chemistry as in ambient air. The characterization of this instrument was performed through laboratory and modelling experiments to assess the accuracy of $P(O_3)$ measurements. Finally, the instrument was deployed during the IRRONIC campaign to investigate the $P(O_3)$ sensitivity to NO in a forested area. Comparison between measured and modeled $P(O_3)$ values allowed assessment of the performances and limitations of this new instrument and evaluate the feasibility of direct $P(O_3)$ measurements.

Keywords: atmospheric chemistry, ozone, ozone production sensitivity, instrumental development, in-situ measurements, field measurements, box modeling, air quality